

Perspective

Intestinal organoids as tools for enriching and studying specific and rare cell types: advances and future directions

Kim E. Boonekamp^{1, †}, Talya L. Dayton^{1, †}, and Hans Clevers^{1,2,*}

¹ Oncode Institute, Hubrecht Institute, Royal Netherlands Academy of Arts and Sciences (KNAW) and University Medical Centre (UMC) Utrecht, 3584 CT Utrecht, The Netherlands

² Princess Máxima Centre for Paediatric Oncology, 3584 CS Utrecht, The Netherlands

† These authors contributed equally to this work

* Correspondence to: Hans Clevers, E-mail: h.clevers@hubrecht.eu

Keywords

Organoids, cell types, intestine, signaling, *in vitro*

Adult tissue-derived organoids allow for the expansion and maintenance of primary epithelial cells in a near-native state. These 3-dimensional and self-organizing organotypic cultures derived from adult tissues have been increasingly used in fundamental and translational research. A key feature of this organoid system is that it recapitulates the stem cell lineage and thus, the differentiated cell type heterogeneity of the *in vivo* tissue of origin. Importantly, we and others have shown that organoids can be manipulated to expand different cell lineages, allowing for the study of rare cell types that would otherwise be very difficult to analyze. Here, focusing specifically on organoids of the small intestine, we discuss recent advances and future directions of this new avenue of organoid research. We highlight methods used to enrich for specific cell types including stem cells, enterocytes, Paneth cells, goblet cells, micro-fold (M)-cells, tuft cells, and enteroendocrine cells (EECs) in intestinal organoids, and focus on what each of these methods has taught us about the differentiation of adult intestinal stem cells (ISCs) to specific cell fates. Furthermore, we highlight how these new cell type-enriched intestinal organoids can be used to answer a diversity of questions relevant to human biology and disease.

The intestinal cellular landscape

The small intestine is part of the gastrointestinal tract and functions mainly in the digestion of food and absorption of nutrients. The inner lining of the intestine is made up of finger-like protrusions called villi, which maximize the absorptive surface. At the base of the villi are invaginations called crypts, which are home to the intestinal crypt columnar base cells (CBCs), the ISCs that contribute to self-renewal of the small intestinal epithelium and give rise to all the differentiated epithelial cell types in this tissue. There are six main cell types in the absorptive epithelium of the small intestine, which differ in their relative abundance and their location along the crypt–villus axis (Figure 1A). The cells with the highest abundance are the absorptive enterocytes, which make up ~80% of all epithelial cells. Paneth cells, which are secretory cells in the intestinal crypts, and mucus-producing goblet cells, which are found in both the crypt and villus account for ~3%–8% and 4%–12% of all intestinal epithelial cells, respectively. The cells with the lowest abundance include environment sensing M-cells (<1%), chemosensory tuft cells (0.4%–2%), and hormone-producing EECs (<1%) (Sternini, Anselmi and Rozengurt 2008; van der Flier and Clevers 2009; Gerbe, Legraverend and Jay 2012; Haber *et al.* 2017).

The small intestinal epithelium is the fastest self-renewing tissue in mammals and it has served as the principle model for the study of adult stem cell biology (van der Flier and Clevers 2009). Strict regulation of ISC maintenance and differentiation toward specific lineages is the result of different signaling microenvironments along the crypt–villus axis. While the signals that promote self-renewal and the stem cell state are restricted to the crypt, signals that drive differentiation can be found in different gradients along the villus axis. The primary signaling pathways involved in these processes include Wnt, Notch, bone morphogenic protein (BMP), and epidermal growth factor (EGF) signaling (Figure 1A). These signals are tightly regulated, and changes in the abundance or source of one or more often directly result in a disturbed balance in cell type abundance and/or intestinal homeostasis. Our knowledge of these signaling pathways and their role in ISC self-renewal have contributed to the development of adult tissue-derived intestinal organoids (discussed in more detail later). In turn, recent advances in our understanding of the essential minimal signals required for ISC fate specification have been made possible by the organoid system.

Wnt

Wnt signaling is essential for homeostatic ISC renewal in the intestine, and activating mutations of Wnt pathway components are often found in colorectal cancer (CRC) (The Cancer Genome Atlas 2012; Zhan, Rindtorff and Boutros 2017). Canonical Wnt signaling results in the transcription of target genes β -catenin/TCF/LEF. In the absence of Wnt ligands, β -catenin is targeted for degradation by a destruction complex. Binding of Wnt ligands to Frizzled receptors and LRP5/6 at the plasma membrane inactivates the destruction complex, leading to accumulation of β -catenin and its translocation to the nucleus, where it binds to TCF/LEF transcription factors and activates target gene expression.

The importance of Wnt target gene expression to ISCs was first demonstrated by the finding that knockout of *Tcf4* in mice resulted in loss of nearly all proliferative crypts (Korinek *et al.* 1998). Since then, it has been shown that Wnt signaling regulates the expression of a number of genes involved in stem cell maintenance and proliferation. Some of these Wnt target genes include genes that act as positive and negative feedback regulators of the pathway (Zhan, Rindtorff and Boutros 2017). The Wnt target genes, *Rnf43* and *Znrf3*, for example, encode for ubiquitin ligases that downregulate Wnt pathway activity by enabling downregulation of the Frizzled receptors at the plasma membrane (Koo *et al.* 2012). *Lgr5*, a cell surface receptor involved in positive regulation of Wnt signaling, is also a Wnt target gene. Secreted R-

spondin proteins bind to Lgr5 and together they sequester Rnf43/Znrf3, thereby potentiating Wnt signaling by removing inhibitory signals (Lau *et al.* 2011).

Wnt3 ligands secreted by Paneth cells and Wnt2B and R-spondin1 ligands secreted by the subepithelial mesenchyme surrounding the crypt restrict Wnt pathway activation to the crypts (Sato *et al.* 2011a; Farin, van Es and Clevers 2012; Moor *et al.* 2016). Importantly, these ligands act in a non-redundant, cooperative manner to regulate ISC maintenance and self-renewal. Wnt ligands are required to prime ISCs to express Lgr5 and therefore are responsive to potentiate the pathway by R-spondin (Yan *et al.* 2017). The cooperative action of these two ligands further ensures tight regulation of Wnt pathway activation in the intestine.

BMP

BMP signals have also been shown to be important for the control of intestinal tissue homeostasis, and mutations in BMP pathway components are highly associated with CRC (The Cancer Genome Atlas 2012). Upon binding of BMP ligands to BMP receptors (BMPRs) at the cell surface, an intracellular signaling cascade is enabled resulting in SMAD phosphorylation and transcription of BMP target genes. In the intestine, the main BMP ligands, BMP2 and BMP4, are expressed in the mesenchyme and epithelium of the villus. Likewise, BMPRs are also expressed in both the epithelium and mesenchyme of the small intestine, suggesting the importance of this pathway to both of these cellular compartments. The main BMPR in the intestinal epithelium is BMPR1A. BMP inhibitors Noggin, Gremlin 1/2, and Chordin-like 1 are produced in the mesenchyme underlying the crypt (Wang and Chen 2018). As a result, BMP pathway activation is the highest at the villus tip and decreases along the villus axis toward the crypt. The first indication that BMP signaling inhibits the ISC identity was the finding that transgenic mice expressing *Xenopus* Noggin formed ectopic crypts in the villi (Haramis *et al.* 2004). Similarly, loss of BMPR1A in the intestinal epithelium resulted in expansion of the ISC compartment in mice (Qi *et al.* 2017).

Notch

Notch signaling has been shown to both promote ISC self-renewal and homeostasis and regulate cell fate decisions. Furthermore, activated Notch signaling has been observed in CRC (Noah and Shroyer 2013). Notch signaling occurs via cell–cell contact. Binding of any of the five canonical Notch ligands to any of the four Notch receptors results in γ -secretase-mediated proteolytic cleavage of the receptor and release of the Notch intracellular domain (NICD). The NICD then translocates to the nucleus where it binds to the DNA binding

protein, RBPjk, and activates transcription of Notch target genes. Direct Notch target genes include the hairy/enhancer of split (HES) class of transcriptional repressors, which, upon activation, act as Notch signaling effectors.

While Notch ligands DLL1 and DLL4 are presented by Paneth cells and secretory progenitor cells, Notch receptors such as NOTCH1 are expressed by ISCs, and their interactions in the crypt contribute to stem cell maintenance. Notch signaling is also involved in cell type specification in the intestine. Whereas active Notch signaling in cells undergoing specification promotes the absorptive cell fate, lack of Notch signals leads to induction of a secretory cell fate via expression of *Math1*, the main transcription factor involved in determining secretory lineages (Noah and Shroyer 2013). Once specified, secretory progenitors upregulate the expression of Notch ligands and therefore promote the absorptive cell fate in surrounding cells. Inactivation of the Notch effectors, *Hes1*, *Hes3*, and *Hes5*, in mice resulted in decreased proliferation and increased differentiation toward the secretory lineage (Ueo *et al.* 2012).

EGF

EGF signaling is one of the major contributors to ISC proliferation, and mutations in EGF pathway components, including EGF receptor (EGFR) and the downstream effector, KRAS, are frequent in CRC (The Cancer Genome Atlas 2012). Binding of EGF to its receptors EGFR/ErbB1 and other ErbB family members induces tyrosine kinase activity and activates downstream pro-proliferative and pro-survival signaling cascades, such as those of the MAPK and PI3K pathways. In the intestine, EGF ligands are produced by Paneth cells and the mesenchyme underlying the crypt. The ISCs, in turn, co-express EGFRs (ErbB family) and their negative regulator, leucine-rich repeats and immunoglobulin-like domains protein 1 (LRIG1). The importance of this co-expression to maintaining ISC homeostasis is highlighted by the fact that *Lrig1* knockout mice show both increased EGFR activation and crypt hyperplasia (Wong *et al.* 2012).

***In vitro* modeling of the intestine in organoid cultures**

In 2009, Sato and colleagues applied what was known about the ISC niche to grow small intestinal epithelium from isolated ISCs. The resulting culture system, which was based on growing isolated ISCs in extracellular matrix and a specific growth factor cocktail, was referred to as intestinal adult stem cell organoid culture technology (Sato *et al.* 2009). The

specific growth factor cocktail consisted of EGF, R-spondin, and the BMP antagonist Noggin, which was therefore termed ENR. Modification of this medium by providing additional components allowed for the expansion of human small intestinal and colon organoids (Sato *et al.* 2011b). Under basal growth conditions, mouse and human intestinal organoids show cell type heterogeneity similar to that of the tissue of origin. Over the years, through further modification of the system, a diverse array of adult tissue-derived cultures from other epithelial tissues and from many different kinds of tumors have been successfully established (Kretzschmar and Clevers 2016). It is important to note that similar organoid structures can also be derived from induced pluripotent stem cells (iPSCs), and these culture systems have contributed significantly to our understanding of stem cell biology and disease (Kretzschmar and Clevers 2016). For the purposes of this perspective article, we will focus on adult tissue-derived intestinal organoids.

Mouse and human small intestinal organoids have been used in a wide variety of applications including disease modeling, regenerative medicine, drug screening, and proof of concept correction of genetic defects *in vitro*. An exciting new application for adult tissue-derived organoids is the study of rare cell types and how these contribute to human biology and disease.

***In vitro* cell type enrichment in intestinal organoids**

Under basic conditions, murine intestinal organoids contain ISCs, Paneth cells, goblet cells, EECs, and enterocytes with the abundance similar to that in the *in vivo* tissue. To allow for research into specific (and rare) cell types, intestinal organoid protocols have been adapted to push cellular homeostasis within the organoid toward specific cell fates.

Primary epithelial cell types of the intestine: stem cells, enterocytes, Paneth cells, and goblet cells

Stem cells and enterocytes. Stem cell-enriched organoid cultures are a prime example of this (Figure 1B). Addition of Wnt3A-conditioned medium to the standard ENR medium (WENR medium) results in stem cell-enriched organoids that homogeneously proliferate (Sato *et al.* 2011b). Intestinal organoid cultures can be even further enriched for stem cells by simultaneous stimulation of Wnt signaling and activation of the Notch pathway through addition of the GSK3 β -inhibitor CHIR990221 (CHIR) and the HDAC inhibitor valproic acid (ENR-CV medium) (Yin *et al.* 2014). Similarly, organoid cellular homeostasis can be pushed

in the opposite direction, by simply removing the Wnt potentiator, R-spondin, from the standard ENR medium (EN medium), thereby recapitulating the absence of Wnt signaling in the villi *in vivo* (Yin *et al.* 2014). These stem cell-enriched and stem cell-depleted intestinal organoid cultures have been exploited to identify defining features of stem cells vs. differentiated cells and to further understand the molecular mechanisms that drive differentiation. For example, through multi-omic analysis of standard ENR, stem cell-enriched CV-ENR, and enterocyte-enriched EN organoids, researchers identified the transcription factor hepatocyte nuclear factor 4 gamma (Hnf4g) as a driver of differentiation towards the enterocyte lineage (Lindeboom *et al.* 2018).

Paneth and goblet cells. Paneth and goblet cells are two related cell types of the secretory lineage with different functions. In addition to acting as anti-microbial cells that produce lysozyme and various defensins, Paneth cells function as niche cells that surround ISCs in the crypts and provide growth signaling molecules that are required for ISC proliferation and maintenance (Sato *et al.* 2011a). Goblet cells produce mucus, which lubricates the intestinal lining and serves as a protective layer against mechanical and biological damage and pathogen entry. As mentioned above, absence of Notch signaling during cell type specification leads to differentiation toward a secretory cell fate (Noah and Shroyer 2013). The Wnt signaling context under which a cell experiences absence of Notch signaling determines which of these specific secretory cell types, Paneth cell or goblet cell, is generated. Consistent with their location along the crypt–villus axis *in vivo*, Paneth cells, found in the crypt, are dependent on high Wnt signaling, while goblet cells, found mostly, though not exclusively, along the villus are not (Farin, van Es and Clevers 2012; Yin *et al.* 2014).

Addition of the NOTCH inhibitor DAPT to stem cell-enriched murine intestinal organoids promotes secretory cell differentiation but does not appear to favor one secretory lineage vs. the other beyond what would be expected given the natural abundance of each lineage *in vivo*. However, simultaneous addition of DAPT and CHIR (ENR+CD), to stimulate the Wnt pathway in these cultures, results in a clear preference for Paneth cell differentiation (Figure 1B) (Yin *et al.* 2014). Simultaneous addition of DAPT and the Wnt pathway inhibitor IWP2 (ENR+DI), on the other hand, results in intestinal organoid cultures in which goblet cell differentiation is favored (Figure 1B) (Yin *et al.* 2014). This system has been used to identify cell type-specific regulators of Paneth and goblet cells through transcriptomic analysis and comparison of ENR organoids to Paneth and goblet cell-enriched organoids (Treveil *et al.*

2019). In a separate study, using single-cell RNA sequencing (scRNA-seq) of ENR organoids, Paneth cell-enriched organoids, and freshly isolated primary mouse intestine tissue, researchers identified *Nupr1* as a potentially important transcription factor for the survival and development of Paneth cells (Mead *et al.* 2018).

Rare intestinal epithelial cell types: M-cells, tuft cells, and EECs

M-cells. M-cells are specialized epithelial cells located in the follicle associated epithelium (FAE) overlaying gut associated lymphoid tissue (GALT), including Peyer's patches (PP) and isolated lymphoid follicles (ILF). In the FAE, M-cells function as gatekeeper cells, sampling antigens from the intestinal lumen and transferring them to lymphocytes in the GALT where immune surveillance takes place (Randall, Carragher and Rangel-Moreno 2008). The direct lineage relationship between *Lgr5*⁺ ISCs and M-cells was first established in 2012 through genetic lineage tracing of *Lgr5*⁺ cells in mice (de Lau *et al.* 2012). In the same study, researchers showed that treatment of intestinal organoids with RANKL, a cytokine that is expressed by the reticular cells below the FAE, resulted in increased M-cell differentiation in these cultures. This was the first example of an intestinal organoid culture system enriched for a very rare cell type.

The authors of this study further showed that RANKL-induced M-cell differentiation of ISCs in organoids was dependent on expression of the Ets transcription factor *SpiB* – a finding consistent with their observation *in vivo* that *SpiB*^{-/-} mice lack M-cells (de Lau *et al.* 2012). This differentiation protocol was later applied in combination with scRNA-seq to identify an M-cell-specific gene expression signature, which was previously not possible due to scarcity of these cells *in vitro* (Haber *et al.* 2017).

Tuft cells. Chemosensory tuft cells are rare cells in the small intestinal epithelium with an abundance of <2%. In mice, these cells have been shown to orchestrate type-2 immune responses to a variety of stimuli, including infection with the parasite Helminth (Gerbe *et al.* 2016; Howitt *et al.* 2016). The tuft cell-mediated type-2 immune response to Helminth infection was accompanied by an expansion of tuft cell number, implicating a positive feedback loop in which tuft cell activation resulted in further differentiation of stem cells toward the tuft cell fate. Interleukin-4 receptor α (IL-4R α) signaling is important for type-2 immune responses to Helminth infection, and treatment of mice with recombinant IL-4 and IL-13, two cytokines that signal through IL-4R α , was sufficient to induce expansion of both

goblet and tuft cells *in vivo* (Gerbe *et al.* 2016). Stimulation of intestinal organoid cultures with recombinant IL-4 and/or IL-13 led to an increase of goblet and tuft cells *in vitro*, suggesting that tuft cell responses to immune signaling can be recapitulated in organoids. These experiments in organoids confirmed the data from *in vivo* experiments in mice and concurrently provided a new ISC differentiation protocol that can be used as a tool to enrich and study tuft cells *in vitro*. Through scRNA-seq profiling of mouse small intestinal epithelium, Haber *et al.* (2017) identified two subtypes of tuft cells, tuft-1 and tuft-2, which were characterized by a neuronal-like signature and an immune-like signature, respectively. Enrichment for tuft cells in human small intestinal organoids by stimulation with IL-4 and IL-13 might allow researchers to not only identify similar heterogeneity in human tuft cells but also perform functional analyses of these cells in a defined *in vitro* system.

EECs. Among the rare cell types of the intestinal epithelium, EECs show the highest degree of complexity. Based on their hormone expression patterns, EECs can be divided into seven major lineages, K-cells, L-cells, delta-cells, X-cells, I-cells S-cells, and N-cells. Classification based on combinatorial expression patterns of different EEC-produced hormones, however, can result in up to 20 subtypes (Habib *et al.* 2012, 2017). These numbers support the need for a method to enrich the full diversity of EECs *in vitro*. Studies in intestinal organoids have provided fundamental insights into the cellular signals and transcriptional programs that drive EEC differentiation.

In particular, shRNA-mediated knockdown of the transcription factor Neurogenin 3 (*NEUROG3*) in human iPSC-derived intestinal organoids confirmed previous studies in mice showing that *Neurog3* is required for EEC development (Spence *et al.* 2011). Furthermore, overexpression of *NEUROG3* in the same system showed that it is also sufficient to induce EEC differentiation in human cells.

EEC differentiation in murine adult tissue-derived organoids has been achieved by applying an EEC differentiation cocktail for combined inhibition of Notch, Wnt, and MAPK signaling (Figure 1B) (Basak *et al.* 2014). Importantly, this system recapitulates the EEC subtype distribution observed *in vivo* across the length of the small intestine, i.e. ileum-derived organoids favor ileal EEC subtypes and duodenum-derived organoids favor duodenal EEC subtypes. Likewise, a follow-up study showed that while the original EEC differentiation cocktail gave rise to EEC subtypes found in the crypt region including GLP-1-producing L-cells, stimulation of organoids with the EEC differentiation cocktail and BMP4 resulted in EECs consistent with those found in the villus, such as Secretin (*Sct*)-producing S-cells

(Beumer *et al.* 2018). Treatment of mice with an inhibitor of the BMP receptor, BMPRI1A, resulted in the loss of S-cells concomitant with an increase in L-cells specifically in the villus. This EEC differentiation protocol for intestinal organoids has also proven useful for assessing gene function in the context of EEC differentiation. Using scRNA-seq of sorted EECs at different stages of their differentiation trajectory from early NEUROG3-expressing cell to mature EEC, researchers characterized spatiotemporal gene expression in the EEC lineage and identified potential regulators of the process. CRISPR-based knockout of these candidate regulators of EEC differentiation in mouse intestinal organoids followed by induction of EEC differentiation in knockout organoids allowed researchers to assess their function. Knockout of *Rfx6* and *Tox3* in mouse intestinal organoids, for example, resulted in skewed EEC subtype specification upon EEC differentiation (Gehart *et al.* 2019).

Future perspectives

The ability to easily modify *in vitro* organoid cultures by modulating the media composition and thereby influencing their differentiation state has made it possible to perform experiments on cells that are too sparse *in vivo* to study (Figure 2). Enrichment for specific cell types in organoids has increased the feasibility of performing large-scale single-cell transcriptomic analysis of specific cell types along their differentiation trajectory from stem cell to mature differentiated cell. Furthermore, organoid differentiation protocols provide a platform for the study of cell type-specific responses to external soluble stimuli such as small molecules and drugs. As certain pathogens are known to infect only specific cell types that harbor expression of certain membrane proteins, it is easy to imagine how organoids enriched for specific cell types might serve as a platform to study mechanisms of infection as well as cell type-specific responses to infection *in vitro*. Some of the examples we have provided here highlight how organoids enriched for specific cell types can be used for faster assessment of gene function and phenotypes in rare cell types than is possible *in vivo*.

Small intestinal organoids enriched for EECs could, for example, be challenged with panels of small molecules to identify those that stimulate the production and secretion of specific hormones. *In vitro* insights into the molecular mechanisms that drive hormone production and secretion could potentially be translated to the clinic for patients in need of more hormone production. Small molecules that enrich and activate L-cells, which produce GLP-1, a hormone that induces the release of insulin, could be used to treat diabetic patients. Similar

scenarios can be envisioned for tuft cell-enriched organoids, which could be used in combination with type-2 immune response stimuli to elucidate tuft cell intrinsic mechanisms of type-2 immune responses or to model how these responses might be overactivated in immune-mediated diseases.

Altogether, the studies emphasized here exemplify how *in vivo* systems can be used to inform the development of *in vitro* organoid models of specific differentiation states to support the study of rare cell types. The ability to drive ISC differentiation toward specific rare cell type lineages by modulating the media components of organoid cultures has made the study of these specific cell types more accessible. Whereas previously, the primary means of studying rare cell types was the use of model organisms or fresh human tissue in combination with surface marker or genetic lineage label-based isolation, rare cell type-enriched organoids have made it possible to study these cell types sometimes even at the level of bulk organoid cultures. Furthermore, while still more labor intensive than 2-dimensional cell lines, organoids are more easily manipulated than an entire organism, and the system opens the door to studying rare cell types in the context of a more simplified cellular milieu allowing researchers to distill specific cell–cell interactions and dynamics. In the future, the complexity of this cellular milieu could be increased in a stepwise manner. Cell type-enriched organoids could be co-cultured with specific cellular components of the non-epithelial microenvironment, such as fibroblasts or specific immune cell types, to study the crosstalk of specific epithelial cell types with their microenvironment. Moreover, many of the differentiation protocols highlighted here have not yet been exploited to their full potential. In the next few years, we envisage rapidly growing implementation of these systems and others in both basic and clinical research.

References

- Basak O, van den Born M, Korving J *et al.* Mapping early fate determination in Lgr 5⁺ crypt stem cells using a novel Ki67-RFP allele. *2014*;**33**:1–12.
- Beumer J, Artegiani B, Post Y *et al.* Enteroendocrine cells switch hormone expression along the crypt-to-villus BMP signalling gradient. *Nat Cell Biol* 2018;**20**:909–16.
- Farin HF, van Es JH, Clevers H. Redundant sources of Wnt regulate intestinal stem cells and promote formation of paneth cells. *Gastroenterology* 2012;**143**:1518–29.
- van der Flier LG, Clevers H. Stem Cells, Self-Renewal, and Differentiation in the Intestinal Epithelium. *Annu Rev Physiol* 2009;**71**:241–60.
- Gehart H, van Es JH, Hamer K *et al.* Identification of enteroendocrine regulators by real-time single-cell differentiation mapping. *Cell* 2019;**176**:1158–73.

- Gerbe F, Legraverend C, Jay P. The intestinal epithelium tuft cells: specification and function. *Cell Mol Life Sci* 2012;**69**:2907–17.
- Gerbe F, Sidot E, Smyth DJ *et al.* Intestinal epithelial tuft cells initiate type 2 mucosal immunity to helminth parasites. *Nature* 2016;**529**:226–30.
- Haber AL, Biton M, Rogel N *et al.* A single-cell survey of the small intestinal epithelium. *Nat Publ Gr* 2017;**551**:333–9.
- Habib AM, Richards P, Cairns LS *et al.* Overlap of endocrine hormone expression in the mouse intestine revealed by transcriptional profiling and flow cytometry. *Endocrinology* 2012;**153**:3054–65.
- Haramis A-PG, Begthel H, van den Born M *et al.* De novo crypt formation and juvenile polyposis on BMP inhibition in mouse intestine. *Science* 2004;**303**:1684–6.
- Howitt MR, Lavoie S, Michaud M *et al.* Tuft cells, taste-chemosensory cells, orchestrate parasite type 2 immunity in the gut. *Science* 2016;**351**:1329–1333.
- Koo B-K, Spit M, Jordens I *et al.* Tumour suppressor RNF43 is a stem-cell E3 ligase that induces endocytosis of Wnt receptors. *Nature* 2012;**488**:665–9.
- Korinek V, Barker N, Moerer P *et al.* Depletion of epithelial stem-cell compartments in the small intestine of mice lacking Tcf-4. *Nat Genet* 1998;**19**:379–83.
- Kretzschmar K, Clevers H. Review Organoids: Modeling development and the stem cell niche in a dish. *Dev Cell* 2016;**38**:590–600.
- Lau W De, Barker N, Low TY *et al.* Lgr5 homologues associate with Wnt receptors and mediate R-spondin signalling. *Nature* 2011;**138648**:3–8.
- de Lau W, Kujala P, Schneeberger K *et al.* Peyer's patch M cells derived from Lgr5⁺ stem cells require SpiB and are induced by RankL in cultured "miniguts." *Mol Cell Biol* 2012;**32**:3639–47.
- Lindeboom RGH, van Voorthuijsen L, Oost KC *et al.* Integrative multi-omics analysis of intestinal organoid differentiation. *Mol Syst Biol* 2018;**14**:1–16.
- Mead BE, Ordovas-Montanes J, Braun AP *et al.* Harnessing single-cell genomics to improve the physiological fidelity of organoid-derived cell types. *BMC Biol* 2018;**16**:1–24.
- Moor AE, Cantu C, Aguet M *et al.* Wnt ligands secreted by subepithelial mesenchymal cells are essential for the survival of intestinal stem cells and gut homeostasis. *Cell Report* 2016:911–8.
- Noah TK, Shroyer NF. Notch in the intestine: regulation of homeostasis and pathogenesis. *Annu Rev Physiol* 2013;**75**:263–88.
- Qi Z, Li Y, Zhao B *et al.* BMP restricts stemness of intestinal Lgr5⁺ stem cells by directly suppressing their signature genes. *Nat Commun* 2017;**7**:1–14.
- Randall TD, Carragher DM, Rangel-Moreno J. Development of secondary lymphoid organs. *Annu Rev Immunol* 2008;**26**:627–50.
- Sato T, van Es JH, Snippert HJ *et al.* Paneth cells constitute the niche for Lgr5 stem cells in intestinal crypts. *Nature* 2011a;**469**:415–8.
- Sato T, Stange DE, Ferrante M *et al.* Long-term expansion of epithelial organoids from human colon, adenoma, adenocarcinoma, and Barrett's epithelium. *Gastroenterology* 2011b;**141**:1762–72.
- Sato T, Vries RG, Snippert HJ *et al.* Single Lgr5 stem cells build crypt – villus structures in vitro without a mesenchymal niche. *Nature* 2009;**459**:262–6.
- Spence JR, Mayhew CN, Rankin SA *et al.* Directed differentiation of human pluripotent stem cells into intestinal tissue in vitro. *Nature* 2011;**470**:105–9.

- Sternini C, Anselmi L, Rozengurt E. Enteroendocrine cells: A site of “taste” in gastrointestinal chemosensing. *Curr Opin Endocrinol Diabetes Obes* 2008;**15**:73–8.
- The Cancer Genome Atlas. Comprehensive molecular characterization of human colon and rectal cancer. *Nature* 2012;**487**:330–7.
- Treveil A, Sudhakar P, Matthews ZJ *et al.* Regulatory network analysis of Paneth cell and goblet cell enriched gut organoids using transcriptomics approaches. *Mol Omi* 2019:1–31.
- Ueo T, Imayoshi I, Kobayashi T *et al.* The role of Hes genes in intestinal development, homeostasis and tumor formation. *Development* 2012;**139**:1071–82.
- Wang S, Chen Y-G. BMP signaling in homeostasis, transformation and inflammatory response of intestinal epithelium. *Sci China Life Sci* 2018;**61**:800–7.
- Wong VWY, Stange DE, Page ME *et al.* Lrig1 controls intestinal stem-cell homeostasis by negative regulation of ErbB signalling. *Nat Cell Biol* 2012;**14**:401–8.
- Yan KS, Janda CY, Chang J *et al.* Non-equivalence of Wnt and R-spondin ligands during Lgr5⁺ intestinal stem-cell self-renewal. *Nature* 2017;**545**:238–42.
- Yin X, Farin HF, van Es JH *et al.* Niche-independent high-purity cultures of Lgr5⁺ intestinal stem cells and their progeny. *Nat Methods* 2014;**11**:106–12.
- Zhan T, Rindtorff N, Boutros M. Wnt signaling in cancer. *Oncogene* 2017;**36**:1461–73.

Figure legends

Figure 1 Mouse intestinal cell types and enrichment in organoids. **(A)** Schematic overview of the small intestinal tissue. Indicated are the different cell types and niche signals. **(B)** Indicated modulations of mouse intestinal organoid medium result in enrichment for specific cell types.

Figure 2 Overview on the generation and use of cell type-enriched intestinal organoids. Stimulation of organoids with pathogens, specific niche factors, certain drugs, or nutrients results in cell type enrichment in organoids. These cell type-enriched organoids can be used for a wide variety of different kinds of studies including single-cell (sc)-RNA sequencing analysis, cell–cell or cell–pathogen interaction studies, screens with drugs or small molecules, and studies involving analysis of specific genetic alterations. T, T-cells; NK, natural killer cells; IL, interleukins; IFN, interferons.

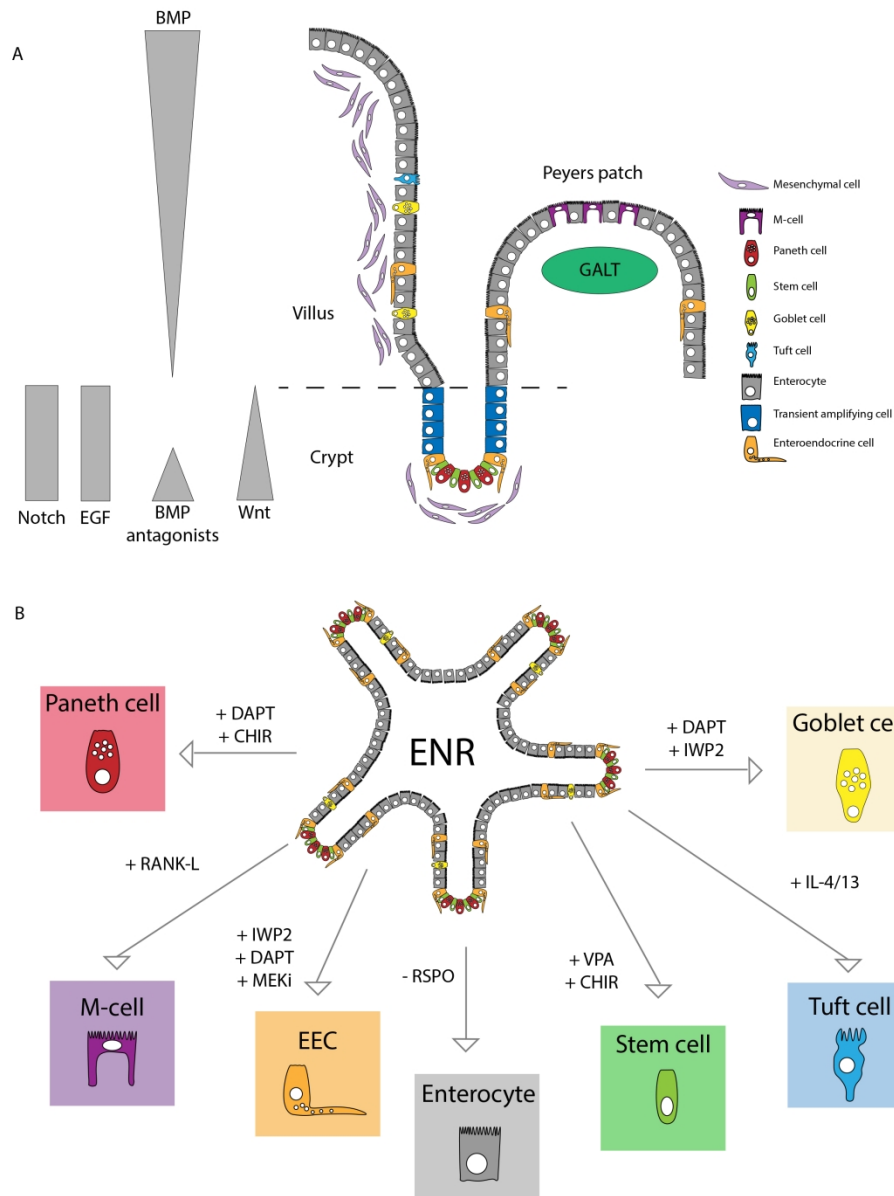


Figure 1. Mouse intestinal cell types and enrichment in organoids. A. Schematic overview of the small intestinal tissue with, indicated are the different cell types and niche signals. B. Indicated modulations of mouse intestinal organoid medium results in enrichment for specific cell types.

207x267mm (300 x 300 DPI)

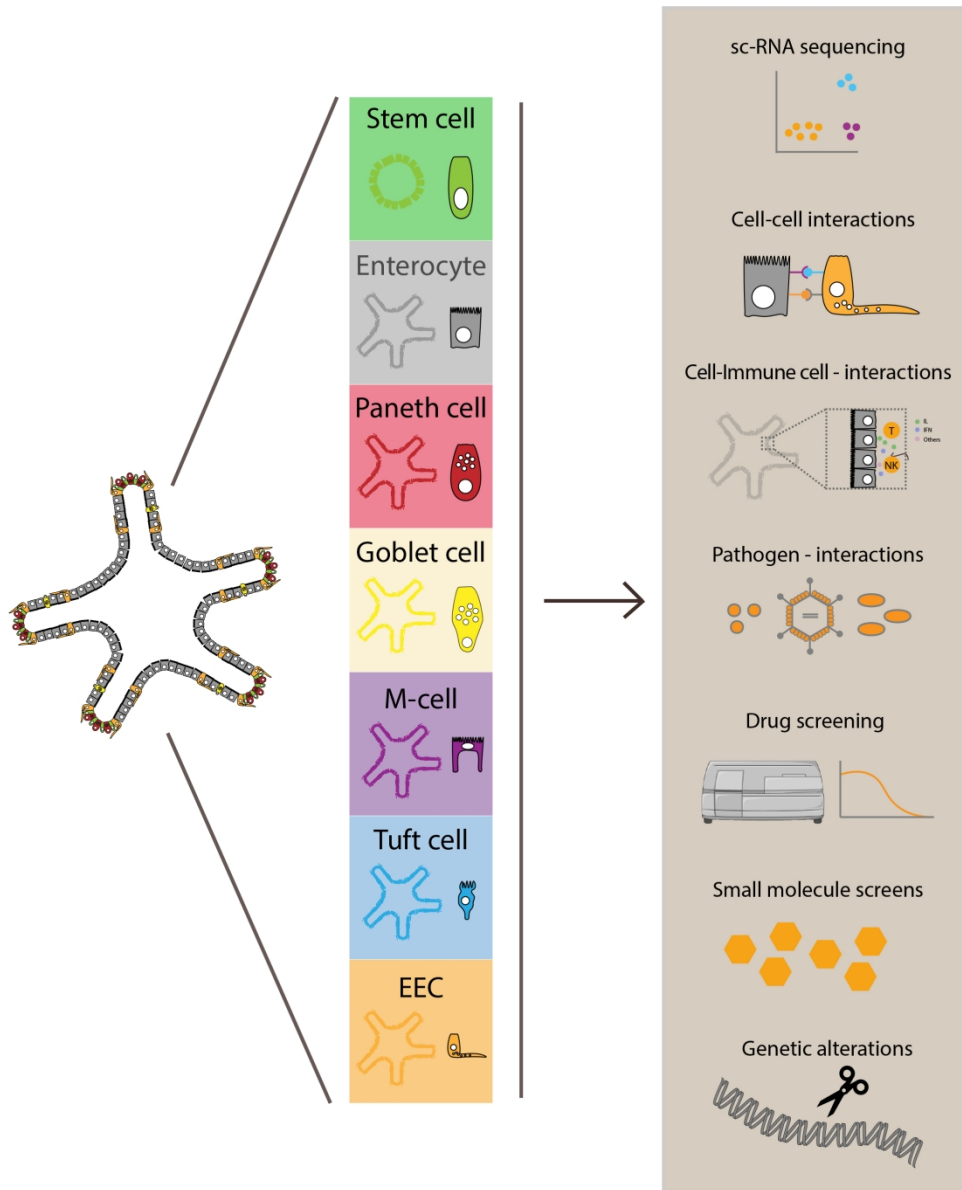
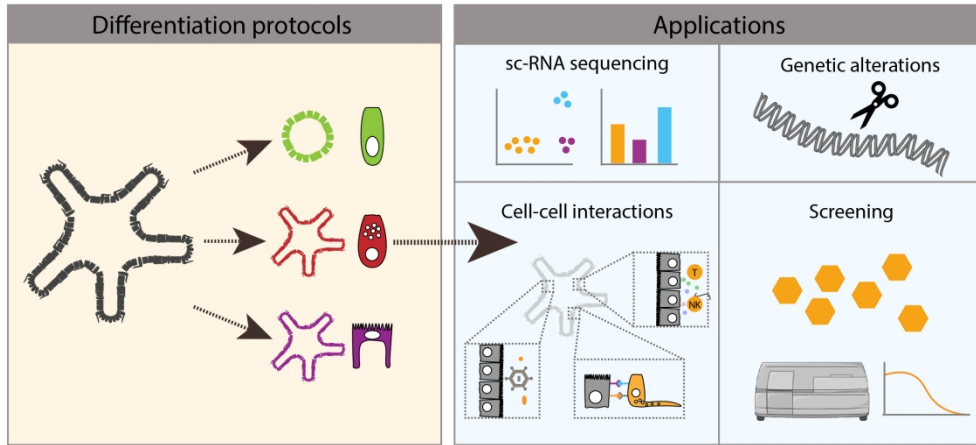


Figure 2. Overview on the generation and use of cell type-enriched intestinal organoids. Stimulation of organoids with pathogens, specific niche factors, certain drugs or nutrients results in cell type-enrichment in organoids. These cell type-enriched organoids can be used for a wide variety of different kinds of studies including single-cell (sc)-RNA sequencing analysis, cell-cell or cell-pathogen interaction studies, screens with drugs or small molecules, and studies involving analysis of specific genetic alterations. T, T-cells; NK, Natural killer cells; IL, Interleukins; IFN; Interferons.

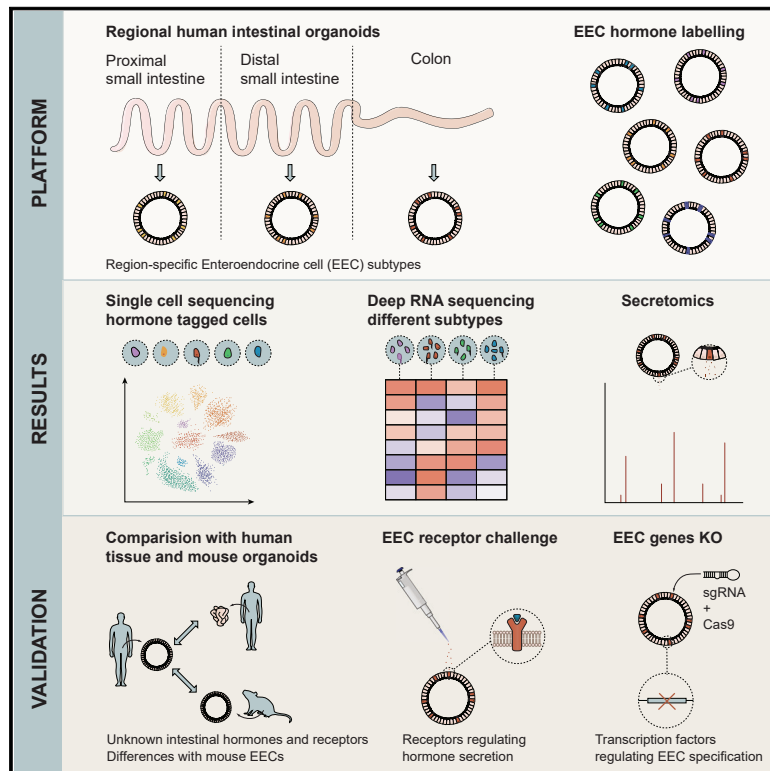
193x233mm (300 x 300 DPI)



207x95mm (300 x 300 DPI)

High-Resolution mRNA and Secretome Atlas of Human Enteroendocrine Cells

Graphical Abstract



Authors

Joep Beumer, Jens Puschhof, Julia Bauzá-Martinez, ..., Sarah A. Teichmann, Wei Wu, Hans Clevers

Correspondence

h.clevers@hubrecht.eu

In Brief

An organoid-based platform for studying human enteroendocrine cells, which sense intestinal content and release hormones to regulate many processes throughout the body, is developed by Beumer et al. and used to describe the landscape of mRNA expression and secreted products.

Highlights

- A human organoid biobank combines hormone labeling and enteroendocrine cell generation
- Transcriptomic profiling of human enteroendocrine cells uncovers differences with mice
- Functional validation of EEC receptors and transcription factors
- Secretome analysis reveals the repertoire of enteroendocrine secreted products



Article

High-Resolution mRNA and Secretome Atlas of Human Enteroendocrine Cells

Joep Beumer,^{1,2,14} Jens Puschhof,^{1,2,14} Julia Bauzá-Martínez,^{3,4,14} Adriana Martínez-Silgado,^{1,2} Rasa Elmentaite,⁵ Kylie R. James,⁵ Alexander Ross,^{6,7} Delilah Hendriks,^{1,2} Benedetta Artegiani,^{1,2} Georg A. Busslinger,^{1,2} Bas Ponsoen,⁸ Amanda Andersson-Rolf,^{1,2} Aurelia Saftien,^{1,2} Charelle Boot,^{1,2} Kai Kretzschmar,^{1,2} Maarten H. Geurts,^{1,2} Yotam E. Bar-Ephraim,^{1,2} Cayetano Pleguezuelos-Manzano,^{1,2} Yorick Post,^{1,2} Harry Begthel,^{1,2} Franka van der Linden,⁹ Carmen Lopez-Iglesias,¹⁰ Willine J. van de Wetering,^{1,10} Reinier van der Linden,^{1,2} Peter J. Peters,¹⁰ Albert J.R. Heck,^{3,4} Joachim Goedhart,⁹ Hugo Snippert,⁸ Matthias Zilbauer,⁷ Sarah A. Teichmann,^{5,11,12} Wei Wu,^{3,4,15} and Hans Clevers^{1,2,13,15,16,*}

¹Hubrecht Institute, Royal Netherlands Academy of Arts and Sciences (KNAW) and UMC Utrecht, 3584 CT Utrecht, the Netherlands

²Oncode Institute, Hubrecht Institute, 3584 CT Utrecht, the Netherlands

³Biomolecular Mass Spectrometry and Proteomics, Bijvoet Center for Biomolecular Research and Utrecht Institute for Pharmaceutical Sciences, Utrecht University, Padualaan 8, 3584 CH Utrecht, the Netherlands

⁴Netherlands Proteomics Centre, Padualaan 8, 3584 CH Utrecht, the Netherlands

⁵Wellcome Sanger Institute, Wellcome Genome Campus, Hinxton CB10 1SA, UK

⁶Department of Surgery, University of Cambridge, Cambridge CB2 0QQ, UK

⁷Department of Paediatrics, University of Cambridge, Cambridge CB2 0QQ, UK

⁸Oncode Institute, Center for Molecular Medicine, University Medical Centre Utrecht, Utrecht, the Netherlands

⁹Swammerdam Institute for Life Sciences, Section of Molecular Cytology, van Leeuwenhoek Centre for Advanced Microscopy, University of Amsterdam, Amsterdam, the Netherlands

¹⁰The Maastricht Multimodal Molecular Imaging Institute, Maastricht University, 6229 ER Maastricht, the Netherlands

¹¹Theory of Condensed Matter, Cavendish Laboratory, Department of Physics, University of Cambridge, Cambridge CB3 0HE, UK

¹²European Molecular Biology Laboratory, European Bioinformatics Institute (EMBL-EBI), Wellcome Genome Campus, Hinxton CB10 1SA, UK

¹³The Princess Maxima Center for Pediatric Oncology, 3584 CS Utrecht, the Netherlands

¹⁴These authors contributed equally

¹⁵Senior author

¹⁶Lead Contact

*Correspondence: h.clevers@hubrecht.eu

<https://doi.org/10.1016/j.cell.2020.04.036>

SUMMARY

Enteroendocrine cells (EECs) sense intestinal content and release hormones to regulate gastrointestinal activity, systemic metabolism, and food intake. Little is known about the molecular make-up of human EEC subtypes and the regulated secretion of individual hormones. Here, we describe an organoid-based platform for functional studies of human EECs. EEC formation is induced *in vitro* by transient expression of *NEUROG3*. A set of gut organoids was engineered in which the major hormones are fluorescently tagged. A single-cell mRNA atlas was generated for the different EEC subtypes, and their secreted products were recorded by mass-spectrometry. We note key differences to murine EECs, including hormones, sensory receptors, and transcription factors. Notably, several hormone-like molecules were identified. Inter-EEC communication is exemplified by secretin-induced GLP-1 secretion. Indeed, individual EEC subtypes carry receptors for various EEC hormones. This study provides a rich resource to study human EEC development and function.

INTRODUCTION

The principal function of the intestine is to digest food and absorb nutrients, but as the largest hormone producing organ, it also secretes hormones through its enteroendocrine cells (EECs) (Gribble and Reimann, 2017). EECs are rare secretory cells, comprising <1% of the epithelial cells. Apical EEC receptors sense chemicals in the intestinal lumen derived from food and microbiota (Furness et al., 2013). Hormones secreted by

EECs signal to the local enteric nervous system and to distant organs including the pancreas and the brain, thus controlling food intake, insulin release, secretion of digestive enzymes, and bowel movement. EECs are therapeutic targets for metabolic diseases (i.e., obesity and diabetes), illustrated by recently introduced type 2 diabetes drugs that stabilize the hormone glucagon-like peptide 1 (GLP-1) or activate its receptor, leading to release of insulin from pancreatic β cells (Sharma et al., 2018).



EECs produce ~20 different hormones. GLP-1 and glucose-dependent insulintropic peptide (GIP) are the incretin hormones that stimulate insulin secretion. The enterochromaffin (EC) cells produce 90% of body serotonin and regulate bowel movement (Worthington et al., 2018). Motilin (MLN) is a human EEC hormone, which controls gut contractions in the inter-digestive state (Worthington et al., 2018). Multiple hormones control appetite, including the appetite-inducing ghrelin (GHRL), the appetite-reducing peptide YY (PYY), and cholecystokinin (CCK). Gastrin (GAST) is secreted in the duodenum to control luminal acid by regulating proton secretion of stomach parietal cells. Somatostatin (SST) is an inhibitory peptide for most other intestinal hormones (Worthington et al., 2018).

Lgr5+ cells generate all differentiated intestinal cell types (Barker et al., 2007). The murine EEC subtypes are historically defined by their principle hormone product: L cells (Glp-1, Pyy), I cells (Cck), K cells (gastric inhibitory protein, Gip), N cells (neurotensin, Nts), S cells (secretin, Sct), EC cells (serotonin/5-HT), X cells (Ghrl), G cells (Gast), and D cells (Sst) (Engelstoft et al., 2013a; Gehart et al., 2019). Although this suggests that EEC phenotypes are hardwired, we have recently found that the crypt-villus BMP-signaling gradient induces hormone switching within individual murine EEC lineages (Beumer et al., 2018). The relative abundance of EEC subtypes greatly differs along the proximal-distal gastrointestinal axis. Studies on EECs have largely focused on murine models, exploiting a variety of reporter mice for subsets of EECs to monitor their responses to nutritional or genetic challenges (Goldspink et al., 2018). We have recently described the developmental hierarchy of murine subtypes EECs using a mouse model in which endogenous Neurogenin-3 expression, the main determinant of EEC fate, was coupled to the production of two separate fluorescent proteins with different half-lives (Gehart et al., 2019). Single-cell RNA sequencing of sorted EEC progenitors allowed for construction of a time-resolved development roadmap of the mouse EEC lineage.

Because the human diet and microbiome and that of rodents differ greatly (Nguyen et al., 2015), secretory hormone responses may also differ between these species. The study of human EECs is challenging because of their rarity and the lack of physiologically relevant *in vitro* models. Few human EEC-immortalized cell lines exist, and these differ substantially from their wild-type counterparts (Goldspink et al., 2018). There is currently no atlas of human EEC subtypes. Although some inducers of hormone secretion have been described in mice, there has been no experimental model to systematically assess such secretagogues for human EECs. Here, we describe an organoid-based platform to provide a detailed molecular and functional description of human EECs.

RESULTS

Production of Region-Specific Human EECs

Previous attempts to create human EECs *in vitro* have relied on growth-factor-based differentiation (Beumer et al., 2018) or overexpression of *NEUROG3*, the key transcription factor to instruct EEC fate (McCracken et al., 2014; Sinagoga et al., 2018). Both induced-pluripotent-stem-cell- (Zhang et al., 2019)

and adult stem cell (ASC)-based (Chang-Graham et al., 2019) approaches allow studying of human EEC biology, such as modeling of hereditary *NEUROG3* mutations and virally induced serotonin release (Chang-Graham et al., 2019). However, imperfect differentiation and regional restriction of the donor material have limited these studies to a subset of human EECs.

To generate the full spectrum of human EECs, we established organoids from healthy adult proximal small intestine (duodenum), distal small intestine (ileum), and the ascending colon (Sato et al., 2011). These organoids were transduced with a doxycycline-inducible *NEUROG3* construct (Figure 1A). dTomato was inserted 3' to the *NEUROG3* reading frame, separated by a self-cleavable P2A sequence to avoid creating a fusion protein. A 48 h-pulsed expression of *NEUROG3* in the basic medium "ENR" promoted the expression of the broad EEC marker chromogranin A (*CHGA*) (Figure 1B). Proximal small intestinal (SI) hormones such as *GAST*, *CCK*, and *MLN* were enriched in duodenal organoids, whereas *NTS*, *PYY*, and *GCG* were predominantly observed in distal SI organoids. Of note, *GCG* encodes the preproglucagon prehormone, a protein precursor to a set of hormones including GLP-1 (see below). *SST* was comparably expressed in proximal and distal organoids, consistent with its profile in the mouse gut. A recent single-cell RNA sequencing study generated the profile of 83 colonic EECs, suggesting that the human colon only contains serotonin-producing ECs and L cells positive for *GCG* and *PYY* (Parikh et al., 2019). Consistently, induced colon organoids only yielded serotonin-producing ECs and *GCG*-expressing EECs. We found that hormone expression peaked 5 days after initiation of *NEUROG3* expression (Figure S1A). Shorter doxycycline inductions stimulated the production of fewer EECs, whereas continuous doxycycline treatment throughout the differentiation window enhanced EC generation at the expense of L cells (Figure S1B). This suggests that Neurogenin-3 expression duration determines EEC subtype. We chose a 48 h doxycycline treatment in ENR, the maximum duration of *NEUROG3* expression *in vivo* (Gehart et al., 2019). Under these conditions, EECs in organoids displayed a normal morphology as visualized by transmission electron microscopy. Note the typical basal concentration of hormone vesicles (Figure 1C).

By immunofluorescent staining (Figure S1C), we observed mutually exclusive expression for *MLN* and *GAST* for *GHRL* and *CHGA* and for Serotonin and GLP-1, whereas a subset of GIP-positive cells co-expressed CCK. This closely resembled the co-expression patterns in mice (with the exception of *MLN*, a pseudogene in mice) (Haber et al., 2017) (Figure S1C). Virtually all EECs, as identified by the broad marker *CHGA*, were derived from *NEUROG3*-overexpressing cells (Figure S1C). A definitive hallmark of a mature EEC is its ability to secrete hormones. Indeed, exposure to forskolin, a stimulator of adenylate cyclase, greatly enhanced secreted GLP-1 levels (Figure 1D). We have previously reported that BMP signaling induces hormone expression changes in mature murine EECs in villi (Beumer et al., 2018). Consistent with our observations in murine EECs, we found that activation of BMP signaling enhances the expression of *NTS* while reducing GLP-1 (Figures S2A and S2B).

Because the initial expression of *NEUROG3* occurs at random positions along the crypt axis in mice (Gehart et al., 2019), we

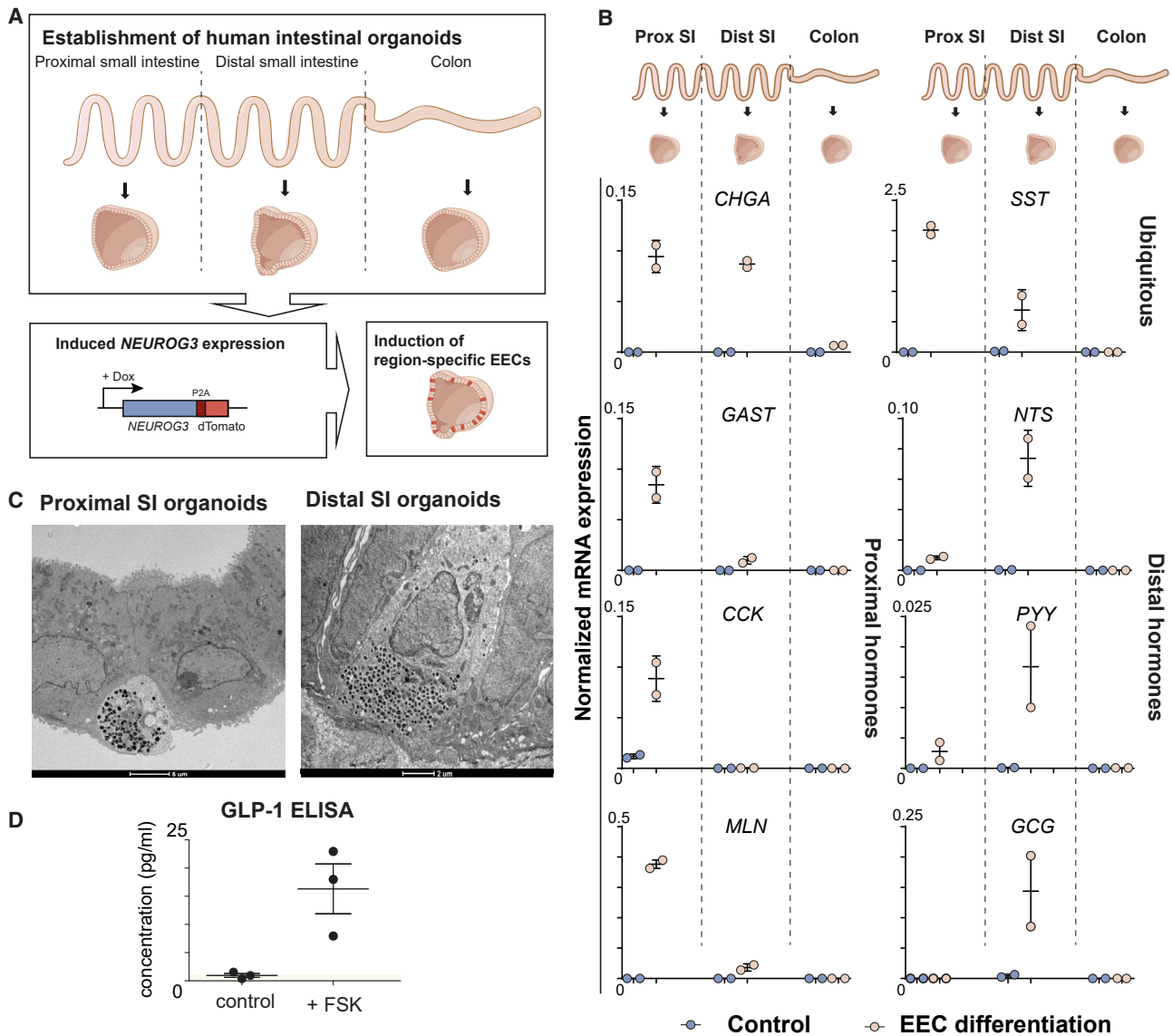


Figure 1. Production of Region-Specific Human Enteroendocrine Cells in Intestinal Organoids

(A) Schematic representation of the generation of region-specific enteroendocrine cells (EECs). Organoids are established from different regions of the intestinal tract of different patients, after which doxycycline (dox)-induced overexpression of neurogenin-3 (*NEUROG3*) can drive the production of EECs.

(B) qPCR analysis showing expression of hormones, control, or differentiation condition after a pulse of dox. Expression levels are normalized to *GADPH*. The experiment was performed in $n = 2$ independent experiments, and the mean expression and SEM are depicted.

(C) Transmission electron microscopy (TEM) of EECs in organoids showing polarized localization of hormone vesicles. Scale bar is 5 μ m (left image) and 2 μ m (right image).

(D) Concentration of supernatant GLP-1 determined by ELISA, in the absence (control) and presence of forskolin (FSK). The brown shaded area presents the detection threshold of GLP-1 (1 pg/mL). Forskolin induces secretion of GLP-1, confirming functionality of EECs. The experiment was performed in $n = 3$ independent experiments, and the mean concentration and SEM are depicted.

hypothesized that exposure to other crypt differentiation signals (i.e., Notch, Wnt) prior to this expression pulse could potentially determine EEC subtype. We modulated these signals prior to inducing *NEUROG3* expression, mimicking the different initiation sites along the intestinal crypt axis (Figure S2C). As a control, we modulated the same signals after *NEUROG3* induction (Figure S2D). Inhibition of Notch before or after expression of

NEUROG3 did not affect EEC differentiation (Figure S2E). Inhibition of Wnt signaling before (but not after) the *NEUROG3* pulse stimulated expression of *MLN* at the expense of *GCG*, while *SST* was unaffected (Figure S2E). Immunofluorescence revealed an increase in the number of *MLN*-producing cells rather than in the “per cell” expression levels (Figure S2F), resulting in a strong shift in L cell/M cell ratio (Figure S2G).

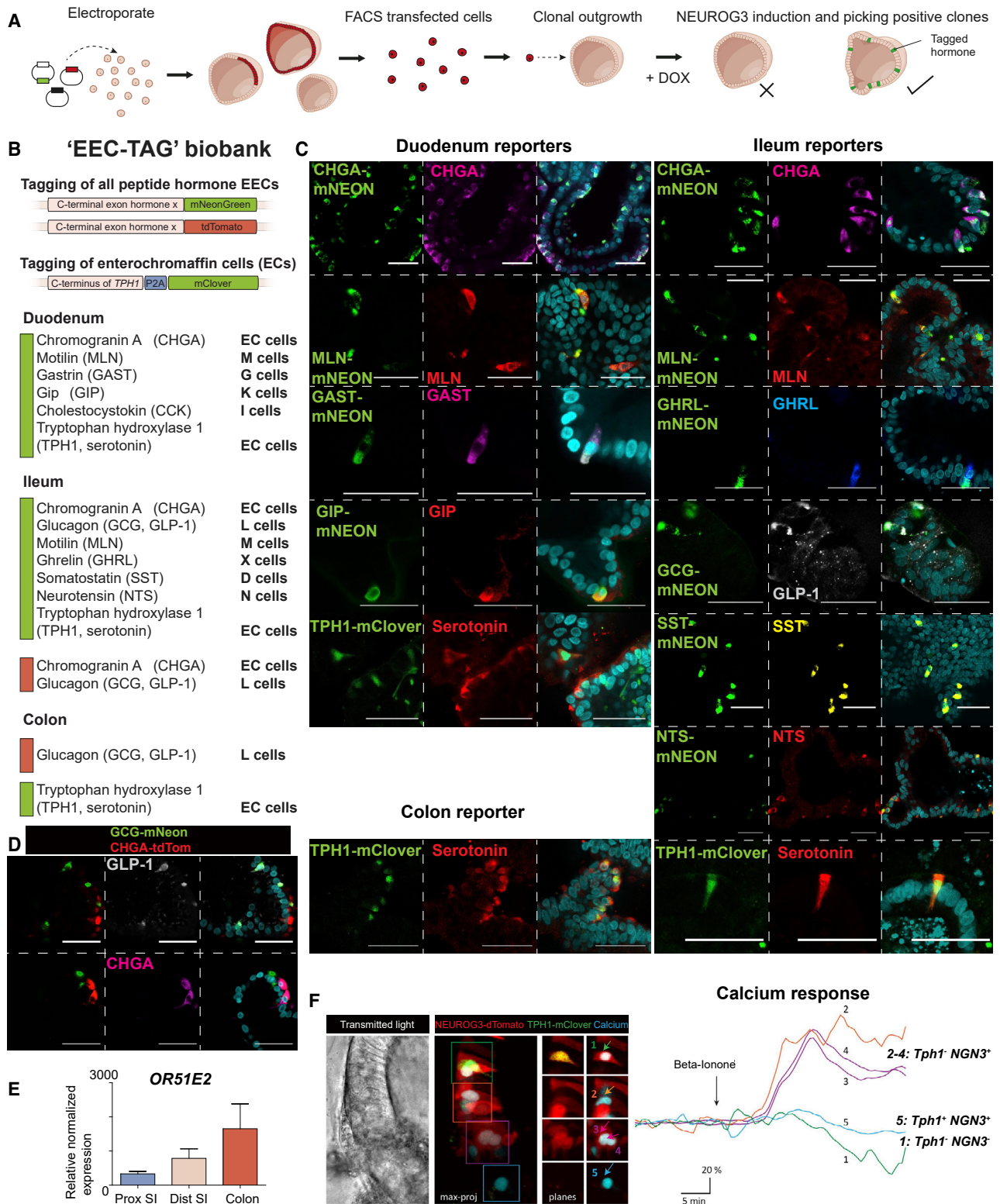


Figure 2. Generation of a Human Enteroendocrine Cell Organoid Toolbox

(A) Schematic workflow of generation of reporter organoids.

(B) Overview of EEC-TAG biobank-comprising reporters for hormones across human duodenum, ileum, and colon organoids. EECs are tagged with NHEJ (mNeon or tdTomato). TPH1-positive ECs are tagged using HDR with mClover.

(legend continued on next page)

Generation of Hormone Reporter Biobank EEC-TAG

Mouse models in which hormones are fluorescently tagged exist for several murine EEC hormones that were instrumental to study EEC subsets: Chga, Gcg, Gip, Cck, Ghrl, and Pyy (Engelstoft et al., 2013b; 2015; Gong et al., 2003; Parker et al., 2009; Reimann et al., 2008; Sommer and Mostoslavsky, 2014). CRISPR-Cas9 targeting followed by homology-directed repair (HDR) or non-homologous end joining (NHEJ) allows the introduction of exogenous genetic material (Bukhari and Müller, 2019; He et al., 2016; Schmid-Burgk et al., 2016). To mark EECs, we labeled tryptophan hydroxylase 1 (TPH1), the rate-limiting enzyme involved in serotonin synthesis. Using HDR, we tagged TPH1 with fluorescent mClover separated by a self-cleaving P2A site. We recently optimized a strategy for site-specific introduction of DNA into organoids using NHEJ (CRISPR-HOT) (Artegiani et al., 2020), which allowed fluorescently labeling of multiple secreted hormones (Figure 2A).

We generated a biobank of hormone reporter organoids termed EEC-TAG, consisting of duodenal, ileal, and colon organoids for a total of 10 human hormones (Figure 2B). All organoid lines showed complete overlap between fluorescent reporters and the corresponding hormone product (Figure 2C). The fluorescently tagged hormones localized to cytoplasmic vesicles. Serial tagging into the same organoid lines for multi-hormone labeling was feasible (Figure 2D).

Calcium signaling induces hormone secretion (Goldspink et al., 2018). We stably introduced a turquoise Ca^{2+} sensor (Tq-Ca-FLITS) into NEUROG3^{dTomato} TPH1^{mClover} reporter organoids using lentiviral transduction. The resulting genotype of the organoids is NEUROG3^{dTomato} TPH1^{mClover} CaFLITS^{Turquoise}. We stimulated the olfactory receptor OR51E2, of which the mouse homolog (*Olf78*) is reported to be expressed in mouse EECs (Fleischer et al., 2015; Jovancevic et al., 2017). HEK cells overexpressing *OR51E2* elicit a calcium response when stimulated with the selective agonist beta-ionone (Pietraszewska-Bogiel et al., 2019). *OR51E2* is most strongly upregulated in distal organoids (Figure 2E). When reporter organoids were stimulated with beta-ionone, we observed calcium spiking in EECs that were TPH1-negative (Figure 2F), illustrating that sensors combined with hormone reporters can visualize activation of human EEC subtypes.

Single-Cell Transcriptomics

Studies have utilized reporter mice to enrich for hormone-producing cells when performing single-cell RNA sequencing. This approach cannot be used for primary human EECs, making the generation of a detailed atlas from SI tissue challenging. Murine

EECs taken from primary tissue and from organoids are essentially identical (Gehart et al., 2019; Grün et al., 2015). We therefore exploited the human NEUROG3-induced organoids to perform single-cell RNA sequencing. NEUROG3 was induced in duodenal, ileal, and colon organoids in the absence or presence of BMP (to generate the crypt- and villus-“versions” of EECs; Figure S2). Data from 8,448 cells were generated and processed by sorting and robot-assisted transcriptome sequencing (SORT-seq; Muraro et al., 2016) (Figures S3A and S3B) and analyzed using RaceID3, a clustering method based on k-meoids (Herman et al., 2018). After filtering, a broad intestinal cell type atlas was built from 4,281 cells (Figures S3B and S3C). This atlas contained five large clusters: *CHGA*-positive EECs (2,255) and the following well-defined “contaminant” lineages: *FABP1*-positive enterocytes (585), *OLFM4*-positive stem cells (113), rare *MUC2*-positive goblet cells (33), *LYZ/MMP7*-positive Paneth cells (11), and several progenitor populations (Figure S3D).

Neuropeptide W (*NPW*) and *VGF*, recently observed in bulk EEC RNA sequencing (Roberts et al., 2019), were broadly expressed (Figure S3C). Although the function of *VGF* remains elusive, *NPW* is known to increase food intake when injected in the hypothalamus (Levine et al., 2005). Immunofluorescence confirmed protein expression of *NPW* by EECs in sections of human intestine (Figure 3A).

All EECs and their progenitors were identified by thresholding for expression of the generic EEC marker *CHGA* and thresholding against *MUC2*, *FABP1*, *LYZ*, and *OLFM4*. An EEC atlas was constructed from 2,255 cells (of which 805 cells were BMP-treated) (Figures 3B, 3C, and S4A). The major clusters overlapped with their mouse equivalents, and the different EEC subtypes followed regional identity (Figure S4B) (Haber et al., 2017). The human EEC atlas significantly differed from the mouse tissue EEC atlas (Figure S4C) (Gehart et al., 2019). To validate the *in vitro* EEC identities, we searched for EECs in a large single-cell dataset obtained from healthy and diseased human small intestines of various ages. Of 11,302 cells represented in this dataset, we derived mRNA signatures for 39 human EECs, underscoring the challenge of deriving single EEC mRNA signatures from human ileal biopsies (Figure S4D).

The largest cluster was formed by *TPH1*-expressing EC cells, highly expressing *CHGA* (as in mouse) and representing the most frequent EEC type *in vivo* (Figures 3B and 3C). EECs occurred in three “flavors”: *REG4* high and *REG4* low cells (in cluster 4), which also exist in murine intestine (Haber et al., 2017). A third population of EECs, not observed in mice, expressed high levels of the secretogranin *SCG2* and occurred

(C) Immunofluorescent staining confirms faithful reporter activity (knockin left, stain middle, and merge on right). Reporter expression always overlaps with the corresponding hormone. Scale bar is 50 μm .

(D) Subsequent rounds of hormone tagging allow the generation of multiple-hormone reporter organoids. Immunofluorescent staining of GCG/CHGA double reporter organoid. Scale bar is 50 μm .

(E) qPCR analysis showing expression of the olfactory receptor *OR51E2* in different organoids enriched for EECs. Expressions levels are normalized to GADPH and relative to control organoids without EECs. The experiment was performed in $n = 2$ independent experiments, and the mean expression and SEM are depicted.

(F) Fluorescent image of a TPH1^{mClover} NEUROG3^{dTomato} organoid that is transduced with the turquoise calcium sensor Tq-Ca-FLITS, containing a nuclear localization signal. Five examples of nuclei are highlighted of which the calcium response is followed after treatment with beta-ionone, the agonist of *OR51E2*. EECs (marked in red) show increases in calcium flux (“2–4”) with the exception of the TPH1⁺ cell (“1”). The non-EEC (“5”) does not show calcium increases upon beta-ionone treatment.

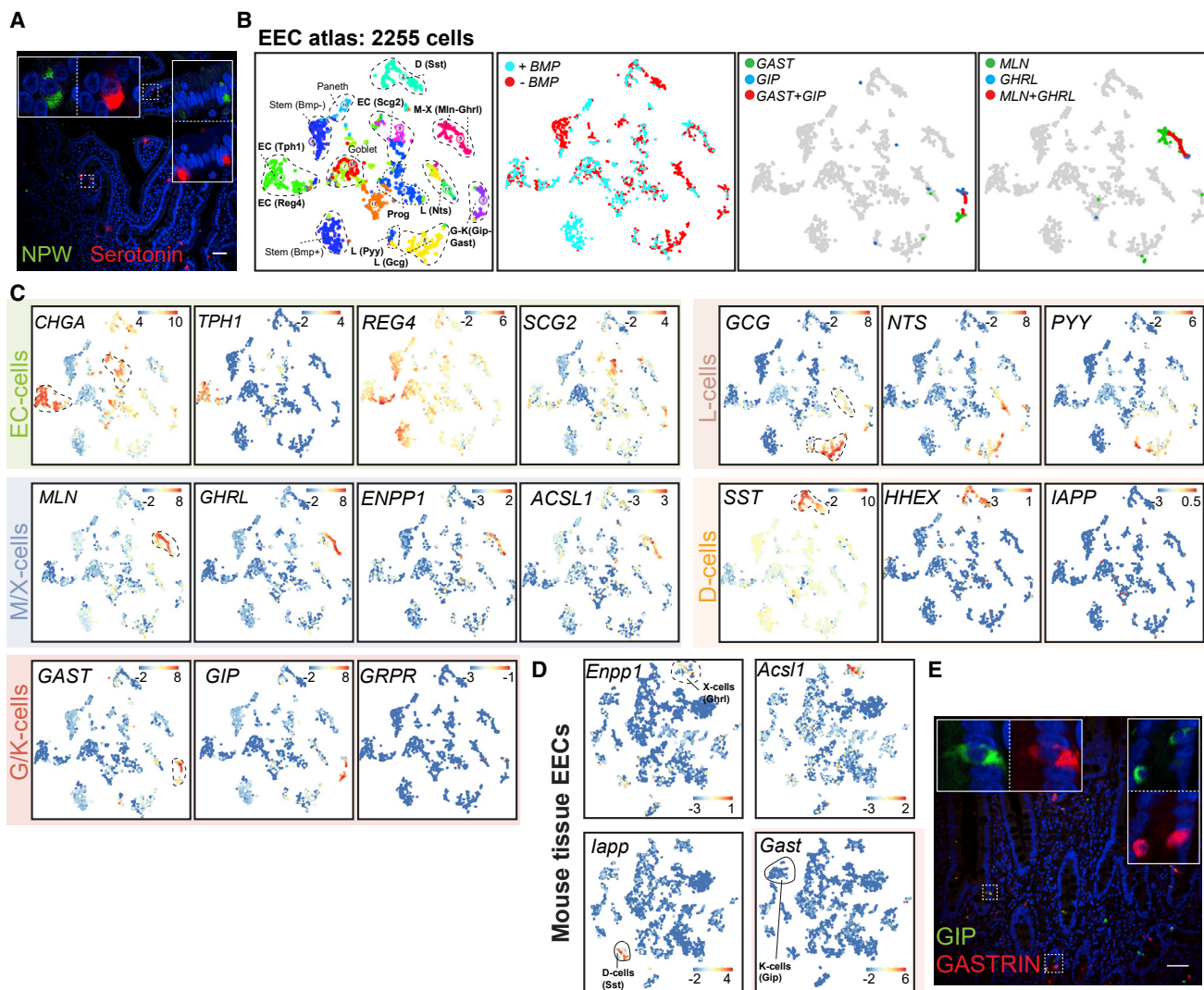


Figure 3. Single-Cell Transcriptome Atlas of Human Enteroendocrine Cells

(A) Immunofluorescent staining on human intestinal section (ileum) confirms EEC-specific expression of NPW. Scale bar is 50 μ m.

(B) t-SNE map displaying the human EEC atlas ($n = 2,255$ cells). Different colors represent the 13 separate clusters, and BMP treated cells are highlighted. GAST- and GIP-positive cells (defined by a minimum of 25 unique transcripts per cell) show partly overlapping expression patterns (middle t-SNE map). GHRL- and MLN-positive cells (defined by a minimum of 25 unique transcripts per cell) also overlap partly (right t-SNE map).

(C) t-SNE maps displaying the expression levels of hormone and marker gene expression in the different human EEC subtypes from intestinal organoids. Bars display color-coded unique transcript expression (logarithmic scale).

(D) t-SNE maps displaying the expression levels of hormone and marker gene expression in murine tissue EECs. Bars display color-coded unique transcript expression (logarithmic scale).

(E) Immunofluorescent staining on duodenal sections confirms co-expression of GIP and GASTRIN. Scale bar is 50 μ m.

mostly in proximal SI organoids (cluster 9) (Figures 3B and 3C). All human ECs highly expressed dopa decarboxylase (*DDC*) involved in serotonin biosynthesis, as well as *SLC18A1*, involved in serotonin transport (Figure S4E) (Lohoff et al., 2006). The prototypical EC markers *CHGB* and *GPR112* were broadly expressed by human ECs, as was the olfactory receptor OR51E1 (mouse homolog *Olf558*), a marker of serotonin-producing neuroendocrine tumors in man (Figure S4E) (Cui et al., 2013).

G cells produce *Gast* and are largely restricted to the mouse stomach, whereas in man, expression continues more distally

along the GI tract in EECs (Engelstoft et al., 2013a). Cells expressing GAST (cluster 3) co-expressed the receptor for *Gast*-releasing peptide, *GRPR*, a marker of G cells in mouse stomach (Figures 3B and 3C). GAST-expression often overlapped with high expression of the incretin *GIP* (same cluster 3), the main hormone product of murine K cells. We named these cells G/K cells (Figures 3B and 3C). In histological sections, we confirmed overlapping expression for these two hormones (Figure 3E). Some cells in cluster 3 almost exclusively produced either *GIP* or *GAST*, as seen on intestinal sections and in the atlas. The L

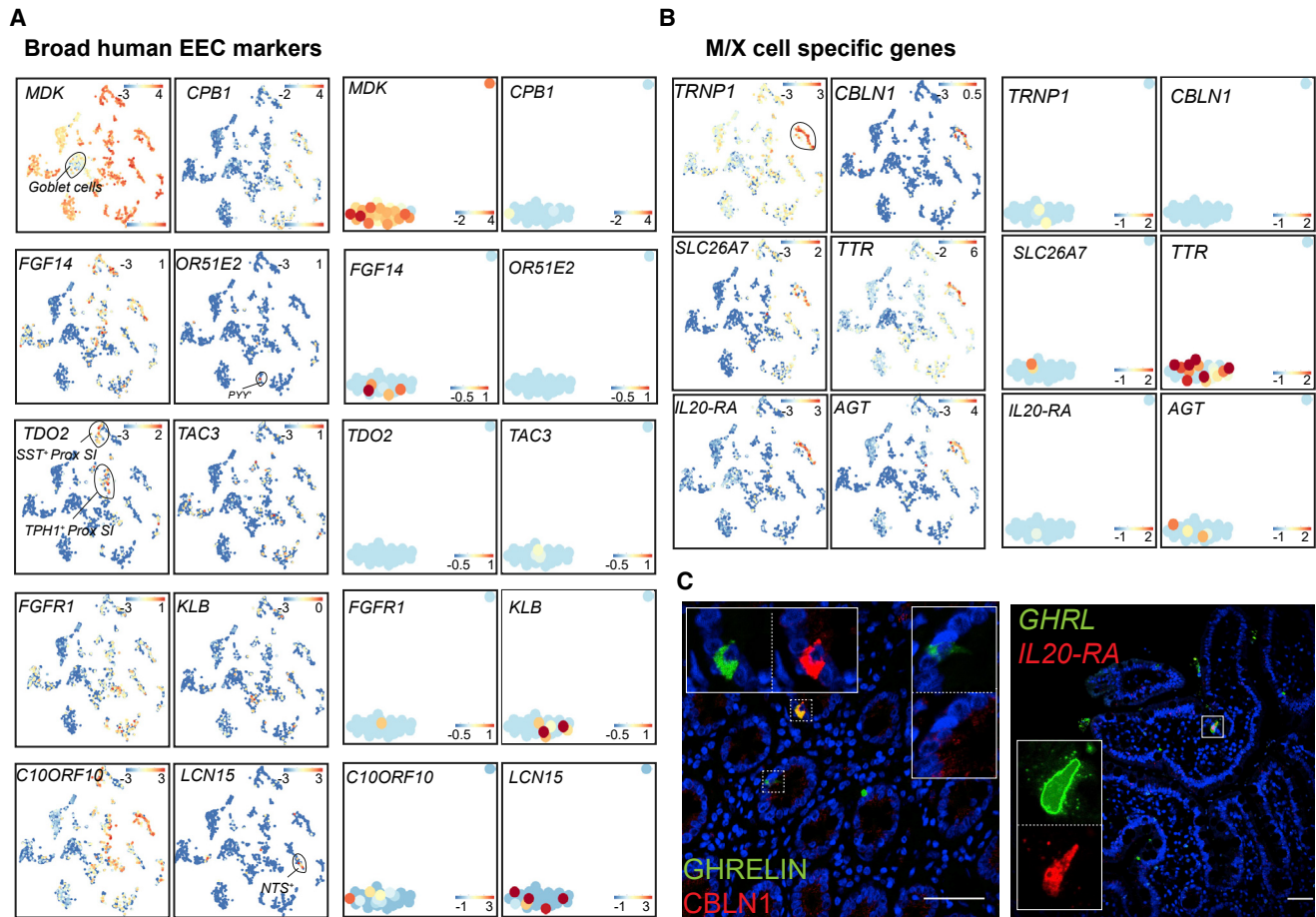


Figure 4. Human Enteroendocrine Cell Markers

(A) t-SNE maps displaying the levels of hormone and marker gene expression in the different human EEC subtypes from intestinal organoids (left) and intestinal tissue (right). Bars display color-coded unique transcript expression (logarithmic scale).

(B) t-SNE maps displaying the levels of hormone and marker gene in M/X cells. Bars display color-coded unique transcript expression (logarithmic scale).

(C) Immunofluorescent staining on intestinal sections confirms co-expression of GHRL and the EEC peptide CBLN1 (left panel). Fluorescent *in situ* hybridization shows that *GHRL*⁺ cells express the cytokine receptor *IL-20RA* (right panel). All sections are from the human duodenum. Scale bar is 50 μ m.

cell lineage clusters 8 and 13 displayed largely overlapping expression of *GCG*, *NTS*, and *PYY* (Figures 3B and 3C). Cluster 2 contained SST-positive D cells, also expressing the transcription factor *HHEX*. *HHEX* has been described in murine pancreatic and intestinal Sst-producing cells (Haber et al., 2017; Zhang et al., 2014). Notably, human D cells in tissue and organoids lacked expression of amylin (*IAPP*), a peptide hormone expressed in mouse D cells (Figures 3B, 3C, and S4D).

Mln⁺ cells do not exist in mice. We identified a cluster of cells producing *MLN* and *GHRL* (cluster 5). A gradient from predominantly *MLN* to predominantly *GHRL*-expressing cells can be observed in t-distributed stochastic neighbor embedding (t-SNE) space (Figures 3C and 3D). We termed these M/X or X/M cells (based on the highest expression of either *MLN* or *GHRL*, respectively) and speculate that these might represent different states of the same cell type. Indeed, BMP treatment reduced levels of *GHRL*, whereas *MLN* levels were slightly increased (Figure S6B). M/X cells were further characterized by *ENPP1* expres-

sion, a known regulator of insulin responses and extracellular ATP levels (Di Paola et al., 2011), similarly expressed by murine X cells (Figures 3C and 3D). *GHRL* requires a specific acyl modification by the acyl-CoA synthetase *Acs1* in mouse stomach X cells (Bando et al., 2016). Human M/X cells and mouse intestinal X cells both expressed high levels of *Acs1* (Figures 3C and 3D).

Genes Uniquely Expressed by Human EEC Subtypes

We next searched for EEC genes differentially expressed between human and mouse (Figure S4F). The heparin-binding growth factor midkine (*MDK*) was highly expressed by all human EEC types but not by, e.g., goblet cells (Figure 4A). *MDK* is a reported biomarker of human intestinal neuroendocrine tumors (Edfeldt et al., 2017). Midkine has been associated with obesity and inhibits insulin signaling in adipocytes (Fan et al., 2014). The carboxypeptidase *CPB1* was produced by most EECs (highest in M/X cells), with the exception of ECs (Figure 4A). Carboxypeptidases are typically involved in hormone processing (Sapio

and Fricker, 2014). Expression of *Cpb1* has been observed in the rat pancreas (Yu et al., 2017). *FGF14* is a human pan-EEC marker—with very limited expression in murine EECs—and belongs to a set of intracellular FGFs, that play a role in the clustering of ion channels in neurons (Figures 4A and S4F) (Pablo and Pitta, 2017). The olfactory receptor *OR51E2* was sporadically expressed by different EEC subtypes, with highest levels occurring in *PYY*⁺ cells (Figure 4A). The mouse homolog *Olf78* was lowly expressed in ECs only (Figure S4F). The enzyme tryptophan 2,3-dioxygenase (*TDO2*) was found in duodenal EECs from the proximal intestine (Figures 4A and S4A). *TDO2* can metabolize tryptophan through the kynurenine pathway and is one of the primary regulators of availability of this amino acid. Tryptophan is the precursor of serotonin and *Tdo2* knockout mice experience increased serotonin levels (Too et al., 2016), suggesting that *Tdo2* could locally regulate serotonin production in the gut. We noted the tachykinin peptide-coding *TAC3* was a broadly expressed gene in human EECs, whereas the mouse homolog *Tac2* is not expressed in the murine intestine (Figure 4A). *TAC3* codes for neurokinin B and has been described as a regulator of secretion of gonadotropin-releasing hormone in the human hypothalamus (Sanger, 2004). However, the main receptor for NKB, NK₃ (coded by *TACR3*), has been implicated in the regulation of gastrointestinal motility (Sanger, 2004). The hepatokine *FGF21* is a regulator of blood glucose. Several *FGF21* mimetics are currently being tested for the treatment of diabetes (Kuro-O, 2019). Although the receptors for *FGF21* are described as a complex of *FGFR1* and *B-Klotho* (*KLB*), the site of action of *FGF21* is debated. We observed broad expression of *FGFR1* and *KLB* by human EECs, suggesting that *FGF21* effects could be partially mediated through the gut (Figure 4A). *Fgfr1* is absent in murine EECs, whereas *Klb* is expressed at very low levels (Figure S4F). We noted an upregulation of multiple hormones after *FGF21* treatment, pointing to a potential role of signaling through *FGFR1/KLB* in EEC function (Figure S4G). *C10ORF10* (also known as *DEPP1*) was widely expressed by human EECs. This gene is negatively regulated by insulin in liver and adipocyte tissue; its product controls the ratio between ketogenesis and gluconeogenesis (Li et al., 2018) (Figure 4A). Finally, *LCN15* was produced by *NTS*⁺ cells (Figure 4A). *LCN15* is a lipocalin and one of the strongest glucose-regulated genes in Caco-2 cells (Boztepe and Gulec, 2018). Although some lipocalins have been implicated in insulin resistance, *LCN15*'s function remains unknown.

We then focused on unique genes expressed by M/X cells but absent in murine X cells. *TRNP1*, involved in cortical folding in the brain (Stahl et al., 2013), was the only transcription factor specific to M/X cells (Figure 4B). A putative hormone, precerebellin 1 (*CBLN1*), was expressed in all M/X cells (Figure 4B). *CBLN1* stimulates food intake upon intracerebroventricular injection (like GHRE) (Gardiner et al., 2010). We confirmed *CBLN1* expression in human *GHRL*⁺ cells *in vivo* using immunofluorescence (Figure 4C). We noted that M/X cells expressed the receptor for cytokines of the IL10-family (IL20-RA), an observation confirmed *in vivo* (Figures 4B and 4C). We detected high expression of the peptide hormone angiotensin (*AGT*), a regulator of blood pressure, but also of contraction of the human intestinal musculature (similar to motilin) (Ewert et al., 2006) (Figure 4B). Finally,

M/X cells displayed the highest expression of all EECs of the sulfate transporter *SLC26A7* and of T₄- and retinol-binding transthyretin (*TTR*) (Figure 4B). We confirmed the expression of these EEC genes in the (limited) number of single-cell sequenced human ileal EECs (Figures 4A and 4B).

To identify heterogeneity among the different EEC subtypes, we subclustered cells sorted from organoids carrying the individual hormone reporters. Expression of the fluorescent reporters directly correlated with the levels of the pertinent hormone transcripts within the same cell (Figure S5A). A substantial number of the cells sorted for *MLN*-reporter expression (yet with low *MLN* expression) were L cells (Figures S5A and S5B). Surprisingly, we identified a rare subcluster of *GCG*⁺-reporter cells that highly expressed *PPY* (Cox, 2007), a well-described pancreas hormone involved in appetite regulation, never seen in human or mouse small intestine. We confirmed its expression and partial overlap with *GLP-1* by staining on human intestinal sections (Figures S5B and S5C).

Transcriptional Networks

We analyzed expression of transcription factors known from mice to specify individual lineages (Figure 5A). *PAX4* specifies D/EC cells, whereas expression of *ARX* promotes all other EEC fates (Beucher et al., 2012), in agreement with our expression profiles. *HHEX* and *LMX1A* defined human D and EC lineages respectively, consistent with mouse (Figure 5A) (Gross et al., 2016). The broad murine EEC transcription factors *NKX2-2*, *PAX6*, *SOX4*, and *RFX6* (Gehart et al., 2019) were ubiquitously expressed in human EECs. We additionally identify *ASCL1* as a broad human EEC transcription factor, absent from M/X cells and from all mouse EECs (Figures 5A and 5B). *Ascl1* is expressed in endocrine cells in murine lung (Borges et al., 1997). *MXN1* was highly expressed by human ECs; it promotes neonatal diabetes when mutated (Figures 5A and 5B) (Pan et al., 2015). *MLN*⁺ cells developmentally resembled murine *Ghrl*-producing X cells.

We chose to knock out the EC-specific *LMX1A* gene and the D-cell-specific *HHEX* gene (Figures 5A and 5C). Organoids were transiently transfected with a Cas9-EGFP coding plasmid that included the site-specific guide RNA (gRNA) (Ran et al., 2013). Genotyping of clonal organoids was performed to identify homozygous loss-of-function alleles. *Lmx1a*-null mice die shortly after birth, lacking intestinal *Tph1* and *Chga* expression, indicative of EC loss (Gross et al., 2016). *LMX1A* mutant human organoids displayed a strong reduction in *TPH1* (Figure 5D). We also observed a milder reduction in *SST* derived from D cells. In contrast to mouse EECs, human *LMX1A* is also expressed in D-cells (Figure 5A)

HHEX has been linked to type 2 diabetes (Scott et al., 2007). Although loss of *Hhex* in mice impairs the function of *Sst*-producing cells in pancreatic islets, effects in the murine intestinal tract were not described (Zhang et al., 2014). *HHEX* gene disruption blocked the production of *SST* (Figure 5D). The most striking increase was observed in *GCG* expression (over 20-fold). In *Hhex*-knockout mice, pancreatic glucagon similarly increases (Zhang et al., 2014).

Immunofluorescent staining in *HHEX* and *LMX1A* organoids revealed a 4-fold reduction in the number of *SST*⁺ D cells upon

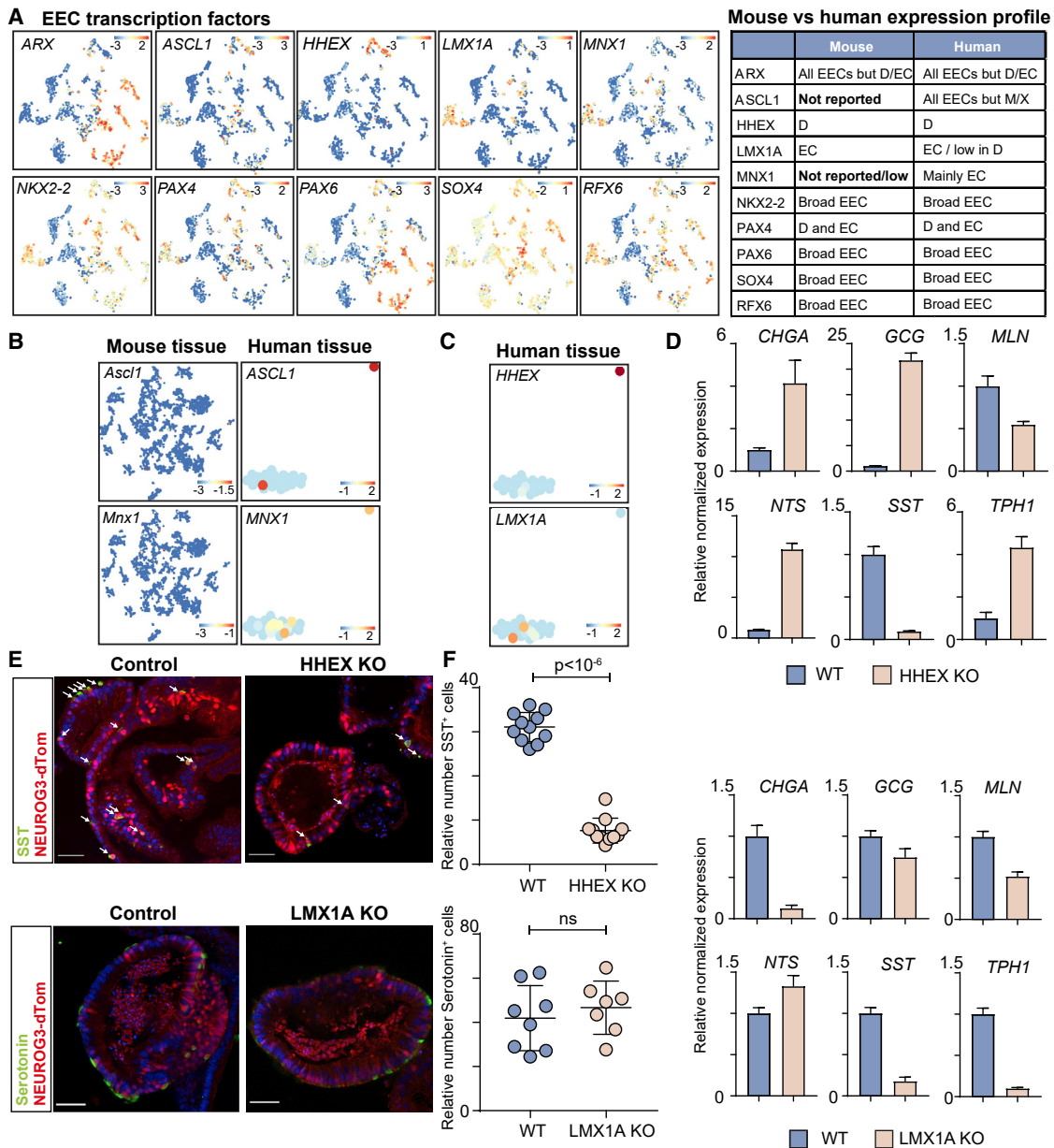


Figure 5. Transcriptional Networks in Human EECs

(A) t-SNE map displaying the expression level of EEC lineage transcription factors. Bars display color-coded unique transcript expression (logarithmic scale). The murine and human patterns of expression of these genes among EEC subtypes are depicted (right table).

(B) t-SNE maps displaying the expression level of EEC transcription factor *ASCL1* and *MNX1* in mouse and human EECs. Bars display color-coded unique transcript expression (logarithmic scale).

(C) t-SNE maps displaying the expression level of EEC transcription factors *HHEX* and *LMX1A* in human tissue EECs. Bars display color-coded unique transcript expression (logarithmic scale).

(D) qPCR analysis showing expression of hormones in wild-type organoids and *LMX1A* and *HHEX* knockout (KO) organoids. Expression is normalized to *GADPH*, and relative to wild type. The experiment was performed as a technical duplicate, and the mean expression and SEM are depicted.

(E) Immunofluorescent staining on wild-type and *HHEX* and *LMX1A* knockout organoids. D cells are reduced after *HHEX* loss, whereas EC cells do not decrease upon *LMX1A* knockout. Scale bar is 50 μ m.

(F) Quantification of (E). Number of hormone positive cells are counted on organoid sections and shown normalized to number of tdTomato⁺ cells and relative to WT. At least n = 7 organoids were counted per condition; p value was calculated using an unpaired two-tailed t test.

HHEX loss, suggesting impaired allocation of progenitors into this lineage (Figures 5E and 5F). Serotonin-producing cells did however not decrease in *LMX1A* knockout organoids, despite a decline in *TPH1* expression (Figures 5D–5F). We conclude that *LMX1A* is not directly important for allocation to the EC fate.

BMP Signaling as Regulator of Hormone Switching in Human EECs

Crypt-villus gradients were observed for human hormones such as *GCG* (Figure S5D). We interrogated BMP dependency of hormone gene expression in the single-cell atlas. BMP activation induced *NTS* in L cells at the expense of *GCG* (Figure S5E). Live-cell imaging of *GCG*-reporter organoids confirmed that BMP activation decreased reporter expression in individual L cells (Figure S5F). Additionally, we observed BMP-mediated repression of *GHRL* in M/X cells, accompanied by a mild increase in *MLN* expression (Figure S5E). In murine intestine, we have found that expression of *GHRL* diminishes with migration of the X cell along the crypt-villus axis (Gehart et al., 2019). Thus, human *MLN/GHRL*-producing EECs appeared to undergo a BMP-controlled switch in hormone expression as previously described in mouse.

High-Definition Transcriptomic and Proteomic Profiling of EECs

Transcriptomics of pooled cells has a superior sensitivity compared to single-cell RNA sequencing. We thus generated a deep transcriptomic signature of sorted and pooled EC, L, and M cells (Figure S6A). In addition, *CHGA*-mNeon⁺ cells were sorted to generate a broad EEC signature. We identified the top 20 uniquely expressed markers from the RNA sequencing dataset for each population (Figure S6B). We thus uncovered multiple EEC subtype features, unnoticed in the single-cell atlas. The transcription factor *IRX3*, member of the Iroquois homeobox family, was one of the most defining markers of *TPH1*⁺ cells, yet has not been described in murine EECs (Haber et al., 2017) (Figure S6B). *IRX3* has gained attention as a neuronal regulator of energy balance, and genetic variants in *IRX3* associate with obesity in humans (Schneeberger, 2019).

We analyzed our bulk transcriptomic datasets for subtype-specific receptors. We noted conserved expression of receptors known from mouse EECs, including *FFAR2* (broad EEC), *GPBAR1* (L cell), *SSTR5* (L cell), *OR51E1* (mouse homolog *Olfir558*; EC), *ADGRG4* (*Gpr112*; EC), and the extracellular calcium sensor *CASR* (broad EEC) (Furness et al., 2013) (Figure S6C). Human EECs expressed multiple orphan receptors, such as *GPR162* (L cells), not found in mice (Figure S6C), and reported to be expressed in brain to regulate food intake. Genetic variants in *GPR162* are linked to glucose deregulation (Caruso et al., 2016). *GPR68* is an orphan GPCR uniquely expressed by ECs (Figure S6C). The orphan peptide CART (cocaine- and amphetamine-regulated protein) activates *GPR68* (Foster et al., 2019); it has a role in the regulation of anxiety, reward, and feeding behaviors (Shcherbina et al., 2018). We find broad expression of the subunit of the GABA-B receptor *GABBR2*, potentially allowing a GABA response (Figure S7C) (Hyland and Cryan, 2010). We identified production of multiple hormone receptors in EECs, including the melanocortin receptor *MC1R* (Fig-

ure S6C). *MC4R* in murine L cells is a regulator of hormone secretion and can be activated by MSH-like producing bacteria (Panaro et al., 2014). ECs selectively expressed the receptor for the thyroid-stimulating hormone, *TSHR* (Figure S6C). Serotonin regulates thyroid hormone levels (Sullo et al., 2011). *TSHR* expression by ECs suggests that this regulation could work bidirectionally. ECs also expressed the receptor for the L cell hormone *PYY*, *NPY1R* (Figure S6C), reported in murine enterocytes as a regulator of electrolyte transport (Goldspink et al., 2018). We did not confirm expression of *NPY1R* in the *CHGA*-mNeon⁻ population, which includes enterocytes. L cells highly expressed the Sct receptor *SCTR* as observed in our single-cell atlas but not in mice (Figures S6C and S6D). Fluorescent *in situ* hybridization (FISH) confirmed the expression of *SCTR* in EECs *in vivo* by overlap with *CHGA* (Figure S6E). Because we observed the highest expression of *SCTR* in L cells, we measured GLP-1 secretion upon a 24 h secretin treatment in organoids. Indeed, Sct induced GLP-1 secretion at levels comparable to forskolin as measured by ELISA, or as seen by the loss of intracellular fluorescence of *GCG*-neon (Figures S6F–S6H).

We next isolated intracellular proteins for mass spectrometry to establish subtype-specific proteomes (Figure S6A). PCA-analysis revealed a clear separation of reporter populations (Figure S7A). The analysis confirmed many of the novel markers for EEC populations, including the L cell hormone *PPY*, EEC marker *MIDKINE*, and the M cell peptidase *CPB1* (Figure S7B). A gene identified at RNA level but not in the proteome was *CRYBA2*, a crystallin family member (Figure S7C), and reported as a marker of human endocrine cells in pancreas and colon (Muraro et al., 2016; Parikh et al., 2019). *CRYBA2* protein was also absent on human intestinal sections using immunohistochemistry (IHC) (Figure S7D). In the human genome, *CRYBA2* maps adjacent to another EEC marker gene, *FEV* (Haber et al., 2017). *CRYBA2* and *FEV* RNAs were expressed in a virtually identical pattern in our single-cell atlas (Figures S7C and S7E).

The Human EEC Secretome

The human EEC organoid cultures uniquely allow proteomic analysis of hormones secreted basolaterally. We isolated supernatants of forskolin-stimulated proximal and distal SI EEC organoids and control organoids, separated into >10kDa and <10kDa fractions. The latter was directly analyzed using liquid chromatography-mass spectrometry (LC-MS), whereas the former was first trypsinised (Figure 6A). Proteins secreted by EEC organoids showed a large non-overlap with the bulk proteome of the different EEC populations (Figure 6B). These proteins were mainly annotated to extracellular processes such as “secretion” when compared to intracellular proteome (Figure 6C). In both the >10kDa and the <10kDa (representing processed hormones) fractions, the expected EEC marker hormones were found among the most abundant proteins and peptides identified (Figure 6D). Control organoids (not enriched for EECs) mostly secreted goblet cell products like mucins and trefoil factors. This provided strong evidence for specific hormone processing and secretion by proximal (e.g., *GAST*, *GHRL*, *MLN*, and *CCK*) and distal (e.g., *PYY*, *NTS* and *GCG*) intestinal organoids.

Hormones known to undergo proteolytic processing were detected in the processed peptides fraction. By contrast, *REG4*

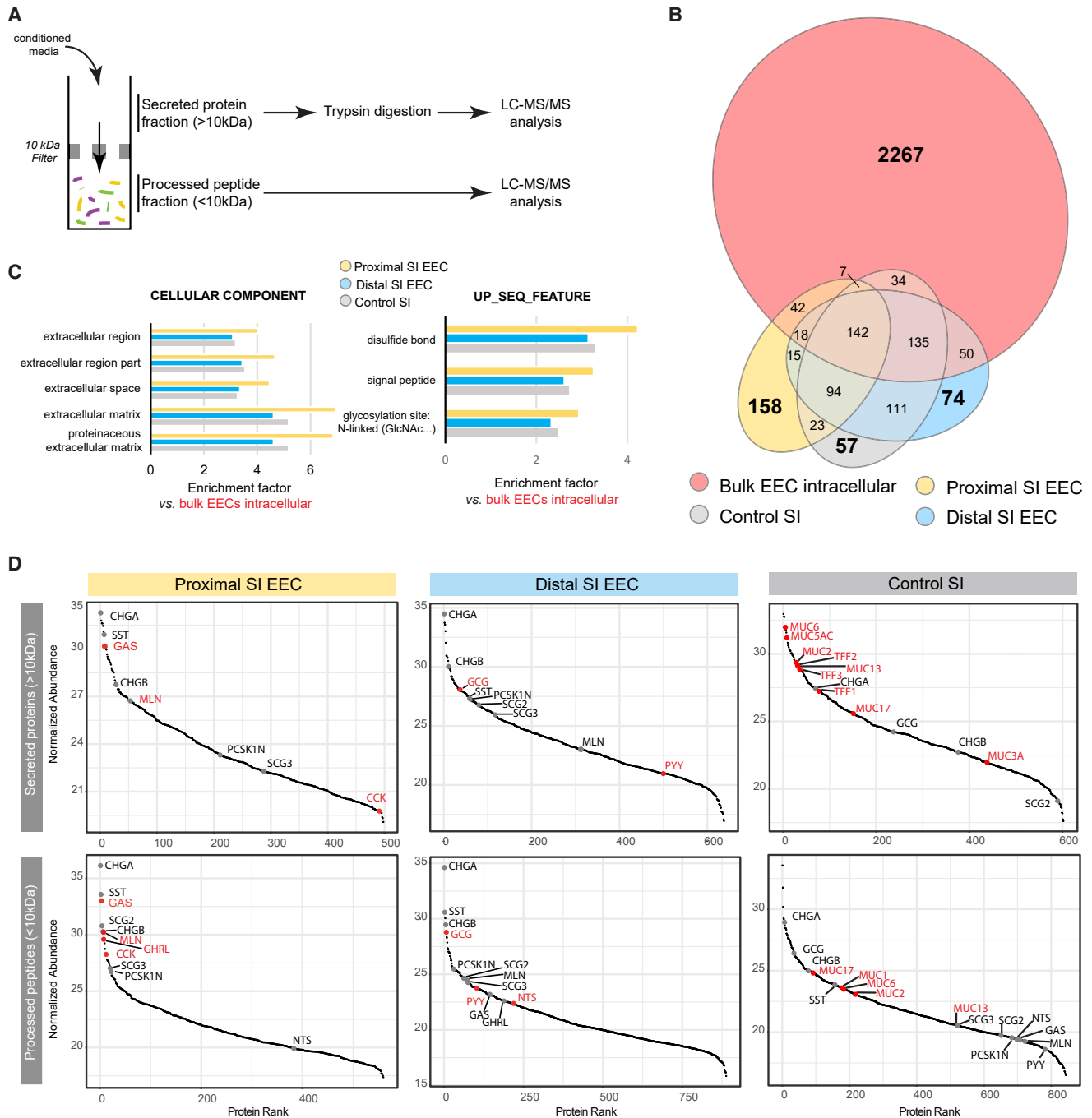


Figure 6. Human EEC Secretome Profiling by Mass Spectrometry

(A) Workflow for the analysis of secreted proteins and processed peptides from conditioned media. NEUROG3 induced or control organoids were stimulated for 24 h with forskolin, after which conditioned media were collected. Before applying the 10 kDa cut-off filter, the conditioned media were denatured for efficient partitioning by molecular weight and to disrupt potential protein-protein and protein-peptide interactions.

(B) Venn diagram showing the overlap in protein identifications between the bulk EEC proteome (red) and the proximal EEC-enriched (orange), distal EEC-enriched (blue), and control (gray) small intestinal (SI) organoid secretomes.

(C) Top-enriched cellular component and sequence feature characteristics of proteins identified in the proximal EEC-enriched, distal EEC-enriched, and non-induced SI organoid secretomes. The proteins detected in the bulk EEC intracellular proteome were used as reference for enrichment.

(D) Ranked abundances of proteins detected in the secreted protein fraction and processed peptide fraction. EEC markers are annotated in gray. Products enriched in the different secretomes are annotated in red. Typical proximal or distal hormones are enriched in the respective organoid types, whereas control organoids uniquely secrete mucins and trefoil factors.

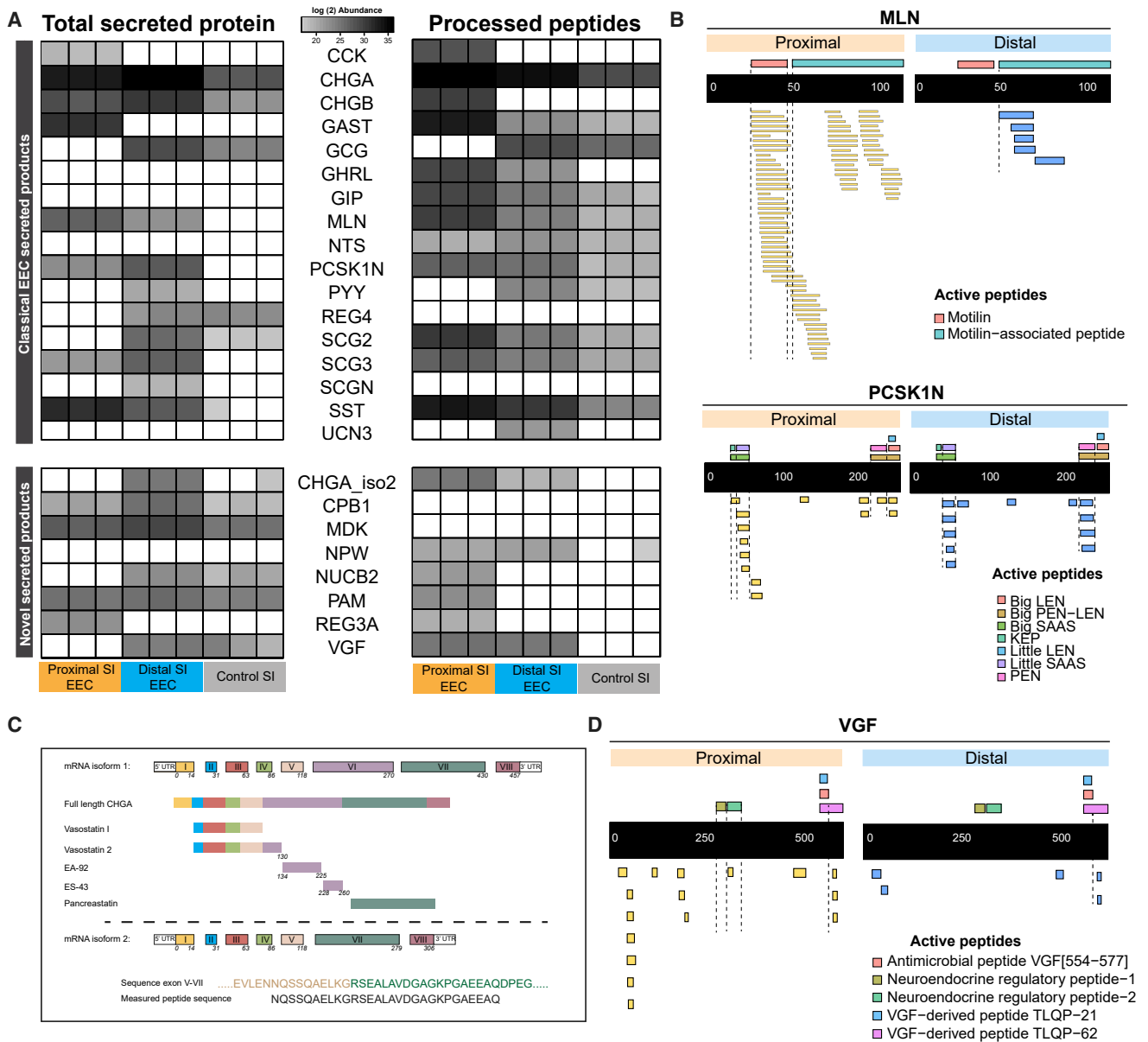


Figure 7. Processing of Region-Specific Human EEC Hormones

(A) Overview of relative abundance of known and novel secreted proteins and processed peptides. MS intensities are plotted as heatmaps for total secreted proteins (>10kDa fraction, left panel) and corresponding processed peptides (<10kDa fraction, right panel).

(B) Measured peptides (<10 kDa) in the supernatant of distal SI organoids mapping to the secreted prohormone MLN and the PCSK1N. Data from proximal (orange) and distal SI organoid (blue) supernatants are displayed. Known bioactive peptides are shown above the black bar.

(C) Alternative processing of chromogranin A (CHGA). Compared to Isoform 1, Isoform 2 of CHGA (lower panel) lacks exon VI. Peptides spanning sequences of both exon V and VII were detected in the supernatant, indicating isoform 2 is produced in human EECs.

(D) Measured peptides (<10 kDa) in the supernatant of proximal and distal SI organoids mapping to the secreted VGF protein. Other than sequences overlapping with known bioactive peptides, numerous other peptides were detected.

(biologically active as a full-length protein) was only found in the >10kDa fraction (Figure 7A). Processed peptides generally displayed C-terminal trimming, likely due to the endogenous activity of carboxypeptidases (Figures 7B and S7F). All known fragments of the proglucagon pro-hormone were observed (Figure S7F). Individual fragments rarely spanned more than a single biologically

active peptide. Neuronostatin, a fragment of the pro-somatostatin hormone (Vainio et al., 2012), was found abundantly in the EEC secretome (Figure S7F). Processed peptides were biased toward bioactive fragments of multiple hormones and enzymes, including for MLN, PCSK1N, and GHRL (Figures 7B and S7F). The signal peptide (20–25 N-terminal amino acids of the

prohormones) was consistently cleaved from all hormones (Figures 7B and S7F). Apart from quantitative differences, we also detected region-specific biases in the ratio between bioactive peptides and those with no known activity. For example, duodenal bioactive peptides from proximal-enriched hormones (GHRL, MLN) were highly overrepresented.

Next, we looked for peptides not shown to be secreted from EECs before. CHGA codes for a 457-amino acid preproprotein, cleaved into many different bioactive products. A shorter second isoform lacks exon 6 and has not been shown to be translated (Loh et al., 2012). We now find abundant peptides spanning exon 5 and exon 7 (Figures 7A and 7C). Consistent with the observed RNA expression, other previously unknown EEC products were also observed (Figures 4A and S7). These include NPW, MIDKINE, VGF, and the peptidase CPB1 (Figures 7A and 7D). We found expression and secretion of the antimicrobial peptide REG3A from human EECs (Figures 7A and S7F). We further identified EEC-specific secretion of the enzyme PAM (peptidyl-glycine alpha-amidating monooxygenase), which activates endocrine peptides by C-terminal amidation (Figures 7A and S7F). Coding variants of PAM are associated with type 2 diabetes and can affect insulin secretion (Thomsen et al., 2018). We detected the nucleobindin-2 (NUC2B) precursor, processed to the neuropeptides nesfatin-1, -2, and -3 (Ramesh et al., 2015). Nesfatin-1 has recently gained attention as an anorexigenic and insulinotropic peptide, produced in the hypothalamus and pancreas. Nesfatin-1 has been shown to regulate GLP-1 and GIP secretion *in vitro* (Ramesh et al., 2015).

DISCUSSION

Human EECs are rare and have been largely inaccessible for *in vitro* studies. We have generated a high-resolution transcriptomic and proteomic profile of human EECs from three locations along the gastrointestinal tract, including a first assessment of their secreted products. This dataset yields new hormones, transcription factors, and receptors and can be mined for novel therapeutic targets. The expression atlas highlights key differences with mouse. The transcriptional networks generating the different EEC subtypes have been well worked out in mice (Beucher et al., 2012; Gehart et al., 2019; Gross et al., 2016; Piccand et al., 2019). These networks could result from a stochastically acting system that generates fixed ratios of different EECs. This would explain why organoids generate conserved ratios of EEC subtypes when compared to their tissue of origin (Beumer et al., 2018). A recent study has surveyed a broad human EEC population using antibody-based sorting approaches and bulk RNA sequencing (Roberts et al., 2019) and identified EEC features, such as the expression of neuropeptide W, confirmed by the current study.

We present the first transcriptomic and proteomic profiling of MLN-producing cells. MLN is a regulator of gut motility with intriguing evolutionary dynamics, inactivated independently in lineages leading to the mouse and rat, and guinea pigs (He et al., 2010). The MLN receptor underwent a similar fate (He et al., 2010). This raises questions as to how the cell type (the X cell) that produces MLN diverged from that point. For example, the production of a certain hormone is likely to be

accompanied by the expression of dedicated sensory receptors. We found many similarities between mouse X cells and the human counterparts, M/X cells. Transcription factors are conserved (Figure 5A), as is expression of genes required for GHRL modifications such as *Acs11* (Figures 3C and 3D). We noted important differences also, like the expression of putative hormones including *CBLN1* and *AGT*. The latter has been proposed as motility regulator similar to MLN (Figure 4). We also identify a cytokine receptor in M/X cells, *IL-20RA*, which could link a sensory mechanism for pathogens to an expelling motility response.

The expression of receptors for some EEC hormones by EECs has been reported in mouse, particularly for *SST* (e.g., *Sstr5* in L cells) (Chisholm and Greenberg, 2002). We now find that human EECs can sense extracellular PYY (NPY1R) and Sct (SCTR). The PYY-receptor *Npy1r* has been suggested as an enterocyte marker in mouse, which we do not confirm in human (Goldspink et al., 2018). Rather, we observe exclusive expression in human serotonin-producing ECs. *SCTR* expression is low in ECs and enriched in EECs producing *GCG* and *GAST/GIP*. We show that Sct can stimulate L cells to secrete GLP-1. Importantly, a Sct stimulation test is commonly used in diagnostics of Zollinger-Ellison syndrome patients that suffer from gastrin-producing tumors (Berna et al., 2006). Sct normally represses blood gastrin by inhibiting the secretion of GAST from stomach G cells (the major site of GAST production), likely through modulating the luminal pH. Patients suffering from SI gastrinoma show sharp increases in serum GAST upon Sct administration. Our data suggest this to occur through SCTR expression by SI GAST-producing G cells. More broadly, our data indicate that human EECs have an extensive capacity to cross-communicate through their hormone products.

Taken together, the EEC atlas and EEC-TAG biobank represent rich resources to identify regulators of human EEC development and function.

STAR★METHODS

Detailed methods are provided in the online version of this paper and include the following:

- KEY RESOURCES TABLE
- RESOURCE AVAILABILITY
 - Lead Contact
 - Materials Availability
 - Data and Code Availability
- EXPERIMENTAL MODEL AND SUBJECT DETAILS
- METHOD DETAILS
 - Cell culture of human intestinal organoids
 - Constructs for EEC-TAG reporter and knockout generation
 - Calcium sensor
 - Live cell imaging of calcium reporter organoids
 - Transmission electron microscopy
 - Immunostaining
 - Fluorescent *in situ* hybridization
 - ELISA
 - RNA isolation and quantitative PCR

- Processing human intestinal tissue for single cell RNA sequencing
- Single cell sorting for RNA sequencing from organoids
- Single cell RNA sequencing analysis from organoids
- Bulk RNA sequencing analysis
- Preparation of secreted peptides and proteins for LC-MS
- Preparation of FACS-sorted EECs for proteome analyses
- LC-MS
- Proteomics data analysis
- **QUANTIFICATION AND STATISTICAL ANALYSIS**

SUPPLEMENTAL INFORMATION

Supplemental Information can be found online at <https://doi.org/10.1016/j.cell.2020.04.036>.

ACKNOWLEDGMENTS

We thank Anko de Graaff and the Hubrecht Imaging Centre (HIC) for microscopy assistance, Single Cell Discoveries for single-cell sequencing, and Folkert Morsink and Johan Offerhaus of the University Medical Center Utrecht for providing sections of human intestinal biopsies. J.B.-M., A.J.R.H., and W.W. acknowledge financial support from the Horizon 2020 program INFRAIA project Epic-XS (Project 823839) and the NWO funded Netherlands Proteomics Centre through the National Road Map for Large-scale Infrastructures program X-Omics (Project 184.034.019). This work was supported by NETRF/Petersen Accelerator (J.B.), CRUK grant OPTIMISTIC (C10674/A27140) (J.P. and C.P.-M.), Netherlands Organ-on-Chip Initiative (024.003.001) from the Netherlands Organisation for Scientific Research (NWO) (J.P., A.M.-S., and C.P.-M.), and ERC Advanced Grant Agreement no. 67013e (H.C.). We thank the Microscopy CORE Lab at M41 Maastricht University for their support in electron microscopy.

AUTHOR CONTRIBUTIONS

J.B., J.P., and H.C. conceptualized the project, designed the experiments, interpreted the results, and wrote the manuscript. J.B.-M., W.W., and A.J.R.H. performed the proteomic and secretomic experiments and analysis. A.M.S. assisted in cell culture experiments supervised by J.B., J.P., and H.C.; J.B. and J.P. generated and analyzed the organoid-derived EEC single-cell atlas. R.E., K.R.J., A.R., M.Z., and S.A.T. generated and analyzed the primary human EEC single-cell dataset. G.A.B. generated and provided the neurogenin-3 overexpression vector. D.H. and B.A. generated and provided the targeting vectors for CRISPR-HOT-mediated reporter organoids. A.A.-R. and M.H.G. provided different constructs. A.S., C.B., Y.P., and C.P.-M. contributed to functional EEC assays. F.v.d.L. and J.G. provided the Tq-Ca-FLITS reporter. B.P. and H.S. performed imaging and quantification of calcium responses. Y.E.B.-E. and R.v.d.L. assisted with FACS experiments. K.K. provided organoid lines. C.L.-I., W.J.v.d.W., and P.J.P. performed transmission electron microscopy.

DECLARATION OF INTERESTS

H.C. is inventor on several patents related to organoid technology; his full disclosure is given at <https://www.uu.nl/staff/JCClevers/>. H.C. is founder of OrganoidZ, which employs organoids for drug development. J.B., J.P., and H.C. are inventors on patents related to this work.

Received: November 29, 2019
 Revised: March 10, 2020
 Accepted: April 21, 2020
 Published: May 13, 2020

REFERENCES

- Artegiani, B., Hendriks, D., Beumer, J., Kok, R., Zheng, X., Joore, I., Chuva de Sousa Lopes, S., van Zon, J., Tans, S., and Clevers, H. (2020). Fast and efficient generation of knock-in human organoids using homology-independent CRISPR-Cas9 precision genome editing. *Nat. Cell Biol.* 22, 321–331.
- Bando, M., Iwakura, H., Koyama, H., Hosoda, H., Shigematsu, Y., Ariyasu, H., Akamizu, T., Kangawa, K., and Nakao, K. (2016). High incorporation of long-chain fatty acids contributes to the efficient production of acylated ghrelin in ghrelin-producing cells. *FEBS Lett.* 590, 992–1001.
- Barker, N., van Es, J.H., Kuipers, J., Kujala, P., van den Born, M., Cozijnsen, M., Haeghebarth, A., Korving, J., Begthel, H., Peters, P.J., and Clevers, H. (2007). Identification of stem cells in small intestine and colon by marker gene *Lgr5*. *Nature* 449, 1003–1007.
- Berna, M.J., Hoffmann, K.M., Long, S.H., Serrano, J., Gibril, F., and Jensen, R.T. (2006). Serum gastrin in Zollinger-Ellison syndrome: II. Prospective study of gastrin provocative testing in 293 patients from the National Institutes of Health and comparison with 537 cases from the literature. evaluation of diagnostic criteria, proposal of new criteria, and correlations with clinical and tumoral features. *Medicine (Baltimore)* 85, 331–364.
- Beucher, A., Gjernes, E., Collin, C., Courtney, M., Meunier, A., Collombat, P., and Gradwohl, G. (2012). The homeodomain-containing transcription factors *Arx* and *Pax4* control enteroendocrine subtype specification in mice. *PLoS ONE* 7, e36449.
- Beumer, J., Artigiani, B., Post, Y., Reimann, F., Gribble, F., Nguyen, T.N., Zeng, H., Van den Born, M., Van Es, J.H., and Clevers, H. (2018). Enterendocrine cells switch hormone expression along the crypt-to-villus BMP signalling gradient. *Nat. Cell Biol.* 20, 909–916.
- Borges, M., Linnoila, R.I., van de Velde, H.J.K., Chen, H., Nelkin, B.D., Mabry, M., Baylin, S.B., and Ball, D.W. (1997). An achaete-scute homologue essential for neuroendocrine differentiation in the lung. *Nature* 386, 852–855.
- Boztope, T., and Gulec, S. (2018). Investigation of the influence of high glucose on molecular and genetic responses: an *in vitro* study using a human intestine model. *Genes Nutr.* 13, 11.
- Bukhari, H., and Müller, T. (2019). Endogenous Fluorescence Tagging by CRISPR. *Trends Cell Biol.* 29, 912–928.
- Caruso, V., Sreedharan, S., Carlini, V.P., Jacobsson, J.A., Haitina, T., Hammer, J., Stephansson, O., Crona, F., Sommer, W.H., Risérus, U., et al. (2016). mRNA GPR162 changes are associated with decreased food intake in rat, and its human genetic variants with impairments in glucose homeostasis in two Swedish cohorts. *Gene* 581, 139–145.
- Chang-Graham, A.L., Danhof, H.A., Engevik, M.A., Tomaro-Duchesneau, C., Karandikar, U.C., Estes, M.K., Versalovic, J., Britton, R.A., and Hyser, J.M. (2019). Human Intestinal Enteroids With Inducible Neurogenin-3 Expression as a Novel Model of Gut Hormone Secretion. *Cell. Mol. Gastroenterol. Hepatol.* 8, 209–229.
- Chisholm, C., and Greenberg, G.R. (2002). Somatostatin-28 regulates GLP-1 secretion via somatostatin receptor subtype 5 in rat intestinal cultures. *Am. J. Physiol. Endocrinol. Metab.* 283, E311–E317.
- Coebergh, J.W.W., van Veen, E.B., Vandenbroucke, J.P., van Diest, P., and Oosterhuis, W. (2006). One-time general consent for research on biological samples: opt out system for patients is optimal and endorsed in many countries. *BMJ* 332, 665.
- Cox, H.M. (2007). Neuropeptide Y receptors; antisecretory control of intestinal epithelial function. *Auton. Neurosci.* 133, 76–85.
- Cui, T., Tsolakis, A.V., Li, S.C., Cunningham, J.L., Lind, T., Öberg, K., and Giandomenico, V. (2013). Olfactory receptor 51E1 protein as a potential novel tissue biomarker for small intestine neuroendocrine carcinomas. *Eur. J. Endocrinol.* 168, 253–261.
- Di Paola, R., Caporarello, N., Marucci, A., Dimatteo, C., Iadicicco, C., Del Guerra, S., Prudente, S., Sudano, D., Miele, C., Parrino, C., et al. (2011). ENPP1 affects insulin action and secretion: evidences from *in vitro* studies. *PLoS ONE* 6, e19462.

- Edfeldt, K., Daskalakis, K., Bäcklin, C., Norlén, O., Tiensuu Janson, E., Westin, G., Hellman, P., and Ståhlberg, P. (2017). DcR3, TFF3, and Midkine Are Novel Serum Biomarkers in Small Intestinal Neuroendocrine Tumors. *Neuroendocrinology* *105*, 170–181.
- Engelstoft, M.S., Egerod, K.L., Lund, M.L., and Schwartz, T.W. (2013a). Enterendocrine cell types revisited. *Curr. Opin. Pharmacol.* *13*, 912–921.
- Engelstoft, M.S., Park, W.M., Sakata, I., Kristensen, L.V., Husted, A.S., Osborne-Lawrence, S., Piper, P.K., Walker, A.K., Pedersen, M.H., Nøhr, M.K., et al. (2013b). Seven transmembrane G protein-coupled receptor repertoire of gastric ghrelin cells. *Mol. Metab.* *2*, 376–392.
- Engelstoft, M.S., Lund, M.L., Grunddal, K.V., Egerod, K.L., Osborne-Lawrence, S., Poulsen, S.S., Zigman, J.M., and Schwartz, T.W. (2015). Research Resource: A Chromogranin A Reporter for Serotonin and Histamine Secreting Enteroendocrine Cells. *Mol. Endocrinol.* *29*, 1658–1671.
- Ewert, S., Spak, E., Olbers, T., Johnsson, E., Edebo, A., and Fändriks, L. (2006). Angiotensin II induced contraction of rat and human small intestinal wall musculature in vitro. *Acta Physiol. (Oxf.)* *188*, 33–40.
- Fan, N., Sun, H., Wang, Y., Zhang, L., Xia, Z., Peng, L., Hou, Y., Shen, W., Liu, R., and Peng, Y. (2014). Midkine, a potential link between obesity and insulin resistance. *PLoS ONE* *9*, e88299.
- Fleischer, J., Bumbalo, R., Bautze, V., Strotmann, J., and Breer, H. (2015). Expression of odorant receptor Olfr78 in enteroendocrine cells of the colon. *Cell Tissue Res.* *361*, 697–710.
- Foster, S.R., Hauser, A.S., Vedel, L., Strachan, R.T., Huang, X.P., Gavin, A.C., Shah, S.D., Nayak, A.P., Haugaard-Kedström, L.M., Penn, R.B., et al. (2019). Discovery of Human Signaling Systems: Pairing Peptides to G Protein-Coupled Receptors. *Cell* *179*, 895–908.e21.
- Fujii, M., Matano, M., Nanki, K., and Sato, T. (2015). Efficient genetic engineering of human intestinal organoids using electroporation. *Nat. Protoc.* *10*, 1474–1485.
- Furness, J.B., Rivera, L.R., Cho, H.-J., Bravo, D.M., and Callaghan, B. (2013). The gut as a sensory organ. *Nat. Rev. Gastroenterol. Hepatol.* *10*, 729–740.
- Gardiner, J.V., Beale, K.E., Roy, D., Boughton, C.K., Bataveljic, A., Campbell, D.C., Bewick, G.A., Patel, N.A., Patterson, M., Leavy, E.M., et al. (2010). Cerbellin1 is a novel orexigenic peptide. *Diabetes Obes. Metab.* *12*, 883–890.
- Gehart, H., van Es, J.H., Hamer, K., Beumer, J., Kretschmar, K., Dekkers, J.F., Rios, A., and Clevers, H. (2019). Identification of Enteroendocrine Regulators by Real-Time Single-Cell Differentiation Mapping. *Cell* *176*, 1158–1173.e16.
- Goldspink, D.A., Reimann, F., and Gribble, F.M. (2018). Models and Tools for Studying Enteroendocrine Cells. *Endocrinology* *159*, 3874–3884.
- Gong, S., Zheng, C., Doughty, M.L., Losos, K., Didkovsky, N., Schambra, U.B., Nowak, N.J., Joyner, A., Leblanc, G., Hatten, M.E., and Heintz, N. (2003). A gene expression atlas of the central nervous system based on bacterial artificial chromosomes. *Nature* *425*, 917–925.
- Gribble, F.M., and Reimann, F. (2017). Signalling in the gut endocrine axis. *Physiol. Behav.* *176*, 183–188.
- Gross, S., Garofalo, D.C., Balderes, D.A., Mastracci, T.L., Dias, J.M., Perlmann, T., Ericson, J., and Sussel, L. (2016). The novel enterochromaffin marker *Lmx1a* regulates serotonin biosynthesis in enteroendocrine cell lineages downstream of *Nkx2.2*. *Development* *143*, 2616–2628.
- Grün, D., Lyubimova, A., Kester, L., Wiebrands, K., Basak, O., Sasaki, N., Clevers, H., and van Oudenaarden, A. (2015). Single-cell messenger RNA sequencing reveals rare intestinal cell types. *Nature* *525*, 251–255.
- Haber, A.L., Biton, M., Rogel, N., Herbst, R.H., Shekhar, K., Smillie, C., Burgin, G., Delorey, T.M., Howitt, M.R., Katz, Y., et al. (2017). A single-cell survey of the small intestinal epithelium. *Nature* *551*, 333–339.
- Hashimshony, T., Senderovich, N., Avital, G., Klochender, A., de Leeuw, Y., Anavy, L., Gennert, D., Li, S., Livak, K.J., Rozenblatt-Rosen, O., et al. (2016). CEL-Seq2: sensitive highly-multiplexed single-cell RNA-Seq. *Genome Biol.* *17*, 77.
- He, J., Irwin, D.M., Chen, R., and Zhang, Y.P. (2010). Stepwise loss of motilin and its specific receptor genes in rodents. *J. Mol. Endocrinol.* *44*, 37–44.
- He, X., Tan, C., Wang, F., Wang, Y., Zhou, R., Cui, D., You, W., Zhao, H., Ren, J., and Feng, B. (2016). Knock-in of large reporter genes in human cells via CRISPR/Cas9-induced homology-dependent and independent DNA repair. *Nucleic Acids Res.* *44*, e85.
- Herman, J.S., Sagar, and Grün, D. (2018). FateID infers cell fate bias in multipotent progenitors from single-cell RNA-seq data. *Nat. Methods* *15*, 379–386.
- Huang, W., Sherman, B.T., and Lempicki, R.A. (2009). Systematic and integrative analysis of large gene lists using DAVID bioinformatics resources. *Nat. Protoc.* *4*, 44–57.
- Hyland, N.P., and Cryan, J.F. (2010). A gut feeling about GABA: Focus on GABA-B receptors. *Front. Pharmacol.* <https://doi.org/10.3389/fphar.2010.00124>.
- Jovancevic, N., Khalfaoui, S., Weinrich, M., Weidinger, D., Simon, A., Kalbe, B., Kernt, M., Kampik, A., Gisselmann, G., Gelis, L., and Hatt, H. (2017). Odorant receptor 51E2 agonist β -ionone regulates RPE cell migration and proliferation. *Front. Physiol.* *8*, 888.
- Koo, B.K., Stange, D.E., Sato, T., Karthaus, W., Farin, H.F., Huch, M., van Es, J.H., and Clevers, H. (2011). Controlled gene expression in primary *Lgr5* organoid cultures. *Nat. Methods* *9*, 81–83.
- Kuro-O, M. (2019). The *Klotho* proteins in health and disease. *Nat. Rev. Nephrol.* *15*, 27–44.
- Levine, A.S., Winsky-Sommerer, R., Huitron-Resendiz, S., Grace, M.K., and de Lecea, L. (2005). Injection of neuropeptide W into paraventricular nucleus of hypothalamus increases food intake. *Am. J. Physiol. Regul. Integr. Comp. Physiol.* *288*, R1727–R1732.
- Li, W., Ji, M., Lin, Y., Miao, Y., Chen, S., and Li, H. (2018). DEPP/DEPP1/C10ORF10 regulates hepatic glucose and fat metabolism partly via ROS-induced FGF21. *FASEB J.* *32*, 5459–5469.
- Lo, C.A., Kays, I., Emran, F., Lin, T.J., Cvetkovska, V., and Chen, B.E. (2015). Quantification of Protein Levels in Single Living Cells. *Cell Rep.* *13*, 2634–2644.
- Loh, Y.P., Cheng, Y., Mahata, S.K., Corti, A., and Tota, B. (2012). Chromogranin A and derived peptides in health and disease. *J. Mol. Neurosci.* *48*, 347–356.
- Lohoff, F.W., Dahl, J.P., Ferraro, T.N., Arnold, S.E., Gallinat, J., Sander, T., and Berrettini, W.H. (2006). Variations in the vesicular monoamine transporter 1 gene (*VMAT1/SLC18A1*) are associated with bipolar I disorder. *Neuropsychopharmacology* *31*, 2739–2747.
- Love, M.I., Huber, W., and Anders, S. (2014). Moderated estimation of fold change and dispersion for RNA-seq data with DESeq2. *Genome Biol.* *15*, 550.
- McCracken, K.W., Catá, E.M., Crawford, C.M., Sinagoga, K.L., Schumacher, M., Rockich, B.E., Tsai, Y.H., Mayhew, C.N., Spence, J.R., Zavros, Y., and Wells, J.M. (2014). Modelling human development and disease in pluripotent stem-cell-derived gastric organoids. *Nature* *516*, 400–404.
- McInnes, L., Healy, J., Saul, N., and Großberger, L. (2018). UMAP: Uniform Manifold Approximation and Projection. *J. Open Source Softw.* *3*, 861.
- Muñoz, J., Stange, D.E., Schepers, A.G., van de Wetering, M., Koo, B.-K., Itzkovitz, S., Volckmann, R., Kung, K.S., Koster, J., Radulescu, S., et al. (2012). The *Lgr5* intestinal stem cell signature: robust expression of proposed quiescent '+4' cell markers. *EMBO J.* *31*, 3079–3091.
- Muraro, M.J., Dharmadhikari, G., Grün, D., Groen, N., Dielen, T., Jansen, E., van Gurp, L., Engelse, M.A., Carlotti, F., de Koning, E.J.P., and van Oudenaarden, A. (2016). A Single-Cell Transcriptome Atlas of the Human Pancreas. *Cell Syst.* *3*, 385–394.e3.
- Nguyen, T.L.A., Vieira-Silva, S., Liston, A., and Raes, J. (2015). How informative is the mouse for human gut microbiota research? *Dis. Model. Mech.* *8*, 1–16.
- Pablo, J.L., and Pitta, G.S. (2017). FGF14 is a regulator of KCNQ2/3 channels. *Proc. Natl. Acad. Sci. U S A.* <https://doi.org/10.1073/pnas.1610158114>.
- Pan, F.C., Brissova, M., Powers, A.C., Pfaff, S., and Wright, C.V.E. (2015). Inactivating the permanent neonatal diabetes gene *Mnx1* switches insulin-producing β -cells to a γ -like fate and reveals a facultative proliferative capacity in aged β -cells. *Dev.* *142*, 3637–3648.

- Panaro, B.L., Tough, I.R., Engelstoft, M.S., Matthews, R.T., Digby, G.J., Møller, C.L., Svendsen, B., Gribble, F., Reimann, F., Holst, J.J., et al. (2014). The melanocortin-4 receptor is expressed in enteroendocrine L cells and regulates the release of peptide YY and glucagon-like peptide 1 in vivo. *Cell Metab.* **20**, 1018–1029.
- Parikh, K., Antanaviciute, A., Fawcner-Corbett, D., Jagielowicz, M., Alicino, A., Lagerholm, C., Davis, S., Kinchen, J., Chen, H.H., Alham, N.K., et al. (2019). Colonic epithelial cell diversity in health and inflammatory bowel disease. *Nature* **567**, 49–55.
- Parker, H.E., Habib, A.M., Rogers, G.J., Gribble, F.M., and Reimann, F. (2009). Nutrient-dependent secretion of glucose-dependent insulinotropic polypeptide from primary murine K cells. *Diabetologia* **52**, 289–298.
- Piccand, J., Vagne, C., Blot, F., Meunier, A., Beucher, A., Strasser, P., Lund, M.L., Ghimire, S., Nivlet, L., Lapp, C., et al. (2019). Rfx6 promotes the differentiation of peptide-secreting enteroendocrine cells while repressing genetic programs controlling serotonin production. *Mol. Metab.* **29**, 24–39.
- Pietraszewski-Bogiel, A., van Weeren, L., and Goedhart, J. (2019). Seeing cells smell: Dynamic optical measurements of Ca²⁺ and cAMP signaling from Olfactory Receptors transiently expressed in HEK293TN cells. [bioRxiv. https://doi.org/10.1101/771261](https://doi.org/10.1101/771261).
- Ramesh, N., Mortazavi, S., and Unniappan, S. (2015). Nesfatin-1 stimulates glucagon-like peptide-1 and glucose-dependent insulinotropic polypeptide secretion from STC-1 cells in vitro. *Biochem. Biophys. Res. Commun.* **462**, 124–130.
- Ran, F.A., Hsu, P.D., Wright, J., Agarwala, V., Scott, D.A., and Zhang, F. (2013). Genome engineering using the CRISPR-Cas9 system. *Nat. Protoc.* **8**, 2281–2308.
- Reimann, F., Habib, A.M., Tolhurst, G., Parker, H.E., Rogers, G.J., and Gribble, F.M. (2008). Glucose Sensing in L Cells: A Primary Cell Study. *Cell Metab* **8**, 532–539.
- Roberts, G.P., Larraufie, P., Richards, P., Kay, R.G., Galvin, S.G., Miedzybrodzka, E.L., Leiter, A., Li, H.J., Glass, L.L., Ma, M.K.L., et al. (2019). Comparison of human and murine enteroendocrine cells by transcriptomic and peptidomic profiling. *Diabetes* **68**, 1062–1072.
- Sachs, N., Pappaspyropoulos, A., Zomer-van Ommen, D.D., Heo, I., Böttiger, L., Klay, D., Weeber, F., Huelsz-Prince, G., Iakobachvili, N., Amatngalim, G.D., et al. (2019). Long-term expanding human airway organoids for disease modeling. *EMBO J.* **38**, e100300.
- Sanger, G.J. (2004). Neurokinin NK1 and NK3 receptors as targets for drugs to treat gastrointestinal motility disorders and pain. *Br. J. Pharmacol.* **141**, 1303–1312.
- Sapio, M.R., and Fricker, L.D. (2014). Carboxypeptidases in disease: insights from peptidomic studies. *Proteomics Clin. Appl.* **8**, 327–337.
- Sato, T., Vries, R.G., Snippert, H.J., van de Wetering, M., Barker, N., Stange, D.E., van Es, J.H., Abo, A., Kujala, P., Peters, P.J., and Clevers, H. (2009). Single Lgr5 stem cells build crypt-villus structures in vitro without a mesenchymal niche. *Nature* **459**, 262–265.
- Sato, T., Stange, D.E., Ferrante, M., Vries, R.G.J., Van Es, J.H., Van den Brink, S., Van Houdt, W.J., Pronk, A., Van Gorp, J., Siersema, P.D., and Clevers, H. (2011). Long-term expansion of epithelial organoids from human colon, adenoma, adenocarcinoma, and Barrett's epithelium. *Gastroenterology* **141**, 1762–1772.
- Schmid-Burgk, J.L., Höning, K., Ebert, T.S., and Hornung, V. (2016). CRISPRaint allows modular base-specific gene tagging using a ligase-4-dependent mechanism. *Nat. Commun.* **7**, 12338.
- Schneeberger, M. (2019). Irx3, a new leader on obesity genetics. *EBioMedicine* **39**, 19–20.
- Scott, L.J., Mohlke, K.L., Bonnycastle, L.L., Willer, C.J., Li, Y., Duren, W.L., Erdos, M.R., Stringham, H.M., Chines, P.S., Jackson, A.U., et al. (2007). A genome-wide association study of type 2 diabetes in finns detects multiple susceptibility variants. *Science* **316**, 1341–1345.
- Sharma, D., Verma, S., Vaidya, S., Kalia, K., and Tiwari, V. (2018). Recent updates on GLP-1 agonists: Current advancements & challenges. *Biomed. Pharmacother.* **108**, 952–962.
- Shcherbina, L., Lindqvist, A., Thorén Fischer, A.H., Ahlqvist, E., Zhang, E., Falkmer, S.E., Renström, E., Koffert, J., Honka, H., and Wierup, N. (2018). Intestinal CART is a regulator of GIP and GLP-1 secretion and expression. *Mol. Cell. Endocrinol.* **476**, 8–16.
- Sinagoga, K.L., McCauley, H.A., Múnera, J.O., Reynolds, N.A., Enriquez, J.R., Watson, C., Yang, H.C., Helmrich, M.A., and Wells, J.M. (2018). Deriving functional human enteroendocrine cells from pluripotent stem cells. *Development* **145**, dev165795.
- Sommer, C.A., and Mostoslavsky, G. (2014). RNA-Seq analysis of enteroendocrine cells reveals a role for FABP5 in the control of GIP secretion. *Mol. Endocrinol.* **28**, 1855–1865.
- Stahl, R., Walcher, T., De Juan Romero, C., Pilz, G.A., Cappello, S., Imler, M., Sanz-Aguela, J.M., Beckers, J., Blum, R., Borrell, V., and Götz, M. (2013). Trnp1 regulates expansion and folding of the mammalian cerebral cortex by control of radial glial fate. *Cell* **153**, 535–549.
- Sullo, A., Brizzi, G., and Maffulli, N. (2011). Chronic peripheral administration of serotonin inhibits thyroid function in the rat. *Muscles Ligaments Tendons J.* **1**, 48–50.
- The, M., MacCoss, M.J., Noble, W.S., and Käll, L. (2016). Fast and Accurate Protein False Discovery Rates on Large-Scale Proteomics Data Sets with Percolator 3.0. *J. Am. Soc. Mass Spectrom.* **27**, 1719–1727.
- Thomsen, S.K., Raimondo, A., Hastoy, B., Sengupta, S., Dai, X.Q., Bautista, A., Censin, J., Payne, A.J., Umaphysivam, M.M., Spigelman, A.F., et al. (2018). Type 2 diabetes risk alleles in PAM impact insulin release from human pancreatic β -cells. *Nat. Genet.* **50**, 1122–1131.
- Too, L.K., Li, K.M., Suarna, C., Maghazal, G.J., Stocker, R., McGregor, I.S., and Hunt, N.H. (2016). Deletion of TDO2, IDO-1 and IDO-2 differentially affects mouse behavior and cognitive function. *Behav. Brain Res.* **312**, 102–117.
- Tyanova, S., Temu, T., Sinitcyn, P., Carlson, A., Hein, M.Y., Geiger, T., Mann, M., and Cox, J. (2016). The Perseus computational platform for comprehensive analysis of (prote)omics data. *Nat. Methods* **13**, 731–740.
- Vainio, L., Perjes, A., Rytö, N., Magga, J., Alakoski, T., Serpi, R., Kaikkonen, L., Piuhola, J., Szokodi, I., Ruskoaho, H., and Kerkelä, R. (2012). Neuronostatin, a novel peptide encoded by somatostatin gene, regulates cardiac contractile function and cardiomyocyte survival. *J. Biol. Chem.* **287**, 4572–4580.
- Wang, F., Flanagan, J., Su, N., Wang, L.C., Bui, S., Nielson, A., Wu, X., Vo, H.T., Ma, X.J., and Luo, Y. (2012). RNAscope: a novel in situ RNA analysis platform for formalin-fixed, paraffin-embedded tissues. *J. Mol. Diagn.* **14**, 22–29.
- Wolf, F.A., Angerer, P., and Theis, F.J. (2018). SCANPY: large-scale single-cell gene expression data analysis. *Genome Biol.* **19**, 15.
- Worthington, J.J., Reimann, F., and Gribble, F.M. (2018). Enteroendocrine cells-sensory sentinels of the intestinal environment and orchestrators of mucosal immunity. *Mucosal Immunol.* **11**, 3–20.
- Yu, S.L., Han, S., Kim, H.R., Park, J.W., Jin, D.I., and Kang, J. (2017). Phosphorylation of carboxypeptidase B1 protein regulates β -cell proliferation. *Int. J. Mol. Med.* **40**, 1397–1404.
- Zhang, J., McKenna, L.B., Bogue, C.W., and Kaestner, K.H. (2014). The diabetes gene Hhex maintains δ -cell differentiation and islet function. *Genes Dev.* **28**, 829–834.
- Zhang, X., McGrath, P.S., Salomone, J., Rahal, M., McCauley, H.A., Schweitzer, J., Kovall, R., Gebelein, B., and Wells, J.M. (2019). A Comprehensive Structure-Function Study of Neurogenin3 Disease-Causing Alleles during Human Pancreas and Intestinal Organoid Development. *Dev. Cell* **50**, 367–380.e7.

STAR★METHODS

KEY RESOURCES TABLE

REAGENT or RESOURCE	SOURCE	IDENTIFIER
Antibodies		
Anti-Chromogranin A	Santa Cruz	sc-1488, RRID: AB_2276319
Anti-Cholestocystokinin	Santa Cruz	sc-21617, RRID: AB_2072464
Anti-Neurotensin	Santa Cruz	sc-20806, RRID: AB_2155562
Anti-Somatostatin	Santa Cruz	sc-7819, RRID: AB_2302603
Anti-Serotonin	Abcam	ab66047, RRID: AB_1142794
Anti-Gastric inhibitory polypeptide	Abcam	ab22624-50, RRID: AB_2109683
Anti-GLP1	Santa Cruz	sc-7782, RRID: AB_2107325
Anti-Motilin	Atlas antibodies	HPA069392, RRID: AB_2686136
Anti-GLP1	Abcam	ab22625, RRID: AB_447206
Anti-Gastrin	Proteintech	60346-1-Ig
Anti-Ghrelin	Santa Cruz	sc-10368, RRID: AB_2232479
Anti-beta-catenin	BD transduction laboratories	#610154, RRID: AB_397555
Anti-Neuropeptide W	Novus biologicals	NBP2-57337
Anti-Precerebellin	Sigma-Aldrich	ABN304
Anti-PPY	Atlas antibodies	HPA032122, RRID: AB_2674164
Alexa Fluor 488 donkey anti-rabbit	Thermo Fisher scientific	A21206, RRID: AB_2535792
Alexa Fluor 488 donkey anti-goat	Thermo Fisher scientific	A11055, RRID: AB_2534102
Alexa Fluor 568 donkey anti-rabbit	Thermo Fisher scientific	A10042, RRID: AB_2534017
Alexa Fluor 568 donkey anti-goat	Thermo Fisher scientific	A11057, RRID: AB_2534104
Alexa Fluor 647 donkey anti-rabbit	Thermo Fisher scientific	A31573, RRID: AB_2536183
Alexa Fluor 647 donkey anti-goat	Thermo Fisher scientific	A32849, RRID: AB_2762840
Alexa Fluor 647 donkey anti-mouse	Thermo Fisher scientific	A31571, RRID: AB_162542
Envision+ System-HRP polymer anti-rabbit	DAKO	K4002
Biological Samples		
Human intestinal tissue for organoids	Utrecht Medical Center	N/A
Human intestinal biopsies for RNA sequencing	Addenbrooke's Hospital, Cambridge	Ethics: REC 17/EE/0265
Chemicals, Peptides, and Recombinant Proteins		
10 kDa Vivaspin centrifugal device	Sartorius, Gottingen, Germany	Catalogue # VS0101
Reversed-phase C18 1cc columns	Waters Corporation, Milford, USA	Catalogue # WAT054925
Trypsin enzyme	Promega, Madison, USA	Catalogue # T1426
Lysyl endopeptidase enzyme (Lys C)	Wako Chemicals GmbH	Catalogue # 129-02541
DNase I	Sigma-Aldrich, Missouri, USA	Catalogue #DN25
RNase A	Sigma-Aldrich, Missouri, USA	Catalogue # R-6513
Advanced DMEM/F12	Thermo Fisher scientific	12634-010
B-27 Supplement	Thermo Fisher scientific	17504044
GlutaMAX	Thermo Fisher scientific	35050061
HEPES	Thermo Fisher scientific	15630080
Penicillin-Streptomycin	Thermo Fisher scientific	15140122
Wnt surrogate	U-Protein Express	Custom order
Noggin conditioned medium	U-Protein Express	Custom order
R-spondin conditioned medium	U-Protein Express	Custom order

(Continued on next page)

Continued

REAGENT or RESOURCE	SOURCE	IDENTIFIER
N-Acetyl-L-cysteine	Sigma-Aldrich	A9165
Nicotinamide	Sigma-Aldrich	N0636
Human EGF	Peprtech	AF-100-15
A83-01	Tocris	2939
Prostaglandin E2	Tocris	2296
Forskolin	Tocris	1099
A83-01	Tocris	2939
SB 202190	Sigma-Aldrich	S7076
Y-27632 dihydrochloride	Abmole	M1817
Primocin	Invivogen	ant-pm-2
BMP-2	Peprtech	120-02C
BMP-4	Peprtech	120-05ET
Secretin	Tocris	1918
Cultrex Basement Membrane Extract (BME), Growth Factor Reduced, Type 2	R&D Systems, Bio-Techne	3533-001-02
DAPI	Thermo Fisher scientific	D1306
Formaldehyde solution 4%	Sigma-Aldrich	1.00496
SYBR Green	Bio Rad	1725270
Donkey serum	Golden Bridge International	E27-100
Triton X-100	Sigma-Aldrich	X100-100ML
SORT-seq reagents	(Muraro et al., 2016)	N/A
Beta-ionone	Sigma-Aldrich	I12603
DAPT	Sigma-Aldrich	D5942
IWP-2	Stemcell Techonologies	72122
Sapl	New England Biolabs	R0569S
NotI	New England Biolabs	R0189S
Phusion High fidelity DNA polymerase	New England Biolabs	M0530S
TrypLE	Thermo Fisher scientific	12605010
Vectashield	Vector Labs	H-1000-10
Hyaluronidase	Merck	#385931-25KU
BTXpress solution	BTX	45-0805
Critical Commercial Assays		
RNeasy Mini Kit	QIAGEN	74104
GLP-1 ELISA kit	Sigma-Aldrich	RAB0201
In-fusion cloning kit	Takara	638910
QIAquick PCR Purification Kit	QIAGEN	28104
Thermo Scientific reagents for CEL-Seq2	(Hashimshony et al., 2016)	N/A
Reagents for library preparation from CEL-Seq2	(Hashimshony et al., 2016)	N/A
Miniprep DNA isolation kit	Thermo Fisher scientific	K210003
Midiprep DNA isolation kit	Thermo Fisher scientific	K210005
Chromium Single Cell 3' Library & Gel Bead Kit v2, 16 rxns	10x Genomics	PN-120237
Deposited Data		
Raw mass spectrometry data	PRIDE repository https://www.ebi.ac.uk/pride/	Accession number PXD017468
Raw and analyzed sequencing	Gene expression omnibus https://www.ncbi.nlm.nih.gov/geo/	GSE146799

(Continued on next page)

Continued

REAGENT or RESOURCE	SOURCE	IDENTIFIER
Software and Algorithms		
Proteome Discoverer 2.3	Thermo Fisher scientific	OPTON-30956 (https://www.thermofisher.com/us/en/home/technical-resources/request-a-quote.OPTON-30956.html?supportType=SL)
Sequest HT	Thermo Fisher scientific	With Proteome Discoverer 2.3 (OPTON-30956)
Percolator	Thermo Fisher scientific	With Proteome Discoverer 2.3 (OPTON-30956)
Perseus 1.6.2.2	Max Planck Institute of Biochemistry	https://maxquant.net/perseus/
Database for Annotation, Visualization and Integrated Discovery (DAVID) version 6.8	(Huang et al., 2009)	https://david.ncifcrf.gov/
Uniprot human database (Organism Species 9606)	Uniprot	https://www.uniprot.org/uniprot/?query=*&fil=organism%3A%22Homo+sapiens+%28Human%29+%5B9606%5D%22+AND+reviewed%3Ayes
CFX manager software	Bio-Rad	N/A
RacelD3	(Herman et al., 2018)	https://github.com/dgrun/RacelD3_StemID2
GraphPad PRISM 8	GraphPad	N/A
Las X	Leica	N/A
Fiji	NIH, Fiji developers	https://imagej.net/Fiji
Rstudio	Rstudio	https://rstudio.com/
Adobe illustrator	Adobe inc.	N/A
Cellranger (Version 2.1.0, reference transcriptome GRCh38-1.2.0)	10x Genomics	https://support.10xgenomics.com/single-cell-gene-expression/software/pipelines/latest/installation
Scanpy (Version 1.4)	N/A	https://icb-scanpy.readthedocs-hosted.com/en/stable/
Pandas (Version 0.25.2)	N/A	https://pandas.pydata.org/
NumPy (Version 1.16.2)	N/A	https://numpy.org/
UMAP	(McInnes et al., 2018)	Python package umap
Scipy (Version 1.2.1)	N/A	https://www.scipy.org/
Anndata (Version 0.6.19)	N/A	https://pypi.org/project/anndata/
Other		
EVOS Cell Imaging System	Thermo Fisher scientific	N/A
EVOS FL Auto 2 Cell Imaging System	Thermo Fisher scientific	N/A
SP8 confocal microscope	Leica	N/A
DM4000	Leica	N/A
NEPA21 electroporator	Nepagene	N/A
FACSAria	BD Biosciences	N/A
FACS BD Influx	BD Biosciences	N/A

RESOURCE AVAILABILITY

Lead Contact

Further information and requests for resources and reagents should be directed to the Lead Contact, Hans Clevers (h.clevers@hubrecht.eu).

Materials Availability

Unique/stable reagents generated in this study are available and can be requested from the Lead Contact, a completed Materials Transfer Agreement may be required.

Data and Code Availability

All bulk and single cell RNA sequencing data of this study have been deposited in the Gene Expression Omnibus (GEO) under accession code GSE146799.

The raw MS data is deposited in PRIDE, with accession number PXD017468.

EXPERIMENTAL MODEL AND SUBJECT DETAILS

Tissues from the human duodenum, ileum and colon were obtained from the UMC Utrecht with informed consent of each patient. All patients were males that were diagnosed with small intestinal or colon adenocarcinoma that was resected. A sample from non-transformed, normal mucosa was taken for this study. The study was approved by the UMC Utrecht (Utrecht, the Netherlands) ethical committee and was in accordance with the Declaration of Helsinki and according to Dutch law. This study is compliant with all relevant ethical regulations regarding research involving human participants.

For immunostainings, sections of formalin-fixed, paraffin embedded human intestinal tissue were obtained from resections performed at the University Medical Center Utrecht, the Netherlands. Anonymized archival pathology material was used according to the guidelines of the UMC Utrecht's Research Ethics Committee (Coebergh et al., 2006).

METHOD DETAILS

Cell culture of human intestinal organoids

Human small intestinal cells were isolated, processed and cultured as described previously (Beumer et al., 2018; Sato et al., 2011). Instead of Wnt conditioned media, the medium was supplemented with Wnt surrogate (0,15 nM, U-Protein Express). Ileal organoids were splitted on average every 10 days, duodenal and colon organoids ever 7 days. For passaging, organoids were removed from the BME using ice-cold AdDMEM/F12 (GIBCO) and mechanically dissociated into small fragments using a Pasteur pipette. Fragments were replated in fresh BME.

For differentiation toward EECs, organoids were treated with 1 μ g/mL doxycycline (Sigma) in 'ENR' medium (Sato et al., 2009). Secretin (Tocris) was used at a concentration of 10 μ g/mL. Beta-ionone (Sigma) was used at 100 mg/mL. BMP activation was achieved by withdrawing Noggin from 'ENR' and addition of BMP-2 (Peprotech, 50 ng/mL) and BMP-4 (Peprotech, 50 ng/mL). Notch signaling was inhibited by treatment with the Gamma-secretase inhibitor DAPT (Sigma, 10 μ M). Wnt inhibition was performed by treatment with the Porcupine inhibitor IWP-2 (StemCell Technologies, Inc., 5 μ M). FGF21 was used at a concentration of 1 μ g/mL (Peprotech).

Constructs for EEC-TAG reporter and knockout generation

The NEUROG3 was cloned in a two insert Gibson reaction into BSKS II vector. Of note, two PCR reactions were done: first, NEUROG3 was amplified from human genomic DNA, since the entire coding region lies in one exon. Second, the BSKS vector was amplified. The forward and reverse primers for Gly linker, FLAG, HA and P2A sequence were annealing to each other (Table S1). All three DNA fragments were then combined in BSKS-NEUROG3-Flag-HA-P2A. In the next step, NEUROG3-P2A sequence was excised using EcoRI enzyme and cloned into previously published pLX-NS2 vector (Sachs et al., 2019). Organoids were lentivirally transduced as described before (Koo et al., 2011). Lentiviral transduction was performed on small clumps of cells (2-10 cells) rather than single cells, achieved after TrypLE (TrypLE Express; Life Technologies) dissociation.

For generation of the reporter organoid lines using CRISPR-HOT, we utilized a method described in (Artegiani et al., 2020). Briefly, we used a targeting plasmid containing a fluorescent protein (mNEON or tdTomato) which can be linearized at a defined base position by a specific sgRNA and Cas9 provided from a second plasmid, which also encodes mCherry (Schmid-Burgk et al., 2016). These two plasmids are co-electroporated with a plasmid encoding the sgRNA for the respective locus (Table S1).

The HDR donor plasmid allows C-terminal knock-in of the fluorescent reporter mClover3 in the TPH1 locus and was generated using pUC118 as a backbone. First, the endogenous Sapl site in PUC118 was inactivated. Then, a selection cassette (PGK promoter driven expression of blasticidin) flanked by LoxP and two Sapl sites was cloned into the Sapl-inactivated pUC118 using infusion cloning (638910, Takara). Subsequently, a P2A sequence and the fluorescent protein mClover3 was PCR amplified (Phusion High fidelity DNA polymerase, M0530S, NEB) from the Addgene plasmid #74252 and cloned upstream of the selection cassette using infusion cloning (638910, Takara) and NotI (R0189S, NEB) digestion of the pUC118 selection-cassette containing plasmid. Next, homology arms corresponding to the genomic regions, approximately 1000bp, upstream and downstream of the *TPH1* stop codon were PCR amplified (Phusion High fidelity DNA polymerase, M0530S, NEB) from genomic DNA (extracted and purified from human small intestinal organoid DNA). The PCR primers contained overhangs allowing subsequent Golden Gate cloning (Table S1).

The PCR amplified homology arms were purified (QIAquick PCR Purification Kit, 28104, QIAGEN) and finally, the targeting vector was generated by Sapl (R0569S, NEB) mediated Golden Gate insertion of the homology arms into the pUC118 selection-cassette containing plasmid.

The sgRNA was selected based on the WTSI website (<https://wge.stemcell.sanger.ac.uk/>) and chosen as close to the TPH1 stop codon as possible. The gRNA sequence overlapped with the stop codon, so that the homology vector was not cut. The target sequence was ordered as two complementary oligos (IDT) and cloned in the Cas9-EGFP vector (addgene plasmid #48138) following the protocol described before (Ran et al., 2013).

For the generation of *HHEX* and *LMX1A* knockout organoids, gRNAs were selected using the WTSI website and cloned in the Cas9-EGFP vector (addgene plasmid #48138) following the protocol described before (Ran et al., 2013). gRNAs used in this story are presented in Table S1.

Human intestinal organoids were transiently transfected using a NEPA21 electroporator and a previously developed protocol (Fujii et al., 2015). For electroporation, organoids were dissociated into small clumps of cells (2–10 cells) and washed twice with OptiMem. The resulting pellet was resuspended in BTXpress solution (BTX) with 15 μ g of plasmids, after which electroporation was performed. 3–7 days after electroporation, either mCherry (for generation of NHEJ-mediated reporter organoids) or EGFP (for generation of *HHEX* and *LMX1A* knockout lines) positive cells were sorted using a FACS-ARIA (BD Biosciences). Rho kinase inhibitor (Y-27632 dihydrochloride; 10 μ M, Abmole) was added to the culture medium up to 1 week after sorting to enhance single cell outgrowth. All reporter organoids were generated in organoid lines also transduced with *NEUROG3*-overexpression (with or without dTomato) vector.

For generation of CRISPR-HOT reporter organoids: Cells were transfected 1) with a gRNA targeting the hormone locus near its stop codon, 2) a vector encoding mNeon or tdTomato and 3) a vector encoding Cas9, a constitutively produced mCherry fluorescent molecule and a gRNA linearizing the vector encoding the fluorescent molecule. Five days later, transfected cells were sorted for mCherry and plated as single cells. After two weeks, *NEUROG3* was induced in the resulting clonal organoids to visualize expression of the fluorescent fusion hormones. Typically, the first fluorescent organoids appeared 2–3 days later and were then clonally expanded. Organoids where fluorescent cells appeared during EEC differentiation were picked, digested using TrypLE (TrypLE Express; Life Technologies) and clonally expanded to establish stable knock-in organoid lines.

Organoids grown from Cas9-EGFP transfected cells were genotyped for *HHEX* and *LMX1A* to confirm homozygous frameshift mutation (primers in Table S1).

Calcium sensor

A red calcium probe (pTorPE-R-GECO1, addgene plasmid #32465) was used as a template to engineer a cyan genetically encoded calcium probe. The cpApple was replaced with a circularly permuted mTurquoise. The resulting probe was dubbed Tq-Ca-FLITS (Turquoise Calcium Fluorescence Lifetime Indicator for Truthful Sensing). A triple nuclear localization signal (3xnlis) was added to the N terminus of the calcium probe to simplify analysis. Details of the engineering and characterization will be described elsewhere (van der Linden et al., unpublished).

PCRs were performed on Tq-Ca-FLITS (Fw AAACAAGCGGGAGACGTGGAGGAAAACCCCTGGACCTCTCGAGatgggatcagatc caaaaagaagag, Rev ATGGCACTAGGCTAGTTCTAGAcCTACTTCGCTGTCATCATTTGGAC) as well as H2B-mMaroon (Fw TC GGCGCGCCACGCGT, Rev CGTCTCCCGCTTGTTCAGTAGACTAAAATTCGTCGCGCCAGATCCGCTAGCattaagttgtgcccc) and the two PCRs were cloned into a lentiviral vector using InPhusion Cloning (Takara), to produce H2B-mMaroon-P2A-Tq-Ca-FLITS, two simultaneously expressed cistrons separated by a de-optimized P2A (Lo et al., 2015).

Live cell imaging of calcium reporter organoids

H2B-mMaroon-P2A-Tq-Ca-FLITS organoids were imaged on a Leica SP8 confocal laser scanning microscope, equipped with Argon laser and White Light Laser, the latter allowing spectral flexibility for optimal visualization of all fluorophores. For cell type identification, cells were first imaged in 5 channels (Tq-Ca-FLITS-mTurquoise2, Clover, TdTomato, H2B-Maroon and transmitted light) and subsequently Tq-Ca-FLITS and H2B-mMaroon were time lapse imaged during administration of beta-ionone in XYZT-mode. Post-acquisitional analysis was done with custom-made Fiji-script.

Transmission electron microscopy

Organoids were fixed with 1.5% glutaraldehyde in 0.1M cacodylate buffer. They were kept in the fixative for 24 h at 4°C. Then, they were washed with 0.1M cacodylate buffer and postfixated with 1% osmium tetroxide in the same buffer containing 1.5% potassium ferricyanide for 1 h (dark) at 4°C. Then the samples were dehydrated in ethanol, infiltrated with Epon resin for 2 days, embedded in the same resin and polymerized at 60°C for 48 h. Ultrathin sections were obtained using a Leica Ultracut UCT ultramicrotome (Leica Microsystems, Vienna) and mounted on Formvar-coated copper grids. They were stained with 2% uranyl acetate in water and lead citrate. Then, sections were observed in a Tecnai T12 electron microscope equipped with an Eagle 4kx4k CCD camera (Thermo Fisher Scientific, the Netherlands).

Alternatively, organoids were chemically fixed at 4°C with a mixture of 2% paraformaldehyde and 0.2% glutaraldehyde in PB buffer. After washing with PB containing 50 mM glycine, cells were embedding in 12% gelatine and infused in 2.3 M sucrose. Mounted gelatine blocks were frozen in liquid nitrogen. Thin sections were prepared in an ultramicrotome (Leica EM Ultracut UC6/FC6, Leica Microsystems, Vienna, Austria). Ultrathin cryosections were collected with 2% methylcellulose in 2.3 M sucrose. The observations were performed in an Electron Microscope Tecnai T12 as mentioned.

Immunostaining

Organoids were stained as described before (Beumer et al., 2018). In brief, organoids were removed from the BME using ice-cold AdDMEM/F12 (GIBCO), after which these were fixed in formalin for at least 2 h at room temperature. Next, the organoids were washed and blocked for at least 15 min in 2% donkey serum in PBS. After blocking, the cells were permeabilized in 0.5% Triton X-100 (Sigma) in PBS for at least 15 min. Primary antibodies used were goat anti-chromogranin A (1:500; Santa Cruz), goat anti-cholecystokinin (sc-21617, 1:100; Santa Cruz), rabbit anti-neurotensin (sc-20806, 1:100; Santa Cruz), goat anti-somatostatin (sc-7819, 1:100; Santa Cruz), goat anti-serotonin (ab66047, 1:1,000; Abcam), rabbit anti-gastric inhibitory polypeptide (ab22624-50, 1:500; Abcam), goat anti-GLP1 (sc-7782, 1:100; Santa Cruz), rabbit anti-GLP1 (ab22625, 1:200; Abcam), rabbit anti-MLN (HPA069392, 1:200, Atlas antibodies), mouse anti-Gastrin (60346, 1:200, Proteintech), mouse anti beta-Catenin (610154, 1:100; BD transduction laboratories), goat anti-Ghrelin (sc-10368, 1:200; Santa Cruz), rabbit anti-Neuropeptide W (NBP2-57337, 1:100; Novus), rabbit anti-Precerebellin (ABN304, 1:100; Sigma) and rabbit anti-PPY (HPA032122, 1:200; Atlas antibodies). Organoids were incubated with the corresponding secondary antibodies Alexa488-, 568- and 647-conjugated anti-rabbit and anti-goat (1:1,000; Molecular Probes) in blocking buffer containing 4',6-diamidino-2-phenylindole (DAPI; 1;1,000, Invitrogen). Sections were embedded in Vectashield (Vector Labs) and imaged using a Sp8 confocal microscope (Leica). Image analysis was performed using ImageJ software.

Fluorescent *in situ* hybridization

FISH was performed using the RNAScope® Multiplex Fluorescent Reagent Kit v2 (Advanced Cell Diagnostics) according to the manufacturer's protocol (Wang et al., 2012). In brief, paraffin embedded ileal surgical sections were deparaffinized, treated with hydrogen peroxide for 10 min and boiled in target retrieval buffer for 15 min before a 30-min protease treatment. Probes directed against *CHGA/SCTR*, *CHGA/GCG* and *GHRL/IL20RA* were multiplexed, respectively, amplified and detected using fluorescent probes based on opal dyes. Slides were counterstained with DAPI for 30 s, mounted using ProLong Gold Antifade Mountant (Thermo Fisher scientific) and images were obtained using a SP8 confocal fluorescent microscope (Leica).

ELISA

The supernatant from organoids either cultured in ENR for 5 days or differentiated toward EECs were collected after a 24 h stimulation with 10 μ M forskolin (Tocris). GLP-1 concentration was measured using a GLP-1 EIA kit (Rab0201 from Sigma that detects both full-length and N-terminal cleaved GLP-1) following the manufacturer's protocol.

RNA isolation and quantitative PCR

Organoid RNA was isolated using a RNeasy kit (QIAGEN), following the manufacturer's protocol. Quantitative PCR (qPCR) analysis was performed using biological and technical duplicates as described before (Muñoz et al., 2012). Primers were designed using the NCBI primer design tool, tested using a standard curve, and are presented in Table S1.

Processing human intestinal tissue for single cell RNA sequencing

Human intestinal mucosal biopsies were obtained from patients undergoing colonoscopy at Addenbrooke's Hospital, Cambridge, UK. All patients gave informed consent for extra biopsy samples to be taken for research use when undergoing elective colonoscopy (REC 17/EE/0265). Only those patients with a macroscopically normal mucosa and subsequent histological confirmation of a normal mucosa with no intestinal pathology were included in this study.

Once acquired, biopsies were immediately placed into Hanks Buffered Saline Solution (HBSS) and washed three times in fresh HBSS. Biopsies were then placed into an HBSS solution containing 1.07 Wünsch units/mL Liberase DH (Roche) and 70 U/mL hyaluronidase (Merck) and incubated at 37°C for 15 min while on a plate shaker at 750 rpm. The samples were then mechanically disrupted by pipetting the solution up and down using a p1000 pipette, and then incubated at 37°C for a further 15 min on a plate-shaker at 750rpm. The samples were then washed three times by pelleting the cells using centrifugation at 400 g for 4 min, removal of the supernatant and resuspending in DMEM/F12 (Thermofisher). On the third wash the cells were left in suspension, and a 10 μ L aliquot was placed into a Countess® Automated Cell Counter to estimate the cellular concentration.

3,000 cells suspended in DMEM/F12 (Thermofisher) were loaded into an individual channel of a 10x single cell chip as per the manufacturer's protocol (version 2, 3') and run in standard conditions by the chromium controller (10X genomics). cDNA libraries were prepared according to the manufacturer's protocol and sequenced on an Illumina Hi-seq 4000 (2x50bp paired-end reads).

Raw sequence reads in FASTQ format were aligned to the human transcriptome GRCh38-1.2.0 using Cellranger v2.1.1(10x Genomics) with default parameters. Scanpy v1.4 (Wolf et al., 2018) was used for data processing, quality control and dimensionality reduction. We excluded cells with less than 200 genes and genes expressed in fewer than 3 cells. After quality control, the dataset contained 11,302 cells. EECs were identified and subclustered based on the expression of at least 10 CHGA counts per cell. “

Single cell sorting for RNA sequencing from organoids

Organoids were dissociated to single cells using a 10-min incubation with TrypLE (TrypLE Express; Life Technologies) and repeated mechanical disruption by pipetting. Cells were sorted using a BD FACS Aria (BD Biosciences) based on fluorescence levels. For single cell RNA sequencing, individual cells were collected in 384-well plates with ERCC spike-ins (Agilent), reverse transcription primers and dNTPs (both Promega). Single cell sequencing was performed according to the Sort-seq method (Muraro et al.,

2016). Sequencing libraries were generated with TruSeq small RNA primers (Illumina) and sequenced paired-end at 60 and 26 bp read length, respectively, on the Illumina NextSeq.

For bulk RNA sequencing, cells were sorted into Eppendorf tubes containing RLT buffer (RNeasy kit, QIAGEN). 5,000–30,000 cells were sorted per reporter in duplicates (and triplicates for tdTomato negative cells). RNA was extracted using the RNeasy mini kit (QIAGEN) following the manufacturer's instructions. Sequencing libraries were generated using a modified CELseq2 protocol (Hashimshony et al., 2016). 75 bp paired-end sequencing of libraries was performed on an Illumina NextSeq platform.

Single cell RNA sequencing analysis from organoids

Reads were mapped to the human GRCh37 genome assembly. Sort-seq read counts were filtered to exclude reads with identical library-, cell- and molecule barcodes. UMI counts were adjusted using Poisson counting statistics (Muraro et al., 2016). Cells with fewer than 2,000 unique transcripts were excluded from further analysis. The remaining cells in the EEC atlas were derived from the following sources: 1446 cells from duodenum, 2145 cells from ileum, 690 cells from colon.

Subsequently, RaceID3 was used for k-medoids based clustering (knn = 10) of cells and differential gene expression analysis between clusters using the standard settings described at https://github.com/dgrun/RaceID3_StemID2_package.

The dataset was then subsetted to require expression of EEC markers and exclude cells based on expression of markers of other cell types with the following transcript count cutoffs: CHGA > 5; MUC2 < 5; FABP1 < 15; LYZ < 15; OLFM4 < 10. The resulting set of EECs was again subjected to clustering (knn = 5) and differential gene expression as described above.

For reporter analyses, cells sorted by fluorescent reporter positivity were analyzed as one dataset per reporter to gain more detailed insights into single EEC subpopulations. The following deviations from standard settings were made per reporter: GCG: knn = 5; outlg = 1; probthr = 0.00001; perplexity = 10; MLN: knn = 10; probthr = 0.0000001; SST: knn = 10; perplexity = 20

For mouse validation, the tissue-derived single cell count tables from Gehart et al. (2019) were reanalyzed using the procedure and settings described above. No subsetting for EECs was performed.

Bulk RNA sequencing analysis

Reads were mapped to the human GRCh37 genome assembly. The counted reads were filtered to exclude reads with identical library- and molecule barcodes. Differential gene expression analysis was performed using the DESeq2 package (Love et al., 2014). For display in heatmaps, genes were ranked by fold change compared against tdTomato negative cells. After filtering for an adjusted p value < 0.05, the row z-score for the top 20 genes was calculated.

Preparation of secreted peptides and proteins for LC-MS

Organoids differentiated for 5 days to EECs were washed extensively in PBS and stimulated with 10 μ M forskolin (Tocris). Conditioned media was collected for 24 h and supplemented with 1x cOmplete Protease Inhibitor Cocktail on harvest (Roche). Potential cell debris was removed by centrifugation at 10,000 \times g, for 5 min at 4°C. Conditioned media supernatant was denatured in final 4 M Urea, 50 mM ammonium bicarbonate and fractionated by molecular weight with a 10 kDa Vivaspin centrifugal device (Sartorius, Göttingen, Germany), at 12,000 \times g, for 10 min at 4°C. (i) Endogenously processed peptides recovered from the filtrate were acidified to 5% formic acid, desalted by reversed phase C18 1 cc columns (Waters Corporation, Milford, USA), further purified by home-made strong cation exchange STAGE tip, and dried by vacuum centrifugation. (ii) Longer secreted proteins in the 10 kDa retentate were recovered and diluted to final 2 M Urea, 50 mM ammonium bicarbonate, for reduction with dithiothreitol, alkylation with iodoacetamide, and overnight digestion with trypsin (Promega, Madison, USA) at 37°C. Digested peptides were similarly acidified to 5% formic acid, desalted by reversed phase C18 1 cc columns (Waters), and dried by vacuum centrifugation.

Preparation of FACS-sorted EECs for proteome analyses

FACS sorted enteroendocrine cells were lysed in 8M Urea, 50 mM Ammonium bicarbonate, 0.5% Sodium deoxycholate, 1x cOmplete protease inhibitor, 50 μ g/mL DNase I, and sonicated with the Biorupter (3 cycles, 20 s on, 20 s off at 4°C) (Diagenode, Liege, Belgium). Cell debris was pelleted by centrifugation at 14,000 \times g for 1 h at 15°C, and supernatant containing extracted proteins were reduced, alkylated, diluted 4 times with 50 mM ammonium bicarbonate, and digested sequentially with Lys-C (Wako) and trypsin (Promega). Peptide digests were quenched to 5% formic acid, and sodium deoxycholate was precipitated and removed by centrifugation at 14,000 \times g, 4°C for 10 min. Peptides in the supernatant were diluted to final 20% acetonitrile and purified by SCX STAGE tips. Eluted peptides were dried by vacuum centrifugation.

LC-MS

Peptides were reconstituted in 2% FA for LC-MS injection. Data was acquired using an UHPLC 1290 system (Agilent, California, USA) coupled to an Orbitrap HF-X mass spectrometer (Thermo Scientific, Massachusetts, USA). Peptides were first trapped in a 2 cm \times 100 μ M Reprosil C18 trap column (Dr Maisch, Ammerbuch, Germany) of 3 μ m pore size for 5 min in solvent A (0.1% formic acid in water). After trapping, samples separated in an analytical column (Agilent Poroshell, EC-C18, 2.7 μ m, 50 cm \times 75 μ m) using a gradient of 0.1% formic acid in 80% acetonitrile (solvent B). Depending on total peptide input, species complexity, and elution profiles, different LC gradient lengths were used for FACS-sorted whole proteomes (35min, 13%–40% solvent B), secreted proteins (65min, 13%–40% solvent B) and endogenously processed peptides (95min, 13%–44% solvent B). MS acquisition was performed

in data-dependent mode. Full scans (MS1) were acquired from 375 to 1600 m/z at resolution 60,000, with 20 ms injection time and 3×10^6 AGC target value. The TOP 15 most intense precursor ions were selected for fragmentation using 1.4 m/z isolation window. Isolated precursors were fragmented using high energy C-trap dissociation (HCD) at normalized collision energy (NCE) of 27%. MS2 scans were acquired at resolution 30,000, with 50 ms injection time and an AGC target value of 1×10^5 . Exclusion times were set to 8, 12 or 16 s for proteomics, digested retentates and endogenously processed peptides respectively. LC-MS injection loads were adjusted to the sample of least quantity, such that all LC-MS measurements to be compared were matched in TIC intensity.

Proteomics data analysis

Collected spectral data was processed using Proteome Discoverer 2.3 (Thermo Scientific, Massachusetts, USA), and searched using Sequest HT search engine, against UniProt *Homo sapiens* database (173235 entries, downloaded in August 2019, including common contaminants). Precursor and fragment mass tolerance were set to 10 ppm and 0.02 Da respectively. Protein N-terminal Acetylation and methionine oxidation were set as variable modifications. For the endogenously processed peptides, peptides of length 6 - 50 amino acids were generated from the database upon unspecific cleavage. For digested retentates and analyses of the FACS-sorted EECs proteomes, cysteine carbamidomethylation was set as fixed modification and up to 2 missed trypsin cleavages were allowed. Identified peptides were filtered to 1% FDR using the Percolator algorithm (The et al., 2016).

In proteome analyses, intensities of proteins detected in 2 out of 3 replicates in at least one group were $\log(2)$ transformed and missing values were imputed from the normal distribution independently for each sample using Perseus software (v_1.6.2.2) (Tyanova et al., 2016). Processed data was assessed for statistical significance among the groups using One-way ANOVA or Student's t test, and resulting *p-values* were corrected for type I error using Benjamini-Hochberg approach (*q-value*). Tukey Honest Significant Difference test was performed to assess difference between the groups when required. Hormone processing plots were generated from peptides identified at high confidence (1% FDR) in at least 2 out of 3 replicates. For novel secreted products, peptides identified in 3 out of 3 replicates and not observed in the secretome of control organoids were used. Peptide sequences identified based on retention time alignment (not supported by spectral evidence) were not used in hormone processing plots. Statistical analysis and plots were generated using *in-house* built R scripts (R version 3.6.0). Gene ontology enrichments were performed with Database for Annotation, Visualization and Integrated Discovery (DAVID) v6.8 (Huang et al., 2009), using all the proteins identified in the bulk EEC proteome as reference list.

QUANTIFICATION AND STATISTICAL ANALYSIS

No statistical methods were used to predetermine sample size. The experiments were not randomized and the investigators were not blinded to the sample allocation during experiments and outcome assessment. All data are presented as mean \pm standard error of the mean (SEM), unless stated otherwise. Value of *n* is always displayed in the figure as individual data points, and in the legends. Statistical tests included unpaired two-tailed t test for Figures 5F and Figure S1G.

Supplemental Figures

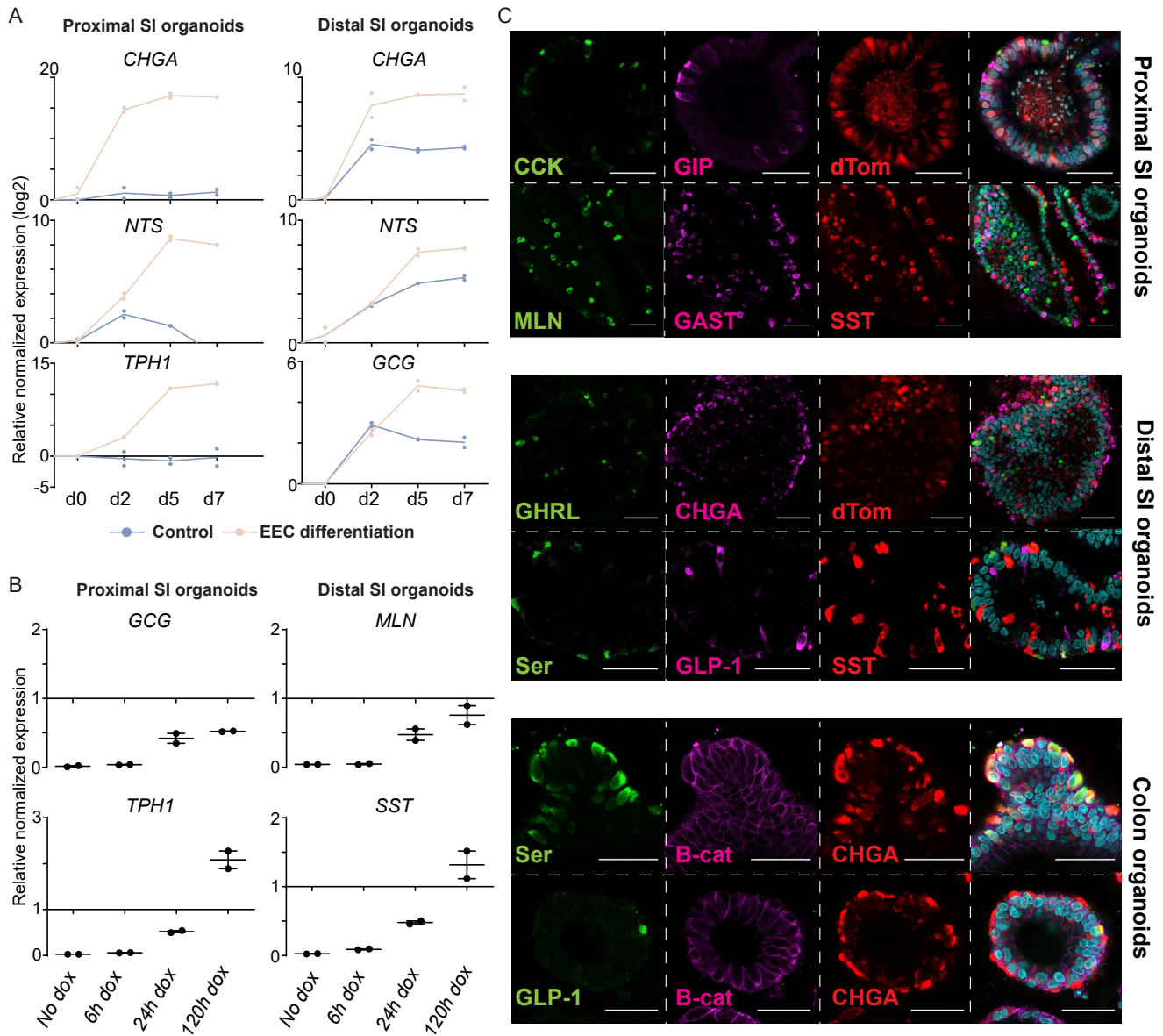


Figure S1. Enteroendocrine Cells in Human Intestinal Organoids Display Normal Co-expression Profiles, Related to Figure 1

(A) qPCR analysis showing expression of hormones over the course of EEC differentiation. Expressions levels are normalized to GADPH and relative to day 0. The experiment was performed in $n = 2$ independent experiments, and the individual datapoints are depicted.

(B) qPCR analysis showing expression of hormones after different durations of doxycycline (Dox) challenge. Organoids were differentiated for 5 days, and treated without dox, for 6 h, 24 h, 48 h or 120 h (the full differentiation time) dox. Expressions levels are normalized to GADPH and relative to 48 h dox treatment. The experiment was performed in $n = 2$ independent experiments, and the individual datapoints are depicted.

(C) Immunofluorescent staining of EEC-enriched organoids. Multiple hormones are expressed mutually exclusive. Scale bar is 50 μ m.

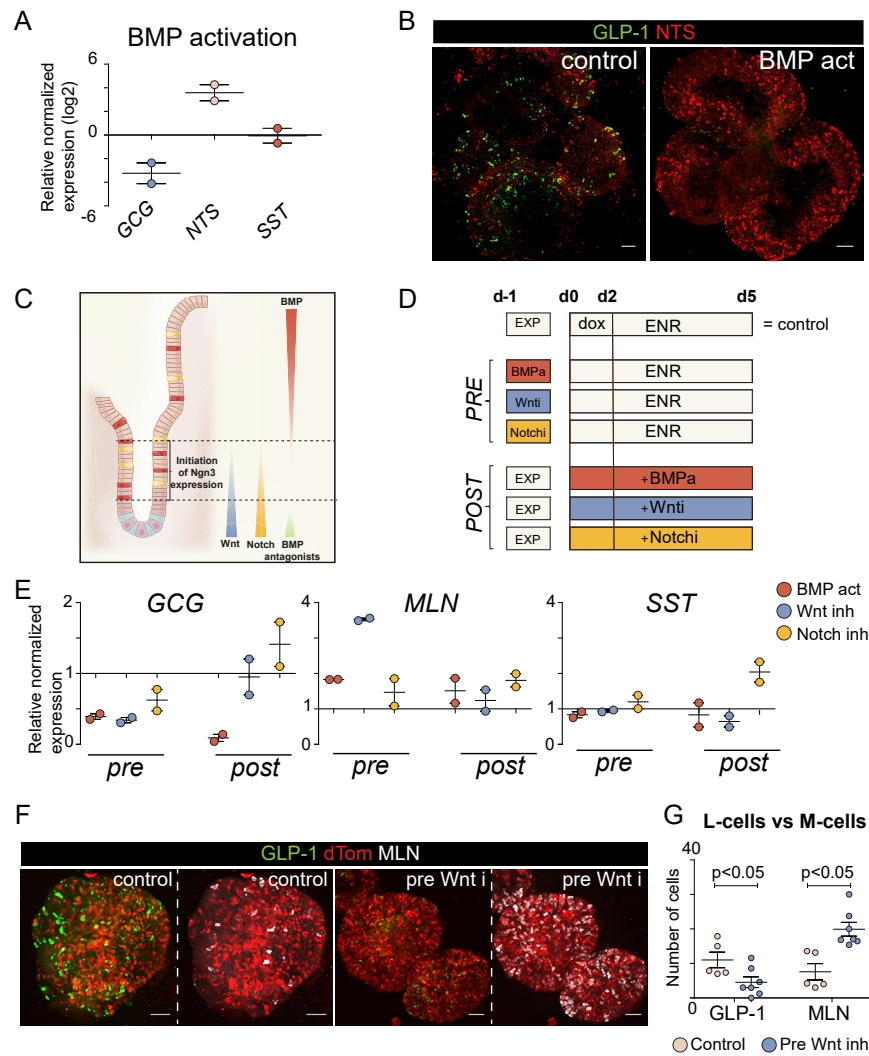


Figure S2. Manipulation of Wnt and BMP Signaling Allows Controlling Subspecification of EECs, Related to Figure 1

(A) qPCR analysis showing expression of hormones after BMP treatment. Expression levels are normalized to GADPH, and relative to a non-treated control. The experiment was performed in $n = 2$ independent experiments, and the mean expression and SEM are depicted.

(B) Immunofluorescent staining of BMP treated organoids. Scale bar is $50 \mu\text{m}$.

(C) Schematic representation of morphogen gradients in the intestinal crypt related to sites of initiation of Neurogenin-3 (Ngn3) expression.

(D) Experimental paradigm. Different signaling pathways were modulated (BMP activation; BMPa, Wnt inhibition; Wnti, Notch inhibition; Notchi) either 24 h before (pre) or at the start (post) of *NEUROG3* expression mediated by doxycycline (dox) treatment. Control organoids were kept in standard expansion conditions (EXP) before dox treatment, and in standard differentiation conditions (ENR) after initiation of dox treatment.

(E) qPCR analysis showing expression of hormones after different treatments shown in d. Expression levels are normalized to GADPH, and relative to a non-treated control. The experiment was performed in $n = 2$ independent experiments, and the mean expression and SEM are depicted.

(F) Immunofluorescent staining of organoids differentiated toward EECs after a 24 h inhibition of Wnt (pre Wnt i). Organoids are shown as a maximum projection. Scale bar is $50 \mu\text{m}$.

(G) Quantification of (F). Number of positive cells were counted on $n = 5$ organoid sections. Pre-inhibition of Wnt signaling caused a shift of L-cell to M-cell differentiation.

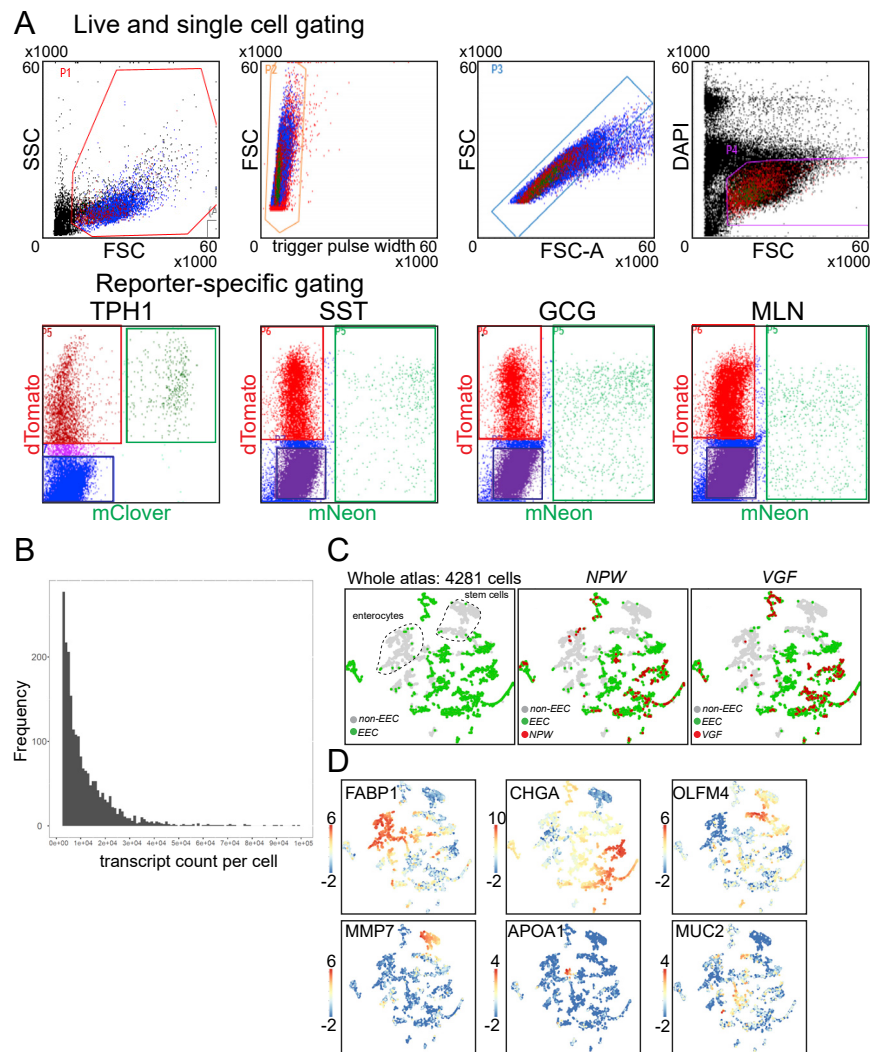


Figure S3. Generation of a Human Single-Cell RNA Sequencing Atlas of the Intestinal Tract Using Organoids, Related to Figure 3

(A) Fluorescence-activated cell sorting (FACS) gating parameters for sorting of different EEC subtypes from reporter organoids.

(B) Histogram displaying the total number of unique transcripts per cell (median number per cell is 7288 transcripts).

(C) A broad human intestinal organoid atlas ($n = 4281$ cells) generated by single cell RNA sequencing and displayed using a t -distributed stochastic neighbor-embedding (t -SNE) map. Cells defined as EECs (see methods) are shown in green. Cells expressing NPW or VGF (> 1 transcripts, respectively) are highlighted in red and are found exclusively in EEC clusters.

(D) t -SNE maps displaying lineage markers in the whole human intestinal organoid cell atlas ($n = 8448$ cells). Bars display color-coded unique transcript expression (logarithmic scale).

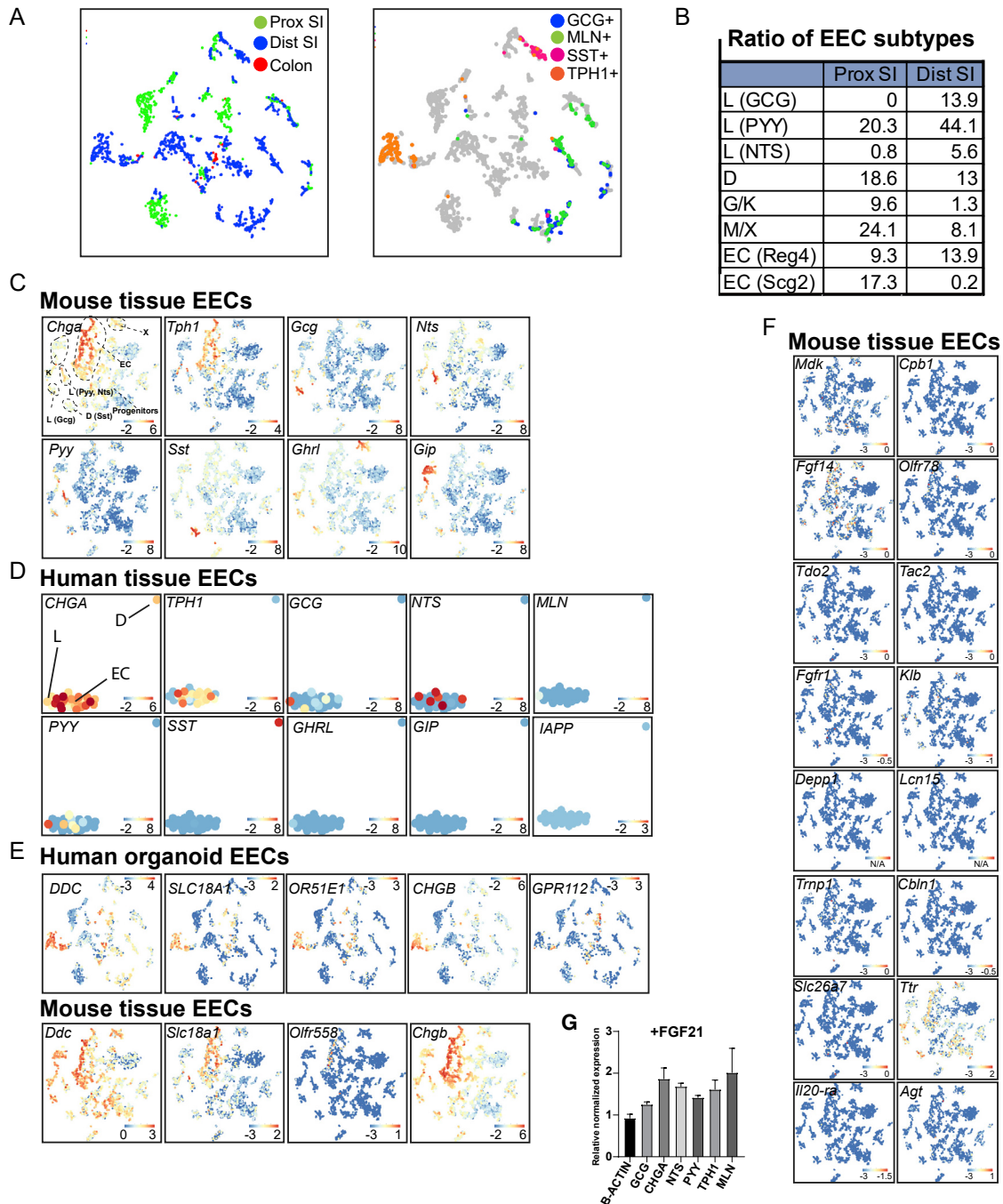


Figure S4. Single-Cell RNA Sequencing of Human EECs from Organoids and Tissue and Mouse EECs from Tissue, Related to Figure 3

(A) t-SNE maps displaying the origin (left, tissue; right, reporter organoid) of cells from the human EEC atlas (n = 2255 cells).

(B) The percentages of EECs corresponding to the different subtypes in proximal and distal SI organoids.

(C) t-SNE maps displaying the expression levels of hormones in the different murine EEC subtypes from intestinal tissue. Bars display color-coded unique transcript expression (logarithmic scale).

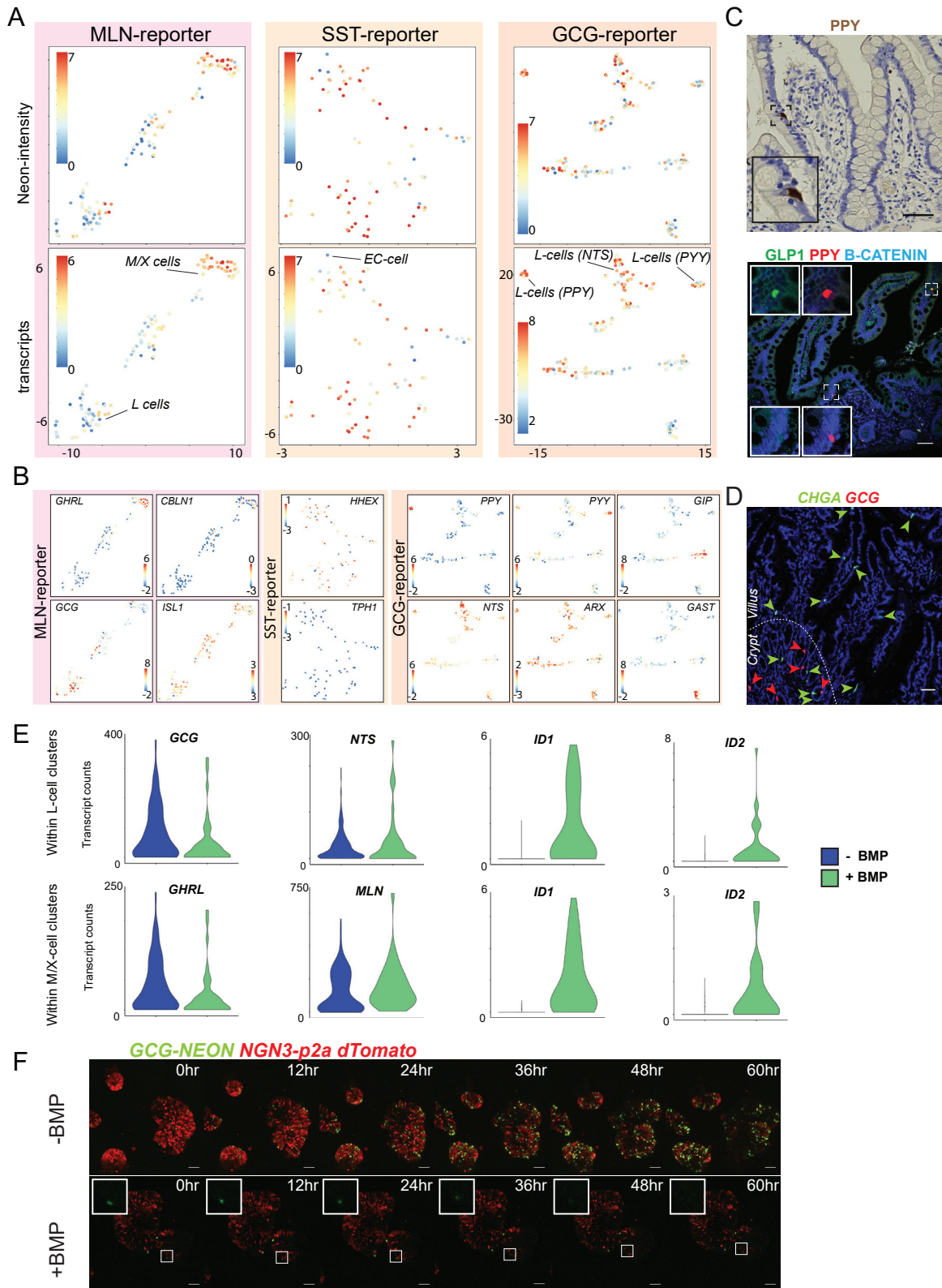
(D) t-SNE maps displaying the expression levels of hormones in the different human EEC subtypes from intestinal tissue. Bars display color-coded unique transcript expression (logarithmic scale).

(E) t-SNE maps displaying conserved expression of different EC markers in human and mouse EECs. Bars display color-coded unique transcript expression (logarithmic scale).

(F) t-SNE maps displaying the levels of hormone and marker gene expression of human M/X cells in the different murine EEC subtypes from intestinal tissue. Bars display color-coded unique transcript expression (logarithmic scale).

(legend continued on next page)

(G) qPCR analysis showing expression of hormones after FGF-21 treatment during the 5 day EEC differentiation. Expressions levels are normalized to GADPH and relative to control organoids that are EEC differentiated without FGF-21 treatment. B-ACTIN is displayed as second housekeeping gene. The experiment was performed in $n = 2$ independent experiments, and the mean expression and SEM are depicted.



(legend on next page)

Figure S5. Subclustering of Human EEC Subtypes and Responses to BMP Activation, Related to Figure 3

(A) Subclustering was performed on EECs sorted from different reporter organoids. t-SNE maps displaying the correlation between transcript levels and reporter intensity

(B) t-SNE maps displaying different hormones in EECs from the different reporter organoids. *PPY*-expressing cell form a distinct cluster of *GCG*⁺ cells.

(C) Immunohistochemistry of human ileal sections confirms *PPY* expression *in vivo*. Scale bar is 50 μ m.

(D) Fluorescent *in situ* hybridization on human ileal section shows crypt-restricted expression of *GCG* (red arrowheads), whereas *CHGA* expression (green arrowheads) is expressed also in the villus. Scale bar is 50 μ m.

(E) Violin plots depict the expression levels of selected hormones in single BMP-treated cells versus untreated cells in the EEC single cell RNA sequencing atlas. *ID1* and *ID2* are BMP target genes that confirm specific pathway activation of BMP agonist-treated cells.

(F) Snapshots are shown of *GCG-neon* reporter organoids that were treated with BMP after 2 days of dox treatment to induce *NEUROG3-dTomato* expression (= 0 h time point). BMP treatment blocks the appearance of *GCG*⁺ cells, while pre-existing L-cells downregulate *GCG* expression. No cell death is observed. Scale bar is 50 μ m.

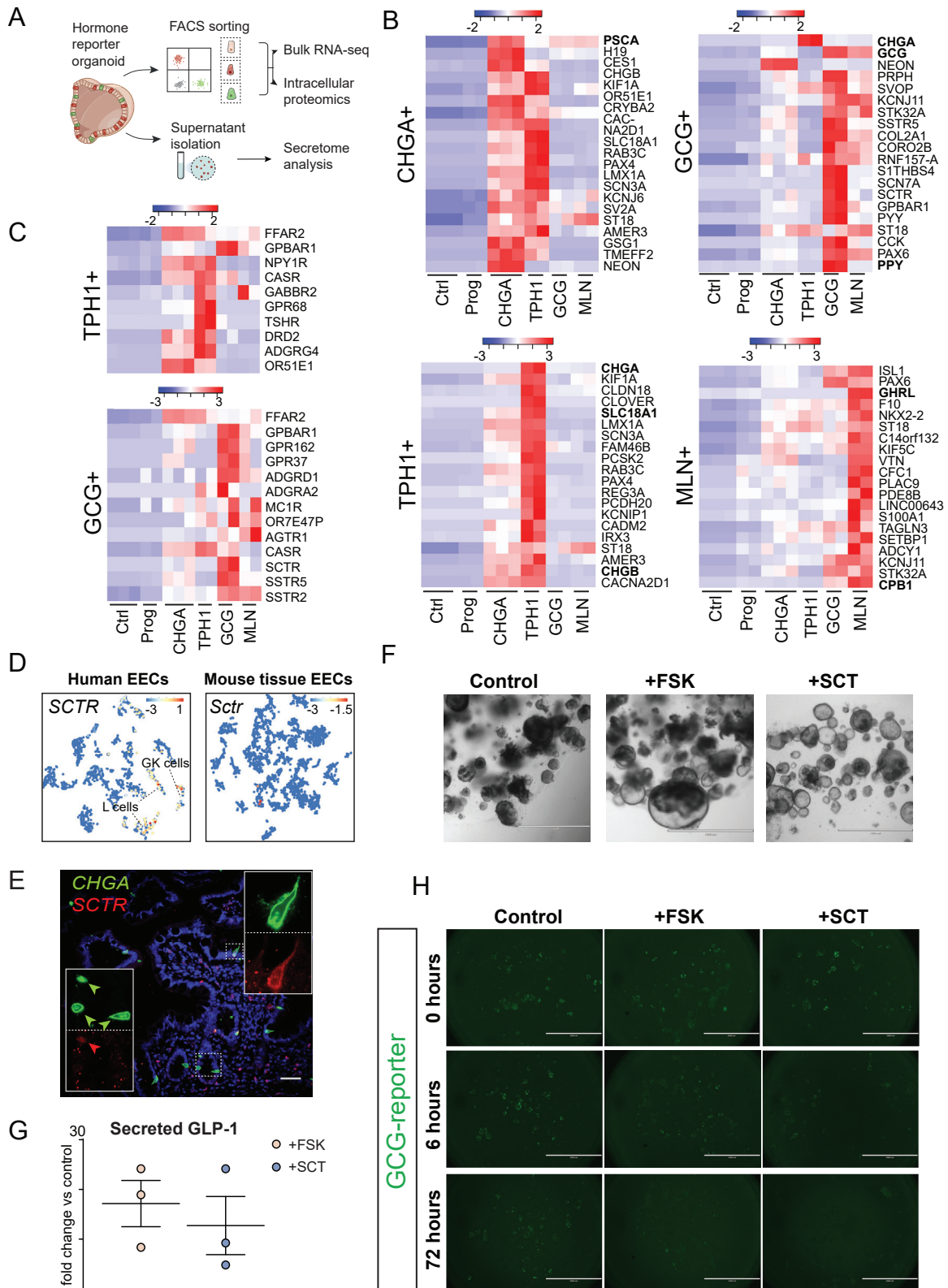


Figure S6. Bulk Transcriptomic Profiling of Sorted Enteroendocrine Cell Subtypes, Related to Figure 6

(A) Experimental paradigm. Hormone reporter organoids are differentiated, after which subpopulations of EECs are sorted using FACS and processed for bulk RNA-sequencing or intracellular proteomics. In a separate experiment, the supernatant of organoids is collected after 24 h forskolin stimulation and processed for proteomic analyses to determine the EEC secretome.

(B) Heatmaps showing the 20 most significant RNA markers enriched in purified reporter populations. In bold genes are highlighted that are also among the 20 most significant markers on protein level. Colored bars represent Z-scores.

(C) Heatmaps showing receptor expression most unique to TPH1⁺ or GCG⁺ cells. The receptor for EEC hormone Secretin (SCTR) is expressed highly in L-cells but not ECs, while ECs display unique expression of the PYY receptor (NPY1R).

(D) t-SNE map displaying the expression level of the Secretin receptor (SCTR) in the EEC single cell sequencing atlas. Bars display color-coded unique transcript expression (logarithmic scale).

(E) Fluorescent *in situ* hybridization on human ileal sections shows rare *SCTR*-expressing cells (red arrowhead) that sometimes co-express *CHGA* (green arrowhead). Scale bar is 50 μ m.

(F) Representative bright-field images of EEC-differentiated organoids after 24 h forskolin (FSK) or Secretin (SCT) treatment. Both FSK and SCT treatment causes swelling of organoids, indicative of cAMP activation. Scale bar is 1 mm.

(G) ELISA showing the fold increase in GLP-1 concentrations of EEC-enriched organoids after treatment with FSK or SCT. The experiment was performed in $n = 3$ independent experiments, and the mean fold change and SEM are depicted.

(H) GCG-reporter organoids were differentiated toward EECs and treated with FSK or SCT. Intracellular levels of GCG-neon reduce over the course of FSK and SCT treatment. Scale bar is 2 mm.

Figure S7. Proteomic and Secretomic Profiling of EECs, Related to Figure 7

(A) Principle component analysis (PCA) of RNA and protein data from different EEC populations. CHGA⁺ cells were used as control. CHGA⁻ cells that were positive for dTomato (induced NEUROG3-expression) were defined as EEC progenitors (Prog).

(B) Heatmaps showing the 20 most significant markers on protein level defining each EEC populations. Colored bars represent Z-scores. In bold genes are highlighted that are also among the 20 most significant markers on RNA level.

(C) t-SNE maps displaying the expressions level of *CRYBA2* and *FEV* in the EEC single cell sequencing atlas, illustrating a high degree of overlap in expression. Bars display color-coded unique transcript expression (logarithmic scale).

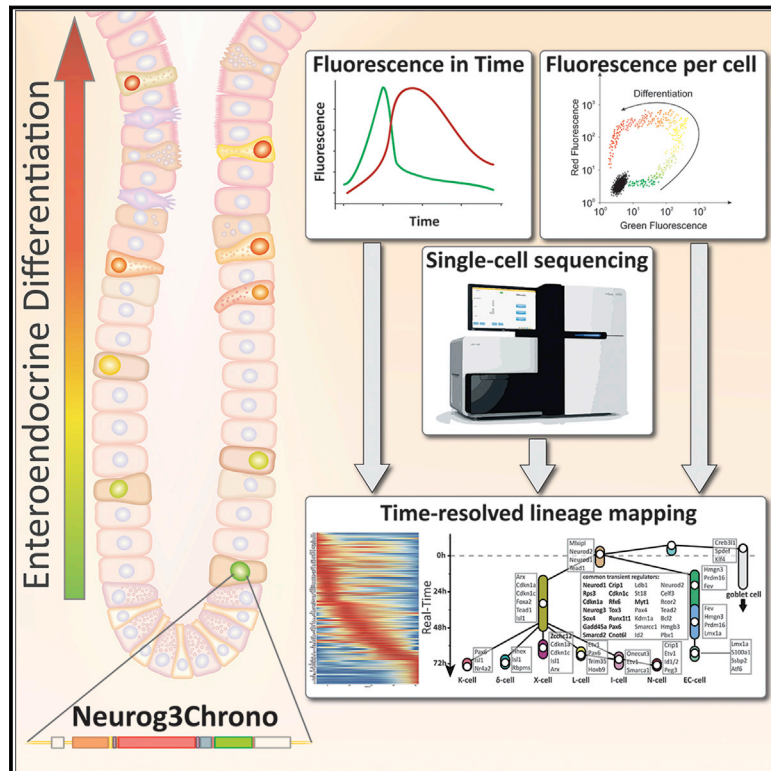
(D) Immunohistochemistry on human duodenal sections shows a lack of *CRYBA2* expression *in vivo*. Scale bar is 50 μ m.

(E) The location of the *CRYBA2* and *FEV* genes on Chromosome 2.

(F) Measured peptides (< 10 kDa) in the secretome mapping to different secreted prehormones are shown below the black bar. Data from proximal (yellow background) and distal SI organoid (blue background) supernatants are displayed.

Identification of Enteroendocrine Regulators by Real-Time Single-Cell Differentiation Mapping

Graphical Abstract



Authors

Helmuth Gehart, Johan H. van Es, Karien Hamer, ..., Johanna F. Dekkers, Anne Rios, Hans Clevers

Correspondence

h.clevers@hubrecht.eu

In Brief

The hierarchical lineage of intestinal enteroendocrine cells is defined at a spatiotemporal single-cell manner and validated using organoid and *in vivo* models.

Highlights

- Neurog3Chrono arranges enteroendocrine single-cell transcriptomes on real-time axis
- Enteroendocrine cells show hormonal plasticity in the course of their maturation
- A time-resolved map characterizes fate specification of all enteroendocrine lineages
- Individual knockout of 6 identified regulators gives robust enteroendocrine phenotypes

Data Resources

GSE113561



Identification of Enteroendocrine Regulators by Real-Time Single-Cell Differentiation Mapping

Helmuth Gehart,¹ Johan H. van Es,^{1,2} Karien Hamer,¹ Joep Beumer,¹ Kai Kretzschmar,^{1,2} Johanna F. Dekkers,^{1,3} Anne Rios,³ and Hans Clevers^{1,2,3,4,*}

¹Hubrecht Institute, Royal Netherlands Academy of Arts and Sciences (KNAW) and University Medical Centre (UMC) Utrecht, 3584 CT Utrecht, the Netherlands

²Onco Institute, Hubrecht Institute, 3584 CT Utrecht, the Netherlands

³Princess Máxima Centre for Paediatric Oncology, 3584 CT Utrecht, the Netherlands

⁴Lead Contact

*Correspondence: h.clevers@hubrecht.eu

<https://doi.org/10.1016/j.cell.2018.12.029>

SUMMARY

Homeostatic regulation of the intestinal enteroendocrine lineage hierarchy is a poorly understood process. We resolved transcriptional changes during enteroendocrine differentiation in real time at single-cell level using a novel knockin allele of *Neurog3*, the master regulator gene briefly expressed at the onset of enteroendocrine specification. A bi-fluorescent reporter, *Neurog3Chrono*, measures time from the onset of enteroendocrine differentiation and enables precise positioning of single-cell transcriptomes along an absolute time axis. This approach yielded a definitive description of the enteroendocrine hierarchy and its sub-lineages, uncovered differential kinetics between sub-lineages, and revealed time-dependent hormonal plasticity in enterochromaffin and L cells. The time-resolved map of transcriptional changes predicted multiple novel molecular regulators. Nine of these were validated by conditional knockout in mice or CRISPR modification in intestinal organoids. Six novel candidate regulators (*Sox4*, *Rfx6*, *Tox3*, *Myt1*, *Runx1t1*, and *Zcchc12*) yielded specific enteroendocrine phenotypes. Our time-resolved single-cell transcriptional map presents a rich resource to unravel enteroendocrine differentiation.

INTRODUCTION

Single cell sequencing is rapidly evolving to become an indispensable tool to investigate cellular composition of tissues (Haber et al., 2017; Halpern et al., 2017). By employing algorithms such as diffusion pseudotime (Haghverdi et al., 2016) or StemID (Grün et al., 2016), single-cell datasets can also be brought in pseudo-temporal order to investigate continuous changes in cellular identity (e.g., differentiation). This approach has proven useful but has inherent limitations: (1) pseudo-temporal order is relative, so no information on actual duration is

available; (2) a densely populated dataset is needed because transition states between cellular identities have to be observed for high-confidence pseudo-temporal relations; and (3) the order is not based on a transcriptome-independent variable and is therefore easily biased by the applied method. Thus, especially rare cell populations with complex differentiation programs are difficult to study based on pseudo-time alone.

The intestinal epithelium renews completely every 3–5 days (Darwich et al., 2014). This rapid turnover necessitates the co-existence of stem cells, progenitors, and mature cells at any given time. All epithelial cells in the intestine originate from continuously cycling LGR5+ stem cells at the bottom of the crypt (Barker et al., 2007). Among their progeny are enteroendocrine (EE) cells, a scarce (<1% of the epithelium) but essential hormone-producing population scattered throughout the gastrointestinal epithelium. Their roles in metabolism and appetite control have put EE hormones at the forefront of the battle against metabolic syndrome and type II diabetes. Additionally, they also control intestinal motility and orchestrate mucosal immunity (Gribble and Reimann, 2017; Worthington et al., 2018). EE cell types are usually classified based on their hormone production: L cells (Glucagon-like peptide 1, GLP1), I cells (Cholecystokinin, Cck), Enterochromaffin (EC) cells (Serotonin, 5-HT), X cells (Ghrelin, GHRL), S cells (Secretin, SEC), K cells (Gastric inhibitory peptide, Gip), delta cells (Somatostatin, Sst), and N cells (Neurotensin, Nts) were originally distinguished, but reports on multihormonal cells make the classification significantly more complicated with up to 20 different cell types (Haber et al., 2017; Habib et al., 2012). A limited number of regulators of EE development, such as *Neurog3* (Mellitzer et al., 2010), *Neurod1* (Naya et al., 1997), or *Arx* (Beucher et al., 2012), have already been identified in knockout studies, but a complete description of the differentiation process of individual lineages is lacking. Understanding the developmental program that controls EE differentiation is of particular interest, as specific subtypes (e.g., L cells and K cells) harbor significant therapeutic potential.

In this study, we combine single-cell RNA sequencing, a fluorescent timer construct and organoid technology to generate a real-time resolved, lineage-specific map of EE differentiation on a single-cell level. In doing so, we identify significant differences in the differentiation speed of individual lineages, changing hormone production within lineages along the temporal



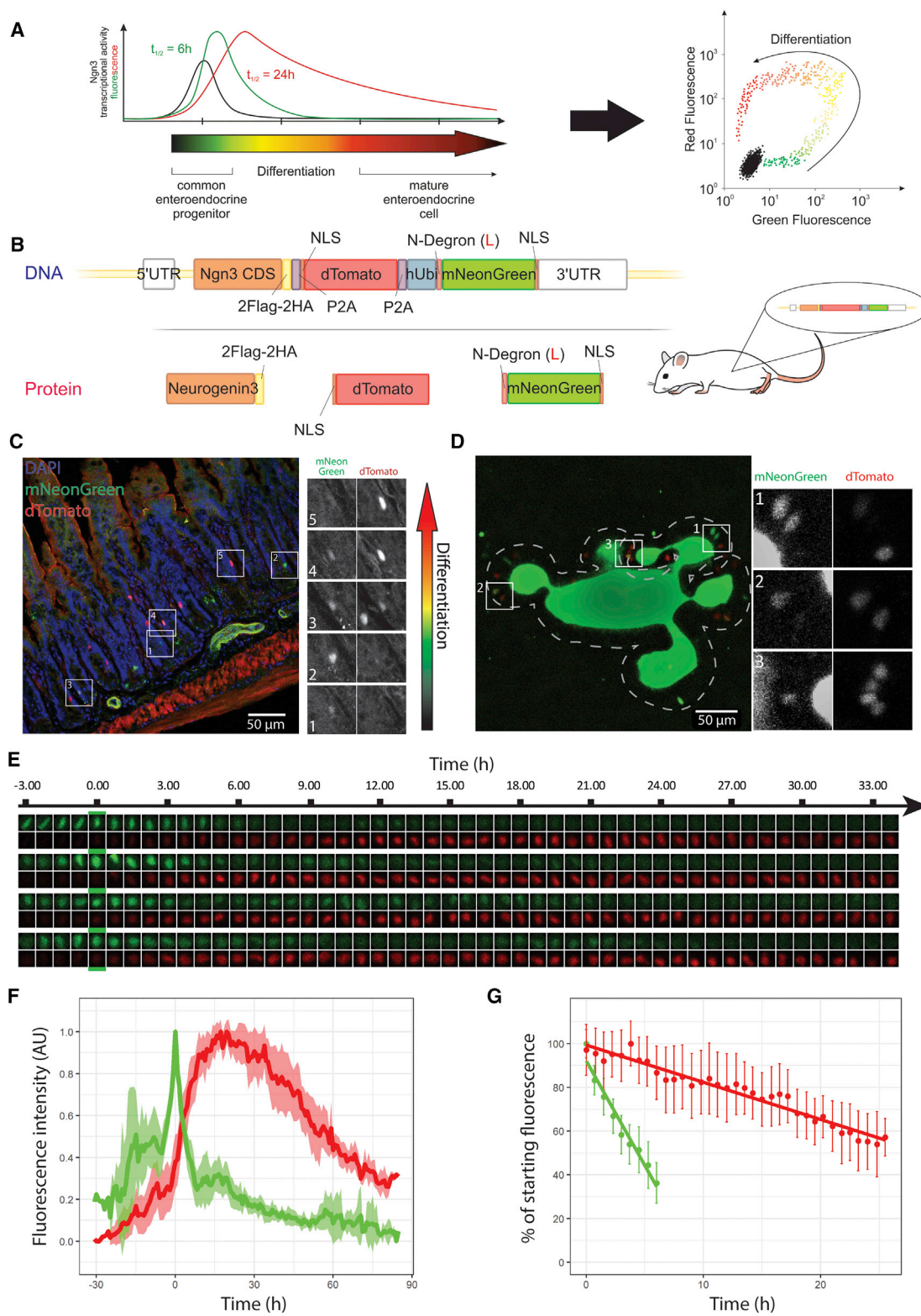


Figure 1. Generation and Characterization of the Neurog3Chrono Reporter

(A) Schematic depiction of reporter strategy.

(B) Structure of Neurog3Chrono reporter on DNA level and protein products.

(legend continued on next page)

trajectory, and novel transcriptional regulators of EE differentiation. Finally, we prove the relevance of our findings by knocking out 9 general and lineage specific candidate regulators in mice or organoids and demonstrate EE phenotypes in two-thirds of all tested genes.

RESULTS

Generation of an EE Real-Time Reporter

Due to the limited time frame from birth in the crypt to shedding at the tips of villi, differentiation of intestinal cells is a highly choreographed process. Neurogenin-3 (*Neurog3*) is transiently expressed in the common EE progenitor that gives rise to all EE cells in the intestine and to a majority of EE cells in the stomach. Thus, the transcriptional pulse of *Neurog3* expression in the course of EE differentiation used in conjunction with a fluorescent pulse-chase reporter can clearly identify a cell's progress on its way from common EE progenitor to mature EE cell.

Classic fluorescent reporters (e.g., EGFP) are of limited use as time-resolved reporters, due to their long half-life and the ambiguity of fluorescence intensity versus time. Previous studies have tried to overcome this limitation with fluorescence shifting fluorophores, such as DsRed-E5 (Miyatsuka et al., 2009). However, especially early gene activation was difficult to detect, due to the low brightness of the protein. Alternatively, coupling an unstable, fast folding fluorescent protein (green) that indicates acute transcriptional activity, with a second, stable, slow folding fluorophore (red) allows cell-tracking long after cessation of reporter gene transcription (Figures 1A and 1B). To generate a reporter with the highest possible sensitivity, accuracy, and temporal resolution, we employed the brightest available fluorescent proteins (mNeonGreen [Shaner et al., 2013] and dTomato [Shaner et al., 2004]) and destabilized mNeonGreen based on the N-end-rule by N-terminally fusing it to a single ubiquitin followed by an N-degron (Tasaki et al., 2012). Since cotranslational cleavage of a single ubiquitin in the polypeptide chain exposes leucine at the N terminus of mNeonGreen, the protein is subject to active removal. The construct was inserted into the *Neurog3* locus at the endogenous stop codon to maintain potential regulatory functions of the 3' UTR (Figure 1B). The knockin gene generates three independent proteins (NEUROG3, dTomato, and destabilized mNeonGreen) from a single polypeptide chain at a 1:1:1 ratio, which hinges changes in green and red fluorescence intensity exclusively on protein stability and thus time.

Neurog3Chrono animals were viable and even homozygous reporter mice showed normal EE differentiation (Figure S1A). The endogenous fluorescence showed the expected spectrum of cells from green over yellow (green + red) to red (Figure 1C). To establish a relationship between fluorescence signal and real time, we tracked individual cells during the differentiation process. Mini-guts (aka organoids) mimic the intestinal epithelium almost perfectly in structure and function and generate all cell types of the epithelial lining, including EE cells (Basak et al., 2017; Sato et al., 2009). We isolated intestinal organoids from homozygous Neurog3Chrono mice and followed spontaneous EE differentiation by live imaging (Figures 1D–1E and Video S1). Fluorescent cells changed sequentially from green over yellow to red (Figures 1E and 1F) indicating that *Neurog3* was—as expected—expressed in a pulse during EE differentiation. The calculated half-lives of mNeonGreen and dTomato were 4.39 ± 0.45 h and 29.78 ± 1.54 h (95% confidence intervals), respectively, which clearly indicates that mNeonGreen is highly destabilized (Figure 1G). We could reliably detect and distinguish cells from 24 h before to around 80 h after peak green fluorescence (our 0 h time point).

lium almost perfectly in structure and function and generate all cell types of the epithelial lining, including EE cells (Basak et al., 2017; Sato et al., 2009). We isolated intestinal organoids from homozygous Neurog3Chrono mice and followed spontaneous EE differentiation by live imaging (Figures 1D–1E and Video S1). Fluorescent cells changed sequentially from green over yellow to red (Figures 1E and 1F) indicating that *Neurog3* was—as expected—expressed in a pulse during EE differentiation. The calculated half-lives of mNeonGreen and dTomato were 4.39 ± 0.45 h and 29.78 ± 1.54 h (95% confidence intervals), respectively, which clearly indicates that mNeonGreen is highly destabilized (Figure 1G). We could reliably detect and distinguish cells from 24 h before to around 80 h after peak green fluorescence (our 0 h time point).

Global Transcriptional Changes during EE Differentiation

Having confirmed correct reporter behavior *in vivo* and *in vitro*, we proceeded to separate reporter-positive from reporter-negative cells by FACS of small intestinal crypts of homozygous Neurog3Chrono mice (Figure 2A). EE-specific genes were strongly expressed in reporter positive cells, whereas markers of epithelial stem cells (*Lgr5*) and other intestinal lineages (*Alpi*, *Muc2*, *Lyz1*, and *Dclk1*) were strongly enriched in the reporter-negative population (Figure 2B). Thus, Neurog3Chrono was correctly expressed and labeled EE cells with high fidelity. Subsequently, we separated the reporter-positive cells into early (green), differentiating (yellow), and mature EE cells (red) (Figure 2A). The chosen gates corresponded approximately to -24 h to 5 h, -5 h to 24 h, and older than 24 h (Figure 2A). Since our system allows us to highlight transcripts that show temporal modulation during the differentiation process, we focused our analysis on genes that are differentially expressed between different stages of EE maturation. A total of 1,418 genes showed significant changes during the differentiation process (Figure 2C).

Based on their temporal expression pattern, we classified transcripts into early, early+intermediate, intermediate, intermediate+late, and late expression genes. Within these categories, we found known markers of the EE differentiation process (Figure 2D). Additionally, we identified a wide array of time-specific genes (Table S1). Among these were 172 transcriptional regulators that showed specific temporal expression (Figure 2E). 54 of these were only transiently upregulated during the maturation process. To validate our findings, we selected several candidate genes in the list of transcription factors and confirmed their temporal expression pattern at protein level *in situ*. TOX3, MYT1, and RFX6 were successfully detected in the small intestine in EE cells of the expected Neurog3Chrono fluorescence (Figure 2F). Likewise, staining for SOX4 protein overlapped widely (but not completely) with expression of NEUROG3, which indicates that expression peaks of both genes in EE cells are only slightly offset

(C and D) Detection of reporter fluorescence in (C) cryosections of homozygous Neurog3Chrono small intestine and (D) homozygous small intestinal Neurog3Chrono organoids in standard culture medium.

(E) Examples of fluorescence tracking of individual cells in Neurog3Chrono organoids over time; aligned on maximum green fluorescence.

(F) Relative mean fluorescence intensities of mNeonGreen (green) and dTomato (red) over time ($n = 25$, mean \pm 95% confidence interval [CI]).

(G) Fluorescence decay of the Neurog3Chrono fluorophores over time ($n = 25$, mean \pm 95% CI).

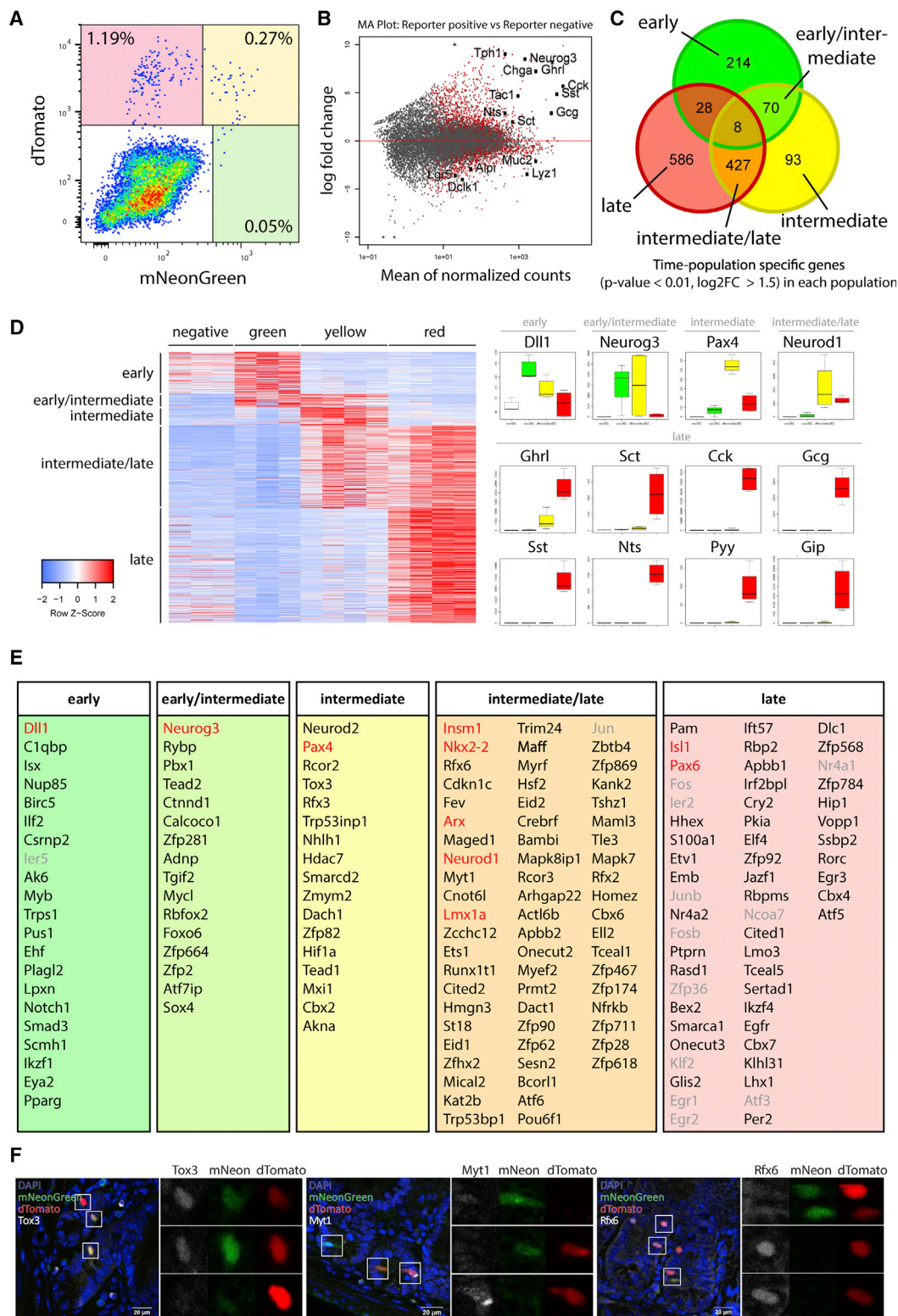


Figure 2. Global Transcriptional Changes during EE Differentiation

(A) Flow cytometry of isolated small intestinal crypt cells from homozygous *Neurog3*Chrono animals. Colored gates indicate the sorting windows for early (green), intermediate (yellow), and late (red) cells. The combination of early, intermediate, and late gate is considered reporter positive.
 (B) MA-Plot of reporter positive versus reporter negative cells. (n = 4 mice).

(legend continued on next page)

from each other (Figure S1B). Taken together, time-resolved bulk sequencing of Neurog3Chrono crypts confirmed the fidelity of the reporter system and identified a wide array of new EE genes with distinct temporal expression profiles.

Generation of a Time-Resolved Dataset of EE Differentiation at Single-Cell Level

Bulk RNA sequencing is a highly sensitive method to assay global transcriptional changes. However, it does not distinguish specific gene-expression in individual EE subspecies. Thus, we performed single cell sequencing on reporter-positive cells from small intestinal crypts and villi. A total number of 6906 cells were sorted and processed following the SORT-Seq method (Muraro et al., 2016). This method is based on CEL-Seq2, which combines immediate barcoding with linear amplification to ensure reliable detection of expression differences even in lowly expressed genes (Hashimshony et al., 2016). Since the majority of reporter-positive cells were mature (Figure 2A), we specifically enriched for earlier (green and yellow) cells to cover the differentiation time frame evenly.

Cell transcriptomes were analyzed with RaceID2 (Grün et al., 2016). After filtering (minimal threshold of 2,000 unique transcripts/cell, see STAR Methods), we retained 2,281 cells for analysis (Figure 3A). Expression of *Dll1* marked the earliest stages of EE differentiation, in line with our bulk dataset (Figure 3B). High levels of *Neurog3* identified cells in the central cluster as progenitors (Figure 3B). In contrast, *Neurod1* and *Isl1* marked late progenitors and mature EE cells (Figure 3B). Two “common” markers of mature EE cells, *Chga* and *Reg4* (Grün et al., 2016), were most abundantly expressed in enterochromaffin (EC) cells, the most numerous EE cell type in the intestine. Whereas *Chga* was present in other EE subtypes, albeit at lower expression levels, *Reg4* appeared highly specific for the EC lineage (Figure 3B). All mature cell clusters were identified based on their hormone expression profile (Figure 3F). We observe well-separated clusters of I cells (*Cck*), L cells (*Gcg*), Delta cells (*Sst*), X cells (*Ghrl*), EC cells (*Tac1/Tph1*), N cells (*Nts*), and K cells (*Gip*). EE cells from proximal, medial, and distal small intestine clustered according to their EE subtype and not according to regional origin within the small intestine (Figure 3C). The distribution of mature cells between crypt and villus varied strongly based on cell type. L cells were almost exclusively crypt derived, whereas nearly all N cells stemmed from the villus (Figures 3D and 3E). S cells did not form a separate cluster, but *Sct*-high cells could be found in most other mature cell clusters, particularly among villus-derived I and N cells (Figure S1C). In addition to the expected clusters of EE cells, we also discerned a Goblet cell cluster (*Agr2*, *Tff3*, *Spink4*, and *Muc2*) and a small cluster of Paneth cells (*Lyz1* and *Defa17*) (Figure S1D), which was in line with previous observations (Schönhoff et al., 2004).

By integrating the recorded fluorescence with the established dynamics of the green and red fluorophore, we could determine the amount of time that had passed since peak NEUROG3 expression for each individual cell (Figures 3G and 3H, see STAR Methods). When projected onto the tSNE map (Figure 3A), the time information correlated perfectly with the established cluster identities (Figure 3I). Thus, we could distinguish EE lineages and link differentiation time with single-cell transcriptomes.

EE Cells Display Hormonal Plasticity

Despite the clear separation of hormone-expression on the tSNE map, only 28.7% of all mature EE cells dedicated more than 90% of their hormone-encoding mRNA to a single gene product. However, the number varied strongly by lineage. Whereas more than 70% of K, X, and Delta cells expressed essentially only their primary hormone, less than 10% of L cells did (Figures S2A and S2B). The majority of L, I, N, and EC cells were bi- or tri-hormonal. The expression of several groups of hormones (e.g., *Nts*, *Pyy*, and *Sct*) was clearly correlated, which matched previous reports of multihormonal cells (Egerod et al., 2012; Habib et al., 2012) (Figure 4A). The strongest positive correlation was found between *Gcg* and *Cck* in L and I cells and between *Tac1* and *Tph1* in EC cells. *Tac1* and *Tph1* showed low correlation with other hormones, emphasizing the difference of the EC lineage to all other lineages.

Given the wide spectrum of observed co-expression in individual cells (Figure S2B), it appeared unlikely that each combination constituted an independent lineage. High variability could also be a sign of hormonal plasticity that allows mature cells to modify their hormonal repertoire based on extrinsic cues. One such cue can be the changing environment along the crypt-villus axis during the journey of EE cells toward the villus tips. In fact, when separated by crypt versus villus origin, EC cells showed striking differences in their hormonal expression (Figure 4B). While crypt EC cells expressed *Tac1* and *Tph1*, villus EC cells expressed *Sct* instead of *Tac1* and even higher levels of *Tph1*. Previously, it had been suggested that different sub-lineages of EC cells exist in parallel. Alternatively, there could be a single lineage, which changes hormone expression in the course of maturation. By increasing our minimal transcript threshold, we resolved a *Tac1*-high and *Sct*-negative and a *Tac1*-low and *Sct*-positive sub-cluster within the EC population (Figure S2C). When arranging these clusters in time, we clearly noticed that these populations arose subsequently, and not in parallel (Figure 4C, top). The median age of *Tac1*+ EC cells was 43.98 h after peak NEUROG3 expression, whereas *Sct*+ EC cells were on average 64.82 h old. The decrease of *Tac1*+ EC cells was concomitant with the appearance of *Sct*+ EC cells, which suggested efficient cell type conversion. This observation was further supported by plotting hormone expression in the EC lineage versus time (Figure 4C, bottom) and confirmed in a

(C) Venn diagram of population-specific genes ($p < 0.01$, $\log_2FC > 1.5$).

(D) Heatmap of cluster specific genes ($p < 0.01$, $\log_2FC > 1.5$, row Z scores) and examples for genes in each group (y axis = normalized counts). For a complete list, see Table S1.

(E) Time-resolved list of transcriptional regulators. Genes with known EE function are in red. Grayed-out genes have been reported to be associated with cell dissociation (van den Brink et al., 2017).

(F) Immunofluorescent stainings for TOX3, MYT1, and RFX6 on vibratome sections of homozygous Neurog3Chrono small intestine.

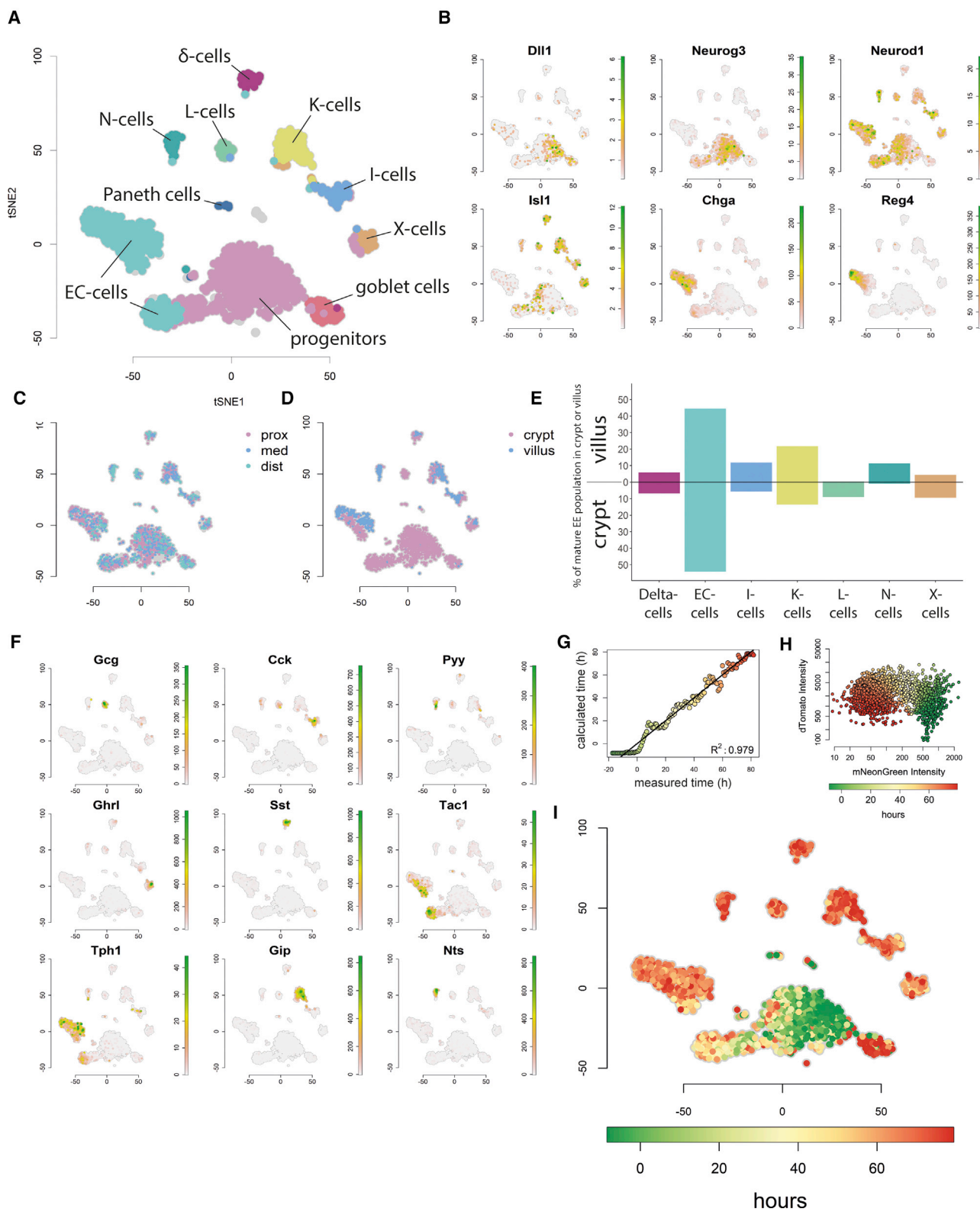


Figure 3. Generation of a Time-Resolved Dataset of EE Differentiation on a Single-Cell Level

(A) tSNE plot of sorted Neurog3Chrono cells (min. 2,000 unique transcripts/cell, 2,281 cells, n = 17 sorts of 2–3 mice each).

(B) General marker expression of EE cells (normalized unique transcript counts).

(legend continued on next page)

reporter-independent manner in organoids (Figure S3C). Tracking of *Tac1+* cells on an individual and population level in Tac1Cre-LSL-tdTomato organoids excluded premature cell death of *Tac1+* cells (Figures S3A and S3B). Plasticity, on the other hand, was clearly supported by lineage analysis with the “destiny/dpt” package (Angerer et al., 2016; Haghverdi et al., 2016). The EC lineage formed a continuous trajectory in diffusion space from progenitors over *Tac1+* EC cells (blue) to *Sct+* EC cells (green) (Figures 4D and S4B). This illustrates that *Tac1+* EC cells represent the link between progenitors and *Sct+* EC cells, and not a separate lineage. As a complementary approach, we also employed RNA velocity, a method that establishes differentiation trajectories in single-cell datasets based on the ratio of unspliced to spliced mRNA (La Manno et al., 2018). Transcripts of *Chgb*, a marker strongly expressed in the later EC population, showed high ratios of retained introns in the earlier EC cluster (Figure 4E). This indicated the start of a transition from early to late EC cell identity. The same behavior could be seen slightly later along the EC maturation path for the gene *Reg4* (Figure S2D). Thus, based on Neurog3Chrono time, the lack of premature cell death in the *Tac1+* EC population, the differentiation trajectory in diffusion space and RNA velocity information we conclude that the two EC sub-populations are not independent parallel lineages, but subsequent stages in EC-cell maturation.

However, plasticity is not limited to EC cells. A similar relationship was observed for the closely linked L, I, and N cells (Figures 4F–4H and S2E). The number of L cells decreased from 70 h onward, while the number of I cells and N cells increased concomitantly (Figure 4G, top). This behavior was also reflected by the transient nature of *Gcg* expression in the LIN cell population (Figure 4G, bottom), which indicated that L cells start to acquire transcriptional I- or N-cell identity around 70 h into their lifetime. The ILN lineage trajectory in diffusion space visualizes the progression from L over I to N cell (Figure 4D), which was further corroborated by RNA velocity analysis for *Cck* (Figure 4H) and *Nts* (Figure S2F). It is important to note, however, that L cells that acquire transcriptional I- or N-cell identity still retain GLP1/2 protein for a significant time. This explains why an overlap of GLP1 (highest RNA expression in L cell cluster) and PYY (highest RNA expression in N cell cluster) is observed in cells on protein level.

EE Cells Do Not Move Freely with the Intestinal “Conveyor Belt”

For both EC cells and LIN cells, the switch in identity occurred at around 70 h after the peak of NEUROG3 expression. Thus, we wondered whether this time coincided with movement of EE cells along the crypt-villus axis. We recorded confocal images of Neurog3Chrono small intestine and reconstructed the crypts in 3D (Video S2, Figure S3E). Subsequently, we measured the

fluorescence intensities of EE cells and correlated thereby their distance from the +4 position with differentiation time (Figure S3D). As expected, we observed the youngest EE cells in the lower half of the crypt close to the +4 position. Unexpectedly, however, EE cells did not immediately move up the crypt-villus axis. The first EE cells were observed outside the crypt at around 60 h, after which their number steadily increased. Nevertheless, a significant portion of EE cells remained in the crypt even at 80 h. Since enterocytes travel from the bottom of the crypt to the tip of villi within 72 h regardless of small intestinal region (Darwich et al., 2014), it was obvious that EE cells do not travel freely with the epithelial “conveyor belt”. 97.2% ± 2.2% (n = 145 cells in 9 sections) of all red (old) cells in crypts expressed CHGA either at high (EC cell) or low levels (non-EC cell) (Figures S3F and S3G). Thus, the vast majority of these cells was mature. Notably, the time the first EE cells reached the base of villi did coincide with hormonal switches in EE lineages (e.g., EC and L cells). This is well in line with a recent publication that described changes in hormonal expression in EE cells in response to BMP signaling, which is known to form a gradient of increasing signal strength from the crypt to the villus (Beumer et al., 2018). Thus, our data strongly support the ability of EE cells to change their hormonal repertoire dynamically in response to environmental cues, such as position along the crypt-villus axis.

Establishing Differentiation Trajectories with Real-Time Information

To follow the process of EE differentiation and subsequently identify its regulators, we established the order of events from common progenitor to mature cell. By further subclustering progenitor cells, we resolved 7 populations with differing temporal profiles (Figures 5A and 5B). The earliest population (early progenitor) covered a tight time span around the –10 h position. It was followed by two clusters of immediate offspring. One of these (goblet cell progenitors) showed a clear bias for the goblet cell fate with increased expression of markers such as *Fcgbp* and *Agr2* (Figure 5C). The other cluster (common EE progenitor) expressed markers of EE differentiation, e.g., *Neurod1*, and was distinctly positive of *Olfm1* (Figure 5C). Following the common EE progenitor were two equi-temporal populations of biased progenitors: one expressing markers of early EC cells (e.g., *Fev*, *Chgb*), the other markers of non-EC EE populations (e.g., *Isl1*) (Figure S4A). Each of these was followed by a cluster of the earliest mature cells of the two respective lineages: *Tac1+* early EC cells and X cells (Figures 5A and 5B). To visualize the branching point between EC and non-EC lineage and identify potential actors in the decision process, we analyzed all progenitors of the EE branch together with early EC and non-EC cells (younger than 48 h) in diffusion space (Figure 5D). The diffusion

(C) Proximal (pink), medial (blue), or distal (turquoise) origin of cells along the proximal-distal axis. Gray cells stem from whole SI preparations.

(D) Crypt (pink) or villus (blue) origin of cells on tSNE map. Gray cells are of mixed origin.

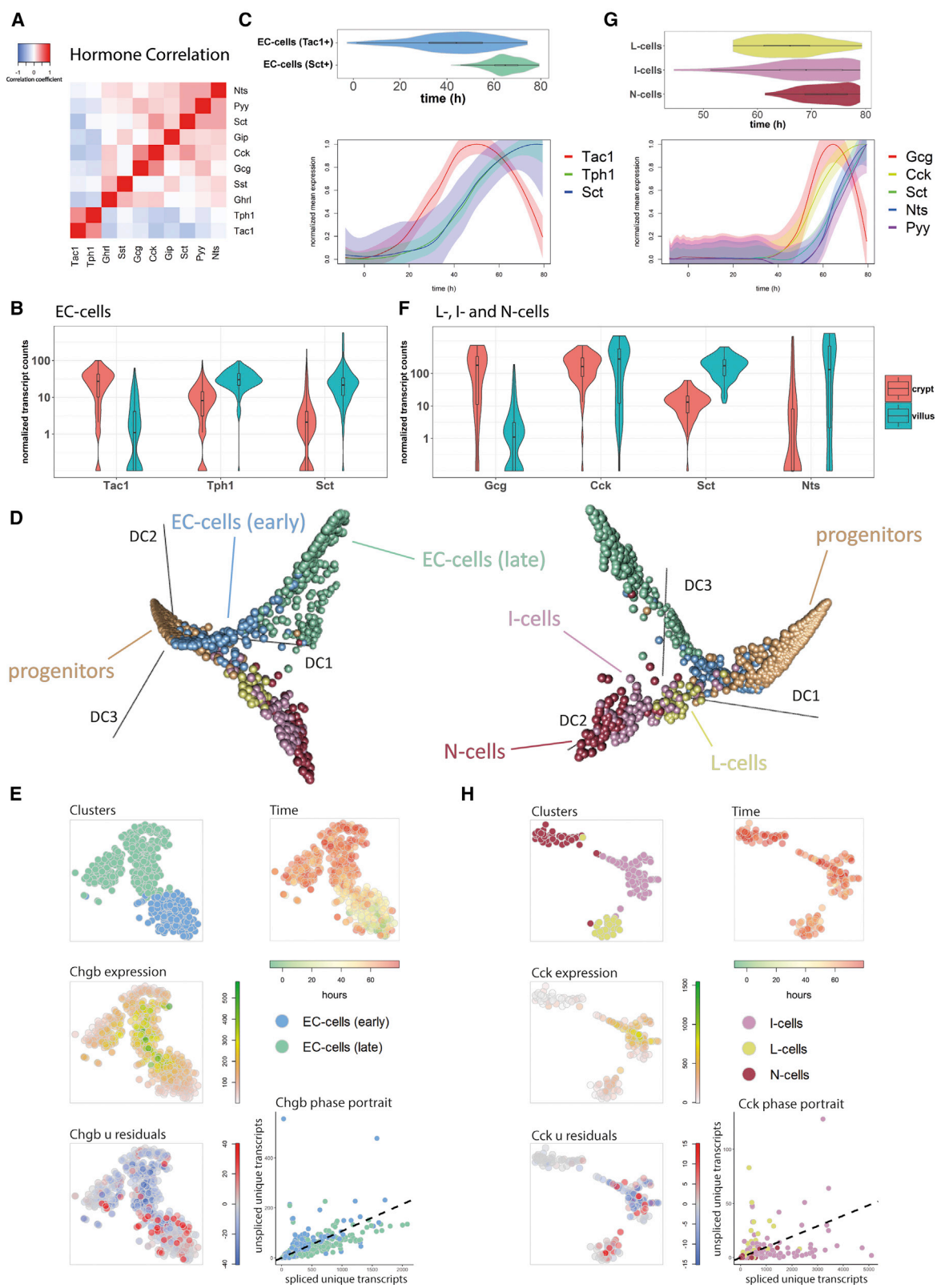
(E) Relative frequency of individual mature EE cell types in crypt and villus.

(F) Hormone expression projected on the tSNE map (normalized unique transcript counts).

(G) Correlation between measured (real) time and calculated time based on fluorescence intensities. Colored dots correspond to reference values measured by live-imaging.

(H) Projection of calculated differentiation time on flow-cytometry data.

(I) Projection of calculated differentiation time on tSNE map.



(legend on next page)

map clearly illustrated the branching point and identified *Hmgn3*, *Prdm16*, and *Fev* as the highest enriched transcriptional regulators at the EC side of the branch (Figure 5E). *Isl1*, *Cdkn1a*, and *Arx* clearly marked cells on the non-EC trajectory (Figure 5E). To establish relations from progenitors to mature cell populations, we transferred cell identities established in the progenitor subclustering to our high-sensitivity dataset of all EE cells (Figure 5F). Cluster distribution along the time axis showed clear differences in the maturation speed of individual lineages. Peaking at 44 h after maximal NEUROG3 expression, *Tac1*⁺ early EC cells were the first hormone-producing cells to develop (Figure 5G). This was in line with a previous study that utilized BrdU incorporation to demonstrate that TAC1 is the earliest detectable hormone (Aiken and Roth, 1992). At 60 h, *Ghrl*⁺ X cells were the first non-EC cells to appear in high numbers, followed by L cells. Around 70 h, all other EE lineages were readily detectable. Based on their expression of transcription factors such as *Arx*, *Cdkn1a*, and *Isl1*, X cells, I cells, L cells, and K cells were derived from non-EC biased EE progenitors (Figure S4A). Early EC cells, on the other hand, arose from EC-biased progenitors (based on low *Arx*, *Isl1*, and *Cdkn1a* and high levels of *Fev* and *Chgb*) (Figure S4A). This was further corroborated by the fact that the number of non-EC biased progenitors decreased in time concomitantly with the rise of early EC cells (Figure 5G). While delta cells shared *Cdkn1a* and *Isl1* expression with the non-EC biased progenitor, they did not express *Arx* (similar to the EC biased progenitor) (Figure S4A). The temporal profile favored the non-EC-biased progenitor as origin because very few cells remained in the EC-biased progenitor state at the time delta cells arose. Indeed, *Arx* knockout causes a strong increase in delta-cell numbers at the expense of I cells, L cells, and K cells. EC cells are not affected and arise in normal numbers, while X cells increase slightly (Beucher et al., 2012; Du et al., 2012). If *Arx* was the main regulator at the decision point between EC-biased (low *Arx*) and non-EC-biased (high *Arx*) progenitor, we would have expected increased numbers of EC cells upon knockout and complete loss of all cells that arise from non-EC progenitors. Therefore, it was more likely that *Arx* controls a secondary decision within the non-EC lineage between I cells, L cells, and K cells (high *Arx*) and delta cells (low *Arx*). Finally, when projected in diffusion space, delta cells follow a similar trajectory as other non-EC cells (Figure 5H) and are distinct from the ILN lineage (Figure S4B). Thus, due to expression of *Isl1* and

Cdkn1a, the fitting temporal profile, the *Arx* knockout phenotype and the diffusion map trajectory, we also assigned delta cells to the non-EC lineage.

Transcriptional Regulators of Lineage Specification

Having established the relationship between clusters, we proceeded to map the transcriptional order of events during lineage specification. By ordering peak expression of highly modulated transcriptional regulators in time, we generated a comprehensive description of each lineage and its maturation stages (Figures 6A and S5A–S5F). Among the modulated genes of the EC lineage, we noticed known regulators of EE differentiation (e.g., *Neurog3*, *Pax4*, *Pax6*, *Neurod1*, and *Lmx1a*) (Figure 6A). Whereas the modulated expression pattern of genes like *Sox4*, *Neurog3*, *Tox3*, or *Myt1* did not differ between lineages, others (such as *Hmgn3*, *Fev*, *Cdkn1a*, *Etv1*, or *Crip1*) deviated between lineages at specific time points during the maturation process (Figures 6B and 6D).

Having established the expression order of transcriptional regulators, we proceeded to determine which factors define individual cell types. Because differential gene expression analysis among mature populations alone (Figure S5G) would miss the observed transient lineage differences (Figure 6B), we opted to examine differences in gene expression at three time intervals. The first two intervals (10–20 and 30–50 h) contained genes that predominantly separate EC from non-EC lineage (e.g., *Hmgn3*, *Fev*, *Cdkn1a*, *Isl1*, *Atf6*, *Arx*), while the third interval (>50 h) highlighted genes that were specific for individual non-EC lineages. Among these, we identified *Hhex* as delta-cell-specific transcription factors. *Hhex* has been previously described to be necessary for differentiation of SST-producing delta cells in the pancreas (Zhang et al., 2014) and was thus a strong candidate to fulfill the same role in the intestine. *Zcchc12* was specifically expressed in X cells but has so far not been functionally linked to endocrine development. *Lmx1a*, *Atf6*, *Gtf2f2*, and *Taf1* were specific for EC cells. *Lmx1a* has been recently described to control serotonin biosynthesis in the intestine (Gross et al., 2016). In addition to single-lineage factors, we also found various regulators with specific expression in two or more lineages. For example, expression of *Onecut3* separated I and N cells from all other lineages, while *Parp1* was specifically active in L, delta, and EC cells. Likewise, *Etv1* was enriched in L, I, and N cells, whereas *Pax6* was highly expressed in L and K cells.

Figure 4. Hormonal Plasticity in EC and LIN Cells

- (A) Heatmap of correlation coefficients of log transformed normalized hormone transcript counts.
 (B) Normalized unique hormone transcript counts in crypt- versus villus-derived EC cells.
 (C) Temporal profiles of *Tac1*⁺ and *Sct*⁺ subclusters of EC cells and Loess-smoothed normalized mean expression of *Tac1* (red), *Tph1* (green), and *Sct* (blue) within the EC lineage over time. Shaded regions denote 95% CIs.
 (D) Diffusion map showing all EE progenitors plus all cells of the EC and ILN-lineages (min. 4,000 unique transcripts/cell, 2 viewing angles).
 (E) tSNE map of 461 early and late EC cells (min. 4,000 unique transcripts/cell) (top-left), time projection on tSNE (top-right), expression levels of *Chgb* (middle-left, normalized unique transcript counts), phase portrait (bottom-right) showing regions of increasing (over dotted line) or decreasing (under dotted line) expression based on unspliced/spliced mRNA balance (colors correspond to clusters), unspliced unique transcript count residuals projected on the tSNE map (red indicates high relative levels of unspliced mRNA = begin of gene expression, blue indicates low relative levels of unspliced mRNA = downregulation of gene expression, bottom left) (related to Figure S2D).
 (F) Normalized unique hormone transcript counts in crypt- versus villus-derived combined L, I, and N cells.
 (G) Temporal profiles of L, I, and N cell clusters and Loess-smoothed normalized mean expression of *Gcg* (red), *Cck* (yellow), *Sct* (green), *Nts* (blue), and *Pyy* (purple) within the combined LIN lineage over time. Shaded regions denote 95% CIs.
 (H) As (E) but for *Cck* mRNA in 176 ILN cells (related to Figure S2F).

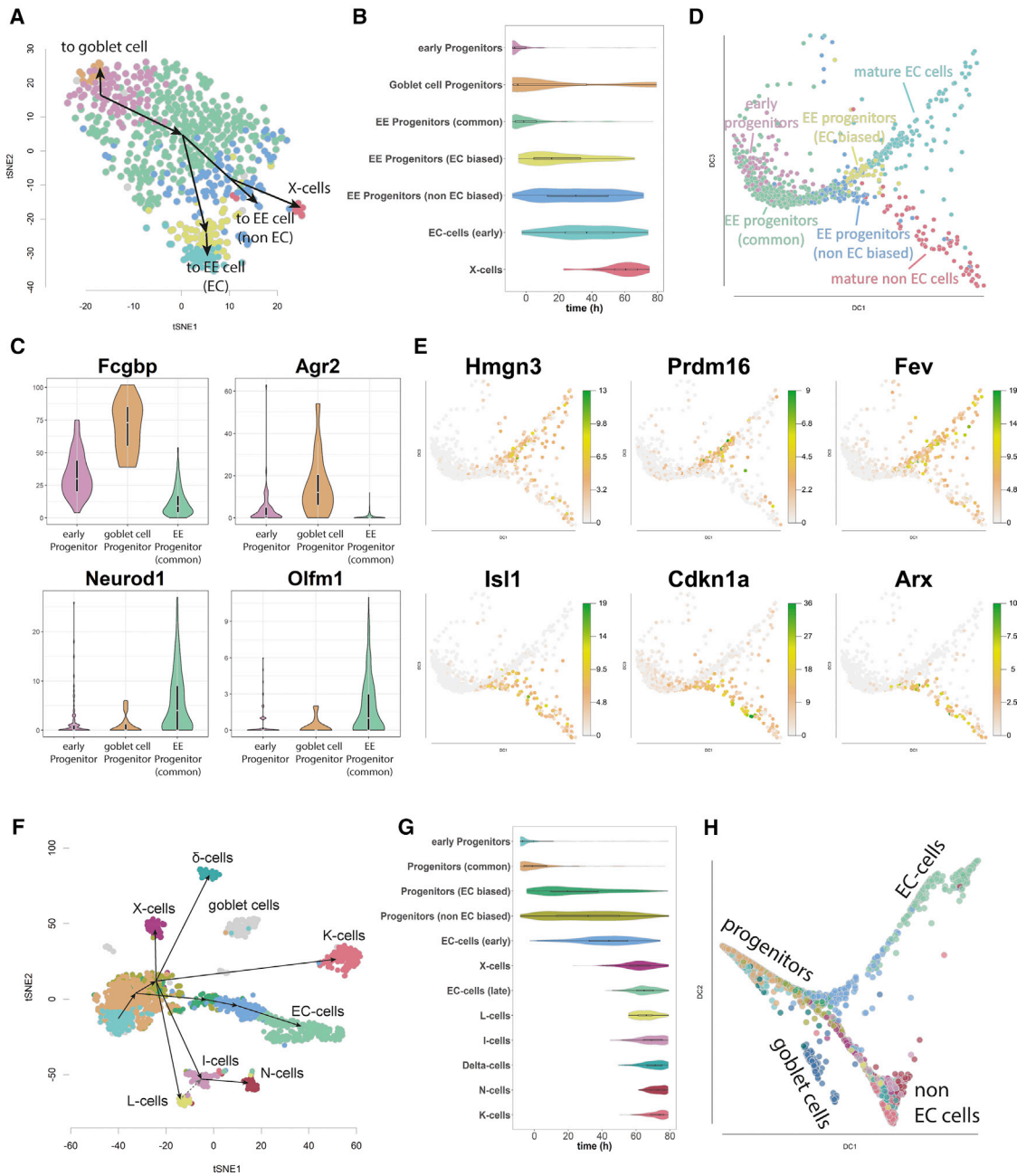


Figure 5. Establishing Differentiation Trajectories with Real-Time Information

(A) tSNE map of 613 EE progenitor cells (min. 5,000 unique transcripts/cell). Arrows indicate lineage relationships. Cells in gray could not be clearly identified.

(B) Violin/boxplots of time distribution within progenitor clusters in Figure 5A.

(C) Violin/boxplot of selected differentially expressed genes between early progenitors (light purple), goblet cell progenitors (orange) and common EE progenitors (green). Numbers indicate normalized unique transcript counts.

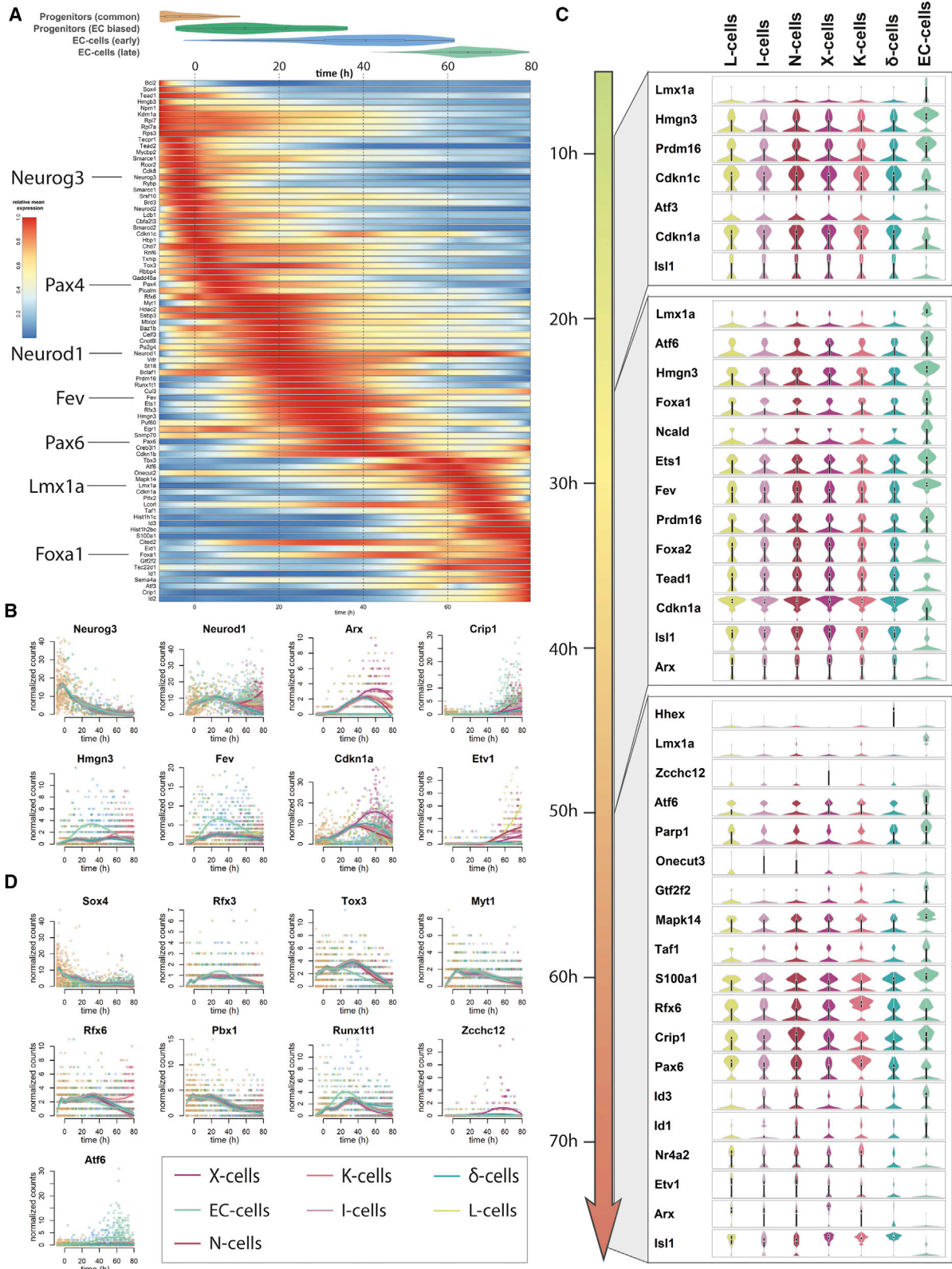
(D) Diffusion map of all EE progenitor cells with cells of mature EE cluster (<48 h of age).

(E) Differentially expressed transcriptional regulators at the branching region between EC and non-EC cells, projected on a diffusion map (normalized unique transcript counts).

(F) High sensitivity dataset of 1,750 cells (min. 4,000 unique transcripts/cell). Arrows indicate lineage relationships. Cells in gray mark non-EE cells.

(G) Violin/boxplots of time distribution within clusters in Figure 5E.

(H) Diffusion map of all cells in the high sensitivity dataset, illustrating the points of lineage decisions.



(legend on next page)

Knockout of Candidate Genes

To corroborate the validity of our findings, we chose 9 candidate genes (Figure 6D) for loss-of-function experiments. We chose *Sox4* due to the similarity of its expression profile to *Neurog3*. *Rfx3*, *Tox3*, *Myt1*, *Pbx1*, and *Runx1t1* represented genes that were transiently activated in progenitors but mostly lost in mature populations. *Rfx6*, has been reported to be a K-cell-specific gene (Suzuki et al., 2013). Indeed, we observed that *Rfx6* expression was only maintained in mature K cells (Figure 6D), but all lineages expressed *Rfx6* highly at earlier stages. Thus, we selected *Rfx6* to investigate whether its function was broader than conventional analysis would suggest. Finally, we chose *Zcchc12* and *Atf6*—two lineage-specific transcription factors for X and EC cells, respectively—which have not yet been linked to EE differentiation.

As confirmed by immunohistochemistry, SOX4 expression is limited to rare cells close to the +4 position (Figure S6A). This corresponds well to the short time frame of *Sox4* expression at the start of EE differentiation (Figure 6D, S1B, and S6B). To study *Sox4* function, we conditionally deleted the gene in the intestine by using the beta-naphthoflavone-inducible *AhCre* transgene crossed into *Sox4*^{loxP/loxP} mice (Penzo-Méndez et al., 2007) (Figures 7A and S6A). Upon *Sox4* deletion, the animals lost all GLP1-positive cells in duodenum and jejunum (Figure 7B). In the ileum, a reduced number of GLP1-positive cells was observed, most likely a result of the incomplete deletion by *AhCre* in the distal small intestine (Ireland et al., 2004) (Figures S6B and S6C). Concomitant with loss of GLP1, CCK-, SST-, and GIP-positive cells were significantly reduced, while the number of GHRL-expressing cells increased (Figures 7B and S6D). This phenotype was further corroborated by microarray analysis (Figures S6E and S6F). These findings are well in line with another very recently published study that explored the role of *Sox4* in *Atoh1* independent lineage allocation of Tuft and EE cells (Gracz et al., 2018). Thus, *Sox4* plays a broad but essential role for correct fate specification during EE differentiation.

Because generation and analysis of conditional knockout animals is a technique with extremely low throughput, it was not compatible with the number of candidate genes we aimed to analyze. Intestinal organoids are a well-established system to study intestinal epithelial biology. However, for organoids to serve as a faithful model for EE lineage specification, the EE differentiation process *in vitro* and *in vivo* needs to be comparable. Therefore, we induced EE differentiation in homozygous *Neurog3*Chrono organoids (Figure S7A) and investigated the transcriptome of reporter positive. 950 organoid cells containing a minimum of 4,000 unique transcripts/cell were combined with

the 1,750 cells from our primary tissue dataset. Cells clustered according to cell type irrespective of tissue or organoid origin (Figure S7 and S7E). In fact, we could detect organoid cells in all previously identified EE progenitor and mature cell clusters (Figure S7D), and they maintained the same differentiation dynamics as primary cells (Figure S7C). Consequently, organoids represent an excellent tool to study EE lineage allocation *in vitro* due to their faithful representation of EE fate specification.

To create loss-of-function organoids, we generated a mouse line with constitutive expression of Cas9 from the *Rosa26* locus. In contrast to previously published Cas9 animals (Platt et al., 2014), these animals do not express EGFP, which enables fluorescence-based readouts. Organoids generated from *Rosa-Cas9* animals were transiently transfected with *in vitro*-transcribed gRNA (Figure 7C). Subsequently, we picked and genotyped clones to identify organoids carrying homozygous loss-of-function alleles. Knockout clones were expanded and differentiated under EE-inducing conditions (Basak et al., 2017). Phenotypes in EE differentiation were then assessed by hormone-specific quantitative real-time PCR and whole-mount immunofluorescent staining of multiple independent knockout clones. As proof of principle, we first knocked out *Neurog3* and confirmed loss of all hormone expression (Figure S7F).

Among the 6 transiently expressed candidate regulators (*Rfx6*, *Rfx3*, *Tox3*, *Myt1*, *Pbx1*, and *Runx1t1*), only *Rfx3* and *Pbx1* showed no EE phenotype. Loss of *Rfx6* induced severe loss of K, X, and L cells and significant reduction in I and EC lineages (Figures 7D and 7E). Despite the strong reduction in EE cells, there was no detectable decrease in *Neurog3* expression, which indicated that *Rfx6* acts downstream of *Neurog3*. This order of events is further supported by our own temporal map of transcription factor activation (Figure 6A) and *Rfx6* knockout studies in the endocrine pancreas (Soyer et al., 2010). Thus, despite being maintained exclusively in adult K cells (Figure 6D), *Rfx6* controls the differentiation of multiple EE lineages due to its transient expression in all lineages during maturation.

Tox3 is a member of the HMG-box protein family and has so far not been linked to endocrine development. Knockout of *Tox3* caused a strong decrease in *Tph1* and thus in serotonin (Figures 7F and 7G). However, *Tox3*-deficient organoids produced significantly higher numbers of X cells. A similar phenotype was observed in *Myt1* knockouts, where EC cells were also strongly reduced (Figures 7G and 7H). Even though *Myt1* has been proposed to act in a reciprocal feed-forward loop with *Neurog3* in the endocrine pancreas (Wang et al., 2008), we could not find evidence to support a similar mechanism in EE cells. *Neurog3* levels did not decrease upon loss of *Myt1*,

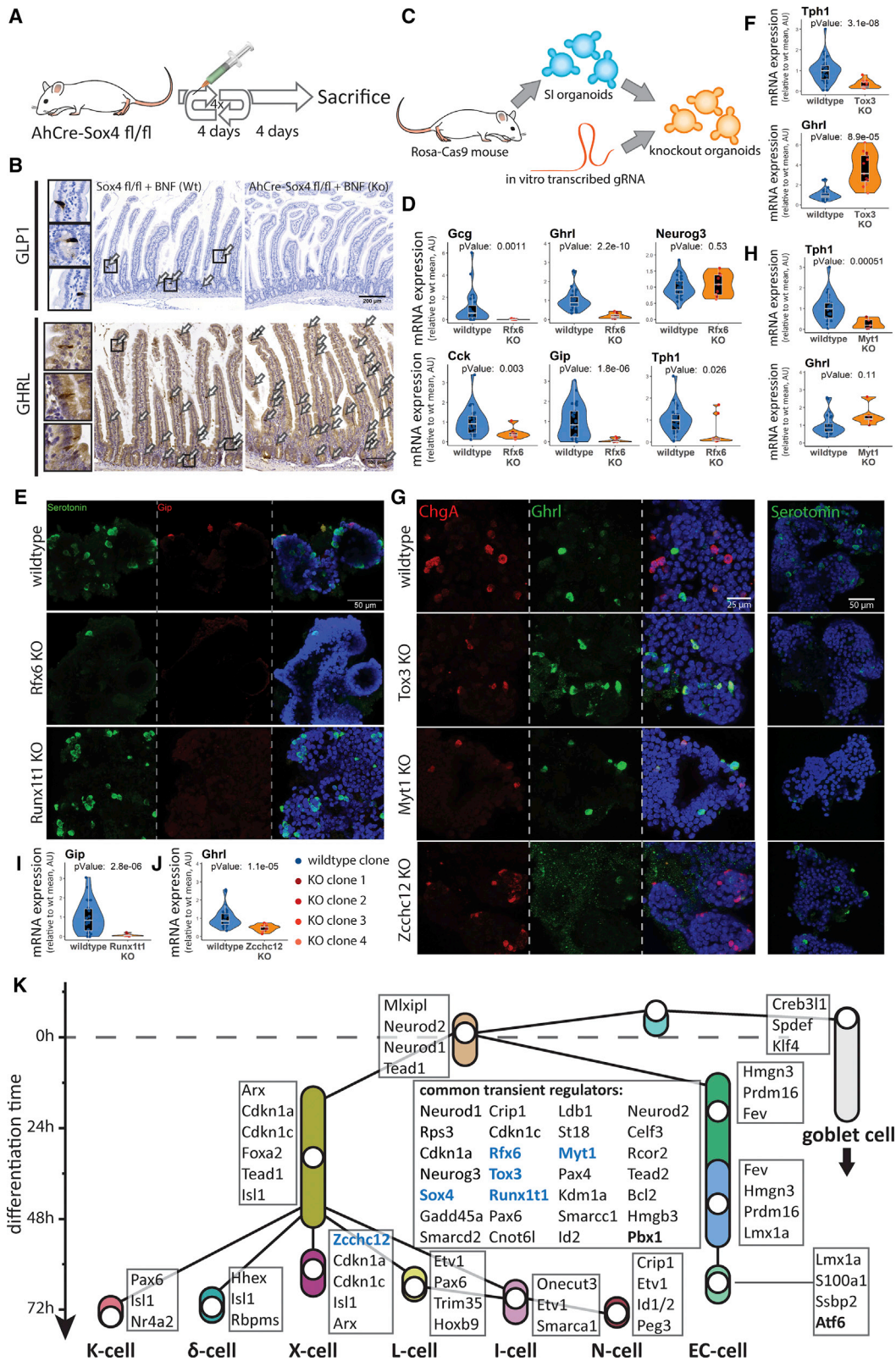
Figure 6. Identification of General and Lineage-Specific Regulators of EE Differentiation

(A) Modulated transcriptional regulators (UniProt: KW-0805) in the EC lineage ordered by peak relative mean transcript count along the time axis (mean modulation > 80%, mean transcripts > 0.9). Colors indicate Loess-smoothed mean expression relative to maximum expression in time. Graphs for other lineages can be found in Figures S5A–S5E.

(B) Lineage-resolved expression profiles of selected genes. Colored lines represent lineage-specific Loess-smoothed expression means. Numbers indicate normalized unique transcript counts.

(C) Differential gene expression between lineages at 3 depicted time intervals ($p < 0.01$, min. FC > 3). Violin/boxplots depict log-transformed normalized unique transcript counts + 0.1.

(D) Lineage-resolved expression profiles of genes chosen for knockout confirmation. Colored lines represent lineage-specific Loess-smoothed expression means. Numbers indicate normalized unique transcript counts.



(legend on next page)

and the temporal expression profile indicated that *Myt1* peaks after *Neurog3* starts to taper off (Figures S7G and S7H). It was thus more likely that *Myt1* acts downstream of *Neurog3* in EE differentiation.

In line with its broad expression during EE lineage specification, loss of *Runx1t1* affected K, I, and delta cells (Figures 7E, 7I, and S7I). The fact that it is also expressed in other lineages (e.g., EC cells), suggests that it is not the primary driver for these fates, but a necessary co-factor. Among the lineage-specific candidates, *Atf6* did not show an EE phenotype. However, knockout of *Zcchc12*, a highly lineage-specific transcription factor in X cells, led to strongly reduced levels of *Ghrl* expression and significant loss of X cells (Figures 7G and 7J).

Thus, we demonstrate that 6 out of 9 candidate genes identified by real-time-resolved, lineage-specific, single-cell RNA sequencing show significant EE phenotypes upon knockout in mice or organoids. This result showcases the ability of our method to correctly identify important transiently expressed genes that would not be highlighted in a conventional differential expression analysis. Finally, we summarized our results in a time-resolved EE differentiation tree that depicts common and lineage-specific transcriptional regulators (Figure 7K).

DISCUSSION

Our method of real-time resolved single-cell transcriptomics is applicable for all cellular processes that display transient activation of a marker gene. Due to the choice of fluorescent proteins, our reporter construct provides high signal-to-noise ratio even for lowly expressed genes without interfering with gene function. Furthermore, the observed time frame is tunable by exchanging the first amino-acid after the N-degron of mNeonGreen. This makes the technology suitable for a wide range of applications from studying short-term oscillations of cellular signals to long differentiation processes lasting more than a week. The system is especially well suited to study rare cell types with complex differentiation dynamics, such as the EE lineage.

Recently, two other high-profile publications surveyed the EE compartment at a single-cell level (Haber et al., 2017; Yan et al., 2017). Using a conventional differential gene expression analysis, Haber et al. (2017) identified many genes that we see upre-

gulated in mature populations. However, due to the lack of time information, these authors did not pick up transiently expressed regulators such as *Tox3*, *Runx1t1*, *Rfx6*, or *Myt1*, all of which yield EE phenotypes when knocked out. Additionally, Haber et al. (2017) created a new lineage nomenclature based on observed hormone co-expression. Our method demonstrates, however, that some of the observed subtypes (e.g., “EC” and “EC Reg4”) are not separate lineages but are consecutive stages in EE cell maturation. The study of Yan et al. (2017) showed that *Prox1*⁺ and *Bmi1*⁺ EE cells possess stem cell potential. *Prox1* and *Bmi1* were, according to our dataset, already expressed in early EE progenitors (Figure S5H). Thus, it is not clear whether the crypt repopulation capacity that Yan et al. (2017) observed rests indeed within mature EE cells or in early progenitors. The cluster that Yan et al. (2017) identified as common EE precursor shows a transcriptional profile that our data, based on transcriptome and temporal profile, clearly identified as mature I cells. Due to the appearance of I cells long after *Tac1*⁺ EC cells, simultaneous with most other EE lineages, this relationship is highly unlikely. This highlights the difficulty of inferring lineage relationships based on transcriptomic data alone. The dataset generated in our study thus appears to be an excellent tool to train a new generation of algorithms for higher-accuracy predictions of pseudo-time and lineage relationships.

In primary tissue, we saw that EE cells do not move with the intestinal “conveyor” belt. Given that most EE cell types appeared only around 60 h after the NEUROG3 pulse, this is likely a biological necessity due to the otherwise exceedingly narrow window of cell activity. On the transcriptome level, our method highlighted not only intrinsic differences in the maturation speed of EE cell types but showcased unexpected plasticity in mature EE populations. Hormonal plasticity is of interest for therapeutic application, as it may present an accessible route to modulate endogenous levels of specific hormones. A proof-of-concept study has already demonstrated that BMP levels can control the hormonal repertoire of EE cells *in vivo* (Beumer et al., 2018). In summary, our study describes a new technique to link real-time with single-cell sequencing information and provides a rich resource to understand and eventually manipulate EE differentiation for scientific and medical purposes.

Figure 7. Confirmation of Candidate Genes

- (A) Schematic representation of *Sox4* deletion in AhCre-*Sox4*^{loxP/loxP} animals. The syringe indicates injection of beta-naphthoflavone (BNF).
 (B) Immunohistochemical detection of GLP1 and GHRL in the proximal intestine of the indicated genotypes.
 (C) Schematic representation of the knockout strategy in intestinal organoids.
 (D) mRNA expression of indicated genes measured by quantitative real-time PCR (qPCR) relative to mean expression of all wild-type clones (3 independent knockout clones, distinguished by different point colors).
 (E) Whole-mount immunofluorescent staining of the indicated hormones in wild-type and knockout organoids.
 (F) mRNA expression of indicated genes measured by qPCR relative to mean expression of all wild-type clones (4 independent knockout clones, marked by different point colors).
 (G) Whole-mount immunofluorescent staining of the indicated hormones in wild-type and knockout organoids.
 (H–J) mRNA expression of indicated genes measured by qPCR relative to mean expression of all wild-type clones. (H) 2, (I) 3, and (J) 3 independent knockout clones, marked by different point colors.
 (K) Time-resolved EE differentiation tree. Begin and end of colored boxes indicate first and third quartile of time-distribution within the cluster. White circles mark the median. Cluster-specific transcriptional regulators are indicated next to the cluster and common regulators are listed in the middle. Bold Regulators were knocked out, bold blue regulators gave an EE phenotype.
 Statistical significance for (D, F, H, I and J) was determined by unpaired Student’s t-test.

STAR★METHODS

Detailed methods are provided in the online version of this paper and include the following:

- **KEY RESOURCES TABLE**
- **CONTACT FOR REAGENT AND RESOURCE SHARING**
- **EXPERIMENTAL MODEL AND SUBJECT DETAILS**
 - Mice
- **METHODS DETAILS**
 - Isolation of single cells from Neurog3Chrono animals or organoids
 - Flow Cytometric Purification
 - Establishing and imaging intestinal Organoid cultures
 - Preparation of intestinal tissue for imaging
 - *In vitro*-transcription of gRNAs
 - CRISPR-Cas9 mediated knockout in intestinal organoids
 - Enteroendocrine differentiation of intestinal Organoids
 - Whole-mount staining of intestinal organoids
 - Deletion of Sox4 in AhCre x Sox4^{loxP/loxP} animals
 - Messenger RNA Sequencing
- **QUANTIFICATION AND STATISTICAL ANALYSIS**
 - Quantification of decay dynamics of Neurog3Chrono
 - Fluorescence time conversion
 - Quantification of Tac1Cre-LSL-tdTomato organoids
 - Quantification of enteroendocrine cell migration
 - Bioinformatics Analysis
 - Statistics
- **DATA AND SOFTWARE AVAILABILITY**
 - Data Resources

SUPPLEMENTAL INFORMATION

Supplemental Information includes seven figures, three tables, and two videos and can be found with this article online at <https://doi.org/10.1016/j.cell.2018.12.029>.

ACKNOWLEDGMENTS

We thank Stefan vd Elst and Reinier vd Linden for flow cytometry assistance, Harry Begthel for immunohistochemistry help, Judith Vivie for SORT-seq support, the Utrecht Sequencing Facility (USF) and Genome Scan for sequencing, Anna Alemany Arias and Alexander van Oudenaarden for mapping RNA velocity data, Anko de Graaff and the Hubrecht Imaging Centre (HIC) for microscopy assistance, Jeroen Korving for help with mouse generation, Cayetano Pleguezuelos Manzano for experimental help, and Zoraide Granchi for careful reading of the manuscript. Tac1Cre-LSL-tdTomato organoids were kindly provided by Hongkui Zeng. This work was supported by an EMBO long-term fellowship (ALTF 240-2014 to H.G.) and a VENI grant from the Netherlands Organization for Scientific Research (NWO-ZonMW, 016.166.119 to H.G.) as well as an HFSP fellowship (LT771/2015 to K.K.) and VENI fellowship (NWO-ZonMW, 016.166.140 to K.K.).

AUTHOR CONTRIBUTIONS

H.G. and H.C. conceived the project. H.G. generated the Neurog3Chrono mouse model, designed experiments, interpreted results, and performed bioinformatics analysis. H.G. designed experiments and interpreted results. H.G. and J.H.v.E. performed animal experiments. H.G., J.F.D., and A.R. performed histology and imaging experiments. H.G. and K.H. performed all organoid experiments. J.B. provided reagents and conceptual input, K.K. mapped and

managed data, and J.H.v.E. generated the Rosa26-Cas9 mouse model. H.G. and H.C. acquired funding and wrote the manuscript with input from all other authors.

DECLARATION OF INTERESTS

H.C. holds several patents on organoid technology.

Received: April 21, 2018

Revised: September 21, 2018

Accepted: December 17, 2018

Published: January 31, 2019

REFERENCES

- Aiken, K.D., and Roth, K.A. (1992). Temporal differentiation and migration of substance P, serotonin, and secretin immunoreactive enteroendocrine cells in the mouse proximal small intestine. *Dev. Dyn.* 194, 303–310.
- Angerer, P., Haghverdi, L., Büttner, M., Theis, F.J., Marr, C., and Büttner, F. (2016). destiny: diffusion maps for large-scale single-cell data in R. *Bioinformatics* 32, 1241–1243.
- Barker, N., van Es, J.H., Kuipers, J., Kujala, P., van den Born, M., Cozijnsen, M., Haegerbarth, A., Korving, J., Begthel, H., Peters, P.J., and Clevers, H. (2007). Identification of stem cells in small intestine and colon by marker gene Lgr5. *Nature* 449, 1003–1007.
- Basak, O., Beumer, J., Wiebrands, K., Seno, H., van Oudenaarden, A., and Clevers, H. (2017). Induced Quiescence of Lgr5+ Stem Cells in Intestinal Organoids Enables Differentiation of Hormone-Producing Enteroendocrine Cells. *Cell Stem Cell* 20, 177–190.
- Beucher, A., Gjernes, E., Collin, C., Courtney, M., Meunier, A., Collombat, P., and Gradwohl, G. (2012). The homeodomain-containing transcription factors Arx and Pax4 control enteroendocrine subtype specification in mice. *PLoS ONE* 7, e36449.
- Beumer, J., Artegiani, B., Post, Y., Reimann, F., Gribble, F., Nguyen, T.N., Zeng, H., Van den Born, M., Van Es, J.H., and Clevers, H. (2018). Enteroendocrine cells switch hormone expression along the crypt-to-villus BMP signalling gradient. *Nat. Cell Biol.* 20, 909–916.
- Darwich, A.S., Aslam, U., Ashcroft, D.M., and Rostami-Hodjegan, A. (2014). Meta-analysis of the turnover of intestinal epithelia in preclinical animal species and humans. *Drug Metab. Dispos.* 42, 2016–2022.
- Du, A., McCracken, K.W., Walp, E.R., Terry, N.A., Klein, T.J., Han, A., Wells, J.M., and May, C.L. (2012). Arx is required for normal enteroendocrine cell development in mice and humans. *Dev. Biol.* 365, 175–188.
- Egerod, K.L., Engelstoft, M.S., Grunddal, K.V., Nøhr, M.K., Secher, A., Sakata, I., Pedersen, J., Windeløv, J.A., Füchtbauer, E.M., Olsen, J., et al. (2012). A major lineage of enteroendocrine cells coexpress CCK, secretin, GIP, GLP-1, PYY, and neurotensin but not somatostatin. *Endocrinology* 153, 5782–5795.
- Gracz, A.D., Samsa, L.A., Fordham, M.J., Trotier, D.C., Zwarycz, B., Lo, Y.H., Bao, K., Starmer, J., Raab, J.R., Shroyer, N.F., et al. (2018). SOX4 Promotes ATOH1-independent Intestinal Secretory Differentiation Toward Tuft and Enteroendocrine Fates. *Gastroenterology* 155, 1508–1523.
- Gribble, F.M., and Reimann, F. (2017). Signalling in the gut endocrine axis. *Physiol. Behav.* 176, 183–188.
- Gross, S., Garofalo, D.C., Balderes, D.A., Mastracci, T.L., Dias, J.M., Perlmann, T., Ericson, J., and Sussel, L. (2016). The novel enterochromaffin marker Lmx1a regulates serotonin biosynthesis in enteroendocrine cell lineages downstream of Nkx2.2. *Development* 143, 2616–2628.
- Grün, D., Lyubimova, A., Kester, L., Wiebrands, K., Basak, O., Sasaki, N., Clevers, H., and van Oudenaarden, A. (2015). Single-cell messenger RNA sequencing reveals rare intestinal cell types. *Nature* 525, 251–255.
- Grün, D., Muraro, M.J., Boisset, J.C., Wiebrands, K., Lyubimova, A., Dharmadhikari, G., van den Born, M., van Es, J., Jansen, E., Clevers, H., et al. (2016). De Novo Prediction of Stem Cell Identity using Single-Cell Transcriptome Data. *Cell Stem Cell* 19, 266–277.

- Haber, A.L., Biton, M., Rogel, N., Herbst, R.H., Shekhar, K., Smillie, C., Burgin, G., Delorey, T.M., Howitt, M.R., Katz, Y., et al. (2017). A single-cell survey of the small intestinal epithelium. *Nature* *551*, 333–339.
- Habib, A.M., Richards, P., Cairns, L.S., Rogers, G.J., Bannon, C.A., Parker, H.E., Morley, T.C., Yeo, G.S., Reimann, F., and Gribble, F.M. (2012). Overlap of endocrine hormone expression in the mouse intestine revealed by transcriptional profiling and flow cytometry. *Endocrinology* *153*, 3054–3065.
- Haghighverdi, L., Büttner, M., Wolf, F.A., Buettner, F., and Theis, F.J. (2016). Diffusion pseudotime robustly reconstructs lineage branching. *Nat. Methods* *13*, 845–848.
- Halpern, K.B., Shenav, R., Matcovitch-Natan, O., Toth, B., Lemze, D., Golan, M., Massasa, E.E., Baydatch, S., Landen, S., Moor, A.E., et al. (2017). Single-cell spatial reconstruction reveals global division of labour in the mammalian liver. *Nature* *542*, 352–356.
- Harris, J.A., Hirokawa, K.E., Sorensen, S.A., Gu, H., Mills, M., Ng, L.L., Bohn, P., Mortrud, M., Ouellette, B., Kidney, J., et al. (2014). Anatomical characterization of Cre driver mice for neural circuit mapping and manipulation. *Front. Neural Circuits* *8*, 76.
- Hashimshony, T., Senderovich, N., Avital, G., Klochendler, A., de Leeuw, Y., Anavy, L., Gennert, D., Li, S., Livak, K.J., Rozenblatt-Rosen, O., et al. (2016). CEL-Seq2: sensitive highly-multiplexed single-cell RNA-Seq. *Genome Biol.* *17*, 77.
- Ireland, H., Kemp, R., Houghton, C., Howard, L., Clarke, A.R., Sansom, O.J., and Winton, D.J. (2004). Inducible Cre-mediated control of gene expression in the murine gastrointestinal tract: effect of loss of beta-catenin. *Gastroenterology* *126*, 1236–1246.
- Kassambara, A. (2018). **ggpubr: 'ggplot2' Based Publication Ready Plots.** Available online: <https://cran.r-project.org/web/packages/ggpubr/index.html>.
- La Manno, G., Soldatov, R., Zeisel, A., Braun, E., Hochgerner, H., Petukhov, V., Lidschreiber, K., Kastrioti, M.E., Lönnberg, P., Furlan, A., et al. (2018). RNA velocity of single cells. *Nature* *560*, 494–498.
- Love, M.I., Huber, W., and Anders, S. (2014). Moderated estimation of fold change and dispersion for RNA-seq data with DESeq2. *Genome Biol.* *15*, 550.
- Mellitzer, G., Beucher, A., Lobstein, V., Michel, P., Robine, S., Kedinger, M., and Gradwohl, G. (2010). Loss of enteroendocrine cells in mice alters lipid absorption and glucose homeostasis and impairs postnatal survival. *J. Clin. Invest.* *120*, 1708–1721.
- Miyatsuka, T., Li, Z., and German, M.S. (2009). Chronology of islet differentiation revealed by temporal cell labeling. *Diabetes* *58*, 1863–1868.
- Muraro, M.J., Dharmadhikari, G., Grun, D., Groen, N., Dielen, T., Jansen, E., van Gurp, L., Engelse, M.A., Carlotti, F., de Koning, E.J., et al. (2016). A Single-Cell Transcriptome Atlas of the Human Pancreas. *Cell Syst.* *3*, 385–394.
- Naya, F.J., Huang, H.P., Qiu, Y., Mutoh, H., DeMayo, F.J., Leiter, A.B., and Tsai, M.J. (1997). Diabetes, defective pancreatic morphogenesis, and abnormal enteroendocrine differentiation in BETA2/neuroD-deficient mice. *Genes Dev.* *11*, 2323–2334.
- Penzo-Méndez, A., Dy, P., Pallavi, B., and Lefebvre, V. (2007). Generation of mice harboring a Sox4 conditional null allele. *Genesis* *45*, 776–780.
- Platt, R.J., Chen, S., Zhou, Y., Yim, M.J., Swiech, L., Kempton, H.R., Dahlman, J.E., Parnas, O., Eisenhaure, T.M., Jovanovic, M., et al. (2014). CRISPR-Cas9 knockin mice for genome editing and cancer modeling. *Cell* *159*, 440–455.
- Sato, T., Vries, R.G., Snippert, H.J., van de Wetering, M., Barker, N., Stange, D.E., van Es, J.H., Abo, A., Kujala, P., Peters, P.J., and Clevers, H. (2009). Single Lgr5 stem cells build crypt-villus structures in vitro without a mesenchymal niche. *Nature* *459*, 262–265.
- Scheele, C.L., Hannezo, E., Muraro, M.J., Zomer, A., Langedijk, N.S., van Oudenaarden, A., Simons, B.D., and van Rheenen, J. (2017). Identity and dynamics of mammary stem cells during branching morphogenesis. *Nature* *542*, 313–317.
- Schonhoff, S.E., Giel-Moloney, M., and Leiter, A.B. (2004). Neurogenin 3-expressing progenitor cells in the gastrointestinal tract differentiate into both endocrine and non-endocrine cell types. *Dev. Biol.* *270*, 443–454.
- Shaner, N.C., Campbell, R.E., Steinbach, P.A., Giepmans, B.N., Palmer, A.E., and Tsien, R.Y. (2004). Improved monomeric red, orange and yellow fluorescent proteins derived from *Discosoma* sp. red fluorescent protein. *Nat. Biotechnol.* *22*, 1567–1572.
- Shaner, N.C., Lambert, G.G., Chamma, A., Ni, Y., Cranfill, P.J., Baird, M.A., Sell, B.R., Allen, J.R., Day, R.N., Israelsson, M., et al. (2013). A bright monomeric green fluorescent protein derived from *Branchiostoma lanceolatum*. *Nat. Methods* *10*, 407–409.
- Soyer, J., Flasse, L., Raffelsberger, W., Beucher, A., Orvain, C., Peers, B., Ravassard, P., Vermot, J., Voz, M.L., Mellitzer, G., and Gradwohl, G. (2010). Rfx6 is an Ngn3-dependent winged helix transcription factor required for pancreatic islet cell development. *Development* *137*, 203–212.
- Suzuki, K., Harada, N., Yamane, S., Nakamura, Y., Sasaki, K., Nasteska, D., Joo, E., Shibue, K., Harada, T., Hamasaki, A., et al. (2013). Transcriptional regulatory factor X6 (Rfx6) increases gastric inhibitory polypeptide (GIP) expression in enteroendocrine K-cells and is involved in GIP hypersecretion in high fat diet-induced obesity. *J. Biol. Chem.* *288*, 1929–1938.
- Tasaki, T., Sriram, S.M., Park, K.S., and Kwon, Y.T. (2012). The N-end rule pathway. *Annu. Rev. Biochem.* *81*, 261–289.
- van den Brink, S.C., Sage, F., Vértessy, Á., Spanjaard, B., Peterson-Maduro, J., Baron, C.S., Robin, C., and van Oudenaarden, A. (2017). Single-cell sequencing reveals dissociation-induced gene expression in tissue subpopulations. *Nat. Methods* *14*, 935–936.
- Wang, S., Hecksher-Sorensen, J., Xu, Y., Zhao, A., Dor, Y., Rosenberg, L., Serup, P., and Gu, G. (2008). Myt1 and Ngn3 form a feed-forward expression loop to promote endocrine islet cell differentiation. *Dev. Biol.* *317*, 531–540.
- Warnes, G.R., Bolker, B., Bonebakker, L., Gentleman, R., Liaw, W.H.A., Lumley, T., Maechler, M., Magnusson, A., Moeller, S., Schwartz, M., et al. (2016). **gplots: Various R Programming Tools for Plotting Data.** Available online: <https://cran.r-project.org/web/packages/gplots/index.html>.
- Wickham, H. (2009). **Ggplot2: elegant graphics for data analysis** (New York: Springer).
- Wickham, H. (2011). **The Split-Apply-Combine Strategy for Data Analysis.** *J. Stat. Soft.* *40*. <https://doi.org/10.18637/jss.v040.i01>.
- Worthington, J.J., Reimann, F., and Gribble, F.M. (2018). Enteroendocrine cells—sensory sentinels of the intestinal environment and orchestrators of mucosal immunity. *Mucosal Immunol.* *11*, 3–20.
- Yan, K.S., Gevaert, O., Zheng, G.X.Y., Anchang, B., Probert, C.S., Larkin, K.A., Davies, P.S., Cheng, Z.F., Kaddis, J.S., Han, A., et al. (2017). Intestinal Enteroendocrine Lineage Cells Possess Homeostatic and Injury-Inducible Stem Cell Activity. *Cell Stem Cell* *21*, 78–90.
- Zhang, J., McKenna, L.B., Bogue, C.W., and Kaestner, K.H. (2014). The diabetes gene Hhex maintains δ -cell differentiation and islet function. *Genes Dev.* *28*, 829–834.

STAR★METHODS

KEY RESOURCES TABLE

REAGENT or RESOURCE	SOURCE	IDENTIFIER
Antibodies		
Ghrelin antibody (C-18)	Santa Cruz	Cat # Sc-10368; RRID:AB_2232479
Chga antibody	Labned.com	Cat # LN1401487
Serotonin antibody	Abcam	Cat # Ab66047; RRID:AB_1142794
Gip antibody	Abcam	Cat # Ab22624; RRID:AB_2109683
Cck antibody (C-20)	Santa Cruz	Cat # Sc-21617; RRID:AB_2072464
Glp1 antibody (C-17)	Santa Cruz	Cat # Sc-7782; RRID:AB_2107325
Sst antibody	Novus biologicals	Cat # NB100-91966; RRID:AB_1217955
Alexa Fluor 568 donkey anti-rabbit IgG (H+L)	Thermo Scientific	Cat # A10042; RRID:AB_2534017
Alexa Fluor 568 donkey anti-goat IgG (H+L)	Thermo Scientific	Cat # A11057; RRID:AB_2534104
Alexa Fluor 488 donkey anti-goat IgG (H+L)	Thermo Scientific	Cat # A11055; RRID:AB_2534102
Alexa Fluor 488 donkey anti-rabbit IgG (H+L)	Thermo Scientific	Cat # A21206; RRID:AB_2535792
Dako EnVision+ System- HRP Labeled Polymer Anti-Rabbit	Dako	Cat # K4003; RRID:AB_2630375
Rabbit anti-Goat bridging antibody	Southern Biotech	Cat # 6160-01
Alexa Fluor 647 phalloidin	Thermo Scientific	Cat # A22287; RRID:AB_2620155
Sox4 antibody	Atlas antibodies	Cat # AMAb91380; RRID:AB_2716661
Neurog3 antibody	Developmental Studies Hybridoma Bank	Cat # F25A1B3; RRID:AB_528401
Tox3 antibody	Sigma Aldrich	Cat # HPA040376; RRID:AB_10795522
Myt1 antibody	Sigma Aldrich	Cat # HPA006303; RRID:AB_1079446
Rfx6 antibody	Millipore	Cat # ABD28; RRID:AB_11205418
Chemicals, Peptides, and Recombinant Proteins		
Advanced DMEM/F12	Thermo Scientific	Cat # 12634-010
EGF	Peptotech	Cat # AF-100-15
Noggin conditioned medium	U-Protein Express	Custom order
R-spondin 1 conditioned medium	In-house production	-
N-Acetylcysteine	Sigma Aldrich	Cat # A9165
IWP-2	Stemgent	Cat # 130-105-335
DAPT	Sigma Aldrich	Cat # D5942
Y-27632	Selleckchem	Cat # S1049
PD0325901	Sigma Aldrich	Cat # PZ0162
BME	Amsbio	Cat # 3533-005-02
DAPI	Thermo Scientific	Cat # D1306
TRIzol	Thermo Scientific	Cat # 15596026
SORT-seq reagents	Muraro et al., 2016	-
HEPES	Thermo Scientific	Cat # 15630-56
Glutamax	Thermo Scientific	Cat # 35050-038
Penicillin/Streptomycin	Thermo Scientific	Cat # 15140-122
B27 Supplement	GIBCO	Cat # 17504-44
TrypLE Express	GIBCO	Cat # 12605036
10x TrypLE Select (10x)	GIBCO	Cat # A1217701
Tissue Freezing Medium	Leica	Cat # 14020108926

(Continued on next page)

Continued		
REAGENT or RESOURCE	SOURCE	IDENTIFIER
Dispase II	Thermo Scientific	Cat # 17105041
EGFP mRNA	Stemgent	Cat # 05-0020
β -Naphthoflavone	Sigma Aldrich	Cat # N3633
Triton X-100	Sigma Aldrich	Cat # X100-100ML
CS&T Research Beads	BD Biosciences	Cat # 650621
ProLong Gold Antifade Mounting Medium with DAPI	Thermo Scientific	Cat # P36935
Critical Commercial Assays		
Thermo Scientific reagents for CEL-Seq2	Hashimshony et al., 2016	N/A
Reagents for library preparation from CEL-Seq2	Hashimshony et al., 2016	N/A
Megashortscript T7 Transcription Kit	Ambion	Cat # AM1354
TransIT mRNA transfection kit	Mirus	Cat # MIR 2225
pGEM-T easy cloning kit	Promega	Cat # A1360
Alexa Fluor 488 Tyramide Superboost kit	invitrogen	Cat # B40941
iQ SybrGreen Supermix	Bio-Rad	Cat # 1708887
Experimental Models: Organisms/Strains		
<i>Neurog3Chrono</i>	This study	Hans Clevers, h.clevers@hubrecht.eu
<i>AhCre</i>	(Ireland et al., 2004)	MGI:3052655
<i>Sox4^{loxP/loxP}</i>	(Penzo-Méndez et al., 2007)	Veronique Lefebvre, lefebvv@ccf.org
<i>Tac1Cre LSL-tdTomato</i>	(Harris et al., 2014)	Hongkui Zeng, hongkuiz@alleninstitute.org
<i>Rosa26-Cas9</i>	J.v.Es and H. Clevers, to be published separately	Hans Clevers, h.clevers@hubrecht.eu
Software and Algorithms		
DESeq2 algorithm	(Love et al., 2014)	http://bioconductor.org/packages/release/bioc/html/DESeq2.html
RacelD2 (StemID) algorithm	(Grün et al., 2016)	https://github.com/dgrun/StemID
ImageJ	NIH	https://imagej.nih.gov/ij/
ggplot2	(Wickham, 2009)	https://cran.r-project.org/web/packages/ggplot2/
ggpubr	Kassambara, 2018	https://cran.r-project.org/web/packages/ggpubr/
plyr	(Wickham, 2011)	https://cran.r-project.org/web/packages/plyr/
gplots	Warnes et al., 2016	https://cran.r-project.org/web/packages/gplots/
R	R Foundation	http://www.r-project.org
destiny & dpt	(Angerer et al., 2016; Haghverdi et al., 2016)	https://bioconductor.org/packages/release/bioc/html/destiny.html
RNA velocity (velocyto)	(La Manno et al., 2018)	http://velocyto.org/
RStudio	RStudio	https://www.rstudio.com
Other		
Appliances needed for SORT-seq	Muraro et al., 2016	N/A
SP8 or SP8X confocal microscope	Leica	N/A
Olympus FV3000 microscope	Leica	N/A
FACSAria II	BD	N/A
Complete Dataset	This study	GEO: GSE113561

CONTACT FOR REAGENT AND RESOURCE SHARING

Further information and requests for reagents and resources should be directed to the Lead Contact, Hans Clevers (h.clevers@hubrecht.eu).

EXPERIMENTAL MODEL AND SUBJECT DETAILS

Mice

Neurog3Chrono mice were generated by homologous recombination in mouse embryonic stem cells. The Chrono-reporter cassette (Figure 1B) was inserted just before the *Neurog3* stop-codon to maintain normal expression of the transcription factor and retain potential regulatory effects of the 3' UTR. Genotyping primers for Neurog3Chrono can be found in the Table S4. Generation and genotyping of AhCre (Ireland et al., 2004), Sox4^{loxP/loxP} (Penzo-Méndez et al., 2007) and Rosa26-Cas9 (J.H.v.E. et al., unpublished data) and Tac1Cre LSL-tdTomato (Harris et al., 2014) animals is/will be described elsewhere. All alleles were maintained on a mixed C57BL/6 background. All mouse experiments were conducted under a project license granted by the Dier Experiment Commissie / Animal Experimentation Committee (DEC) or Central Committee Animal Experimentation (CCD) of the Dutch government and approved by the Hubrecht Institute Animal Welfare Body (IvD). In all experiments animals were aged between 8 and 24 weeks and littermates were used as controls. Homozygous Neurog3Chrono animals/organoids were used for all experiments. Both male and female mice were used, except for isolation of organoids from Rosa26-Cas9 mice. Only male Rosa26-Cas9 organoids were isolated to simplify the knockout of genes located on the X chromosome.

METHODS DETAILS

Isolation of single cells from Neurog3Chrono animals or organoids

Mouse small intestines were harvested, cleaned, flushed with PBS and separated into proximal, medial and distal parts. Pieces were cut open and villi were scraped off with glass slides and processed separately. After repeated washes, the crypt fraction was incubated with 2 mM EDTA in PBS (without Ca²⁺, Mg²⁺) for 30 min to separate crypts from the muscle layer. Subsequently, crypts were mechanically detached, strained, washed and pelleted. The crypt pellet and the washed and pelleted villus fraction were then resuspended in warm TrypLE Express (GIBCO) and digested to single cells at 37°C. Samples were repeatedly taken to avoid over- or under-digestion. Alternatively, pellets were digested for 1.5 min in 10xTrypLE select diluted 1:1 with HBSS with continuous mechanic disruption by pipetting, which generally improves yields but generates larger numbers of doublets. Single cell suspensions were pelleted, washed, strained and resuspended in cold FACS buffer (Advanced DMEM/F12 + 4 mM EDTA).

Neurog3Chrono organoids at 0h, 24h, 48h and 72h after induction of EE differentiation (see “Enterendocrine differentiation of intestinal Organoids” below) were harvested in cold medium, washed and digested to single cells with 10xTrypLE select diluted 1:1 with HBSS with continuous mechanic disruption. Single cell suspensions were pelleted, washed, strained and resuspended in cold FACS buffer (Advanced DMEM/F12 + 4 mM EDTA).

Flow Cytometric Purification

Flow cytometers were calibrated with CS&T beads, to insure reproducibility between experiments. 4',6-diamidino-2-phenylindole (DAPI) was added just before flow sorting. DAPI-negative living cells were sorted into TRIzol reagent (Thermo Scientific) for bulk mRNA-sequencing or into 384-well plates containing 96 or 384 unique molecular identifier (UMI) barcode primer-sets, ERCC92 spike-ins (Agilent) and dNTPs (Promega) for single-cell mRNA-sequencing (SORT-seq) (Muraro et al., 2016) using a FACSaria II (BD). Fluorescence values for all sorted cells were recorded for later analysis. Samples in Trizol or plates were stored at –80°C until further processing.

Establishing and imaging intestinal Organoid cultures

To establish organoids, crypts were isolated as described above, however, crypt pellets were not digested, but resuspended in cold BME and plated at approximately 100 crypts/50 ul drop of BME (see also (Sato et al., 2009)). After 10–20 min in the incubator, full growth medium was added. Growth medium consists of Advanced DMEM/F12 with 50 ng/mL EGF (Peprotech), 5% R-spondin 1 conditioned medium (made in-house), 1% Noggin conditioned medium (U Protein Express), 1x B27 (GIBCO) and 1.25 mM n-Acetylcysteine (Sigma Aldrich). Organoids were maintained at 37°C and medium was changed twice a week. Cultures were split weekly at 1:4 ratio by mechanical disruption of organoids.

For imaging spontaneous enteroendocrine differentiation in Neurog3Chrono organoids, cultures were split and seeded in BME at low density on glass bottom plates three days prior to image acquisition. To reduce potential background, we used phenol-free growth medium. Organoids were imaged for 96 on a Leica SP8 confocal microscope. Data for the fluorescence-time conversion dataset were collected in intervals of 45 min between recorded z stacks of individual organoids in 3 independent experiments.

Imaging of Tac1Cre-LSL-tdTomato mice was performed in the same fashion but imaging was started 3h after induction of EE differentiation and continued for 120h at 30 min intervals.

Preparation of intestinal tissue for imaging

For detection of reporter fluorescence, intestines from Neurog3Chrono animals were harvested and flushed with cold PBS. Subsequently, freshly prepared 4% PFA was flushed through the intestine and the tissue was fixed for 15 min at room temperature. Subsequently, tissue was washed with PBS, flushed with diluted Tissue Freezing Medium (Leica) and frozen in undiluted tissue Freezing Medium (Leica). Sections were cut on a cryotome and mounted with ProLong Gold Antifade Mounting Medium with DAPI (Thermo

Scientific). Alternatively, fixed intestines were embedded in UltraPure Low Melting Point Agarose (Thermo Fischer Scientific) and cut on a Microm HM 650V vibratome. Sections were blocked, incubated with primary antibody overnight and stained with secondary antibodies for 2h on the following day. Finally, sections were mounted with ProLong Gold Antifade Mounting Medium with DAPI (Thermo Scientific) and imaged on a Leica SP8 confocal microscope.

For crypt reconstruction the intestines were dissected, rinsed twice with ice-cold 4% paraformaldehyde, and incubated for 2h in 4% paraformaldehyde. The intestine was then washed with PBT (PBS, 0.1% Tween), dissected into pieces of 5 × 7 mm, and incubated overnight at 4°C with Alexa Fluor-647 Phalloidin (Thermo Fischer Scientific). The following day, the pieces were washed and embedded in 4% UltraPure Low Melting Point Agarose (Thermo Fischer Scientific) before 3D imaging using an Olympus FV3000 confocal microscope.

For immunohistochemistry intestines were fixed overnight in Formalin, dehydrated using ethanol and embedded in paraffin. 4 μm-sections were processed using standard methods and antigen retrieval was performed using citrate buffer (pH 6.0). Dewaxed sections were blocked, incubated with primary antibody overnight at 4°C and then incubated for 1 hour at room temperature with BrightVision poly-HRT anti-rabbit (Immunologic). For primary goat antibodies, a rabbit-anti-goat bridging antibody (1h, room temperature) was used in an intermediate step. Immunoreactivity was visualized using 3,3'-diaminobenzidine (DAB).

For immunofluorescent co-staining of SOX4 and NEUROG3 on paraffin sections, samples were processed as other paraffin samples above with the following changes: primary antibody incubation of highly diluted Neurog3 antibody (1:500) was followed by signal amplification with the Alexa Fluor 488 Tyramide Superboost kit (Invitrogen). Subsequently, SOX4 staining was performed as other immunofluorescent stainings above. This step was necessary since Neurog3 and Sox4 antibody are of mouse origin. Absence of false-positive SOX4 signal in NEUROG3 positive cells was confirmed in tissue sections from Sox4 KO mice (see also [Figure S7B](#)).

In vitro-transcription of gRNAs

Two independent gRNAs targeting candidate genes were designed with the CRISPR Design Tool (<http://crispr.mit.edu/>). Oligos ([Table S4](#)) were synthesized and annealed with a common oligo containing a T7 promoter. Strands were filled in with T4 DNA polymerase (NEB), PCR amplified with Phusion high-fidelity polymerase (NEB) and purified. The resulting amplified DNA was sequenced to confirm correct assembly. 200 ng PCR product were *in vitro* transcribed using the Megashortscript T7 transcription kit (Ambion) following the manufacturer's instructions. Finally, gRNAs were purified using an RNeasy mini kit (QIAGEN) and a modified protocol for small RNAs (QIAGEN Supplementary Protocol: Purification of total RNA containing miRNA from animal cells using the RNeasy Plus Mini Kit).

CRISPR-Cas9 mediated knockout in intestinal organoids

Proximal small intestinal organoids were isolated from male Rosa26-Cas9 animals as described above and cultured for several weeks. 4 days after the last split organoids were harvested and digested to single cells with TripLE (GIBCO). *In vitro* transcribed gRNA (170 ng) was mixed with GFP mRNA (80 ng, Stemgent) in OptiMem (GIBCO) and TransIT mRNA transfection (Mirus) components according to the manufacturer's instructions. RNA complexes were added to organoid single-cell suspensions in growth medium supplemented with 10 μM Y-27632 (Selleckchem) in 96-well plates (approximately 50,000 cells/well) and incubated for 4h at 37°C. After the incubation time, cells were resuspended, strained and GFP positive cells were isolated by FACS. GFP positive single-cells were spun down, seeded at low density in BME and grown into organoids by addition of 50% Wnt conditioned medium (in-house production) and 10 μM Y-27632 (Selleckchem) to the full growth medium for the first 4 days. For every gRNA 16 clones were picked, expanded and genotyped by amplification of the region of interest by PCR and cloning of the PCR products into pGEM-T easy (Promega). Resulting vectors were analyzed by Sanger sequencing to identify potential indels in both Allels of each clone. Clones with confirmed out-of-frame insertions or deletions in both Allels were selected and used for further experiments. All clones were compared to mock-transfected wild-type organoids that underwent the same cloning procedure and were derived from the same organoid isolation.

Enteroendocrine differentiation of intestinal Organoids

Intestinal organoids were switched to enteroendocrine differentiation medium ([Basak et al., 2017](#)) 4 days after their last split. Enteroendocrine differentiation medium contains normal growth medium supplemented with 5 μM IWP-2 (Stemgent), 10 μM DAPT (Sigma Aldrich) and 1 μM MEK inhibitor (PD0325901, Sigma Aldrich). 48h after start of differentiation medium was renewed.

For RNA isolation organoids were lysed in 350ul Buffer RLT (RNeasy mini kit (QIAGEN)) and processed following the manufacturer's instructions. For whole-mount stainings, BME was digested by addition of 2 U/mL Dispase II (Thermo) to growth medium for 1h and removed by subsequent repeated washes with cold medium. Then, organoids were incubated in 4% freshly prepared PFA for 30 min, permeabilized with 0.5% Triton X-100 (Sigma) for 20 min and stored in PBS with 1% BSA at 4°C until stained.

Whole-mount staining of intestinal organoids

Organoids were blocked with 1% BSA at room temperature for 1 hour and incubated with primary antibodies in blocking solution overnight. The next day, organoids were washed and incubated with secondary antibody for 1h at room temperature. After washing, organoids were placed in glass-bottom 96-well plates in PBS and imaged on an inverted SP8 confocal microscope (Leica).

Deletion of Sox4 in AhCre x Sox4^{loxP/loxP} animals

For conditional deletion of Sox4, AhCre x Sox4^{loxP/loxP} and Cre-negative Sox4^{loxP/loxP} littermates were treated with 4 injections of 100 μ l (10 mg/mL) β -Naphthoflavone (Sigma Aldrich) at 4 day intervals. 3 days after the last injection, mouse intestines were harvested and fixed in Formalin or processed for RNA isolation.

Messenger RNA Sequencing

Bulk or single cell samples were lysed, barcoded and processed according to the CEL-Seq2 technique (Grün et al., 2016; Hashimshony et al., 2016; Muraro et al., 2016). In short, bulk samples were sorted into TRIzol and RNA was isolated following the manufacturer's instruction with the exception of adding 2 μ g GlycoBlue (Ambion) overnight at -80°C to precipitate RNA. After removal of supernatants RNA precipitates were dissolved in reverse transcription reaction mix (Invitrogen), UMI barcode primers and dNTPs (Promega) were added and the reaction was incubated at 70°C for 2 min. For single-cell mRNA-sequencing, cells were sorted into 384 well plates, containing UMI barcode primers, frozen and incubated at 65°C for 5 min to ensure lysis. First and second strand synthesis (Invitrogen) was performed and all wells of a single plate were pooled. After *in vitro* transcription (Ambion), the amplified RNA was reverse transcribed and amplified for 10-12 cycles with Illumina Truseq primers. Finally, libraries were analyzed on an Illumina NextSeq500 using 75-bp pair-end sequencing.

QUANTIFICATION AND STATISTICAL ANALYSIS

Quantification of decay dynamics of Neurog3Chrono

z stacks taken by confocal live imaging of Neurog3Chrono organoids (25 cells in 8 organoids in 3 independent experiments with identical settings) were summed and reporter positive cells were identified and semi-automatically traced and measured over time in ImageJ. Cells that could not be clearly separated from fluorescent neighbors were excluded from the analysis. Fluorescence raw data was imported into R and normalized per cell after background subtraction (based on the background signal of each individual frame). Cell data were aligned in time based on peak mNeonGreen fluorescence. Time-dependent mean fluorescence and 95% confidence intervals were calculated and depicted in Figure 1F. To compare protein stability of each color, mean fluorescence decay rates after peak fluorescence of each color were compared and approximated by linear regression.

Fluorescence time conversion

Reference fluorescence values (see "Quantification of decay dynamics of Neurog3Chrono") for mNeonGreen and dTomato from live-imaged Neurog3Chrono organoids were normalized relative to maximum intensity in each channel and log transformed. Fluorescence values from flow cytometry (see "Flow Cytometric Purification") were equally normalized and log transformed and subsequently overlaid and aligned with the reference data. On the resulting mNeonGreen versus dTomato intensity graph (which resembles the original mNeonGreen versus dTomato flow cytometry plot with overlaid reference data) the central point in the reference value distribution is chosen. The angle between the vector (centerpoint to datapoint) and the vector $(-1, -1)$ was determined for each reference datapoint and each point of flow cytometry data. Since the time value of each reference datapoint was known, a correlation between angle and time could be established and fitted by non-linear regression to a logistic curve. All unknown time values for flow cytometry datapoints were then interpolated.

Quantification of Tac1Cre-LSL-tdTomato organoids

z stacks for each time point were analyzed with the ImageJ Plugin 3D Object counter (included in Fiji). The object detection cutoff was set to 400 to exclude small fluorescent bodies, such as apoptotic remnants. The volume of tdTomato positive voxels was summed per time point, normalized to maximum values and plotted against time.

Quantification of enteroendocrine cell migration

Crypt axes were established and the relative position of Neurog3Chrono-positive cells between crypt bottom and crypt top along the crypt axes was semi-automatically measured in ImageJ. Fluorescence values (mNeonGreen and dTomato) of each individual cell were quantified and used to calculate time as described above.

Bioinformatics Analysis

For detailed information on DNA library preparation, sequencing, mapping to the mouse reference genome and quantification of transcript abundance please refer to (Muraro et al., 2016).

Bulk sequencing libraries were analyzed using the DESeq2 package (Love et al., 2014). Time-gate specific genes were determined by differential gene expression analysis ($p < 0.01$, $\log_2\text{FC} > 1.5$) comparing each time-gate against all others and including potential batch-effects in the model design.

For single cell analysis, cell clusters and expression comparisons between clusters were generated using the RaceID2 algorithm (Grün et al., 2016). For initial cell type analysis (Figure 3A), single-cell libraries were normalized by downsampling to a minimum number of 2,000 unique transcripts/cell. After an initial RaceID2 run cell clusters enriched for *Kcnq1ot1*, an indicator for necrotic cells and low quality RNA, were removed from the dataset. Likewise, cells with high auto-fluorescence (according to Index sort files) or raw

transcript counts higher than 1.5 times the interquartile range above the upper quartile of the rest of the population were removed as potential doublets. Mitochondrial genes, ERCC92 spike-ins as well as genes associated with clustering artifacts (*Rn45s*, *Malat1*, *Kcnq1ot1*, *A630089N07Rik*, and *Gm17821*) were excluded from the final dataset (Grün et al., 2015; Scheele et al., 2017). RaceID2 was re-run with gap statistics to generate the 2281 cell dataset presented in Figure 3A (RaceID2 settings: MinThresh = 2000, minexpr = 5, minnumber = 2, outminc = 5, probthr = 10^{-4} , outlg = 4). For presentation in the overview figure clusters of the same celltype were merged. For detailed analysis of subpopulations the following clustering parameters were used: Figure 5A (MinThresh = 5000, minexpr = 5, minnumber = 2, outminc = 5, probthr = 10^{-3} , outlg = 2), Figure 5F (MinThresh = 4000, minexpr = 5, minnumber = 2, outminc = 5, probthr = 10^{-4} , outlg = 4). For clustering the combined tissue-organoid dataset the following settings were used: Figure S7B (MinThresh = 4000, minexpr = 5, minnumber = 2, outminc = 5, probthr = 10^{-4} , outlg = 4)

Differentially expressed genes between clusters or cell subsets were determined as described in (Muraro et al., 2016). In short, a negative binomial distribution was calculated reflecting the gene expression variability within each cluster based on the background model for the expected transcript count variability. With these distributions p values were calculated and corrected for multiple testing by the Benjamini-Hochberg method. Cutoffs for adjusted p values and fold changes are given in the corresponding figure legend.

For diffusion map analysis, data were normalized via RaceID2 (as above, min. Threshold of 4000 unique transcripts/cell) and analyzed by principal component analysis. Diffusion components were then calculated from principal components and displayed in 2- or 3-dimensional diffusion maps.

For gene expression analysis in a lineage over time (e.g., Figure 6A), cells of all clusters associated with the lineage in question were arranged according to their age after peak NEUROG3 expression. Temporal outliers were identified (all cells of the previous cluster older than the 33% time quantile of the subsequent cluster) and excluded from the analysis. The expression profile of an individual gene in a particular lineage over time was then generated by Loess regression on normalized unique transcript counts of each individual cell along the time axis. Transcriptional regulators were identified by comparison to all genes associated with UniProt: KW-0805. Only genes that showed at least 80% modulation in amplitude of the Loess smoothed mean and had a minimal mean expression level of 0.9 were included in the list of modulated transcriptional regulators.

For RNA velocity analysis, Fastq files were trimmed with TrimGalore-0.4.3 and mapped with STAR-2.5.3a to the mouse reference genome (mm10). Introns and exons were extracted from the corresponding annotation files. Analysis was performed according to (La Manno et al., 2018). In short, spliced and unspliced unique transcript counts of the gene (e.g., *Chgb*) and cell population (e.g., EC cells) in question were extracted and plotted as a phase diagram. The gamma parameter was fit by least-squares using an extreme quantile fit. Unspliced (u) residuals were then calculated for every cell and plotted on a tSNE map.

All bioinformatics analysis was performed using R version 3.4.0 (R Foundation, <https://www.r-project.org>) and RStudio version 1.0.143 (<https://www.rstudio.com>).

Statistics

No statistical methods were used to predetermine sample size. The experiments were not randomized and the investigators were not blinded to the sample allocation during experiments and outcome assessment. No animals were excluded from analysis. All data are presented as mean \pm standard deviation (SD), unless stated otherwise. Statistically significant differences between wild-type and knockout clones were determined using an unpaired two-tailed Student's t test. Data was obtained from at least two independent clones per knocked out gene and from at least two independent experiments to ensure reproducibility. All statistical analyses were performed using R version 3.4.0 (R Foundation, <https://www.r-project.org>) and RStudio version 1.0.143 (<https://www.rstudio.com>).

DATA AND SOFTWARE AVAILABILITY

Data Resources

Differentially expressed genes between sorting gates (Figure 2A) are provided in Table S1. A chronologically ordered list of transcriptional regulators in each lineage is provided in Table S2. Differentially expressed genes between mature cell clusters are provided in Table S3. RNA-sequencing data, time information, and fluorescence data are available under Gene Expression Omnibus ID GEO: GSE113561.

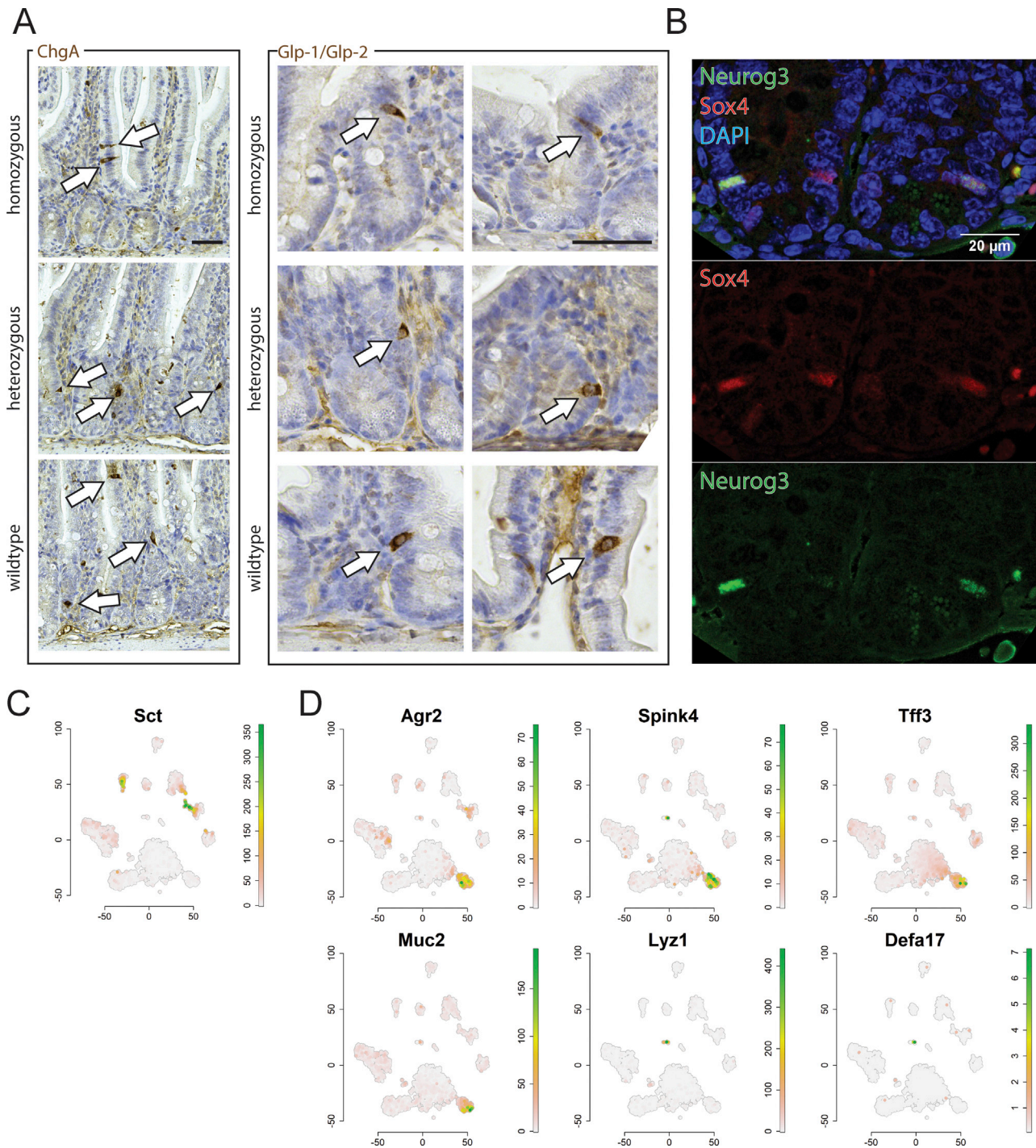


Figure S1. Confirmation of Neurog3 Function and Candidate Gene Identification, Related to Figures 1, 2, and 3

(A) Immunohistochemistry for CHGA and GLP1 in the proximal intestine of wild-type, heterozygous and homozygous Neurog3Chromo animals. Arrows indicate stained cells. (scale bar, 50 μ m).

(B) Immunofluorescent co-staining of NEUROG3 and SOX4 in mouse small intestine.

(C) tSNE map indicating expression of Secretin (Sct). Numbers represent normalized unique transcript counts.

(D) tSNE map indicating expression of goblet cell and Paneth cell markers. Numbers represent normalized unique transcript counts.

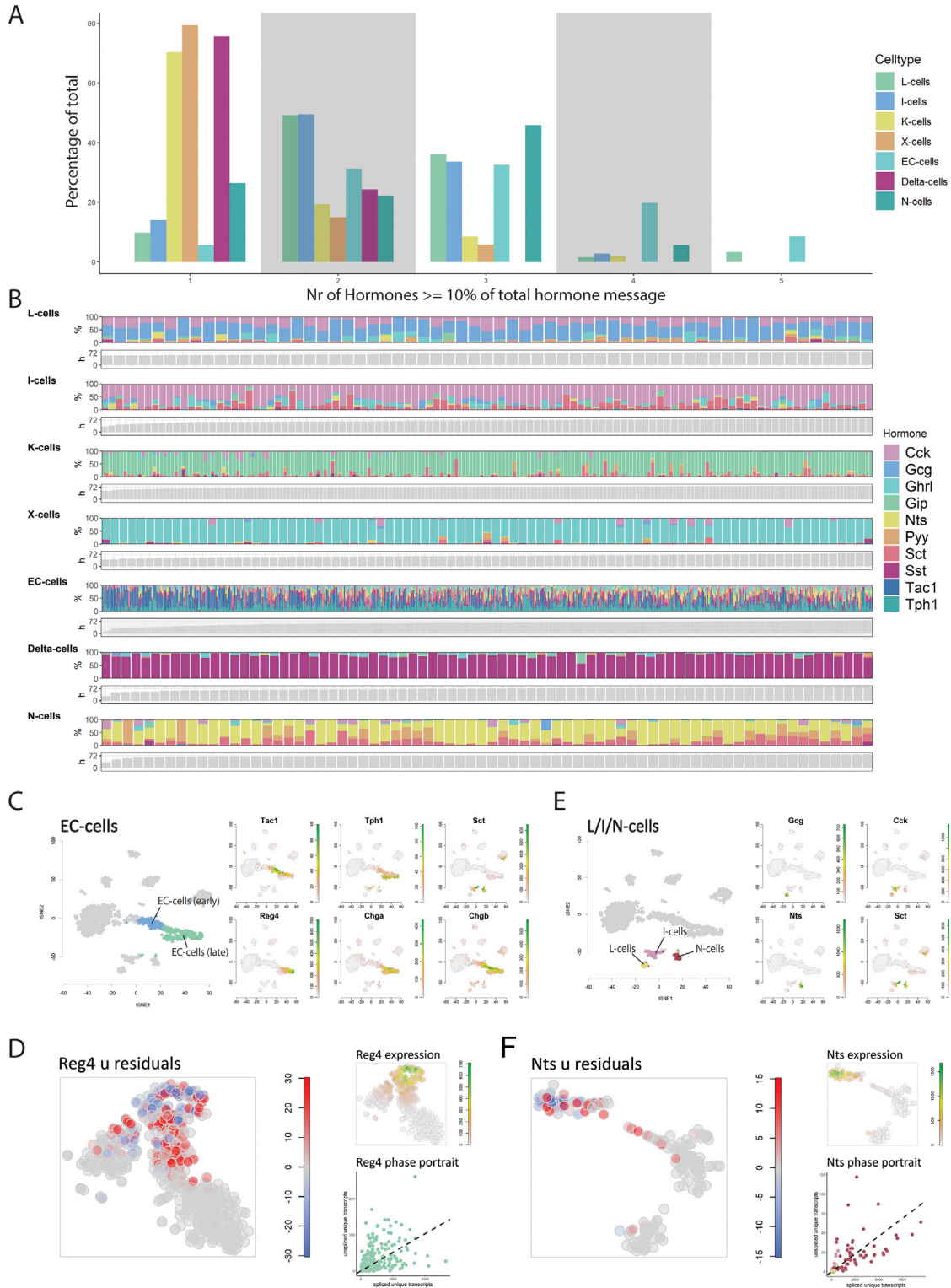


Figure S2. Hormonal Plasticity in the Course of EE Maturation, Related to Figure 4

(A) Quantification of hormonal co-expression in EE cells. The x-Axis indicates the number of different hormones with a contribution of at least 10% to the combined hormonal transcripts in a cell. The y-Axis indicates the percentage of all cells of the same lineage.

(B) Relative contribution of individual hormones to the total hormonal transcript pool in individual cells ordered in time. Please note that apparent higher fluctuations in the EC lineage are due to the generally lower expression of *Tac1/Tph1* when compared to other peptide hormones.

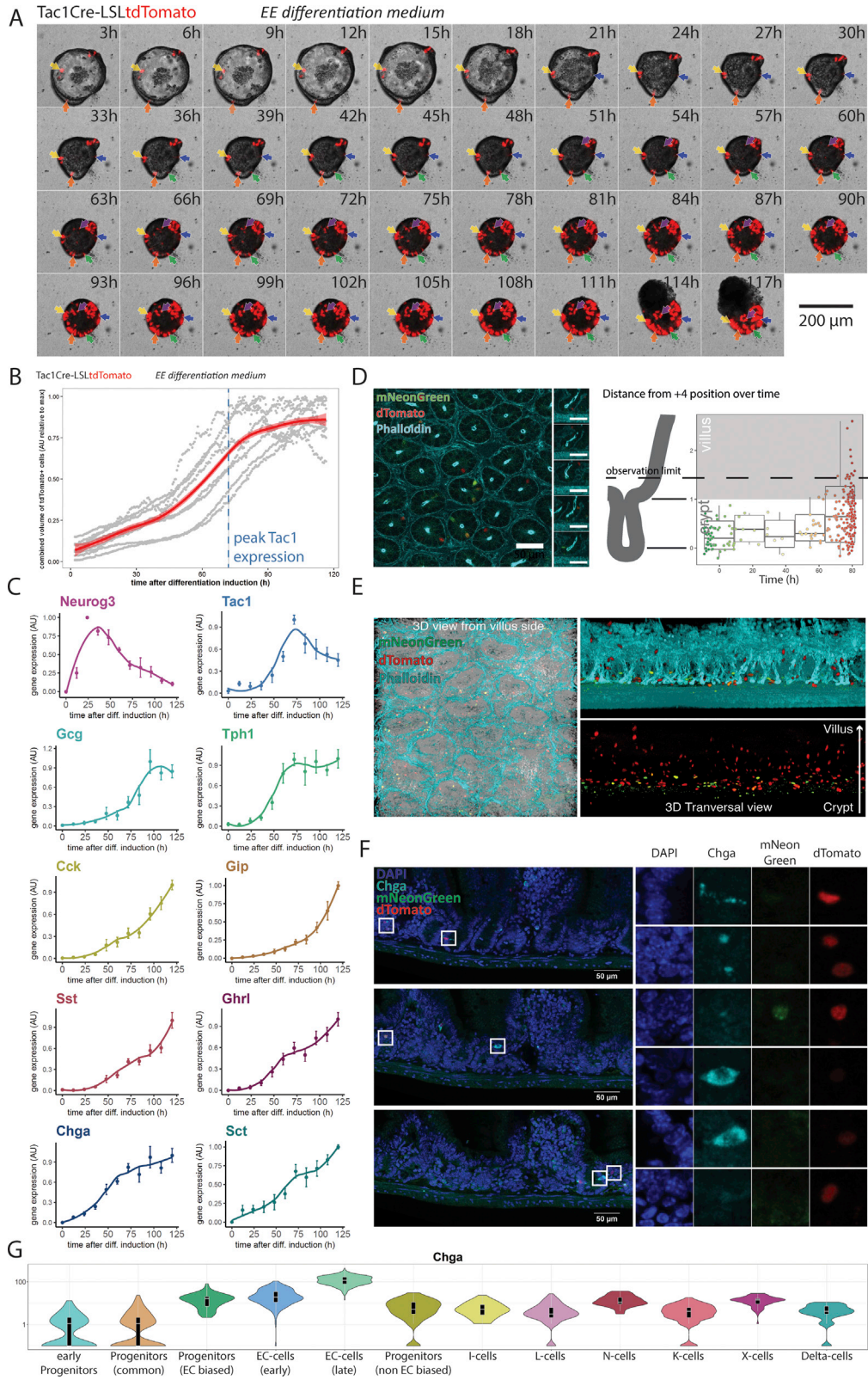
(legend continued on next page)

(C) tSNE map of EC clusters and EC markers after clustering with a raised threshold of 4000 normalized unique transcripts/cell.

(D) tSNE map of 461 early and late EC cells (min. 4000 unique transcripts/cell) (top-left, related to [Fig. 4E](#)), expression levels of *Reg4* (top-right, normalized unique transcript counts), Phase portrait (bottom-right) showing regions of increasing (over dotted line) or decreasing (under dotted line) expression based on unspliced/spliced mRNA balance (colors correspond to clusters), Unspliced unique transcript count residuals projected on the tSNE map (red indicates high relative levels of unspliced mRNA = begin of gene expression, blue indicates low relative levels of unspliced mRNA = downregulation of gene expression, left).

(E) tSNE map of L-, I- and N-cell clusters and hormonal products after clustering with a raised threshold of 4000 normalized unique transcripts/cell.

(F) as (D) but for *Nts* mRNA in LIN cells (related to [Fig. 4H](#)).



(legend on next page)

Figure S3. Organoid Differentiation Dynamics and Migratory Behavior of EE cells *In Vivo*, Related to Figure 4

(A) Live imaging of Tac1Cre LSL-tdTomato small intestinal organoids. EE differentiation was started at $t = 0$ h. Arrows track individual tdTomato positive cells over time.

(B and C) (B) Combined volume of Tac1Cre LSL-tdTomato positive cells over time during EE differentiation; the red line indicates loess smoothed means with 99% confidence interval; the blue line marks the time point of maximal *Tac1* expression according to (C) hormone expression during a 120h, 12h interval EE differentiation time course in organoids (qPCR, mean values relative to max +/- SEM).

(D) (Left) Confocal image of cleared Neurog3Chrono SI crypts. Green and red mark reporter fluorescence. Phalloidin stain outlines crypt structure in turquoise. Small images represent 3D reconstructed side view for positional quantification. (right) Quantification of the distance of Neurog3Chrono positive cells from the bottom of the crypt. 0 indicates the inner crypt bottom, 1 the transition point to the villus ($n = 253$ cells).

(E) 3D reconstruction of Neurog3Chrono crypts.

(F) Immune-fluorescent staining for CHGA in small intestine vibratome sections of homozygous Neurog3Chrono mice.

(G) Expression of CHGA in all EE populations of the high sensitivity EE single cell dataset (min. 4000 unique transcripts/cell). Numbers indicate unique transcripts + 0.1.

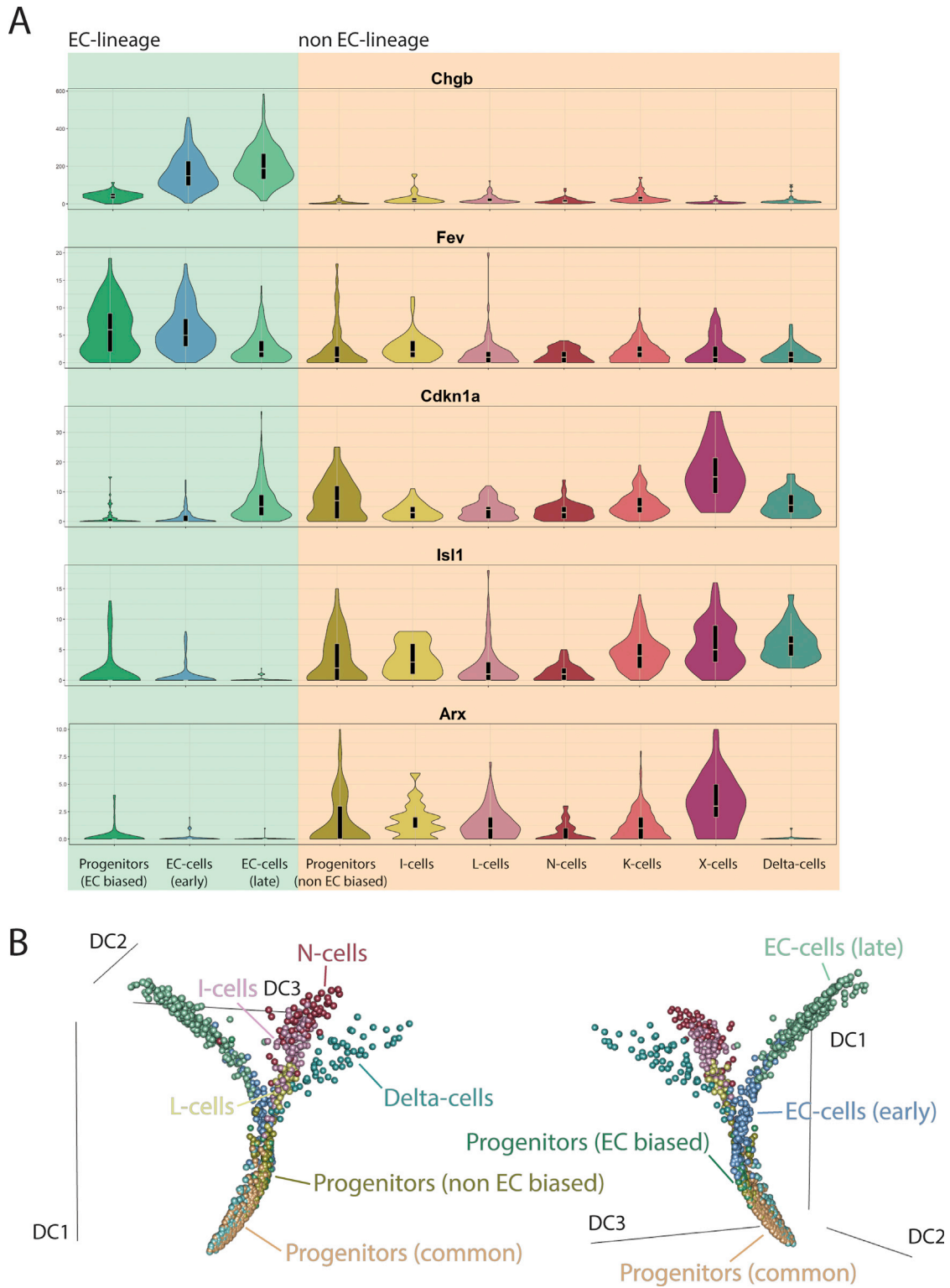


Figure S4. Characteristics of Individual EE Lineages, Related to Figure 5

(A) Violin/Boxplots of genes differentially expressed between EC and non-EC lineages. Numbers indicate normalized unique transcript counts.

(B) Diffusion map visualization showing all EE progenitors in combination with all cells of the EC, ILN- and Delta-cell lineages (min. 4000 unique transcripts/cell).

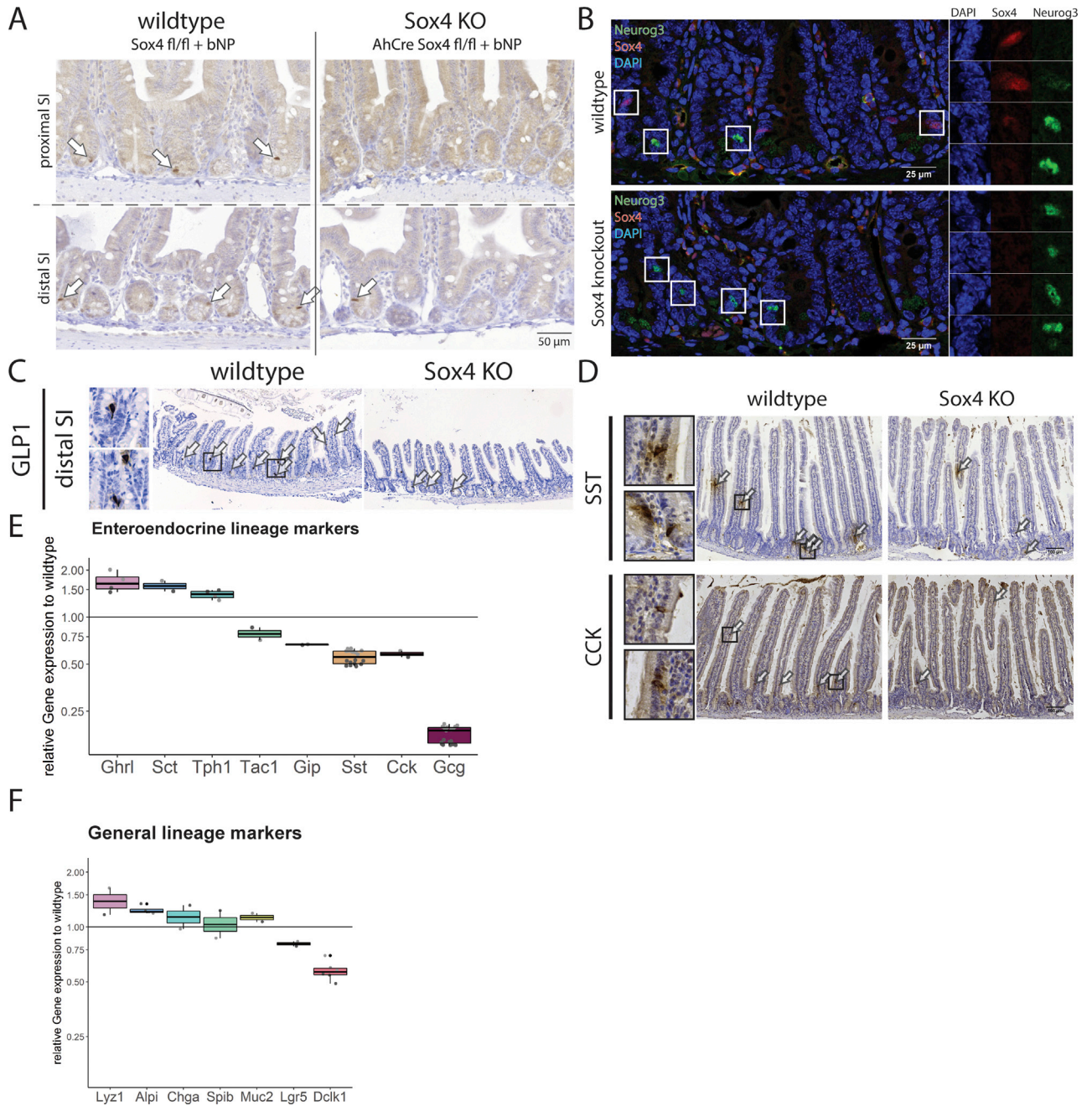


Figure S6. Confirmation of Sox4 as EE Regulator, Related to Figure 7

(A) Immunohistochemistry staining for SOX4 in proximal and distal SI in wild-type and Sox4 KO mice.
 (B) Immunofluorescent co-staining of NEUROG3 and Sox4 in proximal small intestine of wild-type and Sox4 KO mice.
 (C) Immunohistochemistry staining for GLP1 in distal SI of wild-type and Sox4 KO mice.
 (D) Immunohistochemical detection of SST and CCK in the proximal intestine of the indicated genotypes.
 (E and F) (E) EE and (F) general marker expression measured in microarray of wild-type and Sox4 knockout small intestinal RNA. Expression levels are denoted relative to wild-type. Dots mark independent probes; dot color distinguishes independent experiments.

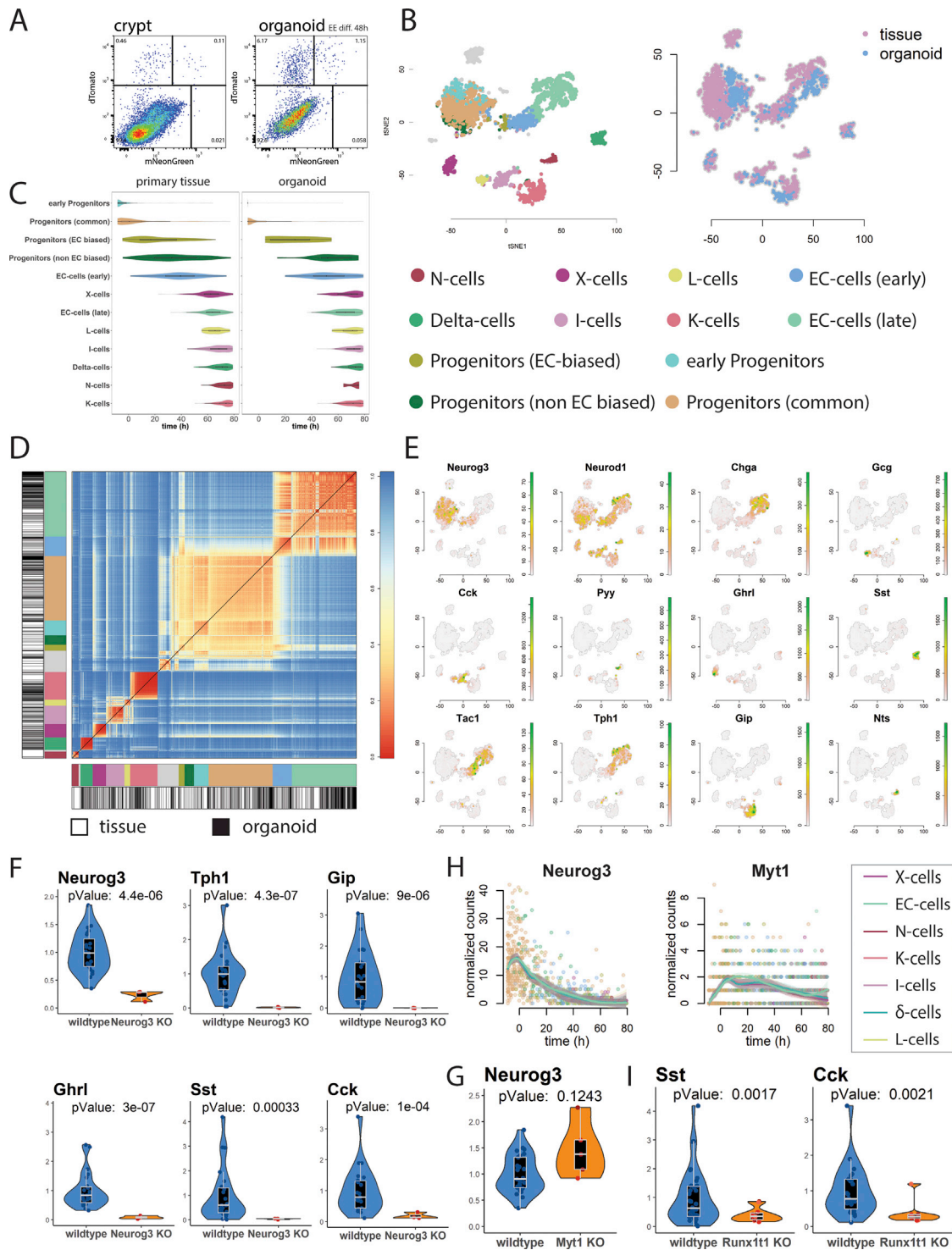


Figure S7. Confirmation of Candidate Genes in Intestinal Organoids, Related to Figure 7

(A) Comparative flow cytometry of isolated small intestinal crypt cells of homozygous *Neurog3*Chrono mice and cells from homozygous *Neurog3*Chrono organoids 48h after start of EE differentiation.

(B) tSNE map of a combined dataset of 1750 *Neurog3*Chrono positive cells and 950 *Neurog3*Chrono positive cells from intestinal organoids sorted 0h, 24h, 48h and 72h after induction of differentiation. (left) cluster identity (right) cell origin.

(C) Violin/Boxplots of time distribution within clusters in (B) separated by cell origin.

(D) Cluster-heatmap corresponding to (B) with annotated cluster identity and cell origin.

(legend continued on next page)

(E) tSNE maps indicating expression of EE marker genes. Numbers represent normalized unique transcript counts.

(F) mRNA expression of indicated genes in *Neurog3* knockout organoids measured by qPCR relative to mean expression of all wild-type clones. Points denote independent experiments.

(G) mRNA expression of *Neurog3* in 2 independent *Myt1* knockout clones (point color) measured by qPCR relative to mean expression of all wild-type clones.

(H) Lineage-resolved expression profiles of *Neurog3* and *Myt1*. Colored lines represent lineage-specific Loess-smoothed expression means. Numbers indicate normalized unique transcript counts.

(I) mRNA expression of indicated genes in 3 independent *Runx1t1* knockout clones (point color) measured by qPCR relative to mean expression of all wild-type clones.

Statistical significance for (F, G and I) was determined by unpaired Student's t-test.

Enteroendocrine cells switch hormone expression along the crypt-to-villus BMP signalling gradient

Joep Beumer¹, Benedetta Artegiani^{1,2}, Yorick Post¹, Frank Reimann³, Fiona Gribble³, Thuc Nghi Nguyen⁴, Hongkui Zeng⁴, Maaïke Van den Born^{1,2}, Johan H. Van Es^{1,2} and Hans Clevers^{1,2*}

Enteroendocrine cells (EECs) control a wide range of physiological processes linked to metabolism¹. We show that EEC hormones are differentially expressed between crypts (for example, Glp1) and villi (for example, secretin). As demonstrated by single-cell mRNA sequencing using murine Lgr5⁺ cell-derived organoids, BMP4 signals alter the hormone expression profiles of individual EECs to resemble those found in the villus. Accordingly, BMP4 induces hormone switching of EECs migrating up the crypt–villus axis in vivo. Our findings imply that EEC lineages in the small intestine exhibit a more flexible hormone repertoire than previously proposed. We also describe a protocol to generate human EECs in organoids and demonstrate a similar regulation of hormone expression by BMP signalling. These findings establish alternative strategies to target EECs with therapeutically relevant hormone production through BMP modulation.

Intestinal enteroendocrine cells (EECs) constitute the largest hormone-producing organ in mammals and are classified according to their hormone products¹. Enterochromaffin cells (ECs) produce serotonin, a regulator of intestinal motility, and tachykinin 1 (Tac1, substance P), a peptide involved in muscle contraction and inflammation². L cells produce Glp1, an inducer of insulin release encoded by the glucagon (*Gcg*) gene, and can co-express *Pyy*¹. Other EEC subtypes include gastric inhibitory protein (*Gip*)-producing K cells, somatostatin (*Sst*)-producing D cells, cholecystokinin (*Cck*)-producing I cells, neurotensin (*Nts*)-producing N cells and secretin (*Sct*)-producing S cells¹. Although this classification suggests well-defined, distinct EEC subtypes, these hormones are often co-expressed, suggesting considerable overlap between lineages^{3,4}. As is the case for all cell types of the intestinal epithelium, the short-lived EECs are constitutively produced by Lgr5⁺ crypt stem cells⁵. Lgr5 stem cells can be cultured to generate epithelial organoids that faithfully recapitulate gut epithelial biology⁶. Single-cell messenger RNA sequencing (scRNA-seq) has shown that a complete set of EECs subtypes is produced in these mini-guts, including some that had previously gone unnoticed in intact gut^{7,8}. However, extrinsic factors that control EEC subtype identity have remained largely unknown.

Previous work has suggested that EECs expressing Tac1 and Glp1 are restricted to crypts, whereas *Sct*-, *Pyy*- and *Nts*-producing EECs are enriched in villi^{9,10}. In agreement with these studies, we found that ileal L cells co-express Glp1 and *Pyy* in the crypt, but mostly lack Glp1 in the villus (Fig. 1a–c and Supplementary Fig. 1a). Serotonin-producing ECs occurred along the length of the crypt–villus axis, but selectively co-expressed Tac1 in the crypt and *Sct* in the villus (Fig. 1d,e and Supplementary Fig. 1a). To

address whether hormone switching occurs during migration of EECs along the crypt–villus axis, we analysed intestines from *Tac1^{iresCre}/Rosa^{tdTomato}* mice, an allele that faithfully labels all Tac1⁺/Serotonin⁺ cells in the crypt (Fig. 1f)¹¹. In adult intestines, almost all serotonin⁺ cells were marked by tdTomato (Fig. 1g). Importantly, >55% of *Sct*⁺ cells on villi were also traced, while being negative for Tac1 (Fig. 1f,g and Supplementary Fig. 1b). The rarity of tdTomato⁺ cells that were negative for serotonin suggests that ECs do not lose serotonin during their lifetime to become single *Sct*⁺ as previously suggested^{9,12}. Serotonin-negative *Sct*⁺ cells not traced by Tac1 must thus be part of another EEC lineage. EECs producing other hormones, including *Cck*, *Gip* and *Sst*, were only rarely derived from Tac1⁺ progenitors (Fig. 1g and Supplementary Fig. 1b). These data imply lineage relationships between crypt and villus EECs; that is, that Tac1⁻/*Sct*⁺ ECs on villi derive from Tac1⁺ crypt ECs. This, in turn, suggests that local niche signals can induce shifts in hormone expression.

Multiple signalling gradients exist along the crypt–villus axis; for example, Wnt levels are high at the crypt base, while BMP is highest at the villus tips^{13,14}. In murine intestinal organoids, EECs are induced through inhibition of the Wnt, MAPK and Notch signalling pathways, in the presence of the BMP inhibitor Noggin⁸. We used this differentiation system as a starting point to modulate selected signalling pathways⁸, while monitoring *Sct* and *Gcg* as a proxy of the villus- and crypt-hormone signatures, respectively. Strikingly, we observed that all ECs in this culture co-expressed serotonin and Tac1, while *Sct* was absent (Fig. 2a). This suggests that niche signals acting on EECs are dominant over a default, temporal differentiation process. Manipulation of the Wnt, TGF- β and Hedgehog pathways did either reduce both *Gcg* and *Sct* transcripts, or had no significant effect on any assessed hormone (Supplementary Fig. 2a). We replaced Noggin by BMP4 in this EEC differentiation cocktail ('EEC BMP^{high}' medium), generating cells immunoreactive for *Sct*, as well as ECs lacking Tac1 (Fig. 2a,b). Glp1⁺ cell numbers and total levels of secreted Glp1 were greatly diminished (Fig. 2a–c and Supplementary Fig. 2b). We next performed bulk RNA-seq on duodenal and ileal organoids stimulated with EEC BMP^{high} or EEC BMP^{low} media (Fig. 2d), and validated the expression of selected genes by quantitative PCR (PCR; Fig. 2e). EEC markers that are homogeneously distributed on crypts and villi (*Chga*, *Tph1* (enzyme catalysing serotonin production), *Cck* and duodenal *Gip*) are only mildly affected by BMP activation (Fig. 2d,e). We did observe an increase in *Sct* and a minor upregulation of *Pyy* and *Nts* (Fig. 2d,e), which are expressed at the highest levels in the villus¹⁰. *Sct* is enriched

¹Hubrecht Institute, Royal Netherlands Academy of Arts and Sciences, University Medical Center Utrecht, Utrecht, the Netherlands. ²Oncode Institute, Utrecht, the Netherlands. ³Metabolic Research Laboratories, Wellcome Trust-MRC Institute of Metabolic Science, Addenbrooke's Hospital, Cambridge, UK. ⁴Allen Institute for Brain Science, Seattle, WA, USA. *e-mail: h.clevers@hubrecht.eu

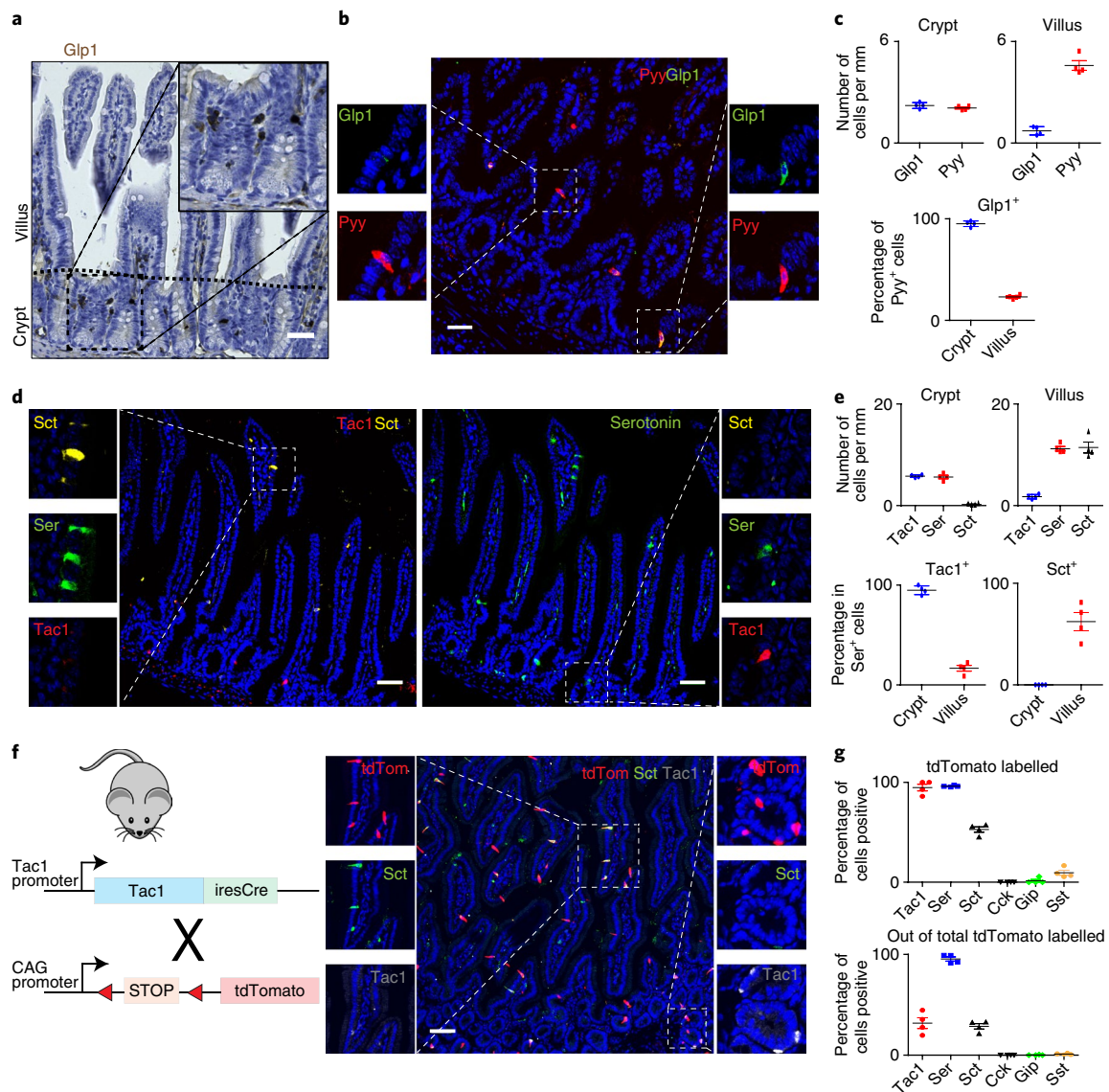


Fig. 1 | Enteroendocrine cells switch hormone expression while migrating from crypt to villus. a, b, Immunohistochemical analysis reveals that Glp1⁺ cells are enriched in the ileal crypt, where they co-express Pyy. The experiment in **a** was repeated two times independently with similar results. **c**, Quantification of **b**. The percentages of Pyy⁺ cells that co-express Glp1 are represented in the lower chart. **d**, ECs express Tac1 in the crypt and Sct in the villus, while serotonin (Ser) is produced in both locations. **e**, Quantification of **d**. The percentages of serotonin⁺ cells that co-express Tac1 or Sct are represented in the lower charts. **f**, Intestine of *Tac1^{iresCre}/Rosa^{Ai14}* mice reveals that ECs lose Tac1 and gain Sct expression from crypt to villus. **g**, Quantification of **f** and Supplementary Fig. 1. The percentages of each hormone that is tdTomato⁺ (upper chart) and of tdTomato⁺ cells that are hormone positive (lower chart) are shown. The mean values are depicted in graphs **c**, **e** and **g**, and the error bars represent s.d. for *n* = 4 mice for each experiment. Scale bars, 50 μ m.

in the proximal part of the SI¹, but we observe that our EEC differentiation protocol generates Sct⁺ cells equally well in the proximal and distal small intestinal organoids. *Trpa1*, an irritant receptor enriched in EECs of the intestinal crypt¹⁵, decreased with BMP activation (Fig. 2d). BMP4-mediated changes in hormone expression could be overridden by the addition of the BMPRI1 inhibitor LDN193189, confirming involvement of the BMPRI1/2 axis (Supplementary Fig. 2c,d).

To address whether BMP signalling can switch hormone expression in individual mature EECs rather than selectively depleting subtypes of EECs, we followed the fate of *Gcg*- or *Tac1*-expressing cells using cultures derived from *Gcg^{Venus}* and *Tac1^{iresCre}/Rosa26^{tdTomato}* mice^{11,16}. Live-cell imaging of *Gcg^{Venus}* organoids demonstrated that BMP activation induced a decrease in Venus levels, suggesting downregulation of *Gcg* (Supplementary Fig. 2e,f). We did not

observe BMP-induced apoptosis of Venus⁺ or tdTomato⁺ cells (Supplementary Fig. 2g).

Changes in hormone expression in individual EECs might be caused by dynamics in transcriptional networks, and accompanied by the production of other sensory receptors. To identify dynamics at a single-cell level, we performed scRNA-seq of traced *Tac1*-, *Gcg*- or *Gip*-expressing murine cells¹⁶. Gip⁺ K cells exist both in crypts and villi and were isolated from organoids derived from a *Gip^{Cre}/Rosa26^{tdRFP}* mouse¹⁷. Guided by their regional in vivo abundance, we isolated organoids from the proximal small intestine of Gip, from the distal small intestine of *Gcg* and from the whole small intestine of *Tac1* reporter mice. Organoids were treated with a MEK inhibitor to limit new EEC generation and either exposed to Noggin (control) or BMP4 for 24 or 96 h (Fig. 3a). Next, EECs derived from the reporters/treatments were sorted for the reporter

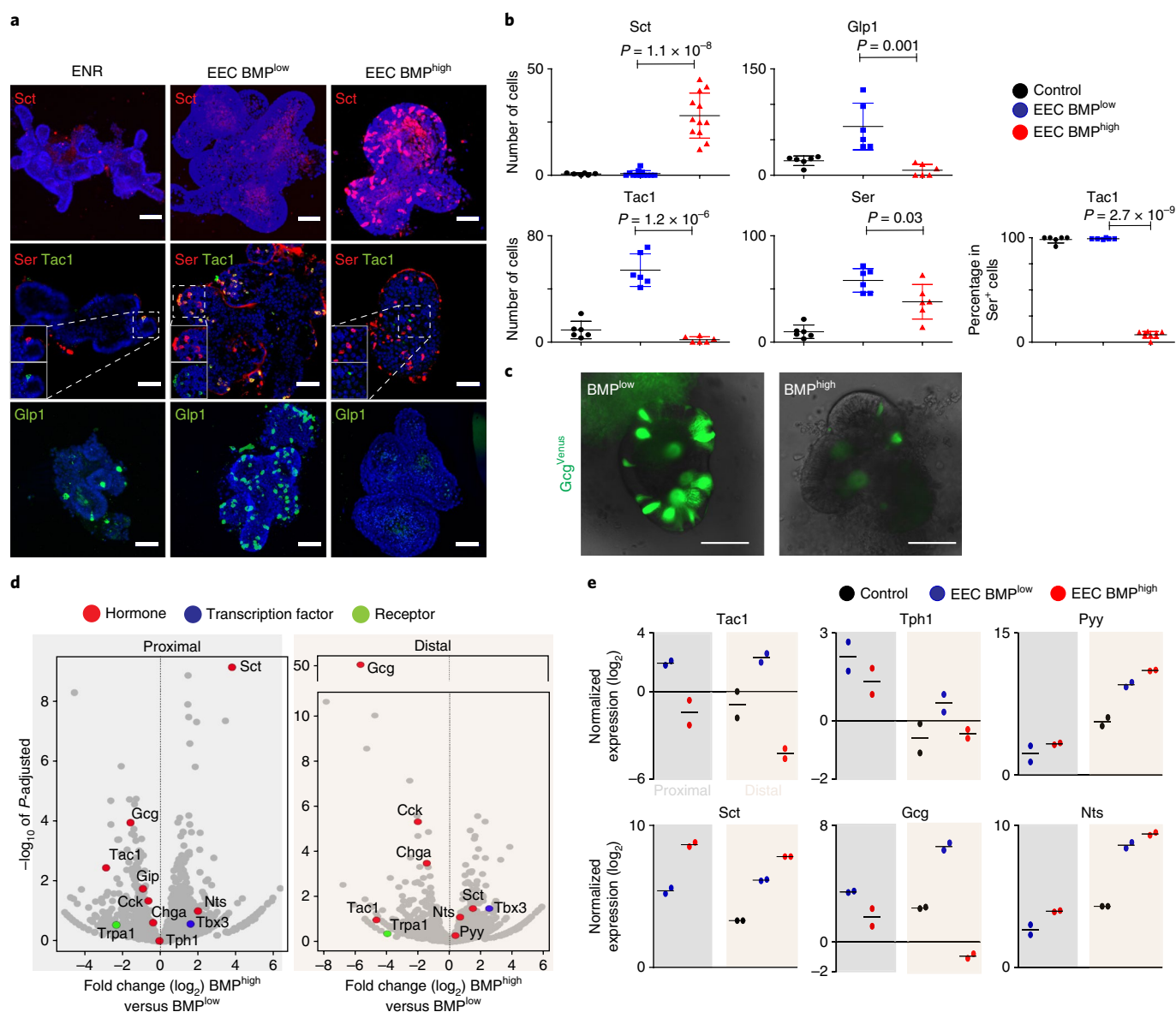


Fig. 2 | Activation of BMP signalling induces a villus-like hormone signature in mouse EECs. a, Organoids are differentiated for 4 days to EECs in the absence (EEC BMP^{low}) or presence of BMP4 (EEC BMP^{high}). ENR is used as a control. Activation of BMP signalling induces expression of *Sct*, while repressing *Tac1* and *Glp1*. Images are presented as maximum projections, and are representative of two independent experiments. **b**, Quantification of **a**. The number of positive cells for each hormone was quantified and is displayed per millimetre of organoid epithelium. The percentages of serotonin⁺ cells that co-express *Tac1* are presented (right). The sample size represents two biologically independent experiments, in which at least three organoids were quantified per replicate and staining. Mean values per treatment are shown and error bars depict s.d. and were derived from $n = 12$ organoids for *Sct*, and $n = 6$ organoids for other hormones in BMP^{low} and BMP^{high} conditions. P values were calculated from these same n numbers using a two-sided t -test. **c**, Overlay of bright-field and Venus images of organoids derived from *Gcg*^{Venus} mice after a four-day treatment with a BMP^{low} or BMP^{high} EEC differentiation cocktail. BMP activation represses expression of *Gcg*, without inducing morphological alterations. The experiment was repeated independently ten times. **d**, Volcano plots showing results from RNA-seq of organoids stimulated for four days with BMP^{low} or BMP^{high} EEC differentiation cocktails, from proximal (left) and distal (right) small intestinal organoids. Gene expression fold change (\log_2) of BMP^{high} versus BMP^{low} is shown on the x axis and significance on the y axis. Each grey dot represents a gene, and dots representing relevant genes are highlighted in different colours, according to their function. Sample size represents two biologically independent experiments, and P -adjusted values were calculated with a Wald test using the DESeq2 package. **e**, qPCR analysis of selected hormones from **d**. Expression levels are shown relative to control organoids in ENR medium. The experiment was performed in $n = 2$ biologically independent experiments, and the mean expression is depicted. Scale bars, 50 μm .

fluorescence and scRNA-seq was performed using SORTseq¹⁸, an automated version of CELseq2 (Fig. 3a and Supplementary Fig. 3a)¹⁹. K-medoids clustering by the RaceID2 algorithm²⁰ showed that *Tac1*⁻, *Gcg*⁻ and *Gip*⁻ traced cells, classically defined as ECs, L- and K- cells, respectively, clustered according to their cell type and mostly independently of the treatment in a t -distributed

stochastic neighbour embedding (t-SNE) space (Fig. 3b,c). We identified *Alpi*⁺ enterocytes and *Muc2*⁺ goblet cells derived from the *Gcg*^{Venus} reporter that displayed the lowest Venus fluorescence intensity (Supplementary Fig. 3b). We also detected a cluster of unknown identity with expression of the vomeronasal receptor *Vmn2r55*, which was identified previously⁷. BMP-stimulated ECs

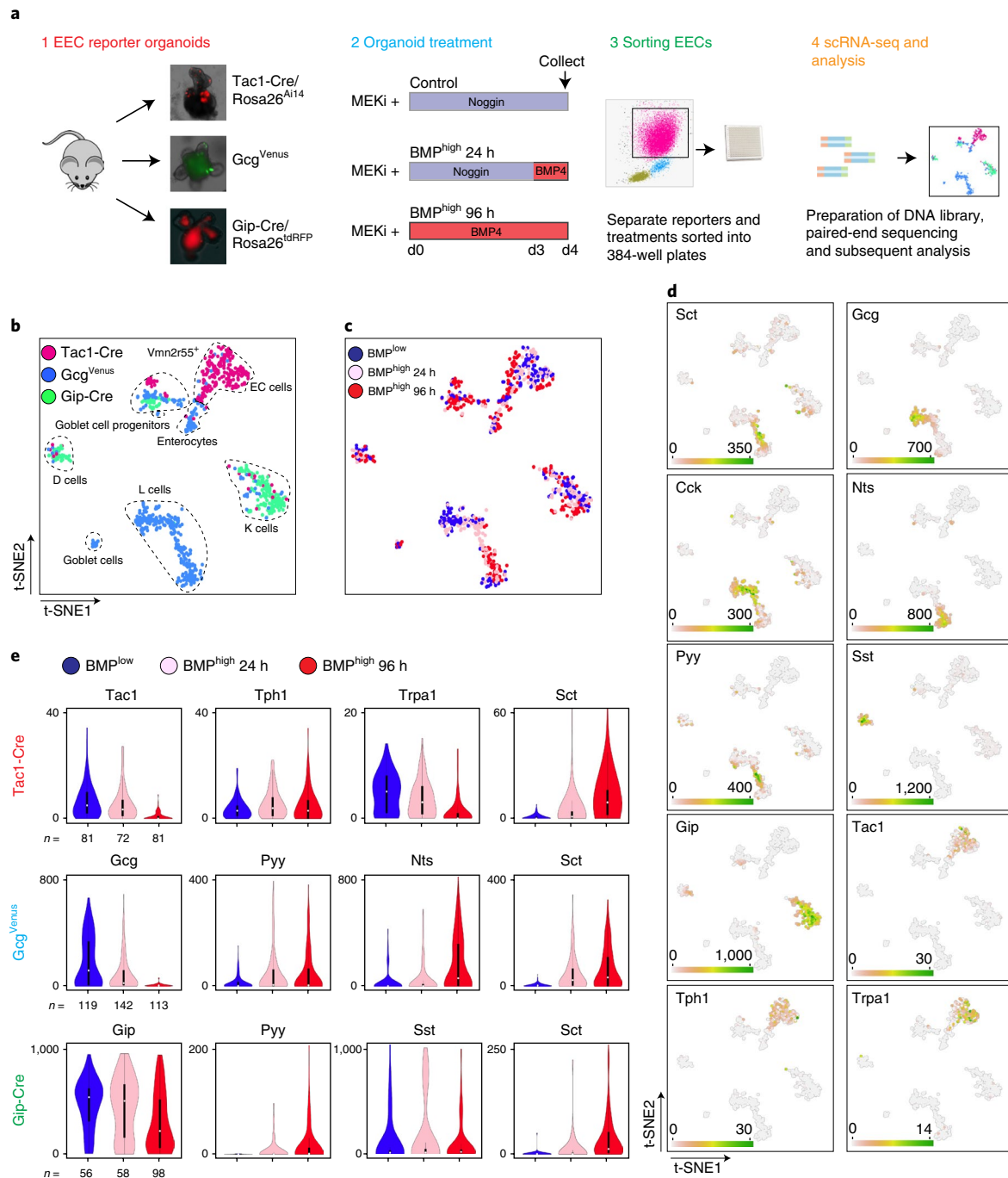


Fig. 3 | scRNA-seq reveals BMP-regulated plasticity among different EEC subtypes. **a**, Experimental paradigm. Different EEC reporter organoids were treated with a MEK inhibitor, while receiving Noggin or BMP4. After four days, organoids were dissociated and traced EECs were sorted and processed for scRNA-seq. **b, c**, t-SNE map of scRNA-sequenced EECs using the RaceID2 algorithm. Different colours, as indicated in the legend, highlight cells isolated from different reporter organoids (**b**) and treatments (**c**). **d**, Expression levels of selected hormones and receptors in the t-SNE space of **b, c**. **e**, Expression of individual hormones within different EEC reporter-sorted cells are presented in violin plots, with different colours for the different treatments (as indicated in the legend). The violin plots depict median values (white dot), 50% of the values (within the thick black line) and 95% of the values (within the thin black line). The n number of cells per treatment and reporter is depicted. Different dynamics of hormone expression were observed over the course of BMP treatment in subtypes of EECs.

displayed a lower *Sct* expression level compared to L and K cells (Fig. 3c–e). Within ECs, expression of *Tph1* remained unchanged during BMP treatment, while *Tac1* decreased (Fig. 3c–e). Cells clustering as classical L cells reduced their *Gcg* (*Glp1*) expression, while activating *Nts* and *Pyy* transcription following BMP treatment (Fig. 3d and Supplementary Fig. 3c). Some *Gcg*^{Venus}-sorted

cells from ileal organoids expressed *Gip*, combined with low levels of *Gcg* (Fig. 3b–d). These cells clustered together with K cells and could not be induced to express *Nts*, indicating that these cells represent K cells and not L cells. (Fig. 3d). L cells and to a lesser extent K cells express *Cck* independent of treatment (Fig. 3d). Within *Gip*-traced K cells, we observed a separate population of

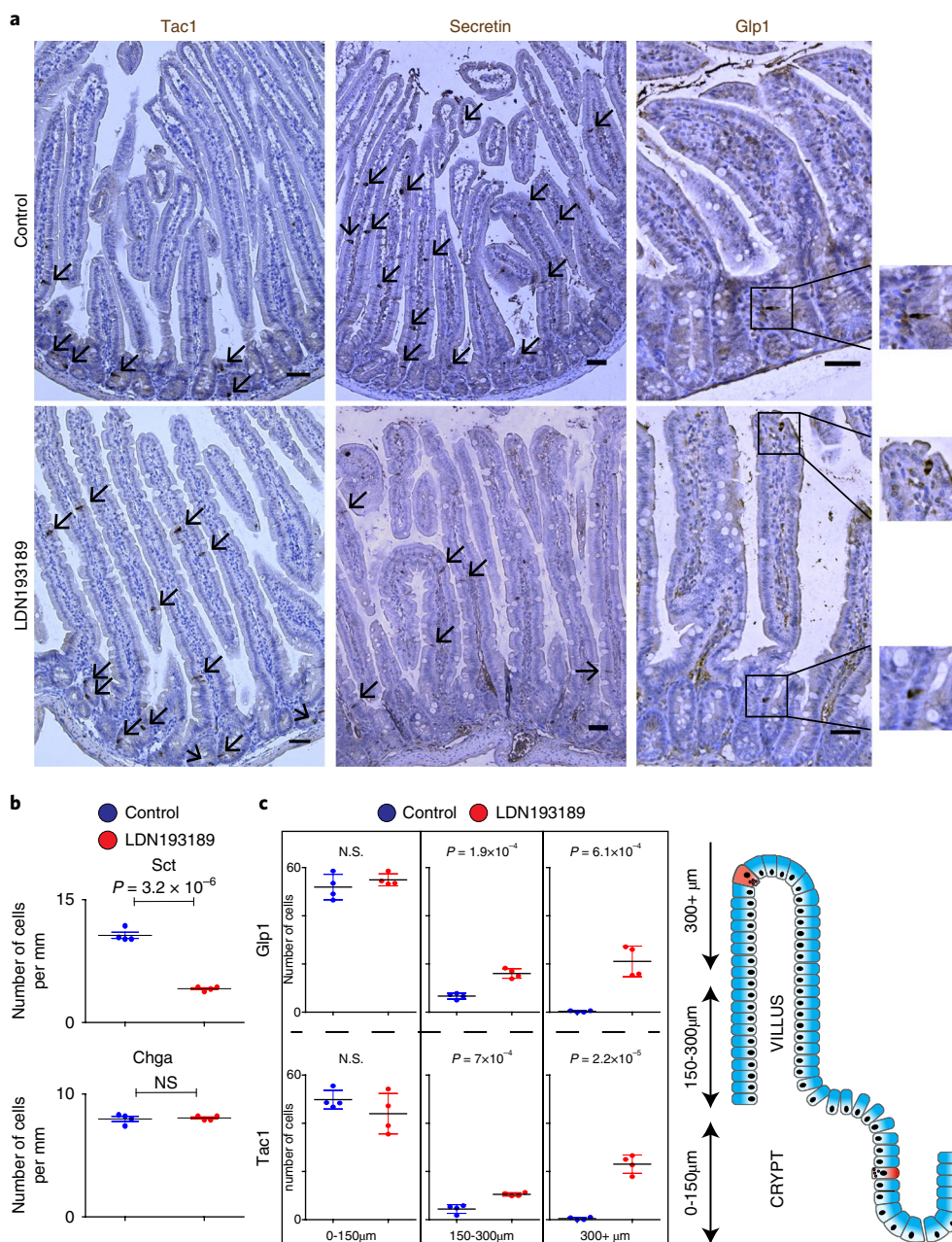


Fig. 4 | Manipulation of BMP gradient alters hormone expression in mice. a, Mice were treated for 80 h with the BMPR1a inhibitor LDN193189. Immunohistochemical analysis of the intestine shows a repression of Sct and induction of Glp1 and Tac1 expression following BMP inhibition. Glp1⁺ and Tac1⁺-expressing cells are mostly restricted to the crypt in control mice, but expand into the upper villus region following BMP inhibition. A representative image is shown from two separate stainings of four independent intestines. Black arrows indicate representative hormone-positive cells. **b**, Quantification of **a**. Number of Chga⁺ and Sct⁺ cells per treatment. **c**, Quantification of **a**. The number of Tac1⁺ or Glp1⁺ cells is displayed for each segment of the crypt-villus axis in the different treatments. Cells positive for Tac1 and Glp1 increase in the higher villus segments following LDN193189 treatment. Tac1⁺ cells are counted and displayed in 10 mm of the proximal small intestine. Glp1⁺ cells are counted and displayed in 30 mm of the distal small intestine. The results presented are derived from $n = 4$ mice per treatment, and statistics were calculated using a two-sided *t*-test. Mean values per staining and treatment are shown, and error bars represent s.d. NS, not significant. Scale bars, 50 μ m.

Sst-producing cells. BMP activation had no effect on *Sst* expression and caused a mild reduction in *Gip* expression in these clusters, while activating *Sct* expression only in *Gip*⁺ but not in *Sst*⁺ cells (Fig. 3d,e and Supplementary Fig. 3c). *Pyy* expression could be induced in both *Gip*⁺ and in *Sst*⁺ cells, but to a lesser extent than in L cells (Supplementary Fig. 3c). We did observe low *Cck*, *Gcg* and no *Nts* expression in K cells, indicating that these represent a separate lineage from ileal L cells (Fig. 3d,e).

We identified uniquely expressed genes in the various clusters that corresponded to known expression or function along the crypt-to-villus axis in vivo. The irritant receptor *Trpa1* (proposed to be involved in serotonin release) is enriched in the crypt^{15,21}. Concordantly, it decreased during BMP treatment within ECs (Fig. 3d,e). We found the orphan receptor *Asic5* to be expressed by *Sst*⁺ cells (Supplementary Fig. 3d). This same population also expressed the islet amyloid polypeptide (Iapp) amylin

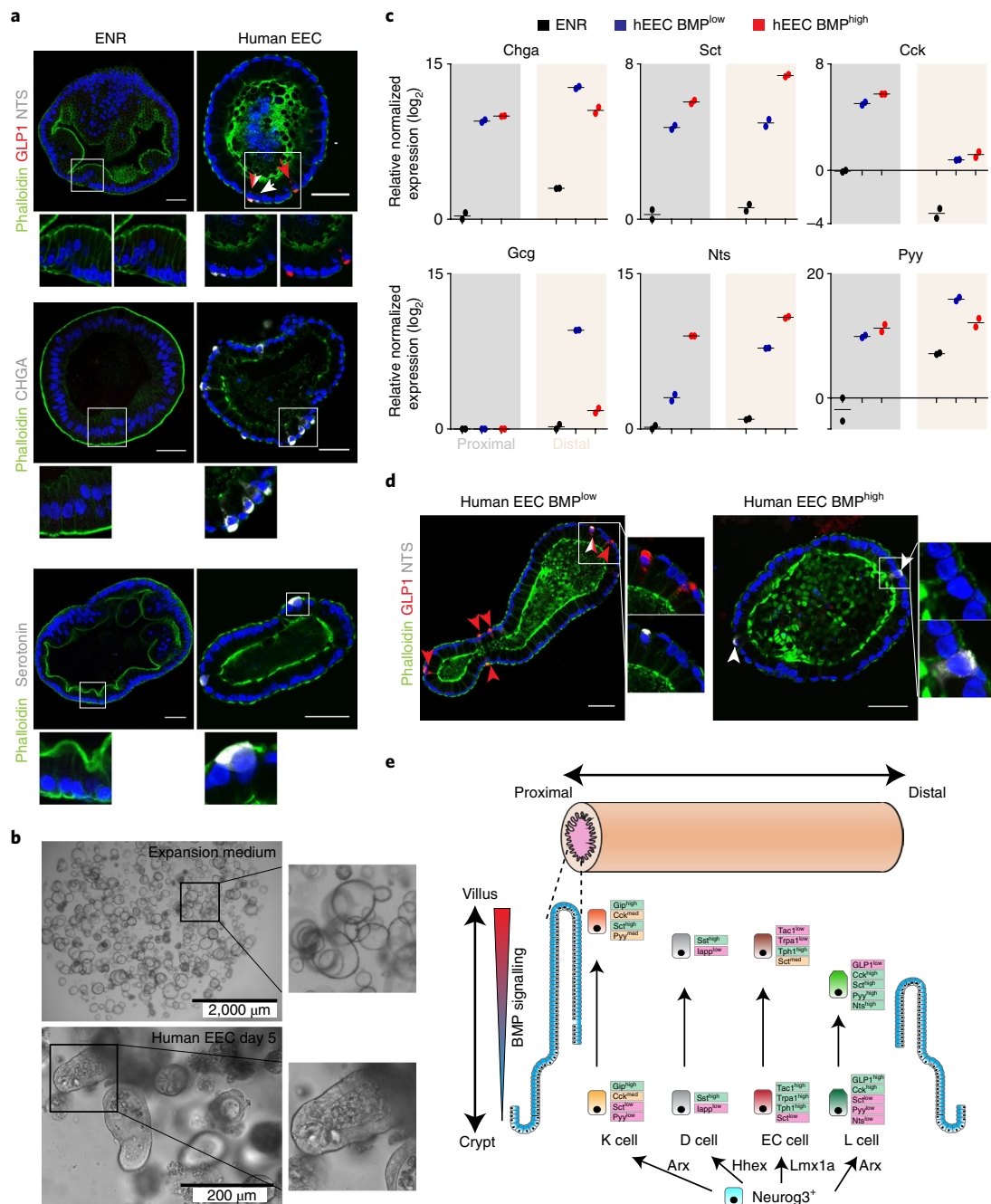


Fig. 5 | The human EEC differentiation protocol implies conserved BMP-controlled hormone expression. **a**, Human small intestinal organoids were induced to differentiate either for five days, by withdrawing Wnt signals (ENR), or to EECs, through additional MEK and Notch inhibition. Immunofluorescence indicates the presence of different subtypes of EECs in human organoids. The white arrows indicate the presence of NTS⁺ cells, red arrows GLP1⁺ cells. The experiment has been repeated four times independently with similar results. **b**, Bright-field images of human intestinal organoids in expansion medium or after a five-day differentiation towards EECs. The experiment was repeated independently four times. **c**, The five-day differentiation protocol of human EECs (hEEC) was performed in the presence and absence of BMP4. Expression levels of hormones were determined by qPCR and are shown relative to a duodenal ENR control. Gcg expression is shown relative to an ileal ENR control, as it was not detected in duodenal organoids. Sample size represents $n = 2$ biologically independent experiments, and the mean expression values are shown. **d**, Human EECs were produced in the absence (BMP^{low}) or presence (BMP^{high}) of BMP4. NTS overlaps with GLP1 in BMP^{low} conditions, while only NTS single-positive cells are observed in BMP^{high} conditions. The experiment was repeated independently four times. Scale bars, 50 μ m. **e**, Model of EEC differentiation. K cells are enriched in the proximal and L cells in the distal part of the small intestine, respectively, whereas ECs and D cells are uniformly distributed. A crypt-to-villus BMP signalling gradient drives alterations in hormone repertoires in these EEC lineages.

(Supplementary Fig. 3d), a peptide previously found in pancreatic β cells with a wide range of metabolic effects²². The LIM homeobox factor *Lmx1a* occurs in ECs, as suggested recently²³. The homeobox protein *Hhex*—not previously observed in the gut—was expressed

by *Sst*-producing cells (Supplementary Fig. 3d). Interestingly, *Hhex* has been described as an essential factor for *Sst*-producing δ cells in the pancreas²⁴. The T-box transcription factor *Tbx3* was produced in BMP-activated EECs (Supplementary Fig. 3d), and enriched in

the villus²⁵. Finally, we found specific activation of classical BMP target genes in BMP-treated cells, such as *Id1*, *Id2* and *Id3*, confirming pathway activation (Supplementary Fig. 3d)²⁶.

Transcript dynamics might not be fully predictive for changes at the peptide hormone level. Therefore, we repeated the same experimental strategy as for scRNA-seq and assessed co-expression of relevant peptide hormones in the *Tac1^{iresCre/Rosa26^{tdTomato}}* and *Gcg^{Venus}* reporter organoids. Over the course of four days, BMP-inhibited tdTomato⁺ cells remained immunoreactive for Tac1 and serotonin, while only rarely expressing Sct (Supplementary Fig. 4a). Strikingly, BMP-activated tdTomato⁺ cells lost Tac1 immunoreactivity, maintained serotonin and gained Sct positivity (Supplementary Fig. 4a). Glp1 positivity was strongly correlated with Venus expression in *Gcg^{Venus}* organoids in BMP-untreated conditions, while this correlation is lost in BMP-treated samples (Supplementary Fig. 4a). Conversely, Venus positivity was increasingly predictive for Sct expression after BMP treatment (Supplementary Fig. 4a). Pyy peptide positivity remained unchanged irrespective of BMP treatment (Supplementary Fig. 4a), in line with the constant peptide levels between the crypt and the villus in vivo¹⁰.

We performed live-cell imaging of the *Tac1^{iresCre/Rosa26^{tdTomato}}* and *Gcg^{Venus}* reporter organoids in BMP-untreated and -treated conditions. tdTomato⁺ cells that existed at the beginning of the BMP treatment continued to persist over the course of 60 h, while losing Tac1 and gaining Sct expression (Supplementary Fig. 4b). Untreated cells retained Tac1 positivity (Supplementary Fig. 4b). In *Gcg^{Venus}* reporter organoids, we observed a similar increase in Sct peptides (Supplementary Fig. 4b). Collectively, these data indicate that individual EECs can rewire their peptide hormone profile following activation of BMP signalling.

The number of tdTomato⁺ and Venus⁺ EECs increased significantly over four days when BMP signalling was inhibited versus activated (Supplementary Fig. 4a). We found that the first transcription factor expressed by and defining the EEC lineage, neurogenin 3²⁷, was inhibited by BMP activation (Supplementary Fig. 4c). To circumvent a bias that occurs at the bulk population level due to this inhibition of EEC specification, we first generated a large pool of ileal EECs using our differentiation protocol for three days. Next, we switched to BMP^{high} conditions for 24 h (Supplementary Fig. 4d). Increases in *Sct*, *Pyy* and *Nts* expression were more pronounced compared to a continuous BMP inhibition (Fig. 2 and Supplementary Fig. 4c). These data imply that initial EEC specification requires BMP^{low} conditions, as exist at the bottom of the crypt.

To investigate whether villus-produced BMP controls hormone expression in vivo, we analysed intestines from mice that ectopically express the BMP inhibitor Noggin in the intestinal epithelium (*Villin^{Noggin}*)¹³. As expected, we observed an increased expression of Tac1 and Glp1 in the villi of these mice, while Sct was reduced (Supplementary Fig. 5a–d). We next tested the feasibility of influencing hormone expression by targeting the BMP gradient with the BMPRIa inhibitor LDN193189²⁸. An 80-h oral treatment caused a reduction in Sct⁺ cell numbers. The overall histology of the intestine was unaffected, and the number of Chga⁺ EECs did not change significantly (Fig. 4a,b), consistent with a previous study²⁹. We quantified the numbers of Tac1⁺ and Glp1⁺ cells along different segments of the crypt–villus axis, assuming that BMP inhibition would not increase these in the BMP^{low} crypt. BMP inhibition did not cause significant changes in the lowest crypt–villus segment in the number of Tac1⁺ or Glp1⁺ EECs (Fig. 4a,c). However, the increase in cells immunoreactive for Tac1 or Glp1 was very pronounced higher up in the villus (Fig. 4a,c).

Finally, we pursued the establishment of a differentiation platform for induction of EECs in human intestinal organoids³⁰. The best results were obtained with dual inhibition of Notch and MEK signalling (Fig. 5a,b). This allowed us to generate all subtypes of EECs in organoids derived from either human duodenal or ileal tissue.

ENR-differentiated organoids did not contain EECs but mostly enterocytes, as evidenced by their extensive brush border (Fig. 5a). In our EEC differentiation protocol, BMP activation induced similar trended alterations in EEC hormone repertoires as it did in murine organoids (Fig. 5c). *NTS* and *SCT* transcripts increased following BMP stimulation, whereas *GCG* transcripts were reduced (Fig. 5c). BMP activation had a neutral effect on total *CHGA* expression, and in contrast to the mouse, *PYY* was not increased following BMP stimulation (Fig. 5c). Although cells positive for GLP1 and *NTS* peptides were observed in control conditions, we observed only *NTS* single-positive cells in BMP-treated conditions (Fig. 5d). This implies that BMP control of the expressed EEC hormone repertoire is a generalizable phenomenon. In line with our observations in the murine organoid system⁸, we found that human intestinal organoids maintained their regional identity in terms of representation of EEC subtypes. *GCG*, *NTS* and *PYY* were highly enriched in distal gut organoids, whereas *CCK* displayed a higher bias towards the duodenum (Fig. 5c).

Taken together, these data provide two main insights into EEC biology. First, the observations support that BMP controls hormone expression of EECs. EECs that are born in crypts from *Lgr5* stem cells encounter increasing levels of BMP signalling when migrating towards the villus tips³¹, and can change their hormone profile during this journey. Second, this insight in combination with the scRNA-seq data proposes a simplification of EEC taxonomy (Fig. 5e). Previous high-resolution imaging and scRNA-seq data suggested that almost every combination of EEC hormones can occur in individual EECs³². Our current data indicate that there might be fewer unrelated differentiation pathways of EECs ('lineages') than previously anticipated and that some of the marker hormones are not hardwired. This implies that EECs uniquely dedicated to the production of Sct or Nts (the so called S or N cells) or Pyy do not exist, and that most EECs initiate expression of Sct when entering the BMP^{high} villus domain. Indeed, we observe that all BMP-activated EECs, except D cells, upregulate Sct to different degrees, while L cells (but not Sst- or serotonin-producing cells) increase Pyy and Nts. Gip-expressing cells can be induced to express lower levels of Pyy, but not Nts. Importantly, we find that *Chga* is a marker of serotonin-positive cells but not of other EECs, and using it as a generic marker would not allow for identifying EEC regulators such as the BMP pathway.

Pulse-chase labelling using BrdU has indicated that EECs do not necessarily follow the conveyor-belt migration pattern in a constant flow from the bottom of the crypt to the tip of the villus^{12,33}. EECs interact with enteric neurons through synapses, which potentially could alter cellular migration^{34,35}. Subpopulations of EECs can be retained in the crypt for two weeks while maintaining expression of Tac1 or Glp1. Cells that migrate onto the villus are destined to lose Tac1 or Glp1^{9,12,33}. This ultimately suggests that controlling EEC migration along the crypt–villus axis and the Wnt/BMP gradients would be a way to influence hormone expression patterns.

Methods

Methods, including statements of data availability and any associated accession codes and references, are available at <https://doi.org/10.1038/s41556-018-0143-y>.

Received: 12 October 2017; Accepted: 14 June 2018;
Published online: 23 July 2018

References

- Furness, J. B., Rivera, L. R., Cho, H.-J., Bravo, D. M. & Callaghan, B. The gut as a sensory organ. *Nat. Rev. Gastroenterol. Hepatol.* **10**(10), 729–740 (2013).
- Connor, T. M. O. et al. The role of substance P in inflammatory disease. *J. Cell. Physiol.* **201**, 167–180 (2004).
- Egerod, K. L. et al. A major lineage of enteroendocrine cells coexpress CCK, secretin, GIP, GLP-1, PYY, and neurotensin but not somatostatin. *Endocrinology* **153**, 5782–5795 (2012).

4. Haber, A. L. et al. A single-cell survey of the small intestinal epithelium. *Nature* **551**, 333–339 (2017).
5. Barker, N. et al. Identification of stem cells in small intestine and colon by marker gene *Lgr5*. *Nature* **449**, 1003–1007 (2007).
6. Sato, T. et al. Single *Lgr5* stem cells build crypt–villus structures in vitro without a mesenchymal niche. *Nature* **459**, 262–265 (2009).
7. Grün, D. et al. Single-cell messenger RNA sequencing reveals rare intestinal cell types. *Nature* **525**, 251–5 (2015).
8. Basak, O. et al. Induced quiescence of *Lgr5*⁺ stem cells in intestinal organoids enables differentiation of hormone-producing enteroendocrine cells. *Cell Stem Cell* **20**, 177–190.e4 (2017).
9. Roth, K. A. & Gordon, J. I. Spatial differentiation of the intestinal epithelium: analysis of enteroendocrine cells containing immunoreactive serotonin, secretin, and substance P in normal and transgenic mice. *Proc. Natl Acad. Sci. USA* **87**, 6408–6412 (1990).
10. Grunddal, K. V. et al. Neurotensin is coexpressed, coreleased, and acts together with GLP-1 and PYY in enteroendocrine control of metabolism. *Endocrinology* **157**, 176–194 (2016).
11. Harris, J. A. et al. Anatomical characterization of Cre driver mice for neural circuit mapping and manipulation. *Front. Neural Circuits* **8**, 78 (2014).
12. Aiken, K. D. & Roth, K. A. Temporal differentiation and migration of substance P, serotonin, and secretin immunoreactive enteroendocrine cells in the mouse proximal small intestine. *Dev. Dyn.* **194**, 303–310 (1992).
13. Haramis, A.-P. G. De novo crypt formation and juvenile polyposis on BMP inhibition in mouse intestine. *Science* **303**, 1684–1686 (2004).
14. Beumer, J. & Clevers, H. Regulation and plasticity of intestinal stem cells during homeostasis and regeneration. *Development* **143**, 3639–3649 (2016).
15. Camacho, S. et al. Anti-obesity and anti-hyperglycemic effects of cinnamaldehyde via altered ghrelin secretion and functional impact on food intake and gastric emptying. *Sci. Rep.* **5**, 7919 (2015).
16. Habib, A. M. et al. Overlap of endocrine hormone expression in the mouse intestine revealed by transcriptional profiling and flow cytometry. *Endocrinology* **153**, 3054–3065 (2012).
17. Svendsen, B. et al. GLP1- and GIP-producing cells rarely overlap and differ by bombesin receptor-2 expression and responsiveness. *J. Endocrinol.* **228**, 39–48 (2016).
18. Muraro, M. J. et al. A Single-cell transcriptome atlas of the human pancreas. *Cell Syst.* **3**, 385–394 (2016).
19. Hashimshony, T. et al. CEL-Seq2: sensitive highly-multiplexed single-cell RNA-Seq. *Genome Biol.* **17**, 77 (2016).
20. Grün, D. et al. De novo prediction of stem cell identity using single-cell transcriptome data. *Cell Stem Cell* **19**, 266–277 (2016).
21. Nozawa, K. et al. TRPA1 regulates gastrointestinal motility through serotonin release from enterochromaffin cells. *Proc. Natl Acad. Sci. USA* **106**, 13 (2009).
22. Zhang, X.-X. et al. Neuroendocrine hormone amylin in diabetes. *World J. Diabetes* **7**, 189–197 (2016).
23. Gross, S. et al. The novel enterochromaffin marker *Lmx1a* regulates serotonin biosynthesis in enteroendocrine cell lineages downstream of *Nkx2.2*. *Development* **143**, 2616–2628 (2016).
24. Zhang, J., McKenna, L. B., Bogue, C. W. & Kaestner, K. H. The diabetes gene *Hhex* maintains δ -cell differentiation and islet function. *Genes Dev.* **28**, 829–834 (2014).
25. Kaaij, L. T. et al. DNA methylation dynamics during intestinal stem cell differentiation reveals enhancers driving gene expression in the villus. *Genome Biol.* **14**, R50 (2013).
26. Hollnagel, A., Oehlmann, V., Heymer, J., Rütter, U. & Nordheim, A. Id genes are direct targets of bone morphogenetic protein induction in embryonic stem cells. *J. Biol. Chem.* **274**, 19838–19845 (1999).
27. Jenny, M. et al. Neurogenin3 is differentially required for endocrine cell fate specification in the intestinal and gastric epithelium. *EMBO J.* **21**, 6338–6347 (2002).
28. Whissell, G. et al. The transcription factor *GATA6* enables self-renewal of colon adenoma stem cells by repressing BMP gene expression. *Nat. Cell Biol.* **16**, 695–707 (2014).
29. Qi, Z. et al. BMP restricts stemness of intestinal *Lgr5*⁺ stem cells by directly suppressing their signature genes. *Nat. Commun.* **8**, 13824 (2017).
30. Sato, T. et al. Long-term expansion of epithelial organoids from human colon, adenoma, adenocarcinoma, and Barrett's epithelium. *Gastroenterology* **141**, 1762–1772 (2011).
31. Clevers, H. The intestinal crypt, a prototype stem cell compartment. *Cell* **154**, 274–284 (2013).
32. Fothergill, L. J., Callaghan, B., Hunne, B., Bravo, D. M. & Furness, J. B. Costorage of enteroendocrine hormones evaluated at the cell and subcellular levels in male mice. *Endocrinology* **158**, 2113–2123 (2017).
33. Aiken, K. D., Kisslinger, J. A. & Roth, K. A. Immunohistochemical studies indicate multiple enteroendocrine cell differentiation pathways in the mouse proximal small intestine. *Dev. Dyn.* **201**, 63–70 (1994).
34. Bellono, N. W. et al. Enterochromaffin cells are gut chemosensors that couple to sensory neural pathways. *Cell* **170**, 185–198.e16 (2017).
35. Bohorquez, D. V. et al. Neuroepithelial circuit formed by innervation of sensory enteroendocrine cells. *J. Clin. Invest.* **125**, 782–786 (2015).

Acknowledgements

We thank S. van der Elst, R. van der Linden and Y. Bar-Ephraim for their help with FACS experiments. B.A. is supported by NWO/VENI 863.15.015.

Author contributions

J.B. and H.C. conceived and designed the project. J.B. designed and performed all experiments. B.A. performed analysis of RNA-seq data. F.R. and E.G. generated the *Gcg* and *Gip* reporter mice. H.Z. generated the *Tac1* reporter mouse, and T.N.N. assisted in providing the tissue. J.H.V.E. supervised and performed the mouse experiments, with the help of M.V.d.B. Y.P. assisted in histology preparation. J.B., B.A. and H.C. wrote the manuscript with input from all other authors.

Competing interests

The authors declare no competing interests.

Additional information

Supplementary information is available for this paper at <https://doi.org/10.1038/s41556-018-0143-y>.

Reprints and permissions information is available at www.nature.com/reprints.

Correspondence and requests for materials should be addressed to H.C.

Publisher's note: Springer Nature remains neutral with regard to jurisdictional claims in published maps and institutional affiliations.

Methods

Mouse strains and experiments. Primary organoid cultures used in this culture were derived from *Gcg^{Venus}*, *Tac1^{iresCre}/Rosa26^{tdTomato}* and *Gip^{iresCre}/Rosa26^{tdRfp}* mice^{11,16}, and established as described before⁶. All mice were bred on a C57BL/6 background. All animal procedures and experiments were performed in accordance with national animal welfare laws and were reviewed by the Animal Ethics Committee of the Royal Netherlands Academy of Arts and Sciences (KNAW). All mouse experiments were conducted under a project licence granted by the Central Committee Animal Experimentation (CCD) of the Dutch government and approved by the Hubrecht Institute Animal Welfare Body (IvD), with project licence number AVD8010020151. All rodents are housed in a barrier facility in conventional cages and are changed without using a change station. All personnel entering the barrier must wear protective clothing (including head caps and special clogs). All animals are received directly from approved vendors (Charles River) or generated in house.

For the BMPR inhibition experiment, LDN193189 (Selleckchem) was dissolved in citric buffer (pH 3–3.1) at 2 mg ml⁻¹. Twelve-week-old mice ($n=4$) were given two oral doses of LDN193189 at 17.5 mg per kilogram of body weight per day. Citric buffer was given to control mice. The total treatment was maintained for 80 h.

Murine and human intestinal organoid culture. The basic culture medium (advanced Dulbecco's modified Eagle's medium/F12 supplemented with penicillin/streptomycin, 10 mM HEPES, Glutamax, B27 (Life Technologies) and 1 mM N-acetylcysteine (Sigma)) was supplemented with 50 ng ml⁻¹ murine recombinant epidermal growth factor (EGF; Peprotech), R-spondin1 (conditioned medium, 5% final volume) and Noggin (conditioned medium, 5% final volume), called ENR medium. Conditioned media were produced using HEK293T cells stably transfected with HA-mouse Rspo1-Fc (gift from C. Kuo, Stanford University) or after transient transfection with mouse Noggin-Fc expression vector. Advanced Dulbecco's modified Eagle's medium/F12 supplemented with penicillin/streptomycin, and Glutamax was conditioned for 1 week.

Human duodenal and ileal tissues were obtained from the UMC Utrecht with informed consent of each patient. The study was approved by the UMC Utrecht (Utrecht, the Netherlands) ethical committee and was in accordance with the Declaration of Helsinki and according to Dutch law. This study is compliant with all relevant ethical regulations regarding research involving human participants. Patients were diagnosed with a small or large intestinal cancer and from the resected intestinal segments, a sample was taken from normal mucosa for this study. Human small intestinal cells were isolated, processed and cultured as described previously³⁰.

Organoids were plated in basement membrane extract (BME; Trevigen). MEK signalling was inhibited using PD0325901 (1 μ M for murine, 100 nM for human organoids; Sigma Aldrich). Wnt secretion was inhibited with IWP-2 (5 μ M; Stemgent) and Notch with DAPT (10 μ M, Sigma Aldrich). BMP signalling was activated by treatment with human recombinant BMP4 (20 ng ml⁻¹, Peprotech) and withdrawal of Noggin from the culture medium. Hedgehog signalling was inhibited with Vismodegib (10 μ M, Selleckchem). TGF- β signalling was activated using recombinant mouse TGF- β 1 (3 ng ml⁻¹, R&D Systems, MAB7666TGF beta-1). TGF- β type-1 receptor signalling was inhibited using A83 (500 nM, Tocris). All control organoids were treated with similar concentrations of the compound solvent, dimethyl sulfoxide (DMSO) or 0.1% BSA in PBS. During treatments, cells were imaged using an EVOS microscope (Electron Microscopy Sciences).

For the induction of enteroendocrine differentiation in murine organoids, cells were cultured in standard culture conditions (ENR). At 4–7 days after plating in BME, medium was removed and organoids were treated with different regimes. The cocktail for mouse EEC differentiation included: IWP2 (5 μ M; Stemgent), DAPT (10 μ M, Sigma Aldrich) and MEK inhibitor PD0325901 (1 μ M; Sigma Aldrich), while BMP4 (20 ng ml⁻¹, Peprotech) was added for activation of BMP signalling. In human organoids, differentiation was achieved by withdrawing the p38 MAPK inhibitor SB202190, the TGF- β inhibitor A83, nicotinamide and Wnt-conditioned medium from the culture medium as described previously³⁰. Differentiation into EECs was performed by, as well as removing these same factors, additionally treating the medium with DAPT (10 μ M, Sigma Aldrich) and the MEK inhibitor PD0325901 (500 nM; Sigma Aldrich); BMP4 (20 ng ml⁻¹, Peprotech) was added for activation of BMP signalling. A step-by-step protocol for human EEC differentiation can be found at Nature Protocol Exchange³⁶.

Immunostaining. Whole organoids were collected by gently dissolving the BME in ice-cold medium, and subsequently fixed at RT in 4% formalin (Sigma) for at least 6 h. Next, organoids were permeabilized and blocked in PBS containing 0.5% Triton X-100 (Sigma) and 2% normal donkey serum (Jackson ImmunoResearch) for 30 min at room temperature. Organoids were incubated for 2 h at room temperature in blocking buffer containing primary antibodies. Primary antibodies used were goat anti-chromogranin A (1:500; Santa Cruz), goat anti-cholecystokinin (sc-21617, 1:100; Santa Cruz), rabbit anti-neurotensin (sc-20806, 1:100; Santa Cruz), goat anti-secretin (sc-26630, 1:100; Santa Cruz),

goat anti-somatostatin (sc-7819, 1:100; Santa Cruz), goat anti-serotonin (ab66047, 1:1,000, Abcam), rabbit anti-gastric inhibitory polypeptide (ab22624-50, 1:500; Abcam), goat anti-GLP1 (sc-7782, 1:100; Santa Cruz), rabbit anti-GLP1 (ab22625, 1:200; Abcam), rabbit anti-peptide YY (ab22663, 1:500; Abcam) and guinea pig anti-substance P (1:200, ab10353; Abcam). Organoids were incubated with the corresponding secondary antibodies Alexa488-, 568- and 647-conjugated anti-rabbit and anti-goat (1:1,000; Molecular Probes) in blocking buffer containing 4',6-diamidino-2-phenylindole (DAPI; 1:1,000, Invitrogen). Sections were embedded in Vectashield (Vector Labs) and imaged using an Sp8 confocal microscope (Leica). Image analysis was performed using ImageJ software.

For immunohistochemistry of organoids within the BME (Supplementary Fig. 4), medium was removed from the wells and replaced with 4% formalin for 1 h. Next, organoids were washed with PBS, permeabilized and blocked in PBS containing 0.5% Triton X-100 (Sigma) and 2% normal donkey serum (Jackson ImmunoResearch) for 30 min at room temperature. The wells were incubated for 2 h at room temperature in blocking buffer containing primary antibodies. After washing, secondary antibodies were added for 1 h at room temperature in blocking buffer. Organoids were subsequently imaged within the plate using an Sp8 confocal microscope (Leica).

For immunohistochemistry of mouse intestinal tissue, intestines were first flushed with 4% formaldehyde. Next, intestines were fixed for 6 h at room temperature in 4% formalin. The tissue was either embedded in paraffin or Tissue-Tek O.C.T. for cryosectioning, and stained as described previously³⁷.

Quantification of the number/location of EECs on intestinal section images was performed in ImageJ software, as well as the intensity of Venus levels in the live-cell imaging experiment in Supplementary Fig. 2e,f. Analysis of Glp1⁺ cell numbers and/or position in Figs. 1a–c and 4–c and Supplementary Fig. 5 was performed in the ileum, and all other hormones were counted along the whole small intestinal tract.

All quantifications were performed on the raw, unprocessed images.

RNA isolation and quantitative PCR. For qPCR analysis and bulk RNA-seq, RNA was isolated from organoids using the RNeasy kit (QIAGEN) as instructed in the manufacturer's protocol. PCR analysis was performed using the SYBR Green and Bio-Rad systems as described previously³⁸. PCR reactions were performed in duplicate with a standard curve for every primer. Changes in expression were calculated using CFX manager software (Bio-Rad). Primers were designed using the NCBI primer design tool. Primers used in this study are presented in Supplementary Table 1.

Glp1 and secretin secreted peptide. The supernatant from organoids was collected after 2-h stimulation with forskolin. The Glp1 concentration in the supernatant was measured with a Glp1 EIA Kit (Rab0201, Sigma, detects both full-length and N-terminal cleaved Glp1) using the manufacturer's protocol. The secretin concentration was measured with a Secretin EIA kit (EK-067-04, Phoenix Pharmaceuticals) using the manufacturer's protocol.

Bulk and scRNA-seq. For bulk RNA-seq analysis, organoids stimulated with EEC BMP^{high} or EEC BMP^{low} media for four days were collected and dissociated in RTL buffer (RNeasy Mini kit, Quiagen). Total RNA was isolated accordingly to the manufacturer's instructions (RNeasy Mini kit, Quiagen). Sequencing libraries were prepared on the basis of a modified CEL-seq2 method³⁹. Briefly, 1 ng of RNA was reverse transcribed using the Ambion kit and in vitro transcription was performed using 1 ng of cDNA as a template. The aRNA was then used to prepare sequencing libraries. These resulting DNA libraries were sequenced with sequenced paired-end at 75 bp read-length on the Illumina NextSeq.

For scRNA-seq, organoids were first dissociated into single cells through mechanical disruption, after 15 min of trypsin treatment at 37 °C (TrypLE Express; Life Technologies). Next, cells were immediately sorted using a BD FACS Aria (BD Biosciences). For the single-cell sequencing experiment, cells were sorted as single cells into 384-well plates containing ERCC spike-ins (Agilent), RT primers and dNTP (Promega) as described before. Plates were prepared using Mosquito HTS (TTPlabtech). scRNA-seq libraries were prepared following the SORT-seq protocol¹⁸, which is based on the CEL-seq2 method³⁹. Briefly, cells were first lysed for 5 min at 65 °C, and RT and second-strand mixes were dispensed by the Nanodrop II liquid handling platform (GC Biotech). Single-cell double-stranded cDNAs were pooled together and in vitro transcribed for linear amplification. Illumina sequencing libraries were prepared using the TruSeq small RNA primers (Illumina) and these DNA libraries were sequenced paired-end at 75 bp read length on the Illumina NextSeq.

RNA-seq data analysis. Paired-end reads from Illumina sequencing were aligned to the mouse transcriptome genome by BWA³⁹. For RNA-seq bulk data, normalization and differential gene expression analyses were performed using the DESeq2 package⁴⁰ and visualized as volcano plots. For scRNA-seq data, read counts were first corrected for UMI barcode by removing duplicate reads that had identical combinations of library, cell-specific and molecular barcodes and were mapped to the same gene. For each cell barcode the number of UMIs for every transcript was counted, and transcript counts were then adjusted to the expected

number of molecules based on counts, 256 possible UMIs and Poissonian counting statistics⁴¹. Samples were then normalized by downsampling to a minimum number of 3,000 transcripts per cell. Cells with fewer transcripts were excluded from the analyses. RaceID2 was used to cluster cells on the basis of the k-medoid method²⁰. All data analyses, quantification and data visualization were run on Rstudio. In total, we sequenced 2,880 cells and, after applying a filtering criterion of 3,000 expressed transcripts per cell, 820 cells were retained for further analysis.

Statistics and reproducibility. Two-sided *t*-tests were performed for all statistical analyses. Precise *P* values are mentioned in the corresponding figures, and the significance level was set at $P < 0.05$. In each figure legend, the number of biology replicates is mentioned for the corresponding experiment ($n = x$). For figures where representative images are shown, the number of times that the experiment has been repeated is mentioned in the legend.

For immunohistochemical experiments, we counted the following number of cells, of organoids or length of intestine: at least 50 cells per hormone and replicate intestine (Fig. 1b–e, $n = 4$ mice), at least 150 tdTomato⁺ cells per co-staining and replicate intestine (Fig. 1f,g, $n = 4$ mice), at least 3 organoids per hormone and replicate (Fig. 2a,b, $n = 2$ biologically independent experiments), 10 organoids per hormone and replicate (Supplementary Fig. 4a, $n = 2$ biologically independent experiments), 10 mm of the proximal small intestine for Tac1 (Fig. 4b,c, $n = 4$ mice per treatment), 30 mm of the distal small intestine for Glp1 (Fig. 4b,c, $n = 4$ mice per treatment). mice per genotype) and at least 50 cells per hormone and replicate intestine (Supplementary Fig. 5b,d; $n = 2$ mice per genotype).

Reporting Summary. Further information on experimental design is available in the Nature Research Reporting Summary linked to this article.

Data availability. Bulk and scRNA-seq data that support the findings of this study have been deposited in the Gene Expression Omnibus (GEO) under accession code [GSE114988](https://www.ncbi.nlm.nih.gov/geo/query/acc.cgi?acc=GSE114988).

Source data for Figs. 1c,e,g, 2b,e, 4b,c, 5c and Supplementary Figs. 1a, 2a,b,d, 3b, 4b,c, 5b,d have been provided as Supplementary Table 2. All other data supporting the findings of this study are available from the corresponding author on reasonable request.

References

36. Beumer, J. & Clevers, H. Induction of different human enteroendocrine cells in intestinal organoids. *Protoc. Exch.* <https://doi.org/10.1038/protex.2018.077> (2018).
37. Farin, H. F. et al. Visualization of a short-range Wnt gradient in the intestinal stem-cell niche. *Nature* **530**, 340–343 (2016).
38. Muñoz, J. et al. The *Lgr5* intestinal stem cell signature: robust expression of proposed quiescent ‘+4’ cell markers. *EMBO J.* **31**, 3079–3091 (2012).
39. Li, H. & Durbin, R. Fast and accurate short read alignment with Burrows–Wheeler transform. *Bioinformatics* **25**, 1754–1760 (2009).
40. Love, M. I., Huber, W. & Anders, S. Moderated estimation of fold change and dispersion for RNA-seq data with DESeq2. *Genome Biol.* **15**, 550 (2014).
41. Grün, D., Kester, L. & van Oudenaarden, A. Validation of noise models for single-cell transcriptomics. *Nat. Methods* **11**, 637–640 (2014).

Reporting Summary

Nature Research wishes to improve the reproducibility of the work that we publish. This form provides structure for consistency and transparency in reporting. For further information on Nature Research policies, see [Authors & Referees](#) and the [Editorial Policy Checklist](#).

Statistical parameters

When statistical analyses are reported, confirm that the following items are present in the relevant location (e.g. figure legend, table legend, main text, or Methods section).

n/a Confirmed

- The exact sample size (n) for each experimental group/condition, given as a discrete number and unit of measurement
- An indication of whether measurements were taken from distinct samples or whether the same sample was measured repeatedly
- The statistical test(s) used AND whether they are one- or two-sided
Only common tests should be described solely by name; describe more complex techniques in the Methods section.
- A description of all covariates tested
- A description of any assumptions or corrections, such as tests of normality and adjustment for multiple comparisons
- A full description of the statistics including central tendency (e.g. means) or other basic estimates (e.g. regression coefficient) AND variation (e.g. standard deviation) or associated estimates of uncertainty (e.g. confidence intervals)
- For null hypothesis testing, the test statistic (e.g. F , t , r) with confidence intervals, effect sizes, degrees of freedom and P value noted
Give P values as exact values whenever suitable.
- For Bayesian analysis, information on the choice of priors and Markov chain Monte Carlo settings
- For hierarchical and complex designs, identification of the appropriate level for tests and full reporting of outcomes
- Estimates of effect sizes (e.g. Cohen's d , Pearson's r), indicating how they were calculated
- Clearly defined error bars
State explicitly what error bars represent (e.g. SD, SE, CI)

Our web collection on [statistics for biologists](#) may be useful.

Software and code

Policy information about [availability of computer code](#)

Data collection Leica LAS X Version 1.1, Bio-Rad CFX Manager Version 3.1.

Data analysis ImageJ (Fiji, Version 1.51n), Microsoft Excel 2016, R Studio (1.1.453), Leica LAS X Version 1.1, FlowJo V10

For manuscripts utilizing custom algorithms or software that are central to the research but not yet described in published literature, software must be made available to editors/reviewers upon request. We strongly encourage code deposition in a community repository (e.g. GitHub). See the Nature Research [guidelines for submitting code & software](#) for further information.

Data

Policy information about [availability of data](#)

All manuscripts must include a [data availability statement](#). This statement should provide the following information, where applicable:

- Accession codes, unique identifiers, or web links for publicly available datasets
- A list of figures that have associated raw data
- A description of any restrictions on data availability

Bulk and single-cell RNA-seq data that support the findings of this study have been deposited in the Gene Expression Omnibus (GEO) under accession code GSE114988.

Source data for Fig. 1c, 1e, 1g, 2b, 2e, 4a, 5b, 5c, 6b and Supplementary Fig. 1a, 2a, 2b, 2d, 3b, 4b, 4c, 5a, 5b and 6 have been provided as Supplementary Table 2.

All other data supporting the findings of this study are available from the corresponding author on reasonable request.

Field-specific reporting

Please select the best fit for your research. If you are not sure, read the appropriate sections before making your selection.

Life sciences Behavioural & social sciences

For a reference copy of the document with all sections, see [nature.com/authors/policies/ReportingSummary-flat.pdf](https://www.nature.com/authors/policies/ReportingSummary-flat.pdf)

Life sciences

Study design

All studies must disclose on these points even when the disclosure is negative.

Sample size	No sample-size calculation was performed. For the mouse experiments, based on our experience, 4 animals per condition are required to answer our scientific question. Results obtained were highly significant and consistent and did not require larger animal experimental groups.
Data exclusions	No experimental animals were excluded. For the single cell sequence analysis we performed some filtering steps which are mentioned in the paper: after quantifying transcript expression in all of the cells, we normalized by down sampling to a minimum number of 3000 transcripts and discarded all cells with less than 3000 transcripts. To reduce noise, we discarded genes which were not expressed with at least 2 transcripts in one of the cells in the data set.
Replication	All attempts at replication were successful. The number of times each experiment has been repeated with similar results is stated in each figure legend. All methods are complete and techniques available and therefore experiments should be easily reproducible.
Randomization	Control and experimental male and female mice were randomly assigned into experimental groups.
Blinding	a) Single-cell and bulk mRNA-sequencing analysis was performed in an unbiased fashion with pooling all data. Experimental conditions were assigned following initial analysis. b) Histological analysis did not allow blinding, since phenotypes were too apparent (either morphologically or after performing stainings).

Materials & experimental systems

Policy information about [availability of materials](#)

n/a	Involvement in the study
<input checked="" type="checkbox"/>	<input type="checkbox"/> Unique materials
<input type="checkbox"/>	<input checked="" type="checkbox"/> Antibodies
<input checked="" type="checkbox"/>	<input type="checkbox"/> Eukaryotic cell lines
<input type="checkbox"/>	<input checked="" type="checkbox"/> Research animals
<input type="checkbox"/>	<input checked="" type="checkbox"/> Human research participants

Antibodies

Antibodies used

Antibodies used
A) goat anti-Chromogranin A from Santa Cruz (1:500). Catalogue number: sc-1488, polyclonal. No lot available anymore, similar results were obtained using rabbit anti-Chromogranin A from Labned (1:1000). Catalogue number: LN1401487
B) goat anti-Cholestocystokin from Santa Cruz (1:100). Catalogue number: sc-21617, polyclonal. Lot #B1816
C) rabbit anti-Neurotensin from Santa Cruz (1:100). Catalogue number sc-20806, polyclonal. Lot #A1910
D) goat anti-Secretin from Santa Cruz (1:100). Catalogue number sc-26630, polyclonal. Lot #H1915
E) goat anti-Somatostatin from Santa Cruz (1:100). Catalogue number sc-7819, polyclonal. Lot #E2912
F) goat anti-Serotonin from Abcam (1:1000). Catalogue number ab66047, polyclonal. Lot GR235902-22
G) rabbit anti-Gastric inhibitory protein from Abcam (1:500). Catalogue number ab22624-50, polyclonal. Lot GR325064-1
H) goat anti-Glp1 from Santa Cruz (1:100). Catalogue number sc-7782, polyclonal. Lot #K0915
I) rabbit anti-Peptide YY from Abcam (1:500). Catalogue number ab22663, polyclonal. Lot GR208949-20
J) guinea pig anti-Substance P from Abcam (1:200). Catalogue number ab10353, polyclonal. Lot GR3195542-1
K) rabbit anti-Glp1 from Abcam (1:200). Catalogue number ab22625, polyclonal. Lot GR3178933
L) donkey anti-rabbit Alexa 488 conjugated from Molecular probes (1:1000). Catalogue number A21206, lot 1927937
M) donkey anti-rabbit Alexa 568 conjugated from Molecular probes (1:1000). Catalogue number A10042, lot 1891789
N) donkey anti-rabbit Alexa 647 conjugated from Molecular probes (1:1000). Catalogue number A31573, lot 1874788
O) donkey anti-goat Alexa 488 conjugated from Molecular probes (1:1000). Catalogue number A11055, lot 1915848
P) donkey anti-goat Alexa 568 conjugated from Molecular probes (1:1000). Catalogue number A11057, lot 1711491
Q) donkey anti-goat Alexa 647 conjugated from Molecular probes (1:1000). Catalogue number A21477, lot 1739289

Validation

Antibodies A, B, C, D, E, F, G, H, L, M, N, O, P, Q are validated for the used purposes by the supplier and used in previous studies such as Basak, Beumer et al. 2017 (Ref 8). Antibody J is validated for the used purposes by the supplier and used in previous studies such as Grun et al. 2015 (Ref 7). Antibody I is validated for the purposes by the supplier and used in previous studies such as Brooks L et al. Fermentable carbohydrate stimulates FFAR2-dependent colonic PYY cell expansion to increase satiety. Mol Metab 6:48-60 (2017). Antibody K is validated for the used purposes by the supplier and used in previous studies such as Bohórquez DV et al. Characterization of basal pseudopod-like processes in ileal and colonic PYY cells. J Mol Histol 42:3-13 (2011). Additional references of all antibodies are found on the supplier websites. Antibodies H and J targeting Glp1 generated similar results, confirming specificity of the target.

Research animals

Policy information about [studies involving animals](#); [ARRIVE guidelines](#) recommended for reporting animal research

Animals/animal-derived materials

- a) Species: Mus Musculus/Strain: Tac1-IRES2-Cre; Rosa26-CAG-loxP-stop-loxP-Ai14 mice/sex: male and female/age: 8-12 weeks
 b) Species: Mus Musculus/Strain: Gcg-Venus mice/sex male: age 12-16 weeks
 c) Species: Mus Musculus/Strain: Gip-Cre; Rosa26-CAG-loxP-stop-loxP-Ai14 mice/sex: male and female/age: 8-12 weeks
 d) Other mice used for experiments were wildtype C57BL/6, male/female and age between 8 and 12 weeks.

Human research participants

Policy information about [studies involving human research participants](#)

Population characteristics

Human duodenal and ileal tissues were obtained from the UMC Utrecht with informed consent and the study was approved by the ethical committee of the UMC Utrecht (The Netherlands). Patients were diagnosed with a small or large intestinal cancer and from the resected intestinal segments, a sample was taken from normal mucosa for this study. Patients were a 75-year old male with a metastatic colorectal carcinoma, a 37-year old male with a ileal neuroendocrine tumor and a patient with a small intestinal cancer (age and gender not disclosed).

Method-specific reporting

n/a	Involvement in the study
<input checked="" type="checkbox"/>	<input type="checkbox"/> ChIP-seq
<input type="checkbox"/>	<input checked="" type="checkbox"/> Flow cytometry
<input checked="" type="checkbox"/>	<input type="checkbox"/> Magnetic resonance imaging

Flow Cytometry

Plots

Confirm that:

- The axis labels state the marker and fluorochrome used (e.g. CD4-FITC).
 The axis scales are clearly visible. Include numbers along axes only for bottom left plot of group (a 'group' is an analysis of identical markers).
 All plots are contour plots with outliers or pseudocolor plots.
 A numerical value for number of cells or percentage (with statistics) is provided.

Methodology

Sample preparation

Single-cell preparations were prepared from intestinal organoids using TrypLE and DNaseI. Single cells were stained with DAPI prior to flow cytometry to select live cells.

Instrument

Cells were sorted with a BD FACSAria II flow sorter.

Software

Data was collected using BD FACSDiva and analyzed using FlowJo (version v10)

Cell population abundance

Index sorting was performed for single cell sequencing. Single cell transcriptomes of sorted reporter positive cells confirmed high purity of each corresponding cell type. Moreover, transcriptomes always indicated presence of one cell type, suggesting no doublets were sorted. This confirms successful sorting of the respective reporters, as well as the viability of sorted cells.

Gating strategy

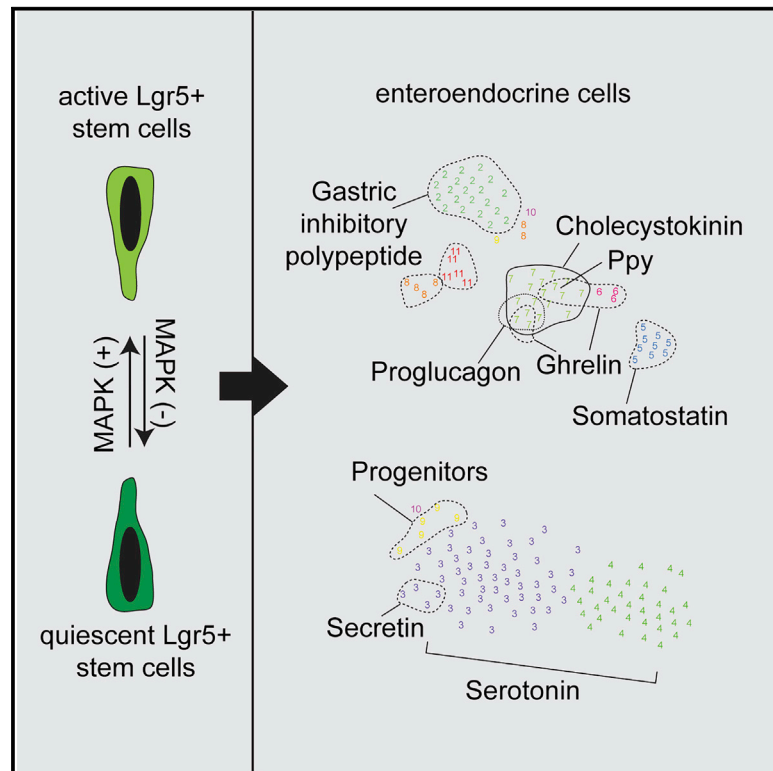
First gate: FSC-A vs DAPI (select for live, DAPI negative cells)
 Second gate: FSC-A vs SSC-A
 Third gate: SSC-W vs SSC-H
 Fourth gates: Venus (Gcg) or RFP (Tac1, GIP) vs FSC-A. Reporter positive cells generated clearly separated populations that could be easily gated for. Gating strategy is provided as Supplementary figure.

- Tick this box to confirm that a figure exemplifying the gating strategy is provided in the Supplementary Information.

Cell Stem Cell

Induced Quiescence of Lgr5+ Stem Cells in Intestinal Organoids Enables Differentiation of Hormone-Producing Enteroendocrine Cells

Graphical Abstract



Authors

Onur Basak, Joep Beumer, Kay Wiebrands, Hiroshi Seno, Alexander van Oudenaarden, Hans Clevers

Correspondence

h.clevers@hubrecht.eu

In Brief

Basak et al. identify signals to generate rare enteroendocrine cells (EECs) at high purity through manipulation of intestinal stem cell quiescence. Single-cell sequencing reveals a high level of heterogeneity in hormonal production, which is influenced by the regional identity of the intestinal organoid cultures.

Highlights

- EGFR inhibition halts DNA replication and proliferation of Lgr5+ ISC through MEK
- Lgr5+ ISCs reactivated from quiescence retain multilineage differentiation potential
- Combined EGFR/Wnt/Notch inhibition produces enteroendocrine cells with high purity
- RNA sequencing shows regional identity and heterogeneity in hormone-producing EECs

Data Resources

GSE80636



Induced Quiescence of Lgr5+ Stem Cells in Intestinal Organoids Enables Differentiation of Hormone-Producing Enteroendocrine Cells

Onur Basak,^{1,2,5} Joep Beumer,^{1,2,5} Kay Wiebrands,^{1,2,5} Hiroshi Seno,⁴ Alexander van Oudenaarden,^{1,2} and Hans Clevers^{1,2,3,6,*}

¹Hubrecht Institute, Royal Netherlands Academy of Arts and Sciences (KNAW), Uppsalalaan 8, 3584 CT, Utrecht the Netherlands

²Cancer Genomics Netherlands, UMC Utrecht, 3584 GC, Utrecht, the Netherlands

³Princess Máxima Centre, 3584 CT, Utrecht, the Netherlands

⁴Department of Gastroenterology and Hepatology, Kyoto University Graduate School of Medicine, Kyoto 606-8507, Japan

⁵Co-first author

⁶Lead Contact

*Correspondence: h.clevers@hubrecht.eu

<http://dx.doi.org/10.1016/j.stem.2016.11.001>

SUMMARY

Lgr5+ adult intestinal stem cells are highly proliferative throughout life. Single Lgr5+ stem cells can be cultured into three-dimensional organoids containing all intestinal epithelial cell types at near-normal ratios. Conditions to generate the main cell types (enterocyte, goblet cells, Paneth cells, and M cells) are well established, but signals to induce the spectrum of hormone-producing enteroendocrine cells (EECs) have remained elusive. Here, we induce Lgr5+ stem cell quiescence *in vitro* by blocking epidermal growth factor receptor (EGFR) or mitogen-associated protein kinase (MAPK) signaling pathways in organoids and show that their quiescent state is readily reverted. Quiescent Lgr5+ stem cells acquire a distinct molecular signature biased toward EEC differentiation. Indeed, combined inhibition of Wnt, Notch, and MAPK pathways efficiently generates a diversity of EEC hormone-expressing subtypes *in vitro*. Our observations uncouple Wnt-dependent stem cell maintenance from EGF-dependent proliferation and provide an approach for the study of the elusive EECs in a defined environment.

INTRODUCTION

Lgr5+ stem cells self-renew constantly throughout life at the base of intestinal crypts (Clevers, 2013). Active Notch signaling in rapidly dividing daughters specifies an enterocyte fate. Alternatively, some daughters upregulate Notch ligands (i.e., Dll1 and Dll4) immediately after leaving the crypt base niche, concomitant with an exit from the cell cycle (van Es et al., 2012). The latter cells represent secretory progenitors that give rise to Paneth, goblet, and enteroendocrine cells (EECs).

Murine Lgr5+ intestinal stem cells divide on average every 21.5 hr (Schepers et al., 2011). A reserve stem cell population

has been shown to reside above the Paneth cells at the “+4” position (Montgomery et al., 2011; Muñoz et al., 2012; Potten et al., 1978; Powell et al., 2012; Sangiorgi and Capecchi, 2008; Schepers et al., 2011; Takeda et al., 2011; Yan et al., 2012). These cells are generally non-proliferative and can replace lost Lgr5+ stem cells. An elegant lineage-tracing strategy identified these label-retaining cells as non-cycling secretory progenitors (Buczacki et al., 2013). Indeed, these secretory progenitors and the +4 cells share several molecular markers, including Hopx, Bmi1, Lrig, and Tert expression (Montgomery et al., 2011; Muñoz et al., 2012; Powell et al., 2012; Schepers et al., 2011; Takeda et al., 2011; Yan et al., 2012). Moreover, dissection of Lgr5+ crypt populations with distinct cell-cycle features suggests that Lgr5^{low} cells with slow cell-cycle kinetics are secretory precursors (Basak et al., 2014). The presence and identity of “professional” quiescent intestinal stem cells has remained elusive.

Traditionally known as defensive units against microbial infections, Paneth cells also act as part of the niche for the juxtaposed Lgr5+ stem cells by secreting Wnt3 and epidermal growth factor (EGF) and by presenting the Notch ligands Dll1 and Dll4 (Pellegrinet et al., 2011; Sato et al., 2011). Mesenchyme surrounding the crypts also contributes to the niche by secreting Wnt2b as well as several BMP inhibitors (Aoki et al., 2016; Farin et al., 2012).

The murine intestinal organoid culture system (Sato et al., 2009) generates all principle cell types of the intestinal epithelium, including Lgr5+ stem cells. The system is based on substitution of *in vivo* niche components (i.e., the Wnt agonist R-spondin-1, EGF, and the BMP inhibitor Noggin). Matrigel mimics the extracellular matrix and provides the structural basis for self-organization. R-spondin-1 is a critical component that, through interaction with its Lgr4 and 5 receptors, amplifies the Wnt3 signal emanating from Paneth cells (de Lau et al., 2011).

Organoids can be programmed to produce relatively pure populations of most epithelial cell types. High-Wnt and high-Notch conditions favoring expansion of Lgr5+ stem cells can be mimicked by the addition of the GSK3 inhibitor CHIR99021 combined with the histone deacetylase (HDAC) inhibitor valproic acid (Yin et al., 2014). Enterocytes appear under conditions of

Wnt inhibition and Notch activation (Yin et al., 2014). The addition of Rank ligand promotes the fate of M cells, which cover Peyer's patches and transport luminal antigens via transcytosis (de Lau et al., 2012). Notch inhibition generally induces secretory fates. In the absence of Wnt, secretory goblet cells are formed (van Es et al., 2005), while in the presence of Wnt, Paneth cells appear (van Es et al., 2012; Yin et al., 2014).

EECs are rare, hormone-secreting cells that are also generated from Lgr5⁺ stem cells (Barker et al., 2007). Hormones expressed by EECs regulate a wide variety of physiological responses, including gastric emptying, release of pancreatic enzymes, blood glucose levels, and appetite and mood changes. Most commonly, subtypes are distinguished based on their secreted hormones and include somatostatin⁺ (Sst) D-cells, gastric inhibitory polypeptide⁺ (Gip) K-cells, secretin⁺ (Sct) S-cells, cholecystokinin (Cck) I-cells, glucagon-like protein 1⁺ (GLP-1) L-cells, neurotensin⁺ (Nts) N-cells, and serotonin-producing enterochromaffin cells (Gunawardene et al., 2011). However, a single EEC may express multiple hormones at varying levels, underscoring a high level of heterogeneity (Egerod et al., 2012). In a recent single-cell-sequencing approach, we demonstrated that organoids faithfully generate the various EEC types and identified three additional subtypes of EECs: Tac1⁺/Cck⁺, Ucn3⁺, and Alb⁺/Afp⁺ (Grün et al., 2015). G-protein-coupled taste receptors have been identified as regulators of hormone secretion in these cells (Janssen and Depoortere, 2013). Indeed, EECs can have direct luminal contact and sense the intestinal content with microvilli. Other EECs, the so-called closed-type cells, are not exposed to the lumen (Janssen and Depoortere, 2013). Their basal process (of varying length) may form synaptic contacts with enteric neurons to connect to the nervous system. While EECs clearly play crucial roles in controlling various aspects of intestinal function and organismal metabolism, their scarcity has posed a hurdle to their in-depth study. Here, we explore methods to program organoids toward EEC fates in vitro.

RESULTS

Inhibition of EGFR Signaling Abolishes Proliferation of Lgr5⁺ Stem Cells and Induces Their Quiescence

To understand how mouse Lgr5⁺ stem cells are kept in cycle, we manipulated key signaling pathways active in the crypt niche. The Lgr5^{GFPDTR} allele (Tian et al., 2011) is never silenced in Lgr5⁺ cells (see below) and is well suited for flow-cytometry-based quantification of Lgr5⁺ cell numbers. Combining flow cytometric analysis of Lgr5^{GFPDTR/+} organoids with antibody staining against Ki67, a marker of cycling cells in all cell-cycle phases, confirmed that the overwhelming majority (94.1% ± 2.1%) of the Lgr5⁺ cells cycle in ENR (EGF, Noggin and R-spondin-1) medium (Figures S1A and S1C). Wnt signaling is reported to induce cell-cycle progression through cyclin D₂ and c-Myc expression (Myant and Sansom, 2011). We inhibited Wnt signaling using two independent methods: (1) withdrawal of R-spondin1 from the culture medium and (2) IWP-2 treatment which inhibits Wnt3 secretion by Paneth cells (Figure S1A). R-spondin-1 withdrawal caused rapid loss of Lgr5^{GFPDTR} expression (Figure S1A). IWP2 treatment (iWnt) poses a slower Wnt inhibition that depends on dilution of ligands through proliferation (Farin et al., 2016). Lgr5^{GFPDTR} expression

was gradually downregulated while stem cells differentiated into Ki67⁺ Lgr5⁻ cells upon iWnt treatment (Figures S1A and S1B). Yet, the remaining Lgr5^{GFPDTR/+} cells maintained Ki67 expression (63.5% ± 2.8% vs. 94.4% ± 2.1% in control; Figure S1C). Withdrawal of the BMP inhibitor Noggin or addition of the Notch inhibitor DAPT (iNotch) both induced a rapid decrease in Lgr5^{GFPDTR/+} cell numbers (Figure S1A) but did not affect proliferation of the remaining Lgr5^{GFPDTR/+} cells (82.3% ± 1.4% in Noggin withdrawal and 45.1% ± 10% in iNotch) (Figure S1C). Next, we inhibited EGF receptor (EGFR) signaling using gefitinib accompanied by withdrawal of EGF from the culture medium (iEGFR). While Lgr5^{GFPDTR} expression persisted (Figures S1A and S1D), the Lgr5^{GFPDTR/+} cells eventually lost Ki67 expression (13.1% ± 1.0% remaining Ki67⁺ cells) indicative of cell-cycle exit (Figures S1C and S1D). After 4 days of iEGFR treatment, Lgr5^{GFPDTR/+} cells comprised 44.4% ± 0.8% (vs. 13.6% ± 6.5% in control) of the organoids when analyzed by fluorescence-activated cell sorting (FACS) (Figures S1A and S1D).

We then focused on the early events associated with EGFR inhibition (Figure 1A). Despite extensive apoptosis of the differentiated compartments of the organoid, buds resembling crypt structures survived iEGFR treatment for at least a week (Figures 1B and S2B). Fluorescent microscopy analysis using both Lgr5^{GFPiresCreER/+} (Figure S2A) and Lgr5^{GFPDTR/+} (Figure S2B) organoids confirmed that these buds contained Lgr5⁺ cells. Of note, the Lgr5^{GFPiresCreER} allele is well suited for lineage tracing and is the strongest GFP-expressing Lgr5 allele, yet it is stochastically silenced in some cells (Barker et al., 2007). We noticed that GFP levels increased upon iEGFR treatment (Figures S2A and S2B). The *Rosa^{TCF-CFP}* Wnt signal reporter allele (Serup et al., 2012) revealed that increased Lgr5 reporter expression coincided with high Wnt activity (Figure S2B). Confocal microscopy revealed that the cellular bridges connecting buds in normal organoid cultures (ENR) slowly converted into cellular debris in iEGFR cultures (Figure 1B). Typically, iEGFR cultures contained round, crypt-like bud structures with many Lgr5⁺ cells intermingled with Lgr5⁻ cells (Figure 1C). We also noticed that organoids in iEGFR cultures were considerably smaller than controls (Figures 1C and 1D). Thus, iEGFR treatment results in smaller organoids mostly consisting of crypt-like buds with high Wnt signal strength and Lgr5 expression.

Next, we analyzed proliferation of organoids using immunofluorescence and confocal microscopy. The Ki67 protein persisted for the first 24 hr but was lost from 48 hr onward (Figures 1E and 1F). Using a short pulse of ethynyldeoxyuridine (EdU) as a measure of S phase cells, we found that iEGFR lead to a rapid halt in DNA replication as early as 24 hr, which persisted for at least a week (Figures 1E and 1F). Consistent with exit from S phase and eventually from the cell cycle, labeling the DNA content of iEGFR-treated organoids using Hoechst DNA staining confirmed that all cells were in G₀/G₁ phase (Figure S2C). 4 days after iEGFR treatment, reconstitution of EGF signaling induced rapid cell-cycle entry within 24 hr (Ki67⁺) and progression to the S phase within 48 hr (EdU⁺) (Figures 1G and S2D). Figure 1H further illustrates that Lgr5⁺ cells in iEGFR-treated organoids lacked the cell-cycle marker Ki67 and the M phase marker pH3 and did not incorporate EdU, excluding that rare dividing cells persisted during iEGFR

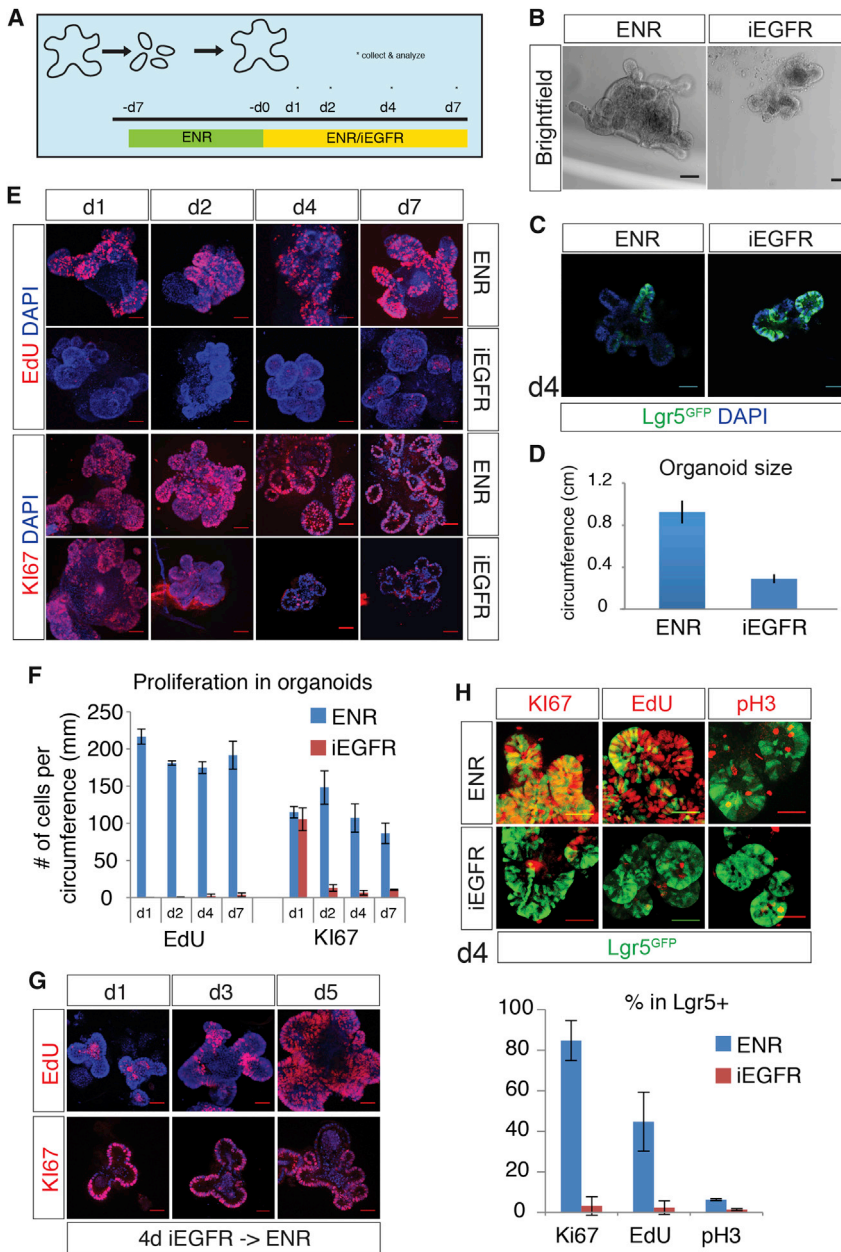


Figure 1. EGFR Inhibition Induces Cell-Cycle Exit in Intestinal Organoids

(A) Experimental setup for (B)–(H). Organoids were treated with either the EGFR inhibitor gefitinib in the absence of EGF (iEGFR) or DMSO in standard ENR medium (control) 1 week after plating in Cultrex® Basement Membrane Extract (BME). Samples were collected 1 day (d1), 2 days (d2), 4 days (d4), or 7 days (d7) after treatment.

(B) Bright-field images of intestinal organoids after 4 days of iEGFR treatment or culture in control (ENR) medium. Crypts and differentiated units are visible in ENR, while iEGFR-treated organoids mainly contain crypt-like structures that are placed closer to each other.

(C) GFP fluorescence of *Lgr5^{GFPiresCreER/+}* (green) organoids shows that *Lgr5⁺* cells persist following iEGFR treatment.

(D) Quantification of circumference of organoids after 4 days of iEGFR treatment or in control cultures.

(E) Analysis of the cell cycle in intestinal organoids. EdU was administered 1 hr prior to the sacrifice. Control (ENR) organoids continuously incorporate EdU (top panels) and express Ki67 (bottom panels), while iEGFR-treated organoids exit the cell cycle over time.

(F) Quantification of (E).

(G) Analysis of the cell cycle of iEGFR-treated organoids following reintroduction of EGF in the culture medium. Ki67 expression and EdU incorporation were analyzed 1 day (d1), 3 days (d3), or 5 days (d5) after replating in ENR.

(H) *Lgr5^{GFPiresCreER/+}* cells exit the cell cycle upon 4 days of iEGFR treatment. Phospho-histone H3 (pH3) staining was used to visualize M phase. The graph at the bottom shows the quantification. DAPI was used to visualize the nuclei.

Scale bars, 50 μ m. Error bars represent SD. All fluorescent images are confocal sections. (B) and (C) are optical sections. (E), (G), and (H) are 3D reconstructions. See also Figures S1 and S2.

treatment (Figure 1H). Altogether, our results reveal that iEGFR treatment abolishes proliferation of organoids and induces generation of quiescent *Lgr5⁺* cells.

Stem Cell Potential Is Maintained in Reactivated *Lgr5⁺* Intestinal Stem Cells

To test whether quiescent *Lgr5⁺* cells maintain stem cell potential, we used *Lgr5^{GFPiresCreER/+}Rosa^{LacZ/YFP}* mice to lineage-trace *Lgr5⁺* cells (Figure S2E). CreER induction using 4-OH tamoxifen (Tmx) led to rapid recombination of the *Rosa^{LacZ}* allele. Cre reporter that could be visualized by X-Gal staining (blue precipitate in Figure S2E). Quiescent *Lgr5⁺* cells generated upon 4 days of iEGFR treatment. Tmx was introduced to the medium during the last day of the treatment and removed

when *Egf* signaling was reactivated. Labeled and reactivated quiescent *Lgr5⁺* cells gave rise to organoids entirely labeled with X-Gal, as visualized two passages after Tmx induction. As control, labeled

Dclk1^{GFPiresCreER}Rosa^{LacZ} cells (marking tuft cells) did not generate new organoids consistent with their differentiated nature (the rare blue cells are persisting Tuft cells). Since only stem cells can generate new organoids in intestinal organoid cultures (Sato et al., 2009), these findings indicated that quiescent *Lgr5⁺* cells generated by EGFR inhibition retain their stemness.

To evaluate the cellular composition of iEGFR-treated organoids, we performed immunofluorescence analysis. Quantification of the number of marker-positive cells per organoid revealed that absolute numbers of LYZ+ Paneth cells and CHGA+ EECs were not significantly increased after 4 days in iEGFR (Figure 2A). Mucin-2 (MUC2) immunostaining revealed that a comparable amount of goblet cells were present following iEGFR treatment (Figure S2F). Tuft cells (intestinal M-cells) are rare

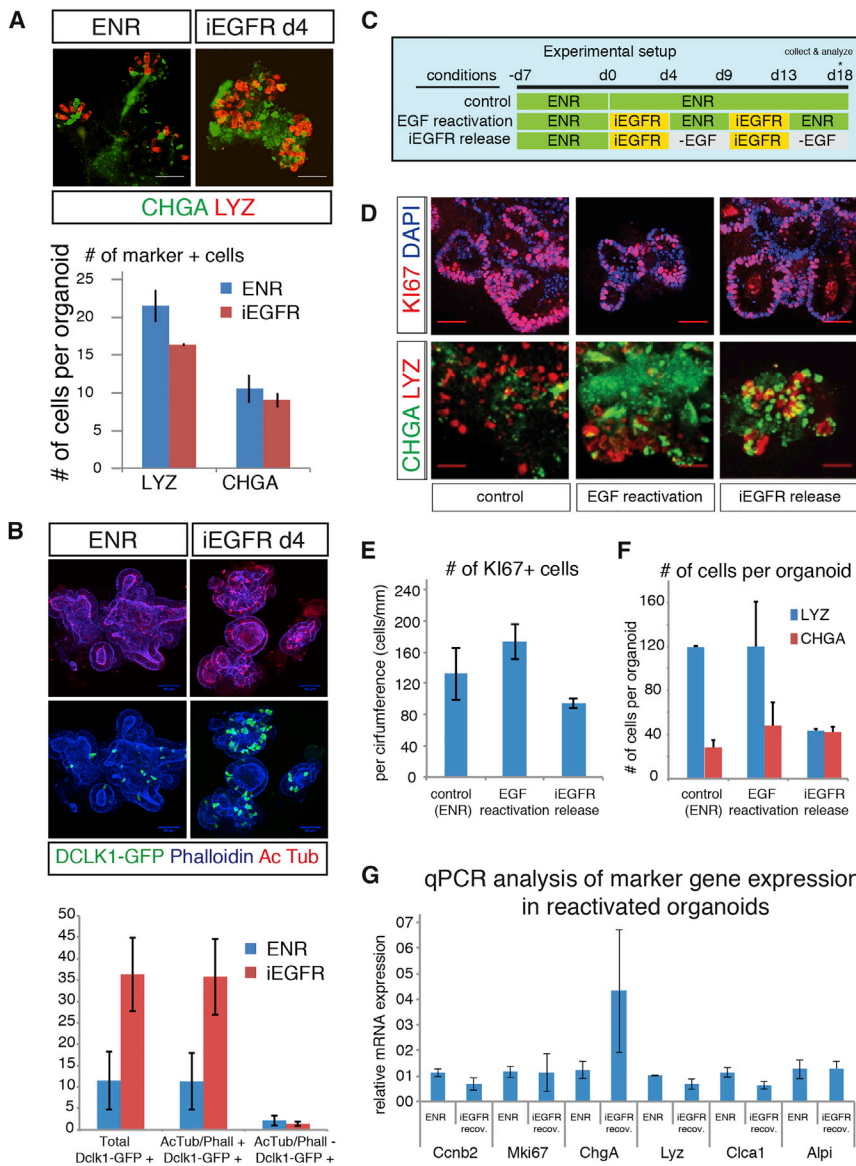


Figure 2. Differentiation Status of EGFR Inhibited and Reactivated Organoids Indicates Lineage Bias toward Enteroendocrine Cells

(A) Marker analysis of enteroendocrine cells (CHGA, green) and Paneth cells (LYZ, red) indicates that both cell types remain unchanged after 4 days of EGFR inhibition (iEGFR).

(B) Tuft cell numbers, quantified using DCLK1^{GFP} expression or with their characteristic apical actin bundles (visualized by Phalloidin and acetylated Tubulin staining), are increased after iEGFR treatment. Graph shows quantification.

(C) Experimental paradigm used to assess proliferation and differentiation potential of reactivated quiescent stem cells. Organoids were treated with EGFR inhibitor and subsequently replated in ENR medium (EGF reactivation) or medium without EGF (iEGFR release) to recover in two consecutive rounds.

(D) Proliferation (Ki67 expression) is restored after recovery from the second iEGFR treatment, indicating cell-cycle inhibition is reversible. The number of enteroendocrine cells (CHGA+), but not Paneth cells (LYZ), was increased after consecutive iEGFR treatment. This was more pronounced after iEGFR release.

(E and F) Quantification of (D). (E) The number of Ki67+ cells normalized to the circumference of the quantified sections. (F) Quantification of the absolute number of CHGA+ and LYZ+ cells per organoid.

(G) qPCR analysis of lineage markers in reactivated organoids that were cultured for 1 week in ENR following 4 days of iEGFR treatment.

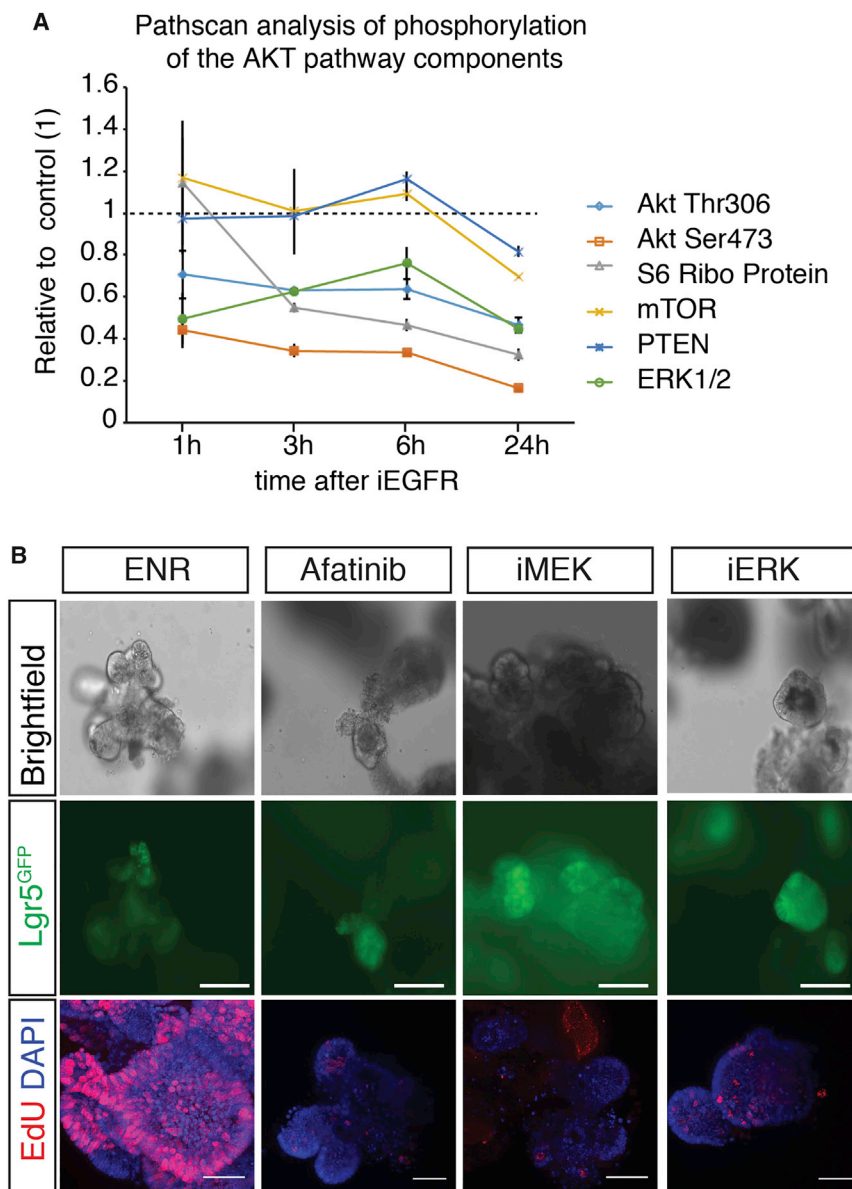
Scale bars, 50 μ m. Error bars represent SD. All fluorescent pictures are 3D reconstructions confocal images, except for top panels in (D) that show optical confocal sections. See also Figure S2.

mechanosensory cells involved in response to parasitic invasion (Howitt et al., 2016). Apical actin bundles that are revealed by acetylated tubulin and F-actin (Phalloidin) staining distinguishes Tuft cells (Höfer and Drenckhahn, 1996). The number of Tuft cells per organoid increased upon iEGFR treatment (Figure 2B). We corroborated these results using the Dclk1^{GFPiresCreER} allele (Nakanishi et al., 2013), revealing that iEGFR treatment increased the absolute number of Dclk1+ Tuft cells 3.2-fold (11.3 ± 6.6 in ENR and 35.8 ± 8.8 in iEGFR; Figure 2B). GFP-marked cells almost invariably contained acetylated tubulin bundles confirming the specificity of the Dclk1 allele (Figure 2B). The absence of EEC, Paneth cell, and Tuft cell markers in Lgr5^{GFPiresCreER} cells argued against upregulation of Lgr5 in differentiated cells (Figure S2G). Thus, continuous EGFR inhibition drives Lgr5+ cells into quiescence and leads to a loss of proliferating cells. However, this treatment provokes no change in the absolute number of differentiated cells, with the exception of inducing an increase in Tuft cell numbers.

restored to control levels (Figures 2C–2E). Some proliferation was even restored in the absence of exogenous EGF, likely due to endogenous EGF secreted by Paneth cells (Figures 2C–2E). These findings indicated that iEGFR-induced quiescence is reversible and that quiescent stem cells maintain their self-renewal potential.

While the absolute number of LYZ+ Paneth cells was not changed upon EGFR reactivation compared to the controls, CHGA+ EEC numbers were somewhat increased (Figures 2D and 2F). Similarly, absolute numbers of CHGA+ cells were higher in the absence of exogenous EGF, even though organoid size was considerably smaller compared to control organoids (Figures 2D, 2E, and S2H).

To corroborate these findings, we analyzed marker gene expression for key cell types in reactivated organoids using qPCR (Figure 2G; Table S5). After 1 week of reactivation, expression of proliferation markers Ki67 and Ccnb2 were restored to control levels. Moreover, lineage markers for Paneth cells (Lyz),



Goblet cells (Gob5), and enterocytes (Alpi) were restored to near-normal ratios. Expression of the EEC marker Chga was elevated upon reactivation (Figure 2G). Thus, all lineages could be generated from reactivated Lgr5⁺ cells, suggesting that EEC generation is enhanced by reduced EGF/EGFR signaling.

MAPK Signaling Downstream of EGFR Controls Intestinal Stem Cell Proliferation

Mitogen-associated protein kinase (MAPK) signaling is a major downstream target of EGFR signaling pathway and regulates cell-cycle progression. MAPK kinase (MEK) phosphorylates MAPK (ERK) to induce its nuclear localization and activation. Phosphatidylinositol 3-kinase (PI3K)/AKT pathway is also downstream of EGFR and is, for instance, implicated in neuroendocrine tumors (Banck et al., 2013). To quantify changes in ERK phosphorylation and AKT pathway activation, we used PathScan array analysis (Figures 3A and S3A). Phosphorylation

Figure 3. EGFR-Signaling-Induced Cell-Cycle Exit Is Mediated by the MAPK Signaling Pathway

(A) PathScan analysis of EGFR-inhibited organoids. AKT and ERK pathways are effectively inhibited after 1 hr of EGFR inhibition, which is maintained over 24 hr.

(B) Single inhibition of MEK (iMEK) or ERK (iERK) as well as simultaneous inhibition of EGFR and ErbB-2 using afatinib yields similar results to gefitinib-induced EGFR inhibition. EdU is added to the culture medium 1 hr before the sacrifice. Middle panels show endogenous GFP expression from the Lgr5^{GFPiresCreER} allele. DAPI is used to visualize the nuclei in the bottom panels.

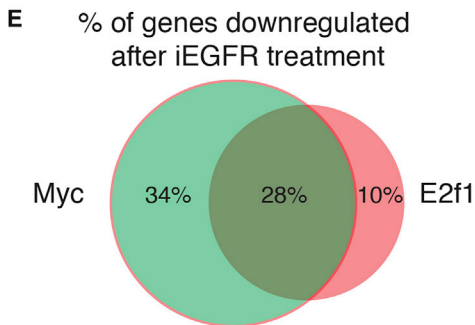
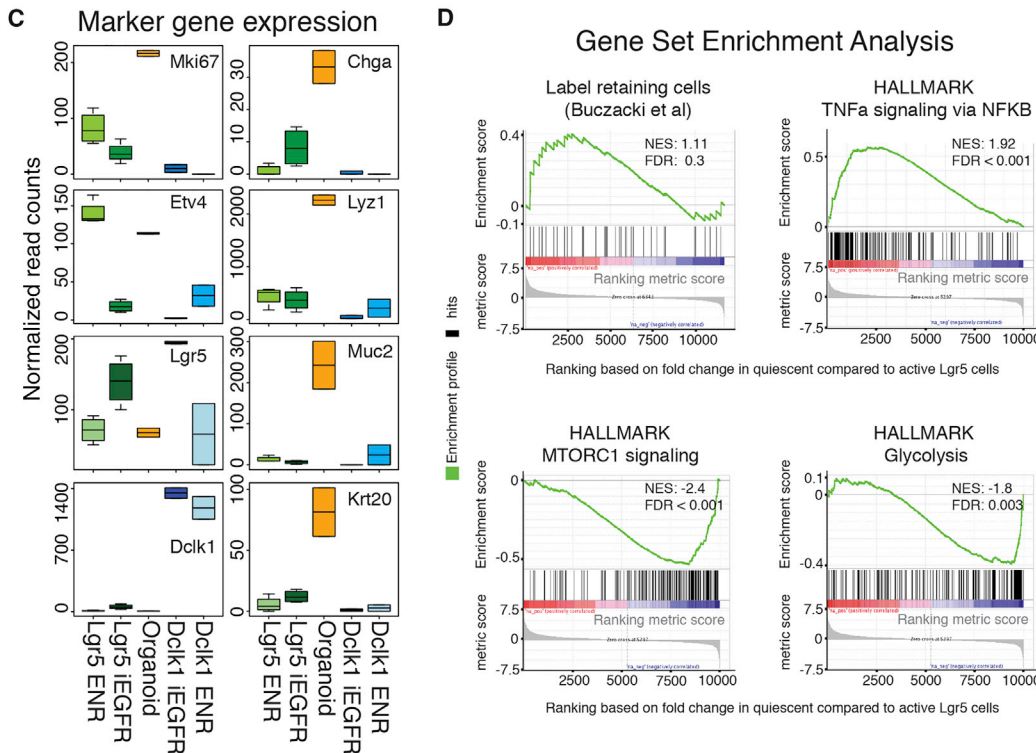
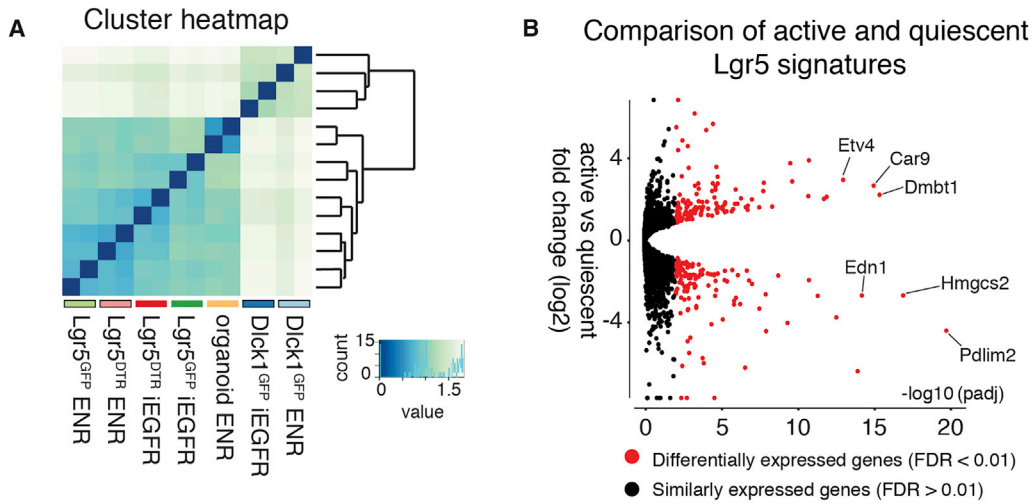
Scale bars, 50 μ m. Error bars represent SD. See also Figure S3.

of both ERK/2 and AKT at Thr306 and Ser473 was reduced as early as 1 hr after iEGFR treatment of organoids and remained low 24 hr after treatment (Figure 3A). S6 ribosomal protein phosphorylation, a target of AKT signaling, dropped after 3 hr, while mTOR and PTEN phosphorylation was reduced only after 24 hr (Figure 3A).

To evaluate the temporal change of ERK phosphorylation upon iEGFR treatment, we performed immunohistochemistry. iEGFR reduced ERK phosphorylation as early as 1 hr after treatment, consistent with the PathScan results (Figure S3B). However, we observed a gradual and partial recovery in phospho-ERK (pERK) levels within 48 hr, despite continuing quiescence (Figure S3B). Thus, we asked whether MEK/ERK signaling is essential for cell-cycle progression of intestinal stem cells using small inhibitors for either MEK (PD0325901; Mek1) or ERK (SCH772984; Erki). Both inhibitors induced quiescence of Lgr5⁺ cells, implying that the ERK pathway downstream of EGFR is required for proliferation of Lgr5⁺ cells (Figure 3B). The use of afatinib, which inhibits both EGFR and ErbB2, yielded similar results (Figure 3B). These results indicated that inhibition of MAPK signaling could induce a reversible quiescent state in intestinal organoid stem cells, similar to iEGFR treatment. These data implied that decreased MAPK/ERK signaling suffices for cell-cycle exit of Lgr5⁺ cells.

RNA Sequencing Reveals the Molecular Signature of Quiescent Lgr5⁺ Stem Cells

To better understand the molecular characteristics of quiescent Lgr5⁺ cells, we performed bulk RNA sequencing on FACS-isolated control (DMSO) and quiescent (iEGFR treatment, day 4) Lgr5⁺ stem cells. We included both Lgr5^{GFPiresCreER/+} (n = 2) and Lgr5^{GFPDTR/+} (n = 2) organoids in our study to observe



(legend on next page)

potential differences in Lgr5 reporter expression. We also included sorted Tuft cells (using the $Dcl1^{GFPiresCreER/+}$ allele) for comparison. Whole control organoids cultures were sequenced as a reference population. Hierarchical clustering and principal-component analysis (PCA) revealed that quiescent Lgr5+ cells were more similar to active Lgr5+ stem cells than to whole organoids or Tuft cells (Figures 4A and S4A). Differential gene expression analysis between active and quiescent Lgr5+ cells revealed 533 differentially regulated genes, 290 of which were enriched in quiescent Lgr5+ cells (false discovery rate [FDR] < 0.01 Figures 4B and S4B; Table S1). Transcriptional targets of the Erk pathway (Etv4 [7.7x, p-adj < 0.001] and Etv5 [7.7x, p-adj < 0.001]) were downregulated in quiescent Lgr5+ stem cells, confirming efficient Erk inhibition (Figures 4C and S4B). Similarly, several cell-cycle-associated genes, such as Ccnb1 (2.1x, p-adj < 0.005) and Ccnb2 (1.9x, p-adj < 0.05), were decreased, consistent with cell-cycle arrest (Figure S4B). Gene Ontology (GO) analysis of the genes downregulated upon iEGFR treatment confirmed a clear loss of cell-cycle-associated genes (Figure S4C). In line with our reporter expression, we observed a significant increase in some of the well-known Wnt target genes, including Rnf43 (2.3x, p-adj < 0.005) and Lgr5 (2x, p-adj < 0.05) (Figure S4B). We also noticed a strong increase of members of the AP-1 family of transcription factors (Junb, Fos, and Fosb) in quiescent Lgr5+ cells (Figures 4C and S4B). Early markers for Paneth cells (Lyz1), enterocytes (Alpi1), and goblet cells (Muc2) remained unchanged (Figure 4C). Chga, expressed by EECs and their precursors, was 7.3-fold higher in quiescent compared to active Lgr5+ stem cells (Figure 4C). Similarly, while Dcl1 (6x, p-adj < 0.05) and some other Tuft cell markers increased upon iEGFR treatment, their levels were significantly lower in quiescent Lgr5+ cells than in Tuft cells (Figure 4C). These results confirmed our confocal analysis and highlighted key molecular changes in Lgr5+ stem cells upon quiescence entry.

The increase in per cell-Chga expression as well as the high CHGA+ cell numbers generated in the absence of EGF (Figures 3D and 3F) were reminiscent of the label-retaining secretory precursors (LRCs) described by Winton and colleagues (Buczacki et al., 2013). Indeed, gene set enrichment analysis (GSEA) revealed that the LRC signature is more similar to quiescent than to active Lgr5+ stem cells (Figure 4D; see STAR Methods). 12 out of 37 of the LRC genes were in the core enrichment group and included the EEC-related genes Chga, Chgb, Cldn4, Gip, and Ghrl2 (Table S2). Next, we analyzed the distribution of the “hallmarks” gene sets provided on the GSEA dataset (Figures 4D and S4D; Table S3). Analysis revealed an enrichment of “E2F targets” and “MYC targets V1 and V2” in active stem cells

(Figure S4D). X2K transcription factor target analysis confirmed that 72% of the genes downregulated after iEGFR were targets of either MYC (62%) or E2F1 (38%) (Figure 4E). In addition, mTORC1-associated genes were downregulated upon EGFR inhibition (Figure 4D). The analysis also revealed a metabolic shift upon quiescence entry; genes associated with glycolysis, oxidative phosphorylation, and cholesterol metabolism were downregulated in quiescent stem cells (Figures 4D and S4D). On the other hand, quiescent stem cells were enriched in genes associated with tumor necrosis factor α (TNF- α) signaling via nuclear factor κ B (NF- κ B), interferon gamma response genes, and JAK-STAT3 signaling (Figure 4D; Table S3). In brief, GSEA analysis suggested that loss of proliferation might be driven by decreased of MYC/E2F1 activity. Quiescent stem cells downregulate several metabolic pathways and upregulate a signature related to TNF- α and JAK-STAT3 signaling (Figures 4D and S4D).

Combined Inhibition of the Wnt, Notch, and EGFR/MAPK Pathways Induces EEC Fate

We next aimed to establish a protocol for EEC differentiation. Inhibition of Notch signaling by DAPT treatment (iNotch) lead to a large increase in the number of LYZ+ Paneth cells (Figure 5A). Inhibition of Wnt secretion using IWP-2 (iWnt) in combination with iNotch abolished Paneth cell differentiation and induced EECs and goblet cells (Figure 5A). iEGFR treatment spared both Paneth cells and EECs (Figure 5A). Combined inhibition of WNT/Notch/EGFR pathways (iWnt/iNotch/iEGFR) resulted in a massive increase in EECs while inhibiting Paneth cell differentiation (Figure 5A). Similarly, inhibiting Mek together with Wnt and Notch signaling pathways (iWnt/iNotch/iMek) increased CHGA+ EEC numbers (Figure 5C). qPCR analysis confirmed that goblet cell differentiation induced by iWnt/iNotch treatment is countered by both iEGFR and iMek treatments (Figure S5A).

We used cleaved caspase-3 staining to evaluate cell death in these organoids. Only rare apoptotic cells were visible in the “crypt domain” of both standard and iWnt/iNotch/iMek-treated (24 hr) organoids. Similar to the controls, apoptosis was restricted to the “villus domain” upon iWnt/iNotch/iMek treatment (Figure S5D). These results implied that EECs are generated by altered cell-fate choice rather than massive apoptosis of remaining cell types.

We further analyzed the expression of EEC-related genes in differentiated organoids (Figure S5A). Expression of the pan-EEC marker Chga was 25-fold higher in iWnt/iNotch/iEGFR-treated organoids and over 100-fold higher in iWnt/iNotch/iMek-treated organoids (Figure S5A). Concordantly, expression of Sst (55x), Gip (14x), Sct (5x), cholecystokinin (15x), and glucagon (Gcg/Proglucagon, 4x) mRNA were upregulated

Figure 4. RNA Sequencing Identifies Key Molecular Differences between Quiescent and Active Lgr5+ Stem Cells

(A) Hierarchical clustering of the whole transcript of sorted Lgr5+ cells using the $Lgr5^{GFPDTR/+}$ ($Lgr5^{DTR}$), $Lgr5^{GFPiresCreER/+}$ ($Lgr5^{GFP}$), and Tuft cells using the $Dcl1^{GFPiresCreER/+}$ ($Dcl1$) organoids cultured in control medium (ENR) or upon EGFR inhibition (iEGFR) based on Pearson's correlation. Control organoids were added as a reference. Colors indicate Pearson correlation.

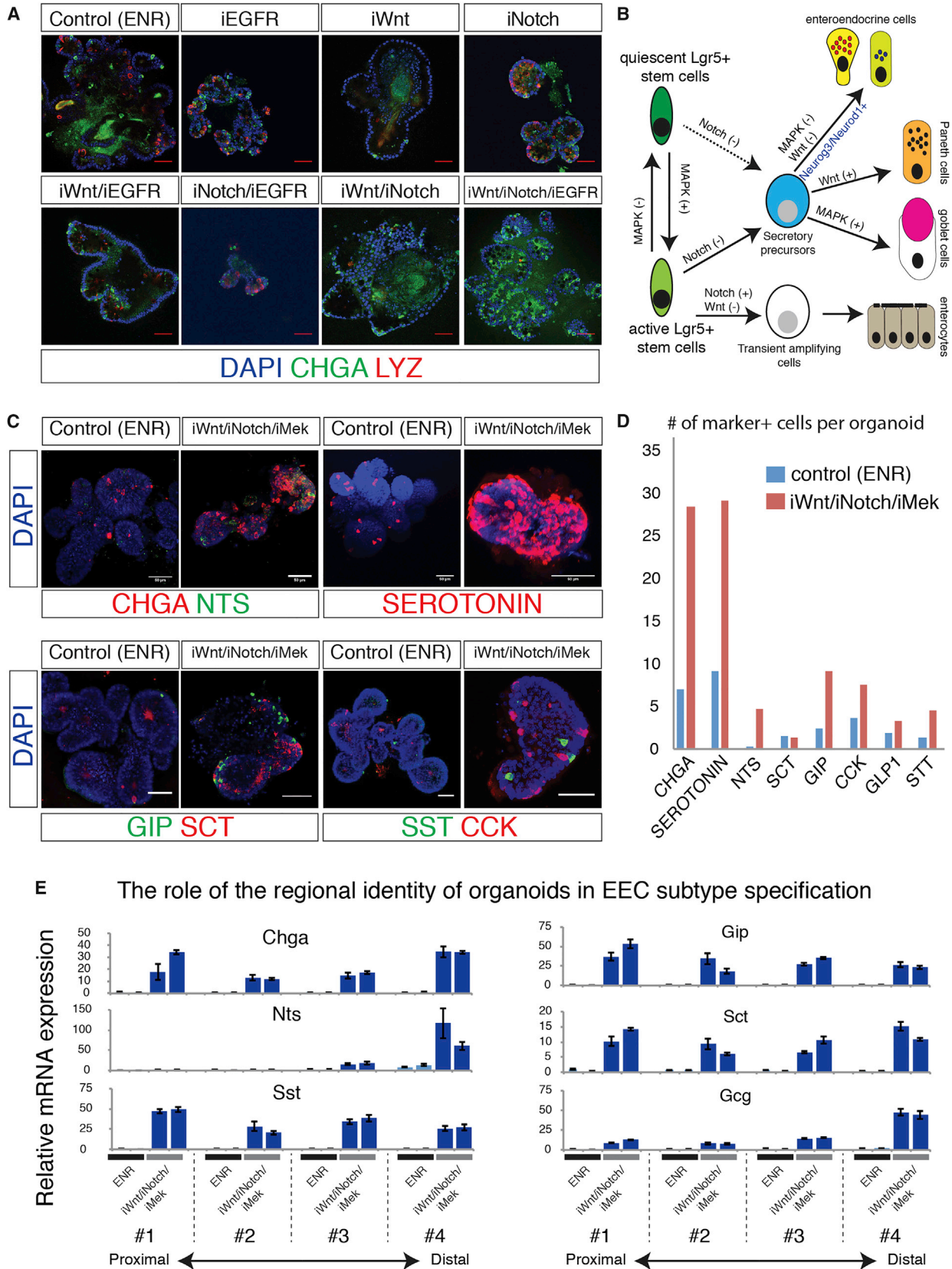
(B) Volcano plot comparing active and quiescent Lgr5 signatures. x axis shows adjusted p value (q value, in $-\log_{10}$), and y axis shows fold change (in \log_2). Each dot represents a gene; differentially expressed genes (false discovery rate < 0.01) are in red.

(C) Boxplots displaying normalized expression values of marker genes.

(D) Gene set enrichment analysis (GSEA). Fold change in gene expression in quiescent and active Lgr5+ stem cells is compared. Green line shows enrichment profile. Black bars show where genes from a given gene set are located (hit). NES, normalized enrichment score; FDR, false discovery rate.

(E) Expression2kinase (X2K) analysis showing key transcription factors targeting the active Lgr5+ stem cell signature.

Error bars indicate SD. See also Figure S4 and Tables S1–S3.



(legend on next page)

upon iWnt/iNotch/iEGFR treatment, following a similar trend to iWnt/iNotch/iMek treatment (Figure S5A). Nts was the sole hormone analyzed that was expressed at control levels. Thus, our protocol generated high numbers of most subtypes of EECs (Egerod et al., 2012).

To visualize hormone production at the protein level, we used immunofluorescence (Figure 5B). We focused on the iWnt/iNotch/iMek condition, which yielded the highest CHGA+ cell numbers among the conditions tested (Figures 5C and 5D). The different EEC subtypes are rare in normal intestinal organoid cultures (Figure 5C). iWnt/iNotch/iMek treatment resulted in a robust increase in the number of CHGA, NTS, SEROTONIN, GIP, SCT, SST, and CCK+ cells (Figures 5C and 5D; Table S5). This implied that EECs induced in our culture system are functionally mature.

Regional Identity of Intestinal Organoids Determines EEC Heterogeneity

The intestinal tract displays regional differences in EEC subtype representation. We asked whether the regional origin of organoid cultures affects the EEC subtypes generated. Of note, a previous study demonstrated that gut organoids retain at least some aspects of their regional identity upon long-term culture (Middendorp et al., 2014). We established organoids from four different regions (duodenum to ileum) of the intestinal tract and analyzed EEC-related gene expression upon iWnt/iNotch/iMek using qPCR. iWnt/iNotch/iMek treatment induced Chga expression in all cultures when compared to standard culture conditions (Figure 5E). Nts- and Gcg-expressing cells predominantly reside in the distal small intestine (SI) region, whereas Gip-expressing cells follow the opposite trend (Drucker and Nauck, 2006; Kitabgi and Freychet, 1978; Parker et al., 2009). Consistently, Nts and Gcg expression was much more strongly upregulated in the distal than the proximal organoids (Figure 5E). Conversely, while all regions upregulated Gip upon iWnt/iNotch/iMek treatment, levels were higher in organoids of a proximal origin. Organoids from all regions efficiently expressed Sst and Sct upon differentiation (Figure 5E). We conclude that while our induction protocol is applicable to organoids from all intestinal regions, the regional source of organoids affects the outcome in terms of specific EEC subtypes.

As the PI3K/Akt/mTOR pathway is reduced upon iEGFR and may also affect EEC differentiation, we inhibited mTOR signaling using Azd8055 (iTOR) (Figure S5B). Inhibition of iTOR on a iWnt/iNotch background did not further increase CHGA+ cell numbers. On the contrary, iTOR treatment abrogated the increase in CHGA+ cell numbers when combined with iWnt/iNotch/iEGFR

treatment (Figure S5B). qPCR analysis revealed decreases in Chga, Sst, Gip, Sct, Cck, and Gcg upon iTOR treatment (Figure S5C). Thus, while its levels are reduced upon iEGFR treatment, iTOR signaling is required for efficient generation of EECs by our induction protocol.

To better characterize the quiescent stem cell (iMek and iEGFR) and EEC (iWnt/iNotch, iWnt/iNotch/iEGFR, and iWnt/iNotch/iMek) induction protocols, we performed RNA sequencing on bulk cultures at 6 hr and 96 hr (Figure 6A). PCA and hierarchical clustering revealed three distinct groups (Figures 6A and S6A). First, all organoids treated for 6h clustered together with untreated organoids isolated at 6 hr and 96 hr. iMek- and iEGFR-treated organoids clustered closely together in PCA space, consistent with the notion that both induce quiescent Lgr5+ stem cells. iWnt/iNotch, iWnt/iNotch/iEGFR, and iWnt/iNotch/iMek cultures were distinct at 96 hr (Figures 6A and S6A). Separate samples from the same treatment group clustered closely together, confirming the reproducibility of the treatments (Figures 6A and S6A). Expression of the Erk target gene *Etv4* is lost at 6 hr in both iMek (7.2-fold; FDR < 0.001) and iEGFR (4.6-fold; FDR < 0.005), confirming efficient inhibition.

Next, we used our dataset to directly compare the effects of iEGFR and iMek treatments. We measured the number of differentially expressed genes (FDR < 0.01) to visualize the differences between samples. At both 6 hr and 96 hr, iEGFR (1,440 and 1,307 differentially expressed genes at 6 hr and 96 hr, respectively) and iMek (1,147 and 1,631 differentially expressed genes at 6 hr and 96 hr, respectively) treatments induced massive changes of the transcriptomes of the organoids (Figure S6B, red dots indicate differentially expressed gene). Transcriptomes of iMek- and iEGFR-treated cultures were almost identical at both time points (5 and 88 differentially expressed genes at 6 hr and 96 hr, respectively). iWnt/iNotch/iEGFR (3,847 differentially expressed genes) and iWnt/iNotch/iMek (3,166 differentially expressed genes) treatments were drastically different from controls at 96 hr. While organoids subjected to both treatments clustered together at 96 hr (Figure S6A), 267 genes were differentially expressed between EEC cultures differentiated with iWnt/iNotch/iEGFR versus iWnt/iNotch/iMek treatments. Most noticeable genes were goblet cell-related factors, such as *Clca1* (2.4-fold, $p < 0.001$) and *Zg16* (2.5-fold, $p < 0.001$; Figure 6B). In conclusion, while iEGFR and iMek treatments can be used interchangeably in the context of quiescent stem cell induction, iMek is more efficient in countering goblet cell differentiation.

Next, we scrutinized EEC differentiation. At 96 hr, Chga and Chgb expression were highly elevated in iWnt/iNotch/iEGFR

Figure 5. Derivation of a High-Purity EEC Culture

- (A) Marker analysis of enteroendocrine cells (CHGA, green) and Paneth cells (LYZ, red). Organoids were treated for 4 days with the Notch inhibitor DAPT (iNotch), the inhibitor of Wnt secretion IWP-2 (iWnt), gefitinib (iEGFR), or a combination of these treatments. DMSO was used as a control. Images show optical sections.
- (B) Model shows critical signaling pathways manipulated in organoids for directed differentiation of intestinal stem cells.
- (C) Inhibition of Mek signaling (iMek) together with Wnt and Notch signaling pathways (iWnt/iNotch/iMek) similarly increases enteroendocrine cell numbers (CHGA+). Neurensin (NTS), serotonin, gastric inhibitory polypeptide (GIP), secretin (SCT), somatostatin (SST), and cholecystokinin (CCK)-positive cell numbers dramatically increase. Representative 3D reconstruction confocal images are shown.
- (D) Quantification of the number of enteroendocrine cell markers per organoid upon iWnt/iNotch/iMek treatment.
- (E) Regional identity of organoids is maintained in terms of enteroendocrine cell subtypes. Organoids were isolated from proximal-to-distal (#1–#4) small intestine. Distal organoids have higher levels of Nts and Gcg levels, while Gip is enriched proximally. Scale bars, 50 μ m. Error bars indicate SD. See also Figure S5 and Table S5.

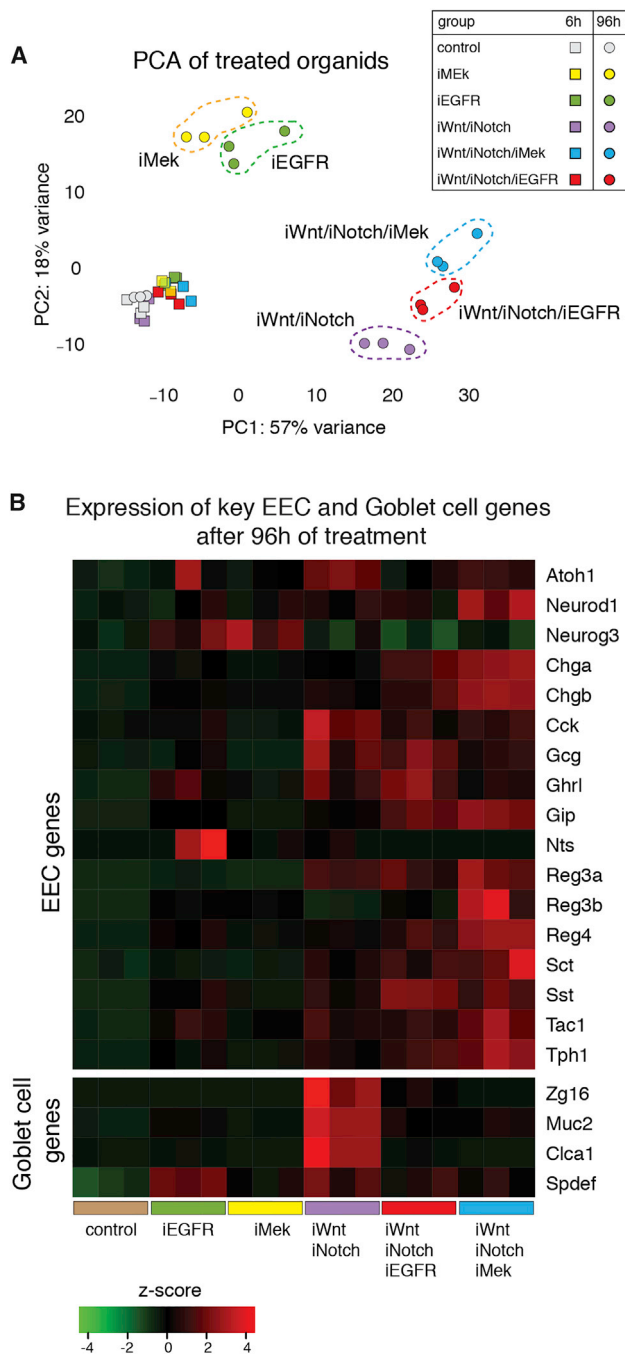


Figure 6. Characterization of Organoids following Different Induction Regimens using RNA Sequencing

(A) Principal-component analysis (PCA) of the transcriptomes of samples treated with iMek, iEGFR, iWnt/iNotch, iWnt/iNotch/iEGFR, iWnt/iNotch/iMek, and DMSO-treated controls. Samples were analyzed after 6 hr (6h, square) or 96 hr (96h, circle) of treatment.

(B) Heatmap showing the expression of key genes related to enteroendocrine cell (EECs) and goblet cells at 96 hr. Color code shows the Z score for each gene along the whole dataset.

See also Figure S6.

and iWnt/iNotch/iMek treatments (Figure 6B). Similarly, most EEC genes, including *Gip*, *Sst*, *Sct*, *Tac1*, *Tph1*, and *Reg4*, were increased in both conditions. We noticed that expression of *Cck*, *Gcg*, *Ghrl*, and *Reg3a* was upregulated in iWnt/iNotch and not further enhanced by the addition of iEGFR and iMek (Figure 6B). *Nts* expression was not enriched following our EEC differentiation protocols, most likely because duodenum organoids were used. Even so, NTS was clearly expressed by rare cells (Figures 5D and 6B). In brief, both iWnt/iNotch/iEGFR and iWnt/iNotch/iMek conditions efficiently induce generation of multiple EEC subtypes, even though the ratio of the subtypes generated is different.

Single-Cell Sequencing Reveals Heterogeneous EECs in Reactivated Cultures

We previously used single-cell sequencing to reveal EEC subtypes in vivo (Grün et al., 2015). To elucidate the cellular composition of induced organoids and the extent of heterogeneity in hormone expression, we performed single-cell RNA sequencing (Figure 7). We sorted live single cells (without additional markers) from iWnt/iNotch/iEGFR- and iWnt/iNotch/iMek-treated organoids. Among the 289 cells that passed our filtering, we identified a cluster of 94 cells as enterocytes enriched in *Aldob* (4.9 \times , p -adj < 0.001), *Apoa1* (12.6 \times , p -adj < 0.001), and *Alpi* (5.6 \times , p -adj < 0.001) (Figures S7A and S7B). These were interpreted as surviving post-mitotic enterocytes and were excluded from further analysis. Cells derived from both iWnt/iNotch/iEGFR- and iWnt/iNotch/iMek-treated organoids were distributed similarly in t-distributed stochastic neighbor embedding (t-SNE) space and were analyzed together (Figure S7C).

Using RaceID2 (Grün et al., 2016), we identified 12 distinct clusters of cells (Figures 7A and 7B). k-medoids clustering of the Pearson correlation of cellular transcriptomes revealed a clear separation between clusters as well as possible heterogeneity within clusters (e.g., 7 and 8, Figure 7A). Differential gene expression analysis revealed signature genes for each cluster, which we used to classify cell types (Table S4). The most prominent clusters (“3” [53 cells] and “4” [35 cells]) expressed the pan-EEC markers *Chga* and *Chgb* (Figures 7C and S7D). *Chga* and *Reg4* expression formed a gradient, both being higher in cluster 4. Hormonal production in these *Chgb* high clusters was best defined by *Tac1* and *Tph1* expression, both markers of enterochromaffin cells (Figures 7B, 7C, and S7D). *Tac1* encodes for the hormone substance P, while *Tph1* encodes for the rate-limiting enzyme in serotonin synthesis (Egerod et al., 2012; Grün et al., 2015). Substance P and serotonin may act as neurotransmitters exciting the connected enteric neurons (Latorre et al., 2016). The other clusters displayed relatively low levels of *Chga* and *Chgb* transcripts but included cells expressing peptide hormones (Figures 7C and S7D). Cluster 2 (21 cells) was marked by *Gip* expression (74 \times) that is expressed by K-cells. *Fabp5* was also highly enriched in this cluster (12.6 \times), consistent with its role in *Gip* secretion (Shibue et al., 2015). Members of cluster 5 (nine cells) expressed very high levels of *Sst* (182 \times), identifying them as D-cells (Figure 7C). Ghrelin (*Ghrl*) expression was present in more than one cluster but was highest in cluster 6 (19 \times , three cells). We also noticed that *Isl1* (*Isl-1*; 9.7 \times) was co-expressed with *Ghrl* in these cells. *Isl1* plays an important role in cell fate specification, and its loss leads

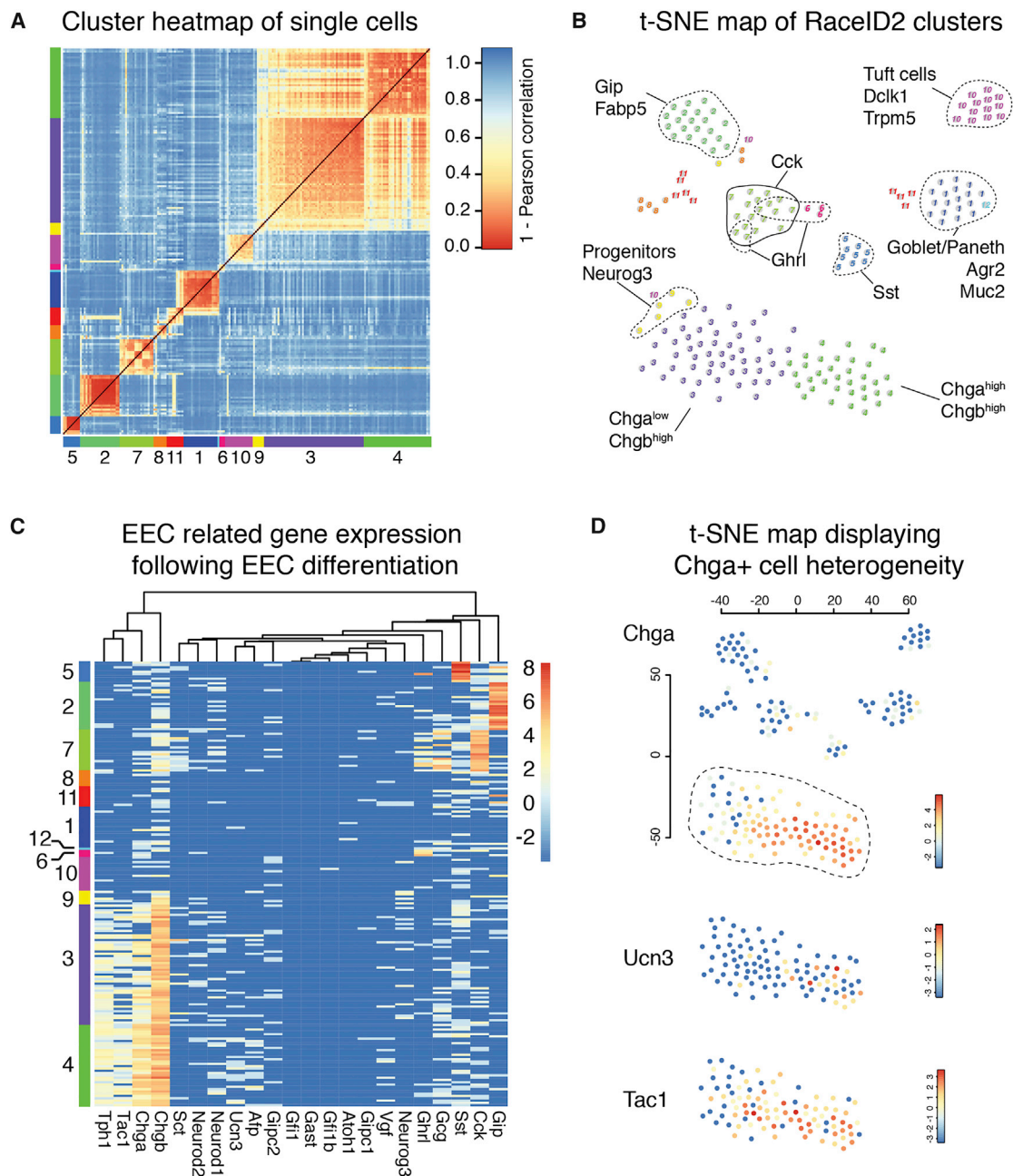


Figure 7. Single-Cell Transcriptome Profiling Reveals Heterogeneity among Induced EECs

(A) Heatmap displaying k-medoids clustering of Pearson's correlation of the whole transcriptome of individual live organoid cells from iWnt/iNotch/iEGFR and iWnt/iNotch/iMek experiments after filtering. Numbers indicates clusters. The colors code for Pearson's correlation.

(B) t-SNE map depicting individual cells and cluster numbers assigned by RaceID2.

(C) Heatmap displaying the log₂ transformed color-coded transcript counts of respective genes related to the enteroendocrine lineage.

(D) t-SNE map displaying the heterogeneous expression of Ecn3 and Tac1 transcripts by Chga high cells.

See also [Figure S7](#) and [Table S4](#).

to impaired glucose homeostasis (Terry et al., 2014). Cells in cluster 7 (18 cells) all highly expressed Cck (55.7 \times).

One of the early inducers of EEC differentiation is neurogenin-3 (Neurog3), which is followed by Neurod1. Neurog3 (5.2 \times) expression was highest in cluster 9 (six cells) and in some cells of cluster 3 that were most similar to cluster 9.

Virtually all EEC clusters contained Neurod1-expressing cells (Figure 7B). Given the temporal expression of these transcription factors, we propose that cluster 9 represents EEC progenitors, which through Neurod1 generate a panel of EECs. Cluster 1 (18 cells) was enriched in goblet cell- and Paneth cell-related genes, such as Agr2 (33 \times), Muc2 (26 \times), Ttf3 (23 \times), and

Defa24 (28 \times). Despite the filtering, some enterocyte-like cells expressing Aldob and Mt1/2 remained (cluster 8, seven cells). Dclk1 and Trpm5 expression identified cluster 10 (15 cells) as Tuft cells (Figures 7B and S7C). In total, 145/289 cells (50% of all cells) analyzed were EECs or their progenitors, confirming the efficiency of our induction protocol.

Since multiple hormones can be co-expressed in the same cell, we addressed the heterogeneity of hormone expression at the single-cell level (Figure 7C). Focusing on EEC-related gene expression, we identified occasional expression of multiple different hormones in a single cell (Figure 7B). This was in line with our previous report on EECs from freshly isolated intestinal epithelium (Grün et al., 2015). A prominent example is cluster 7, where Cck+ cells also expressed Gcg (28.2 \times), Ghrl (5.3 \times), or Pyy (11.4 \times). Consistently, l-cells have been reported to co-express Cck with other hormones at varying levels (Egerod et al., 2012). Transcriptomes of Sst+ cells were more homogeneous, co-expressing low levels of Gip and Cck, while one cell co-expressed Ghrl only. We previously reported partial overlap between Cck+ and Tac1+ cells (Grün et al., 2015). Consistently, some of the Tac1+ cells in clusters 3 and 4 expressed low levels of Cck (Figures 6B and 6C). Similar to their in vivo counterparts, EECs induced with our protocol contained Chga+ Tac1+ Ucn3+, Chga+ Tac1+ Ucn3-, and Chga+ Tac1- Ucn3- cells (Figure 7D). Thus, EECs generated in our cultures recapitulate EEC heterogeneity seen in the intestinal epithelium in vivo. Taken together, our single-cell analysis indicated that the protocol induces EEC fates in ~50% of organoid cells based on marker gene expression.

DISCUSSION

Here, we identify EGF signaling as an indispensable driver of Lgr5+ stem cell proliferation in organoids. Under conditions where Wnt signaling is untouched but EGF signaling is blocked, actively dividing Lgr5+ stem cells convert into quiescent Lgr5+ cells that retain expression of various Wnt target genes. This cellular state can be maintained for up to a week. Yet, the simple restoration of EGF signaling converts the quiescent cells back into their normal active stem cell state. In organoids as well as in crypts, Lgr5+ cells are always the direct neighbors of the Wnt3-secreting Paneth cells (Sato et al., 2011). In this setting, Wnt3 does not diffuse over distances, but is loaded directly onto the Lgr5+ stem cells (Farin et al., 2016). The quiescent Lgr5+ stem cells remain juxtaposed to the Paneth cells in iEGFR treated organoids and are thus exposed to high local Wnt signals. Indeed, three independent Wnt target gene alleles as well as gene expression analyses confirmed robust Wnt signaling upon EGFR inhibition. In sum, our results show that maintenance of stem cell fate requires Wnt, but not EGF, whereas stem cell proliferation depends on the combination of Wnt and EGF. Whether quiescent stem cells are more competent to remain in the niche when in competition with dividing stem cells remains an open question.

Previous studies have identified quiescent cells located close to the zone of differentiation at the +4 position with stem cell potential (Clevers, 2013). We have reported the existence of Dll1+ secretory precursors at this position (van Es et al., 2012). Using a histone label retention assay, Doug Winton's group identified

a chromatin-label-retaining population with secretory differentiation potential. These LRCs share a signature with crypt base columnar cells (CBCs), including the expression of Lgr5, but express significant levels of some of the secretory lineage genes, such as Chga (Buczacki et al., 2013). Taken together, these secretory precursors represent transient states yet can de-differentiate into stem cells when the need arises and can thus be considered facultative stem cells (Buczacki et al., 2013; van Es et al., 2012). A similar situation exists for the abundant enterocyte precursors in the crypt (Tetteh et al., 2016).

We noticed a slight bias of quiescent Lgr5+ cells (induced in culture) toward expression of EEC markers, such as Chga, which made them reminiscent of the in vivo Lgr5+ label-retaining cells identified by Doug Winton. EGFR signaling has been shown to be essential for the production of goblet cells (Heuberger et al., 2014). Our current data show that simultaneous inhibition of enterocyte, Paneth, and goblet cell fate by inhibiting Notch, Wnt, and EGFR signaling, respectively, is the key to the generation of EECs.

This culture system may yield answers toward some of the major outstanding questions about the biology of the enigmatic EECs. It is unclear what signals drive the fate specification of the different subtypes of EECs. It is not known if the physiological processes that are controlled by specific EEC subtypes in turn feed back into the formation of the pertinent subtypes of EECs. Little is known about the triggers that lead to secretion of hormones beyond the identification of a handful of receptors and their ligands (Janssen and Depoortere, 2013). EEC-derived hormones have been implied in conditions of major importance such as depression, glucose insensitivity/diabetes, and obesity (Latorre et al., 2016). A detailed mechanistic understanding of the biology of EECs can be derived using this culture system and may yield insights with broad therapeutic impact.

A detailed description of the materials and methods used in the study is given in the STAR Methods.

STAR★METHODS

Detailed methods are provided in the online version of this paper and include the following:

- KEY RESOURCES TABLE
- CONTACT FOR REAGENT AND RESOURCE SHARING
- EXPERIMENTAL MODEL AND SUBJECT DETAILS
 - Mouse Strains Used to Initiate Organoid Cultures
- METHOD DETAILS
 - Organoid Culture
 - Immunostainings
 - FACS Sorting
 - RNA Isolation
 - Quantitative PCR
 - Single-Cell and Bulk Sequencing
 - PathScan Analysis
- QUANTIFICATION AND STATISTICAL DETAILS
 - Analysis of RNA-Sequencing Data
 - Single-Cell Data Analysis
 - Gene Set Enrichment Analysis
- DATA AND SOFTWARE AVAILABILITY
 - Data Resources

SUPPLEMENTAL INFORMATION

Supplemental Information includes seven figures and five tables and can be found with this article online at <http://dx.doi.org/10.1016/j.stem.2016.11.001>.

AUTHOR CONTRIBUTIONS

O.B., J.B., and H.C. designed the experiments and wrote the manuscript; J.B. performed the cell culture experiments; O.B. and K.W. performed RNA-sequencing experiments under the supervision of A.v.O.; O.B., J.B., and K.W. analyzed the data; J.B. was supervised by O.B. and H.C.; and H.S. contributed the *Dclk1* knockin allele.

ACKNOWLEDGMENTS

The authors would like to express their sincere gratitude to Stieneke van den Brink, Harry Begthel, Mauro Muraro, Stefan van der Elst, and Ewart de Bruijn for their support and excellent technical assistance. We thank Kim Boonekamp and Corina Markodimitraki for critical reading of the manuscript. H.C. is listed as the inventor on several patents related to this work. This work was supported by grants from NWO/ZonMW (114021012), NOW-CAS/ZONMW (116006103), and Friends of the Hubrecht Institute.

Received: April 16, 2016

Revised: August 30, 2016

Accepted: October 28, 2016

Published: December 8, 2016

REFERENCES

- Anders, S., and Huber, W. (2010). Differential expression analysis for sequence count data. *Genome Biol.* **11**, R106.
- Aoki, R., Shoshkes-Carmel, M., Gao, N., Shin, S., May, C.L., Golson, M.L., Zahm, A.M., Ray, M., Wiser, C.L., Wright, C.V., et al. (2016). Foxl1-expressing mesenchymal cells constitute the intestinal stem cell niche. *Cell. Mol. Gastroenterol. Hepatol.* **2**, 175–188.
- Banck, M.S., Kanwar, R., Kulkarni, A.A., Boora, G.K., Metge, F., Kipp, B.R., Zhang, L., Thorland, E.C., Minn, K.T., Tentu, R., et al. (2013). The genomic landscape of small intestine neuroendocrine tumors. *J. Clin. Invest.* **123**, 2502–2508.
- Barker, N., van Es, J.H., Kuipers, J., Kujala, P., van den Born, M., Cozijnsen, M., Haegebarth, A., Korving, J., Begthel, H., Peters, P.J., and Clevers, H. (2007). Identification of stem cells in small intestine and colon by marker gene *Lgr5*. *Nature* **449**, 1003–1007.
- Basak, O., van de Born, M., Korving, J., Beumer, J., van der Elst, S., van Es, J.H., and Clevers, H. (2014). Mapping early fate determination in *Lgr5+* crypt stem cells using a novel *Ki67-RFP* allele. *EMBO J.* **33**, 2057–2068.
- Buczacki, S.J., Zecchini, H.I., Nicholson, A.M., Russell, R., Vermeulen, L., Kemp, R., and Winton, D.J. (2013). Intestinal label-retaining cells are secretory precursors expressing *Lgr5*. *Nature* **495**, 65–69.
- Chen, E.Y., Xu, H., Gordonov, S., Lim, M.P., Perkins, M.H., and Ma'ayan, A. (2012). Expression2Kinases: mRNA profiling linked to multiple upstream regulatory layers. *Bioinformatics* **28**, 105–111.
- Clevers, H. (2013). The intestinal crypt, a prototype stem cell compartment. *Cell* **154**, 274–284.
- de Lau, W., Barker, N., Low, T.Y., Koo, B.K., Li, V.S., Teunissen, H., Kujala, P., Haegebarth, A., Peters, P.J., van de Wetering, M., et al. (2011). *Lgr5* homologues associate with Wnt receptors and mediate R-spondin signalling. *Nature* **476**, 293–297.
- de Lau, W., Kujala, P., Schneeberger, K., Middendorp, S., Li, V.S., Barker, N., Martens, A., Hofhuis, F., DeKoter, R.P., Peters, P.J., et al. (2012). Peyer's patch M cells derived from *Lgr5(+)* stem cells require *Spib* and are induced by *Rankl* in cultured "miniguts". *Mol. Cell. Biol.* **32**, 3639–3647.
- Drucker, D.J., and Nauck, M.A. (2006). The incretin system: glucagon-like peptide-1 receptor agonists and dipeptidyl peptidase-4 inhibitors in type 2 diabetes. *Lancet* **368**, 1696–1705.
- Eden, E., Navon, R., Steinfeld, I., Lipson, D., and Yakhini, Z. (2009). GOrilla: a tool for discovery and visualization of enriched GO terms in ranked gene lists. *BMC Bioinformatics* **10**, 48.
- Egerod, K.L., Engelstoft, M.S., Grunddal, K.V., Nøhr, M.K., Secher, A., Sakata, I., Pedersen, J., Windeløv, J.A., Füchtbauer, E.M., Olsen, J., et al. (2012). A major lineage of enteroendocrine cells coexpress CCK, secretin, GIP, GLP-1, PYY, and neurotensin but not somatostatin. *Endocrinology* **153**, 5782–5795.
- Farin, H.F., Van Es, J.H., and Clevers, H. (2012). Redundant sources of Wnt regulate intestinal stem cells and promote formation of Paneth cells. *Gastroenterology* **143**, 1518–1529.
- Farin, H.F., Jordens, I., Mosa, M.H., Basak, O., Korving, J., Tauriello, D.V., de Punder, K., Angers, S., Peters, P.J., Maurice, M.M., and Clevers, H. (2016). Visualization of a short-range Wnt gradient in the intestinal stem-cell niche. *Nature* **530**, 340–343.
- Grün, D., Lyubimova, A., Kester, L., Wiebrands, K., Basak, O., Sasaki, N., Clevers, H., and van Oudenaarden, A. (2015). Single-cell messenger RNA sequencing reveals rare intestinal cell types. *Nature* **525**, 251–255.
- Grün, D., Muraro, M.J., Boisset, J.C., Wiebrands, K., Lyubimova, A., Dharmadhikari, G., van den Born, M., van Es, J., Jansen, E., Clevers, H., et al. (2016). De novo prediction of stem cell identity using single-cell transcriptome data. *Cell Stem Cell* **19**, 266–277.
- Gunawardene, A.R., Corfe, B.M., and Staton, C.A. (2011). Classification and functions of enteroendocrine cells of the lower gastrointestinal tract. *Int. J. Exp. Pathol.* **92**, 219–231.
- Hashimshony, T., Wagner, F., Sher, N., and Yanai, I. (2012). CEL-Seq: single-cell RNA-Seq by multiplexed linear amplification. *Cell Rep.* **2**, 666–673.
- Heuberger, J., Kosel, F., Qi, J., Grossmann, K.S., Rajewsky, K., and Birchmeier, W. (2014). Shp2/MAPK signaling controls goblet/paneth cell fate decisions in the intestine. *Proc. Natl. Acad. Sci. USA* **111**, 3472–3477.
- Höfer, D., and Drenckhahn, D. (1996). Cytoskeletal markers allowing discrimination between brush cells and other epithelial cells of the gut including enteroendocrine cells. *Histochem. Cell Biol.* **105**, 405–412.
- Howitt, M.R., Lavoie, S., Michaud, M., Blum, A.M., Tran, S.V., Weinstock, J.V., Gallini, C.A., Redding, K., Margolskee, R.F., Osborne, L.C., et al. (2016). Tuft cells, taste-chemosensory cells, orchestrate parasite type 2 immunity in the gut. *Science* **351**, 1329–1333.
- Janssen, S., and Depoortere, I. (2013). Nutrient sensing in the gut: new roads to therapeutics? *Trends Endocrinol. Metab.* **24**, 92–100.
- Kitabgi, P., and Freychet, P. (1978). Effects of neurotensin on isolated intestinal smooth muscles. *Eur. J. Pharmacol.* **50**, 349–357.
- Latorre, R., Sternini, C., De Giorgio, R., and Greenwood-Van Meerveld, B. (2016). Enteroendocrine cells: a review of their role in brain-gut communication. *Neurogastroenterol. Motil.* **28**, 620–630.
- Love, M.I., Huber, W., and Anders, S. (2014). Moderated estimation of fold change and dispersion for RNA-seq data with DESeq2. *Genome Biol.* **15**, 550.
- Middendorp, S., Schneeberger, K., Wiegerinck, C.L., Mokry, M., Akkerman, R.D., van Wijngaarden, S., Clevers, H., and Nieuwenhuis, E.E. (2014). Adult stem cells in the small intestine are intrinsically programmed with their location-specific function. *Stem Cells* **32**, 1083–1091.
- Montgomery, R.K., Carlone, D.L., Richmond, C.A., Farilla, L., Kranendonk, M.E., Henderson, D.E., Baffour-Awuah, N.Y., Ambruzs, D.M., Fogli, L.K., Algra, S., and Breault, D.T. (2011). Mouse telomerase reverse transcriptase (*mTert*) expression marks slowly cycling intestinal stem cells. *Proc. Natl. Acad. Sci. USA* **108**, 179–184.
- Muñoz, J., Stange, D.E., Schepers, A.G., van de Wetering, M., Koo, B.K., Itzkovitz, S., Volckmann, R., Kung, K.S., Koster, J., Radulescu, S., et al. (2012). The *Lgr5* intestinal stem cell signature: robust expression of proposed quiescent '4+' cell markers. *EMBO J.* **31**, 3079–3091.
- Myant, K., and Sansom, O. (2011). Efficient Wnt mediated intestinal hyperproliferation requires the cyclin D2-CDK4/6 complex. *Cell Div.* **6**, 3.
- Nakanishi, Y., Seno, H., Fukuoka, A., Ueo, T., Yamaga, Y., Maruno, T., Nakanishi, N., Kanda, K., Komekado, H., Kawada, M., et al. (2013). *Dclk1* distinguishes between tumor and normal stem cells in the intestine. *Nat. Genet.* **45**, 98–103.

- Parker, H.E., Habib, A.M., Rogers, G.J., Gribble, F.M., and Reimann, F. (2009). Nutrient-dependent secretion of glucose-dependent insulinotropic polypeptide from primary murine K cells. *Diabetologia* 52, 289–298.
- Pellegrinet, L., Rodilla, V., Liu, Z., Chen, S., Koch, U., Espinosa, L., Kaestner, K.H., Kopan, R., Lewis, J., and Radtke, F. (2011). Dll1- and dll4-mediated notch signaling are required for homeostasis of intestinal stem cells. *Gastroenterology* 140, 1230–1240.
- Potten, C.S., Hume, W.J., Reid, P., and Cairns, J. (1978). The segregation of DNA in epithelial stem cells. *Cell* 15, 899–906.
- Powell, A.E., Wang, Y., Li, Y., Poulin, E.J., Means, A.L., Washington, M.K., Higginbotham, J.N., Juchheim, A., Prasad, N., Levy, S.E., et al. (2012). The pan-ErbB negative regulator *Lrig1* is an intestinal stem cell marker that functions as a tumor suppressor. *Cell* 149, 146–158.
- Sangiorgi, E., and Capecchi, M.R. (2008). *Bmi1* is expressed in vivo in intestinal stem cells. *Nat. Genet.* 40, 915–920.
- Sato, T., Vries, R.G., Snippert, H.J., van de Wetering, M., Barker, N., Stange, D.E., van Es, J.H., Abo, A., Kujala, P., Peters, P.J., and Clevers, H. (2009). Single *Lgr5* stem cells build crypt-villus structures in vitro without a mesenchymal niche. *Nature* 459, 262–265.
- Sato, T., van Es, J.H., Snippert, H.J., Stange, D.E., Vries, R.G., van den Born, M., Barker, N., Shroyer, N.F., van de Wetering, M., and Clevers, H. (2011). Paneth cells constitute the niche for *Lgr5* stem cells in intestinal crypts. *Nature* 469, 415–418.
- Schepers, A.G., Vries, R., van den Born, M., van de Wetering, M., and Clevers, H. (2011). *Lgr5* intestinal stem cells have high telomerase activity and randomly segregate their chromosomes. *EMBO J.* 30, 1104–1109.
- Serup, P., Gustavsen, C., Klein, T., Potter, L.A., Lin, R., Mullapudi, N., Wandzioch, E., Hines, A., Davis, A., Bruun, C., et al. (2012). Partial promoter substitutions generating transcriptional sentinels of diverse signaling pathways in embryonic stem cells and mice. *Dis. Model. Mech.* 5, 956–966.
- Shibue, K., Yamane, S., Harada, N., Hamasaki, A., Suzuki, K., Joo, E., Iwasaki, K., Nasteska, D., Harada, T., Hayashi, Y., et al. (2015). Fatty acid-binding protein 5 regulates diet-induced obesity via GIP secretion from enteroendocrine K cells in response to fat ingestion. *Am. J. Physiol. Endocrinol. Metab.* 308, E583–E591.
- Soriano, P. (1999). Generalized *lacZ* expression with the ROSA26 Cre reporter strain. *Nat. Genet.* 21, 70–71.
- Supek, F., Bošnjak, M., Škunca, N., and Šmuc, T. (2011). REVIGO summarizes and visualizes long lists of gene ontology terms. *PLoS ONE* 6, e21800.
- Takeda, N., Jain, R., LeBoeuf, M.R., Wang, Q., Lu, M.M., and Epstein, J.A. (2011). Interconversion between intestinal stem cell populations in distinct niches. *Science* 334, 1420–1424.
- Terry, N.A., Walp, E.R., Lee, R.A., Kaestner, K.H., and May, C.L. (2014). Impaired enteroendocrine development in intestinal-specific *Islet1* mouse mutants causes impaired glucose homeostasis. *Am. J. Physiol. Gastrointest. Liver Physiol.* 307, G979–G991.
- Tetteh, P.W., Basak, O., Farin, H.F., Wiebrands, K., Kretschmar, K., Begthel, H., van den Born, M., Korving, J., de Sauvage, F., van Es, J.H., et al. (2016). Replacement of lost *Lgr5*-positive stem cells through plasticity of their enterocyte-lineage daughters. *Cell Stem Cell* 18, 203–213.
- Tian, H., Biehs, B., Warming, S., Leong, K.G., Rangell, L., Klein, O.D., and de Sauvage, F.J. (2011). A reserve stem cell population in small intestine renders *Lgr5*-positive cells dispensable. *Nature* 478, 255–259.
- van Es, J.H., van Gijn, M.E., Riccio, O., van den Born, M., Vooijs, M., Begthel, H., Cozijnsen, M., Robine, S., Winton, D.J., Radtke, F., and Clevers, H. (2005). Notch/gamma-secretase inhibition turns proliferative cells in intestinal crypts and adenomas into goblet cells. *Nature* 435, 959–963.
- van Es, J.H., Sato, T., van de Wetering, M., Lyubimova, A., Nee, A.N., Gregorieff, A., Sasaki, N., Zeinstra, L., van den Born, M., Korving, J., et al. (2012). *Dll1*+ secretory progenitor cells revert to stem cells upon crypt damage. *Nat. Cell Biol.* 14, 1099–1104.
- Yan, K.S., Chia, L.A., Li, X., Ootani, A., Su, J., Lee, J.Y., Su, N., Luo, Y., Heilshorn, S.C., Amieva, M.R., et al. (2012). The intestinal stem cell markers *Bmi1* and *Lgr5* identify two functionally distinct populations. *Proc. Natl. Acad. Sci. USA* 109, 466–471.
- Yin, X., Farin, H.F., van Es, J.H., Clevers, H., Langer, R., and Karp, J.M. (2014). Niche-independent high-purity cultures of *Lgr5*+ intestinal stem cells and their progeny. *Nat. Methods* 11, 106–112.

STAR★METHODS

KEY RESOURCES TABLE

REAGENT or RESOURCE	SOURCE	IDENTIFIER
Antibodies		
rabbit anti-Lysozyme (EC3.2./17)	DAKO	A0099, RRID: AB_2341230
goat anti-Chromogranin A (C-20)	Santa Cruz	Sc-1488, RRID: AB_2276319
mouse anti-Ki67	BD PharMingen	550609, RRID: AB_393778
rabbit anti-phospho-Histone 3(pH3, Ser10)	Millipore	06-570, RRID: AB_310177
mouse anti-Cytokeratin 20 (KS20.8)	DAKO	M7019, RRID: AB_2133718
goat anti-Cholestocystokin	Santa Cruz	Cat# sc-21617, RRID: AB_2072464
rabbit anti-Neurotensin	Santa Cruz	Cat# sc-20806, RRID: AB_2155562
goat anti-Secretin	Santa Cruz	Cat# sc-26630, RRID: AB_656130
goat anti-Somatostatin	Santa Cruz	Cat# sc-7819, RRID: 2302603
goat anti-Serotonin	Abcam	ab66047, RRID: AB_1142794
rabbit anti-Gastric inhibitory polypeptide	Abcam	ab22624-50, RRID: AB_2109683
mouse anti-acetylated Tubulin	Santa Cruz	Sc-23950, RRID: AB_628409
Mouse anti-mucin2 (clone CCP58)	Monosan	MONX10515
Alexa Fluor 488 goat anti-mouse IgG (H+L)	Thermo Fisher scientific	A11029, RRID: AB_2534088
Alexa Fluor 488 donkey anti-rabbit IgG (H+L)	Thermo Fisher scientific	A21206, RRID: AB_2535792
Alexa Fluor 488 donkey anti-goat IgG (H+L)	Thermo Fisher scientific	A11055, RRID: AB_2534102
Alexa Fluor 568 goat anti-rabbit IgG (H+L)	Thermo Fisher scientific	A11036, RRID: AB_10563566
Alexa Fluor 647 donkey anti-rabbit IgG (H+L)	Thermo Fisher scientific	A31573, RRID: AB_2536183
AlexaFluor 647 donkey anti-mouse IgG (H+L)	Thermo Fisher scientific	A31571, RRID: AB_162542
Alexa Fluor 647 goat anti-rat IgG (H+L)	Thermo Fisher scientific	A21247, RRID: AB_10563568
Envision+ System –HRP polymer anti-mouse	DAKO	K4001
eFluor-660 conjugated rat anti-Ki67 (Clone:SolA15)	eBiosciences	50-5698-80, RRID: AB_2574234
Chemicals, Peptides, and Recombinant Proteins		
DAPI solution (1mg/ml)	Thermo Fisher scientific	62248
AlexaFluor 647 Phalloidin	Thermo Fisher scientific	A22287
Vectashield	Vector Labs	H-1000
Gefitinib	Santa Cruz Biotechnology	sc-202166
Azd8055	Selleckchem	S1555
SCH772984	Selleckchem	S7101
IWP-2	Stemgent	130-105-335
DAPT	Sigma Aldrich	D5942
PD0325901	Sigma Aldrich	PZ0162
Critical Commercial Assays		
Click-iT Assay Kit	Thermo Fisher scientific	C10340
Deposited Data		
Single cell (Figure 7) and bulk sequencing data of sorted cells (Figure 4) or organoids (Figure 6)	This paper	GEO: GSE80636
Experimental Models: Organisms/Strains		
Lgr5-GFPiresCreER	Barker et al., 2007	Hans Clevers, clevers@hubrecht.eu
Lgr5-GFPDTR	Tian et al., 2011	Frederic J. de Sauvage, Department of Molecular Biology, Genentech Inc., 1 DNA Way, South San Francisco, CA 94080, USA
Dcl1-GFPiresCreER(Nakanishi et al., 2013)	Nakanishi et al., 2013	Hiroshi Seno, seno@kuhp.kyoto-u.ac.jp
B6;129S4-Gt(ROSA)26Sor ^{tm1Sor} /J	Soriano, 1999	https://www.jax.org/strain/003309
Gt(ROSA)26Sor ^{tm10.1(Tcf/Lef-CFP)Mgn}	Serup et al., 2012	Kenneth S. Zaret, zaret@upenn.edu

(Continued on next page)

Continued

REAGENT or RESOURCE	SOURCE	IDENTIFIER
Software and Algorithms		
RaceID2	Grün et al., 2016	https://www.github.com/dgrun/StemID
DESeq	Anders and Huber, 2010	https://www.bioconductor.org/packages/release/bioc/html/DESeq.html
Deseq2	Love et al., 2014	https://www.bioconductor.org/packages/release/bioc/html/DESeq2.html

CONTACT FOR REAGENT AND RESOURCE SHARING

Requests for reagents should be directed to Prof. Hans Clevers at clevers@hubrecht.eu.

EXPERIMENTAL MODEL AND SUBJECT DETAILS**Mouse Strains Used to Initiate Organoid Cultures**

Primary organoid cultures used in this study were derived from $Lgr5^{GFPiresCreER/+}$ (Barker et al., 2007), $Lgr5^{GFPDTR/+}$ (Tian et al., 2011), $Dcl1^{GFPiresCreER/+}$ (Nakanishi et al., 2013) and $Rosa^{TCF-CFP/+}$ (Gt(ROSA)26Sor^{tm10.1(Tcf/Lef-CFP)Mgn}) mice (Serup et al., 2012). For lineage tracing experiments, organoids were derived from the $Lgr5^{GFPiresCreER/+};Rosa^{LacZ/YFP}$ and $Dcl1^{GFPiresCreER/+};Rosa^{LacZ/+}$ mice. All mice were bred on a C57BL/6 background. All animal procedures and experiments were performed in accordance with national animal welfare laws under a project license obtained from the Dutch Government, and were reviewed by the Animal Ethics Committee of the Royal Netherlands Academy of Arts and Sciences (KNAW). All rodents are housed in a barrier facility in conventional cages and are changed without using a change stations. All personnel entering the barrier must wear protective clothing (including head caps, special clogs). All animals are received directly from approved vendors (Charles River) or generated in house. Animals arriving from other sources must pass the GDL –quarantine for screening or by embryo-transfer. After screening these SPF mice are housed in micro isolator cages and are transferred to the Hubrecht laboratory.

METHOD DETAILS**Organoid Culture**

The basic culture medium (advanced Dulbecco's modified Eagle's medium/F12 supplemented with penicillin/streptomycin, 10 mM HEPES, Glutamax, B27 [Life Technologies, Carlsbad, CA] and 1 mM N-acetylcysteine [Sigma]) was supplemented with 50 ng/ml murine recombinant epidermal growth factor (EGF; Peprotech, Hamburg, Germany), R-spondin1 (conditioned medium, 5% final volume), and Noggin (conditioned medium, 5% final volume), called "ENR" medium. Conditioned media were produced using HEK293T cells stably transfected with HA-mouse Rspo1-Fc (gift from Calvin Kuo, Stanford University) or after transient transfection with mouse Noggin-Fc expression vector. Advanced Dulbecco's modified Eagle's medium/F12 supplemented with penicillin/streptomycin, and Glutamax was conditioned for 1 week.

Organoids were derived from the duodenum of the $Lgr5^{GFPiresCreER/+}$ (Barker et al., 2007), $Lgr5^{GFPDTR/+}$ (Tian et al., 2011), $Dcl1^{GFPiresCreER/+}$ (Nakanishi et al., 2013) and $Rosa^{TCF-CFP/+}$ (Gt(ROSA)26Sor^{tm10.1(Tcf/Lef-CFP)Mgn}) mice (Serup et al., 2012). For experiment displayed in Figure 5E, organoids were derived from 4 different regions spanning the proximal-distal axis of the intestine. For lineage tracing experiments, organoids were derived from the $Lgr5^{GFPiresCreER/+};Rosa^{LacZ/YFP}$ and $Dcl1^{GFPiresCreER/+};Rosa^{LacZ/+}$ mice.

Organoids were plated in BME (Trevigen) and treated with the EGFR inhibitor Gefitinib (5 μ M; Santa Cruz Biotechnology), EGFR and ErbB-2 inhibitor Afatinib (10 μ M, Selleckchem), MEK inhibitor PD0325901 (5 μ M; Sigma Aldrich) or ERK inhibitor SCH772984 (10 μ M, Selleckchem) while EGF was withdrawn from the medium. Wnt secretion was inhibited with IWP-2 (1.5 μ M; Stemgent) and Notch with DAPT (10 μ M, Sigma Aldrich). All treatments were performed on organoids 5-7 days after passaging. For EGFR reactivation experiments, organoids were replated in fresh BME and ENR medium to make sure EGFR inhibitor is washed away. For the repeated EGF withdrawal experiment in Figures 2C–2E, EGF was omitted in the medium during reactivation. For mTOR inhibition, Azd8055 (Selleckchem) was added to the medium at 0.1 mM concentration. For induction of Cre-ER activity, organoids were treated overnight with 4-OH tamoxifen (1 μ M). All control organoids were treated with similar concentrations of the compound dissolved in dimethyl sulfoxide (DMSO). During treatments, cells were imaged using an EVOS microscope (Electron Microscopy Sciences).

For the induction of enteroendocrine differentiation, cells were either cultured in standard culture conditions (ENR). 5 days after plating in BME, medium was removed and organoids were washed with PBS before re-embedding in BME. The cocktail for EEC differentiation included: IWP2 (1,5 μ M; Stemgent), DAPT (10 μ M, Sigma Aldrich) and MEK inhibitor PD0325901 (1 μ M; Sigma Aldrich) or Gefitinib (5 μ M; Santa Cruz Biotechnology).

Immunostainings

Whole organoids were collected by gently dissolving the BME in ice-cold PBS, and subsequently fixed overnight at 4°C in 4% paraformaldehyde (Sigma). Next, organoids were permeabilized and blocked in PBS containing 0,5% Triton X-100 (Sigma) and 2% normal donkey serum (Jackson ImmunoResearch) for 30 min at room temperature. Organoids were incubated for 2 hr at room temperature in blocking buffer containing primary antibodies. Primary antibodies used were rabbit anti-Lysozyme (1:500; DAKO), goat anti-Chromogranin A (1:500; Santa Cruz), mouse anti-Ki67 (1:250; BD PharMingen), rabbit anti-phospho-Histone 3 (pH3 Ser10, 1:1000; Millipore), mouse anti-Cytokeratin 20 (1:1000; Dako), goat anti-Cholestocystokin (sc-21617, 1:100; Santa Cruz), rabbit anti-Neurotensin (sc-20806, 1:100; Santa Cruz), goat anti-Secretin (sc-26630, 1:100; Santa Cruz), goat anti-Somatostatin (sc-7819, 1:100; Santa Cruz), goat anti-Serotonin (ab66047, 1:1000, Abcam), rabbit anti-Gastric inhibitory polypeptide (ab22624-50, 1:500, Abcam) and mouse anti-acetylated tubulin (1:100; Santa Cruz). Organoids were incubated with the corresponding secondary antibodies Alexa488, 568 and 647 conjugated anti-rabbit, anti-goat and anti-mouse (1:1000; Molecular Probes), in blocking buffer containing DAPI (1:1000, Invitrogen), or with Alexa 647 conjugated Phalloidin (Thermo Fisher scientific, 1:2000). EdU incorporation was visualized using the Click-iT Assay Kit (Thermo Fisher), after 1 hr pre-incubation with EdU (10 μ M). LacZ staining was performed as previously described (Barker et al., 2007). Alexa 647 conjugated Phalloidin (Thermo Fisher scientific, 1:2000) was added together with the secondary antibodies. Sections were embedded in Vectashield (Vector Labs) and imaged using a Sp5 and Sp8 confocal microscope (Leica). Image analysis was performed using ImageJ software.

FACS Sorting

For FACS analysis of Lgr5 and Ki67 expression, Lgr5^{GFPDTR/+} organoids were first dissociated into single cells through mechanical disruption, after 15 min of Trypsin treatment at 37°C (TrypLE Express; Life Technologies). Single cells were fixed on ice using 4% paraformaldehyde for 30 min, and washed 3 times in PBS. Cells were permeabilized in PBS containing 0,5% Triton X-100 for 30 min, and were stained with an eFluor-660 conjugated rat anti-Ki67 (1:1000; eBioscience) antibody for 30 min on ice. For cell cycle analysis, cells were stained in 1 μ g/ml Hoechst 33342 (ThermoFisher). Subsequently, stained cells were analyzed on a BD FACS Calibur (BD Biosciences).

For RNA-sequencing analysis in Figures 4 and 7, organoids were dissociated and immediately sorted using a BD FACS Aria (BD Biosciences). For bulk sequencing experiments in Figure 4, up to 5000 cells were sorted in Trizol in eppendorf tubes. For single cell sequencing experiment, cells were sorted as single cells into 384-well plates containing ERCC spike-ins (Agilent), RT primers (Hashimshony et al., 2012) and dNTP (Promega).

RNA Isolation

For RNA-sequencing of sorted cells in bulk, cells were sorted into Trizol (Life Technologies) and total RNA was isolated according to the manufacturer's instructions, with the following alterations. RNA was precipitated overnight at -20°C, with 2 μ g glycogen (Life Technologies). No additional RNA isolation step was used for cells sorted into 384-wells. For quantitative PCR analysis, RNA was isolated from organoids using the RNAeasy kit (QIAGEN) as instructed in the manufacturers protocol. For bulk sequencing experiment described in Figure 6, organoids were treated in triplicate for 6 or 96 hr in 48-well plates, collected and washed in PBS. RNA was isolated using Trizol as described above. 10 ng RNA was used as starting material for sequencing reactions.

Quantitative PCR

PCR analysis was performed using the SYBR-Green and Bio-Rad systems as described (Muñoz et al., 2012). PCR reactions were performed in triplicate with a standard curve for every primer. Changes in expression were calculated using CFX manager software (Bio-Rad). Primers were designed using the NCBI primer design tool.

Single-Cell and Bulk Sequencing

RNA samples were prepared using a modified version of the CEL-seq protocol as described previously (Grün et al., 2015; Hashimshony et al., 2012). RNA pellets were dissolved in primer mix and incubated for 2 min at 70°C. Cells sorted into 384-well were directly lysed at 65°C for 5 min. cDNA libraries were sequenced on an Illumina NextSeq500 using 75-bp paired-end sequencing. Data processing is described below.

PathScan Analysis

Organoids that were Gefitinib treated for 1h, 3h, 6h or 24h were collected in ice cold DMEM in medium, and lysed according to manufacture instructions (PathScan Akt Signaling Antibody Array Kit with chemoluminescent, Cell Signaling Technology). Lysates were processed according to protocol. Readout of chemoluminescent readout was performed on ImageQuant LAS 4000 (GE Healthcare Life Sciences). Signal intensities were quantified using ImageJ software. Quantification was performed by calculating intensity of each antigen signal relative to independent time point specific control antigens.

QUANTIFICATION AND STATISTICAL DETAILS

Analysis of RNA-Sequencing Data

Paired-end reads were quantified as described before (Grün et al., 2015) with the following exceptions. Reads that did not align or aligned to multiple locations were discarded. For analysis of the bulk sequencing, unique molecular identifiers (UMIs) were ignored; instead read counts for each transcript were determined by the number of reads that uniquely mapped to that transcript. This count was divided by the total number of reads that mapped to all transcripts and multiplied by one million to generate the reads-per-million (RPM) count. RPM was used in preference of RPKM because CEL-seq only allows 3' end sequencing. Differential gene expression was evaluated using the DESeq (Anders and Huber, 2010) and Deseq2 (Love et al., 2014) packages in R platform. Cut-offs in Figure 4 used were an adjusted p value < 0,1 and FDR < 0,1 and at least 2-fold difference to the compared population. To prevent samples with no reads disabling ratiometric analysis, all 0 reads were converted into 0,1 reads prior to ratio calculation and log2 conversion. Gene ontology analysis was performed using the Revigo (Supek et al., 2011) and Gorilla (Eden et al., 2009) software.

Single-Cell Data Analysis

Single-cell sequencing data was analyzed as described previously (Grün et al., 2015). In brief, 288 cells sorted from iNotch/iWnt/iMek and 384 cells sorted from iNotch/iWnt/IEGFR treated organoids were sequenced in parallel. Cells with less than 1000 unique reads were discarded and samples were down-sampled. Genes with maximum expression less than 5 following down-sampling were discarded. Exclusion of Enterocytes was achieved by discarding samples with more than 8 transcripts of ApoA1.

Gene Set Enrichment Analysis

Gene Set Enrichment Analysis (GSEA) was performed following producers' instructions (<http://software.broadinstitute.org/gsea/>). A ranked list comparing the fold changes between quiescent and active Lgr5+ stem cells was created and compared to the label retaining cell gene set (Basak et al., 2014; Buczacki et al., 2013) and the 'HALLMARKS' gene set available on the server (<http://software.broadinstitute.org/gsea/>). Expression2kinase (X2K) software was used to identify the transcription factors targeting the active Lgr5+ stem cell signature (Chen et al., 2012).

DATA AND SOFTWARE AVAILABILITY

Data Resources

The data generated in this paper has been deposited in the Gene Expression Omnibus (GEO) under accession number GEO: GSE80636.

The list of differentially expressed genes between quiescent and active Lgr5+ stem cells are described in Table S1.

Results of the GSEA analysis using the label retaining cell gene set are described in Table S2. GSEA results for the 'HALLMARKS' gene sets are reported in Table S3.

Differentially expressed genes for each cluster described in the single cell analysis are reported in Table S4.

The qPCR primers used in this study are in Table S5.

Cell Stem Cell, Volume 20

Supplemental Information

**Induced Quiescence of Lgr5+ Stem Cells
in Intestinal Organoids Enables Differentiation
of Hormone-Producing Enteroendocrine Cells**

**Onur Basak, Joep Beumer, Kay Wiebrands, Hiroshi Seno, Alexander
van Oudenaarden, and Hans Clevers**

SUPPLEMENTARY FIGURE AND TABLE LEGENDS

Supplementary figure 1. The role of niche signalling pathways in proliferation of Lgr5+ cells. (A-C) FACS plots showing the endogenous fluorescence of Lgr5^{GFPDTR/+} organoids in all live cells (A), KI67^{efluor660} immunostaining among Lgr5^{GFPDTR/+} cells (B) or among all live cells (C) on the x axis. Since Lgr5+ cells are lost after R-Spondin1 withdrawal, few KI67+ cells are seen in respective B panel. PL3 channel is used (y axis) to discriminate background. Gates shows positive cells with respect to wild type controls. (D) Quantification of A-C. Error bars indicate standard deviation. Related to Figure 1.

Supplementary figure 2. EGFR inhibition induces Lgr5+ cell quiescence while maintaining self-renewal and multipotency. (A-B) Brightfield (upper) and fluorescent (lower) images in control (ENR) and EGFR inhibited (iEGFR) Lgr5^{GFPiresCreER/+} (A, green), Lgr5^{GFPDTR/+} (B, green) and Rosa^{TCF-CFP/+} (B, blue) organoids. RFP (Red) channel is used to discriminate background. (C) HOECHST analysis of the DNA content of control or iEGFR treated organoids. Bars on the right show quantification of 3 independent experiments. (D) Relative number of marker protein positive cells following reintroduction of EGF signalling for 1 (d1), 3 (d3) or 5 (d5) days compared to respective controls (DMSO treated, same days in culture). Fluorescent images are shown in Figure 1G. (E) Lineage tracing iEGFR or control (DMSO) treated Lgr5+ or Dclk1+ cells. After 4 days of iEGFR treatment in Lgr5^{iresCreER}Rosa^{LacZ} or Dclk1^{iresCreER}Rosa^{LacZ} organoids, recombination was induced with 4'OH Tamoxifen (T) for 16 hours and EGF signalling was restored by replating in ENR. X-Gal staining was performed to follow recombined cells (blue) and assess stem cell potential of control (upper panel, ENR.T.ENR) or reactivated quiescent stem cells (lower panel, iEGFR.T.ENR). EGFR reactivated stem cells generate full organoids, indicative of multipotency and cell cycle reactivation. (F) MUC2 antibody staining (brown) on paraffin sections of iEGFR treated organoids and controls. Sections are counterstained using haematoxylin (G) After 4 days of iEGFR treatment; Lgr5^{GFP+} stem cells do not express markers of enteroendocrine cells (CHGA), Paneth cells (LYZ) or display characteristics of Tuft cells (apical actin bundles stained by Phalloidin, blue or acetylated Tubulin bundles). (H) Quantification of the organoid circumference on optical sections of organoids described in figures 2C and 2D. EGFR inhibitor was removed to reactivate organoids, either in the presence (EGF reactivation) or absence (iEGFR release) of EGF. EVOS (A, B and E) and confocal (F, optical sections) microscope was used for imaging. Error bars indicate standard deviation. Related to Figure 1.

Supplementary figure 3. Downstream effects on MAPK and AKT components after EGFR inhibition. (A) Quantification of the Pathscan^R analysis of iEGFR treated organoids. Data that is not shown in Figure 3A is displayed. (B) Histological analysis of ERK phosphorylation following EGFR inhibition. A rapid loss in pERK is gradually over 24h, but remains low over 48 hours (upper panels). Lower panels show KI67 staining. Scale bars = 50 μ m. Error bars indicate standard deviation. Related to Figure 3.

Supplementary figure 4. Molecular features of quiescent and active Lgr5+ stem cells. (A) Principal component analysis (PCA) indicating transcriptome differences between bulk samples in different culturing conditions. (B) Heat map showing the relative expression of genes differentially expressed gene between active and quiescent stem cells. Key genes expressed in stem cells (Nav1, Rnf43, Lgr5), Tuft cells (Trpm5, Vav1), those involved in cell cycle progression (Ccnb1, Ccnb2, Rpl27) and transcription factors (Junb, Fos, Fosb, Etv4) are highlighted. Colours show z-score for each row. (C) Plot displaying Gene Ontology (GO) term enriched in active Lgr5+ stem cells. X-axis shows the relative number of genes related to the GO term, x-axis shows the statistical significance (p-value) for each term. (D) Gene set enrichment analysis (GSEA). Fold change in gene expression in quiescent and active Lgr5+ stem cells are compared. Green line shows enrichment profile. Black bars show where genes from a given gene set are located (hit). NES: Normalized enrichment score. FDR: False discovery rate. Related to Figure 4.

Supplementary figure 5. Enteroendocrine cells are effectively induced in Wnt, Notch and EGFR inhibited organoids. (A) qPCR analysis of organoids for enteroendocrine markers after single Wnt inhibition (iWnt), Notch inhibition (iNotch), EGFR inhibition (iEGFR), MEK inhibition (iMek) or combinations. (B) Confocal sections of organoids stained for enteroendocrine marker CHGA (Green) after combinations of Wnt, Notch, mTOR (iTOR) or EGFR inhibition. iTOR completely attenuates the increase in enteroendocrine cell number observed after iWnt/iNotch/iEGFR treatment. (C) qPCR analysis of enteroendocrine markers in iWnt/iNotch treated organoids, with or without mTOR inhibition. iTOR treatment reverses the increase in enteroendocrine cell markers due to iWnt/iNotch treatment. Scale bars = 50 μ m. (D) Cleaved caspase-3 (red) staining is used to visualize apoptosis in organoids. Most apoptotic figures are shed to the lumen after 1 day of control (ENR) or iWnt/iNotch/iMek treatment. Labelling in the crypts is rare. Images in B and D are 3D reconstruction confocal images. Scale bars = 50 μ m. Error bars indicate standard deviation. Related to Figure 5.

Supplementary figure 6. Characterization of organoids after quiescence or enteroendocrine cell induction using RNA sequencing. (A) Heat map indicating transcriptome similarities between bulk samples in different culturing conditions measured by Pearson's correlation coefficient. Samples are ordered according hierarchical clustering. (B-C) Plots display the comparison of the transcriptome of respective populations. (B) Control, iEGFR and iMek conditions were compared after 6h (upper row) or 96h (lower row) of treatment. (C) Control, iWnt/iNotch/iEGFR and iWnt/iNotch/iMek conditions are compared after 96h of treatment. The y-axis shows the fold change in log₂, the x-axis shows the mean value of the transcripts. Each dot represents a gene. Red dots are differentially expressed between the compared populations (FDR < 0.01). Related to Figure 6.

Supplementary figure 7. Single cell analysis of induced enteroendocrine cells. (A) t-distributed stochastic neighbor embedding (t-SNE) map representation of transcriptome similarities. Colours and numbers indicate RaceID2 clusters. (B) t-SNE map showing log₂ transformed transcript counts of *Apoa1*, an enterocyte marker. (C) t-SNE map showing the distribution of cells between two different culturing conditions, as indicated. (D) t-SNE map showing log₂ transformed transcript counts of the key EEC genes indicated. Colours in B and D show normalized expression values. Related to Figure 7.

Supplementary table 1. The list of differentially expressed genes between quiescent and active Lgr5+ stem cells. Related to Figure 4.

Supplementary table 2. Results of the Gene set enrichment analysis (GSEA) results using the label retaining cell gene set. Related to Figure 4.

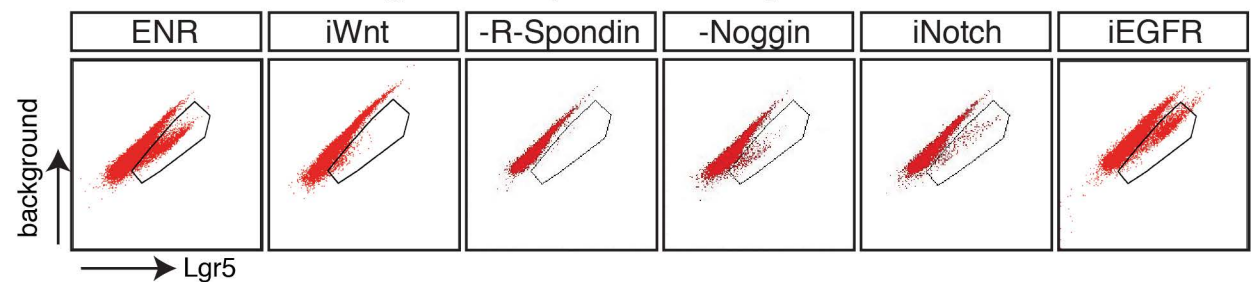
Supplementary table 3. Gene set enrichment analysis (GSEA) results for the 'HALLMARKS' gene sets. Related to Figure 4.

Supplementary table 4. Differentially expressed genes for each cluster described in the single cell analysis. Related to Figure 7.

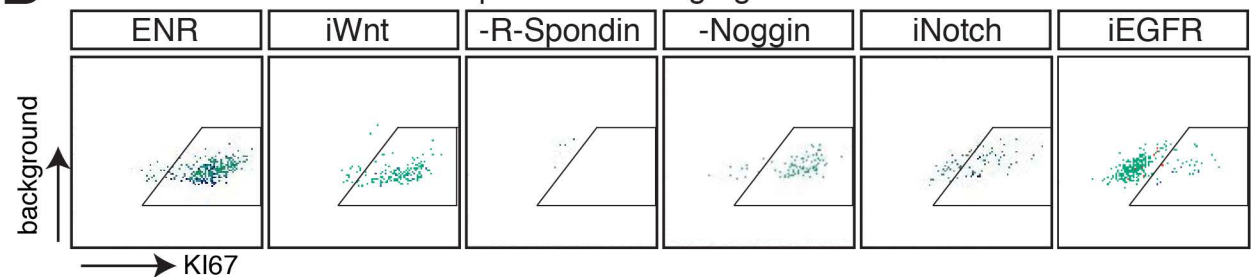
Supplementary table 5. The qPCR primers used in this study. Related to Figure 5.

A

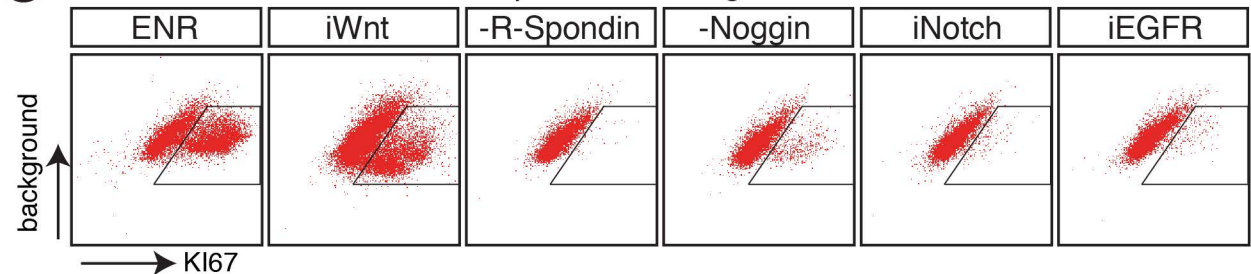
Lgr5-GFP expression among all live cells

**B**

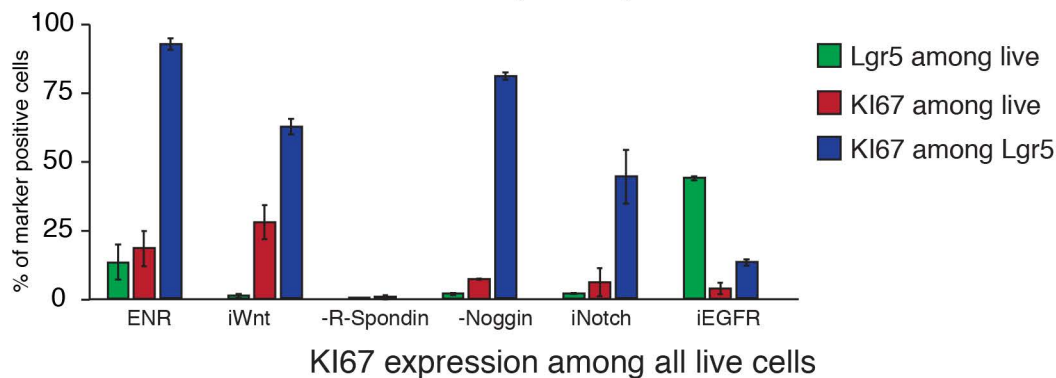
KI67 expression among Lgr5-GFP+ cells

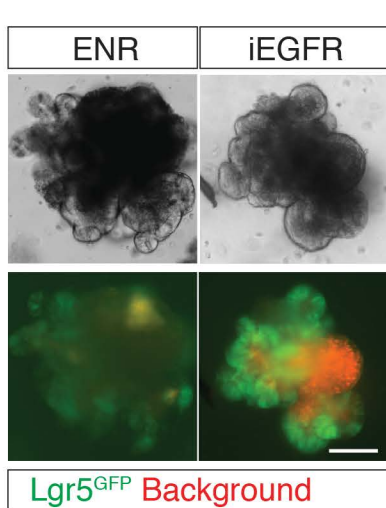
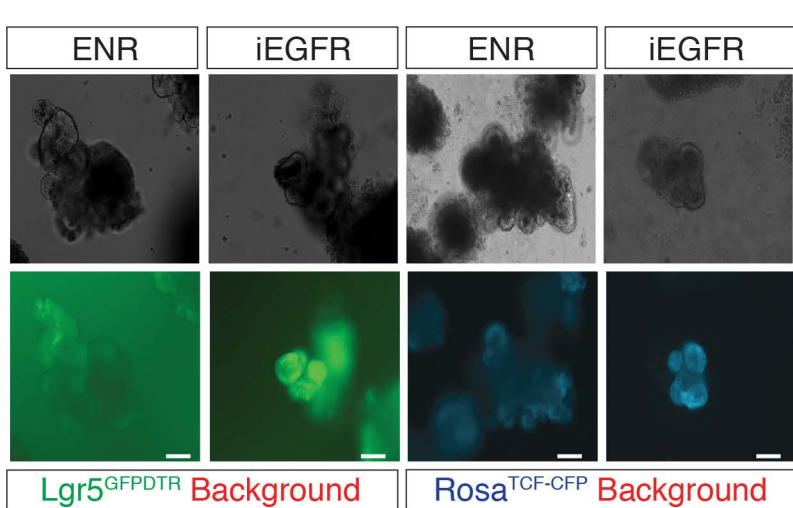
**C**

KI67 expression among all live cells

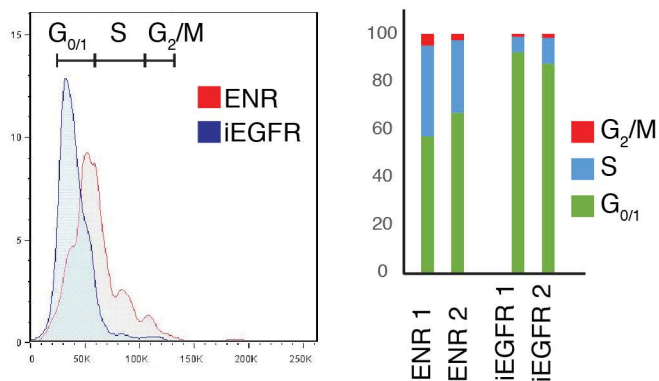
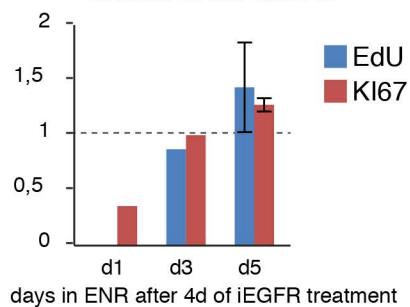
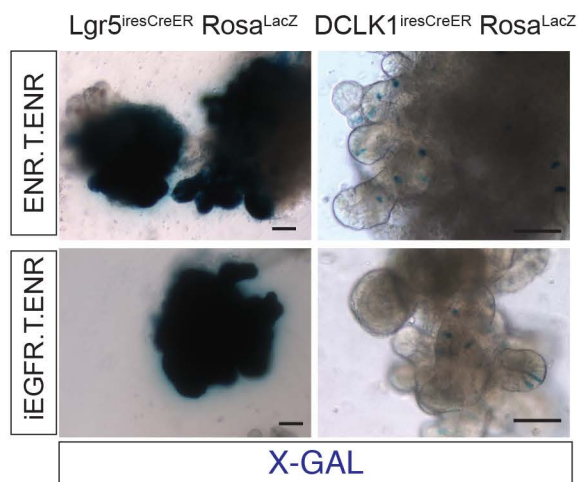
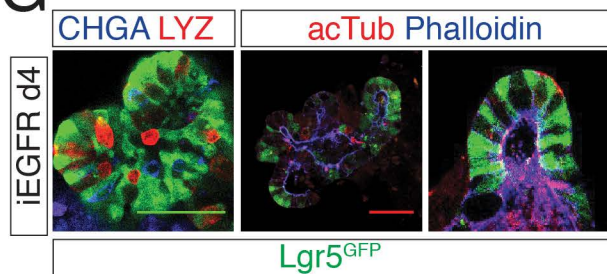
**D**

Quantification of the flow cytometry results

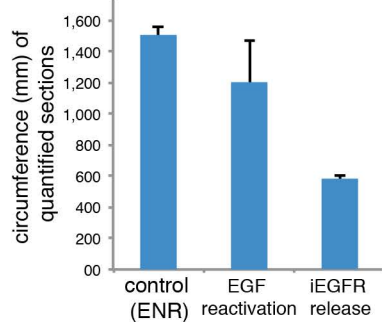
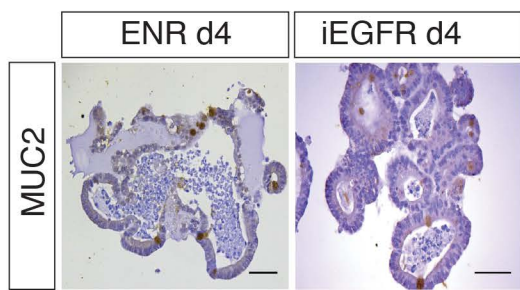


A**B****C**

Cell cycle analysis using the DNA content

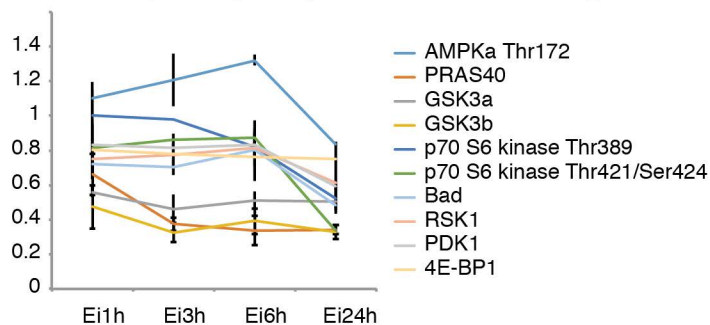
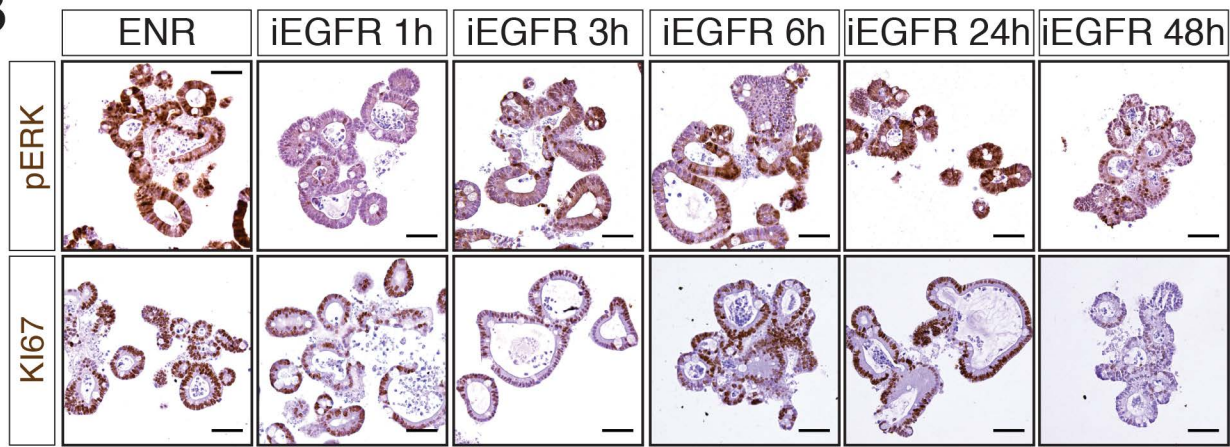
**D** # of cell per circumference (mm) relative to the control**E****G****H**

size of organoid

**F**

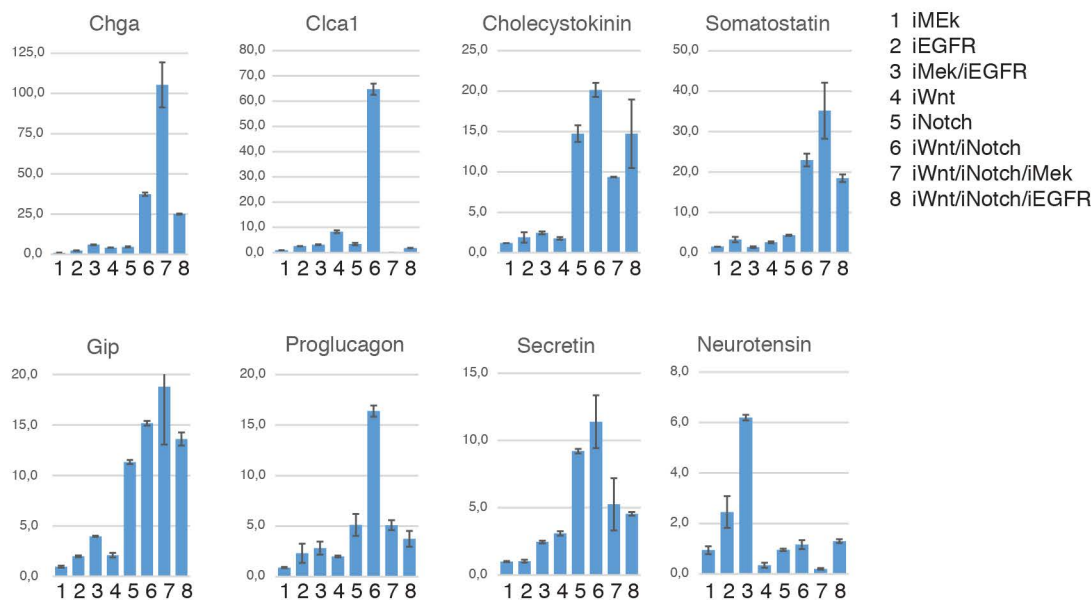
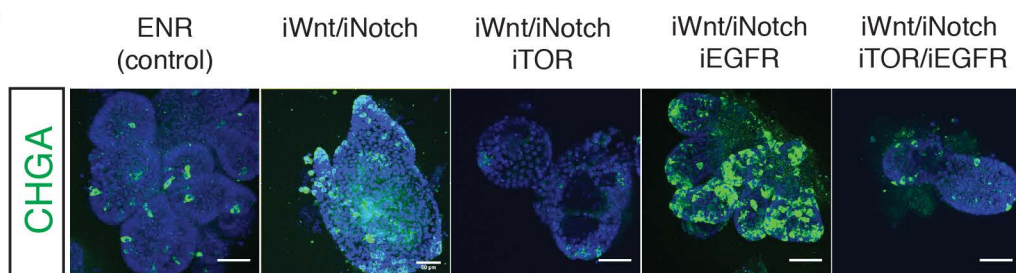
A

Pathscan analysis of phosphorylation
of the AKT pathway components not shown in Figure 3A

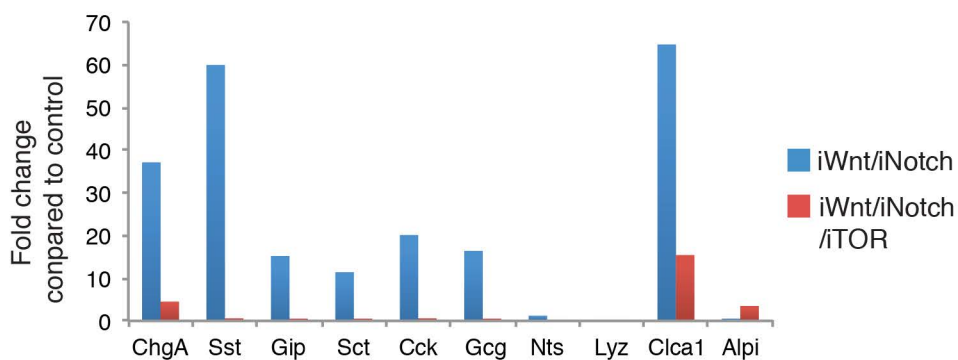
**B**

A

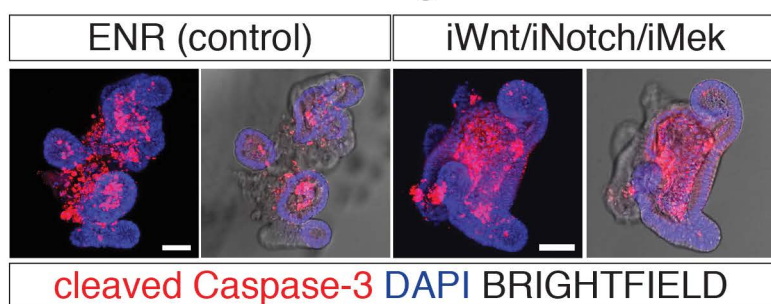
qPCR analysis of marker gene expression

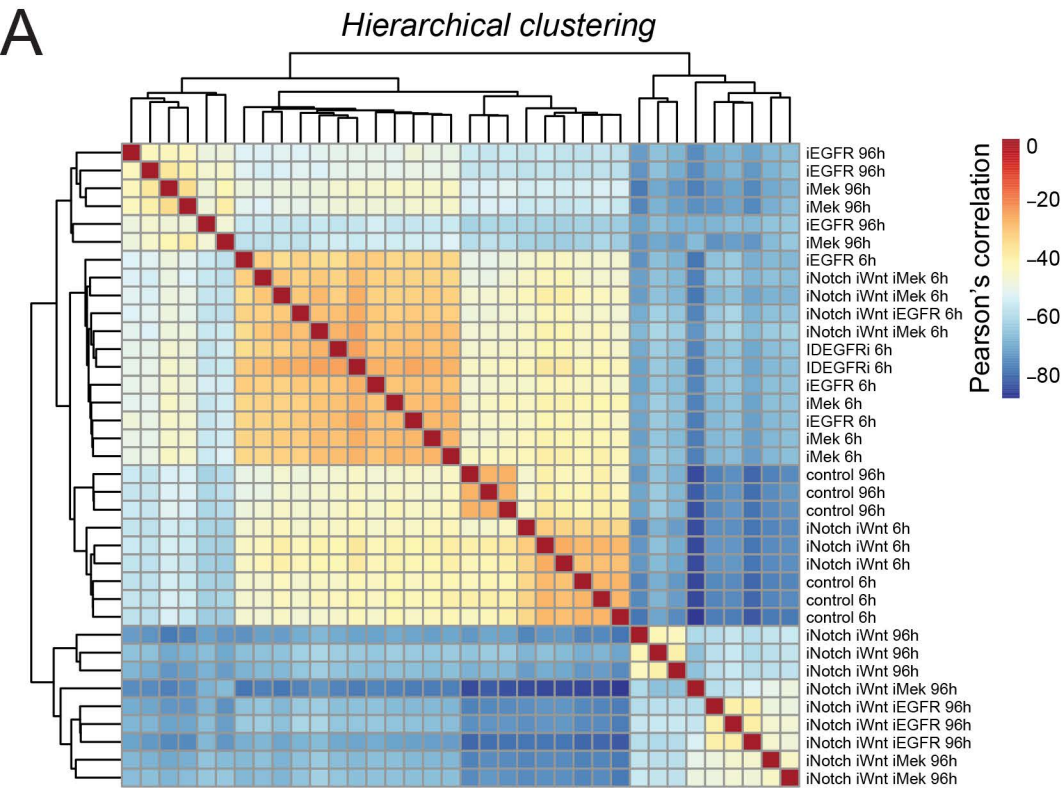
**B****C**

qPCR analysis of marker gene expression

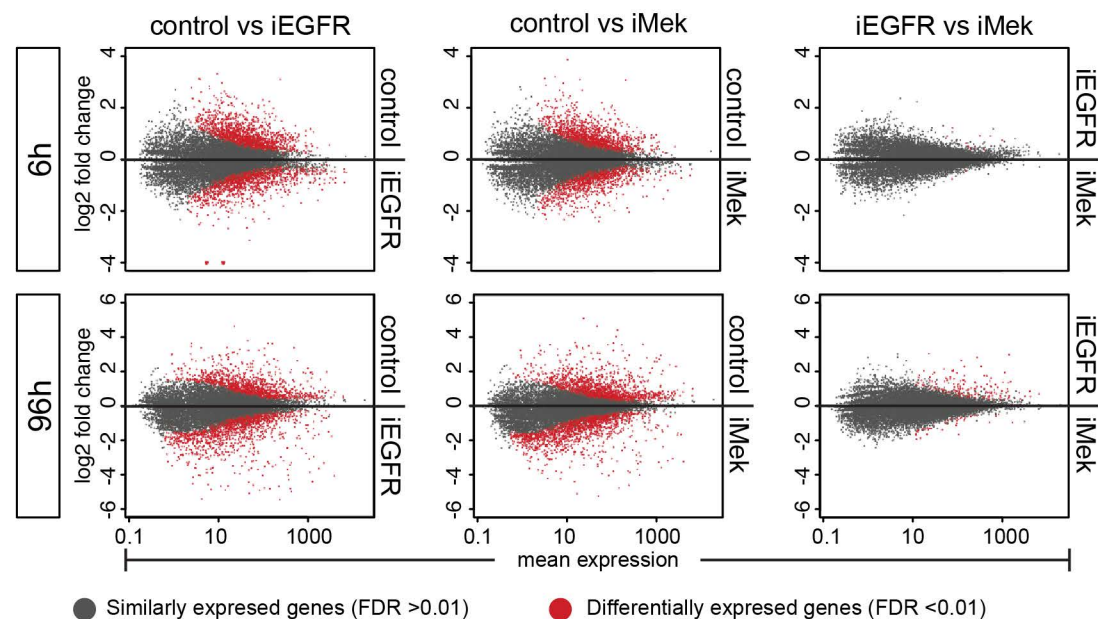
**D**

Cell death in organoids

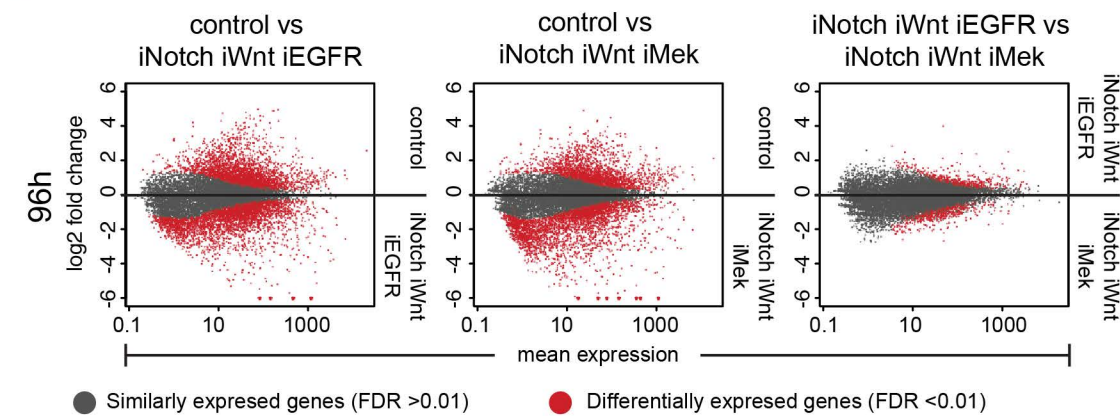


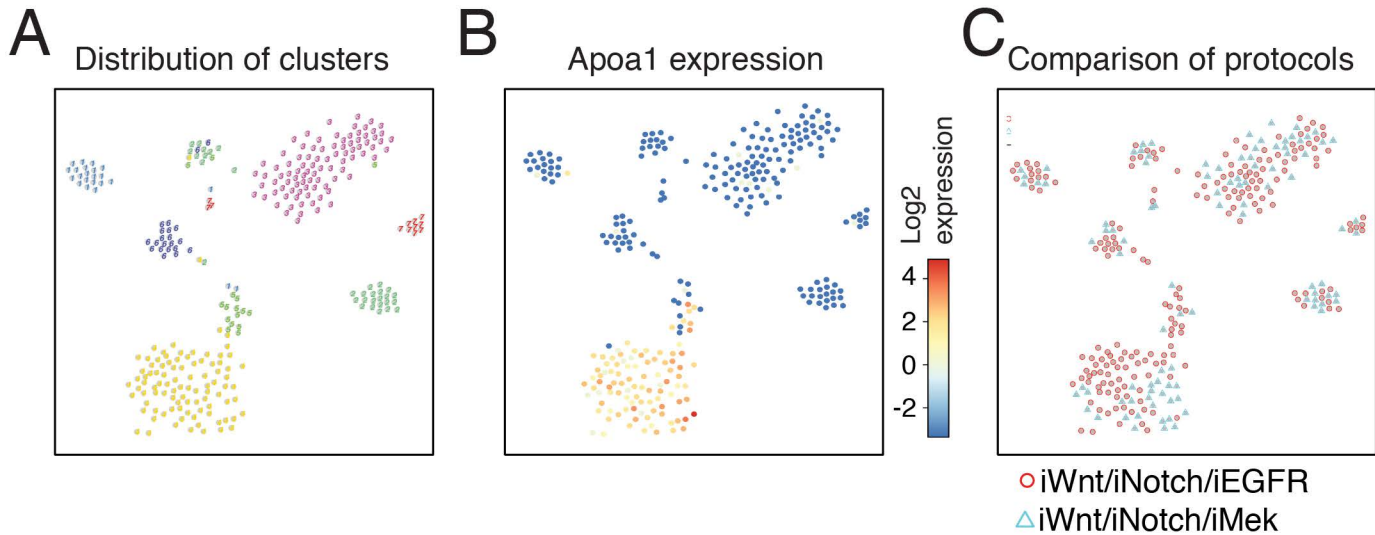


B *Comparison of the transcriptome of treatment groups*

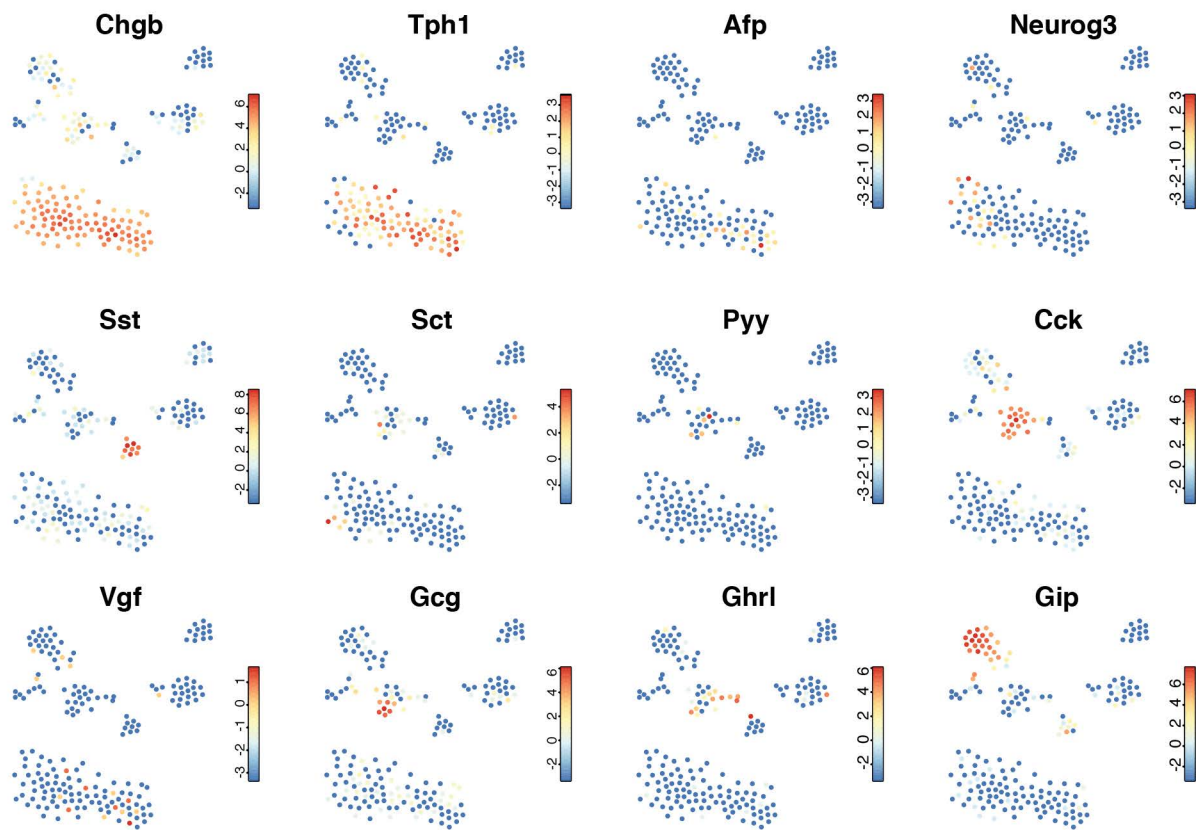


C *Comparison of the transcriptome of treatment groups*





D t-SNE maps displaying the expression of key EEC genes



Supplementary table 2

LRC_WINTON

Profile of the Running ES Score & Positions of GeneSet Members on the Rank Ordered List

Table: GSEA details *[plain text format]*

	PROBE	RANK IN GENE LIST	RANK METRIC SCORE	RUNNING ES	CORE ENRICHMENT
1	Chga	283		2.864 0.0830	Yes
2	Gip	304		2.772 0.1850	Yes
3	Nup98	491		2.169 0.2503	Yes
4	Airm	807		1.651 0.2851	Yes
5	Cldn4	999		1.433 0.3224	Yes
6	Chgb	1203		1.261 0.3522	Yes
7	Plekhg3	1661	0.991	0.3501	Yes
8	Rnd3	1885	0.900	0.3647	Yes
9	Grhl2	2298	0.762	0.3580	Yes
10	Pik3r3	2318	0.757	0.3847	Yes
11	Ano10	2486	0.709	0.3969	Yes
12	Rab23	2729	0.649	0.4005	Yes
13	Ssh2	3352	0.500	0.3659	No
14	Rcn1	3412	0.485	0.3790	No
15	Zfp292	4143	0.336	0.3290	No
16	Arih2	4687	0.246	0.2917	No
17	Hp1bp3	4733	0.240	0.2969	No
18	Fermt1	4806	0.231	0.2993	No
19	Eri3	5306	0.153	0.2623	No
20	9930104L06Rik	5523	0.121	0.2483	No
21	Ccdc77	5625	0.106	0.2437	No
22	Riok1	5898	0.068	0.2229	No
23	Tspan12	5980	0.057	0.2181	No
24	Prelp	6227	0.019	0.1978	No
25	Nfib	6342	0.000	0.1880	No
26	Chd8	6957	-0.085	0.1386	No
27	C230081A13Rik	7401	-0.147	0.1062	No
28	Scnm1	7406	-0.148	0.1113	No
29	Ppat	7759	-0.199	0.0886	No
30	Slc1a5	8138	-0.254	0.0658	No
31	Uevld	8248	-0.273	0.0667	No
32	Fsd1l	9968	-0.588	-0.0586	No
33	Usp1	10018	-0.605	-0.0401	No
34	Rsu1	10560	-0.780	-0.0573	No
35	Myb	10884	-0.947	-0.0495	No
36	Nefm	11207		-1.221 -0.0314	No
37	Mctp2	11520		-1.985 0.0162	No

Supplementary table 3

Gene sets enriched in active Lgr5+ stem cells

GS	SIZE	ES	NES	NOM p-val	FDR q-val	FWER p-val	RANK AT MAX	LEADING EDGE
follow link to MSigDB								
1 HALLMARK_E2F_TARGETS	189	-0.60	-2.72	0.000	0.000	0.000	2658	tags=68%, list=27%, signal=91%
2 HALLMARK_MYC_TARGETS_V1	195	-0.60	-2.66	0.000	0.000	0.000	2891	tags=70%, list=29%, signal=97%
3 HALLMARK_MYC_TARGETS_V2	57	-0.64	-2.43	0.000	0.000	0.000	2333	tags=67%, list=23%, signal=86%
4 HALLMARK_MTORC1_SIGNALING	181	-0.54	-2.42	0.000	0.000	0.000	1564	tags=46%, list=16%, signal=54%
5 HALLMARK_G2M_CHECKPOINT	187	-0.49	-2.21	0.000	0.000	0.000	1923	tags=50%, list=19%, signal=61%
6 HALLMARK_CHOLESTEROL_HOMEOSTASIS	62	-0.52	-1.96	0.000	0.000	0.001	977	tags=44%, list=10%, signal=48%
7 HALLMARK_GLYCOLYSIS	159	-0.39	-1.79	0.000	0.003	0.011	604	tags=19%, list=6%, signal=20%
8 HALLMARK_OXIDATIVE_PHOSPHORYLATION	188	-0.37	-1.67	0.000	0.007	0.030	2980	tags=47%, list=30%, signal=66%
9 HALLMARK_UNFOLDED_PROTEIN_RESPONSE	105	-0.37	-1.52	0.000	0.019	0.090	1677	tags=32%, list=17%, signal=39%
10 HALLMARK_DNA_REPAIR	132	-0.24	-1.05	0.337	0.448	0.908	3024	tags=50%, list=30%, signal=71%
11 HALLMARK_MITOTIC_SPINDLE	182	-0.22	-0.99	0.538	0.563	0.965	1263	tags=20%, list=13%, signal=23%
12 HALLMARK_PI3K_AKT_MTOR_SIGNALING	90	-0.23	-0.95	0.589	0.619	0.981	1491	tags=20%, list=15%, signal=23%
13 HALLMARK_REACTIVE_OXIGEN_SPECIES_PATHWAY	38	-0.25	-0.84	0.731	0.813	0.997	3072	tags=47%, list=31%, signal=68%

Table: Gene sets enriched in quiescent Lgr5+ stem cells

GS	SIZE	ES	NES	NOM p-val	FDR q-val	FWER p-val	RANK AT	LEADING EDGE
follow link to MSigDB								
1 HALLMARK_TNFA_SIGNALING_VIA_NFKB	144	0.57	1.92	0.000	0.001	0.001	2055	tags=47%, list=21%, signal=58%
2 HALLMARK_COAGULATION	67	0.58	1.83	0.000	0.002	0.006	544	tags=25%, list=5%, signal=27%
3 HALLMARK_INFLAMMATORY_RESPONSE	94	0.54	1.78	0.000	0.004	0.015	1544	tags=35%, list=15%, signal=41%
4 HALLMARK_APOPTOSIS	120	0.50	1.67	0.000	0.012	0.051	2025	tags=36%, list=20%, signal=44%
5 HALLMARK_INTERFERON_ALPHA_RESPONSE	66	0.53	1.64	0.002	0.015	0.083	2575	tags=50%, list=26%, signal=67%
6 HALLMARK_IL6_JAK_STAT3_SIGNALING	56	0.53	1.62	0.005	0.016	0.105	2428	tags=48%, list=24%, signal=63%
7 HALLMARK_KRAS_SIGNALING_DN	69	0.52	1.61	0.004	0.015	0.115	1582	tags=39%, list=16%, signal=46%
8 HALLMARK_INTERFERON_GAMMA_RESPONSE	126	0.47	1.56	0.004	0.025	0.207	2300	tags=41%, list=23%, signal=53%
9 HALLMARK_KRAS_SIGNALING_UP	107	0.46	1.54	0.004	0.031	0.278	2464	tags=46%, list=25%, signal=60%
10 HALLMARK_PANCREAS_BETA_CELLS	23	0.56	1.46	0.057	0.064	0.518	1325	tags=30%, list=13%, signal=35%
11 HALLMARK_TGF_BETA_SIGNALING	47	0.47	1.39	0.058	0.124	0.794	2753	tags=49%, list=28%, signal=67%

12	HALLMARK_BILE_ACID_METABOLISM	80	0.41	1.32	0.063	0.204	0.951	2166	tags=31%, list=22%, signal=40%
13	HALLMARK_UV_RESPONSE_DN	102	0.40	1.32	0.061	0.195	0.957	2765	tags=39%, list=28%, signal=54%
14	HALLMARK_COMPLEMENT	110	0.40	1.31	0.066	0.190	0.960	1574	tags=27%, list=16%, signal=32%
15	HALLMARK_MYOGENESIS	96	0.40	1.29	0.094	0.214	0.984	1125	tags=25%, list=11%, signal=28%
16	HALLMARK_EPITHELIAL_MESENCHYMAL_TRANSITION	77	0.39	1.26	0.128	0.248	0.993	2055	tags=38%, list=21%, signal=47%
17	HALLMARK_HEDGEHOG_SIGNALING	19	0.51	1.24	0.216	0.264	0.997	2727	tags=68%, list=27%, signal=94%
18	HALLMARK_ALLOGRAFT_REJECTION	82	0.37	1.20	0.191	0.347	1.000	2025	tags=26%, list=20%, signal=32%
19	HALLMARK_P53_PATHWAY	167	0.35	1.19	0.154	0.335	1.000	1562	tags=26%, list=16%, signal=30%
20	HALLMARK_ESTROGEN_RESPONSE_EARLY	159	0.34	1.17	0.185	0.375	1.000	1618	tags=28%, list=16%, signal=33%
21	HALLMARK_ESTROGEN_RESPONSE_LATE	147	0.33	1.11	0.271	0.500	1.000	1618	tags=24%, list=16%, signal=29%
22	HALLMARK_HYPOXIA	144	0.31	1.06	0.345	0.598	1.000	1383	tags=28%, list=14%, signal=32%
23	HALLMARK_WNT_BETA_CATENIN_SIGNALING	31	0.39	1.06	0.383	0.585	1.000	1250	tags=19%, list=13%, signal=22%
24	HALLMARK_APICAL_SURFACE	24	0.39	1.02	0.443	0.662	1.000	1554	tags=25%, list=16%, signal=30%
25	HALLMARK_ANDROGEN_RESPONSE	81	0.31	1.00	0.492	0.704	1.000	2024	tags=25%, list=20%, signal=31%
26	HALLMARK_ADIPOGENESIS	171	0.29	0.98	0.531	0.714	1.000	1603	tags=18%, list=16%, signal=21%
27	HALLMARK_APICAL_JUNCTION	111	0.30	0.98	0.510	0.696	1.000	2508	tags=31%, list=25%, signal=40%
28	HALLMARK_XENOBIOTIC_METABOLISM	136	0.28	0.92	0.631	0.805	1.000	983	tags=12%, list=10%, signal=13%
29	HALLMARK_HEME_METABOLISM	148	0.27	0.90	0.688	0.821	1.000	2763	tags=33%, list=28%, signal=45%
30	HALLMARK_UV_RESPONSE_UP	115	0.27	0.90	0.639	0.795	1.000	1523	tags=21%, list=15%, signal=24%
31	HALLMARK_PEROXISOME	83	0.28	0.90	0.650	0.771	1.000	2721	tags=31%, list=27%, signal=43%
32	HALLMARK_IL2_STAT5_SIGNALING	133	0.25	0.85	0.761	0.846	1.000	3042	tags=39%, list=30%, signal=55%
33	HALLMARK_SPERMATOGENESIS	66	0.27	0.82	0.780	0.861	1.000	1716	tags=21%, list=17%, signal=25%
34	HALLMARK_FATTY_ACID_METABOLISM	130	0.22	0.74	0.913	0.949	1.000	1599	tags=15%, list=16%, signal=18%
35	HALLMARK_PROTEIN_SECRETION	88	0.15	0.50	0.999	1.000	1.000	3469	tags=27%, list=35%, signal=41%
36	HALLMARK_NOTCH_SIGNALING	25	0.19	0.50	0.985	0.998	1.000	3342	tags=40%, list=33%, signal=60%

Supplementary table 5

qPCR primers used in this study

mRNA name	Forward primer	Reverse primer
Mki67	CCAGCTGCCTGTAGTGTC AA	TCTTGAGGCTCGCCTTGATG
Ccnb2	GCCAAGAGCCATGTGACTATC	CAGAGCTGGTACTTTGGTGTTT
Lgr5	ACCCGCCAGTCTCCTACATC	GCATCTAGGCGCAGGGATTG
Atoh1	GCTGTGCAAGCTGAAGGG	TCTTGTCGTTGTTGAAGG
Chga	CAGCTCGTCCACTCTTTCCG	CCTCTCGTCTCCTTGGAGGG
Lyz1	GGAATGGATGGCTACCGTGG	CATGCCACCCATGCTCGAAT
Clca1	ACTAAGGTGGCCTACCTCAA	GGAGGTGACAGTCAAGGTGAGA
Alpi	AGGATCCATCTGTCCTTTGG	ACGTTGTATGTCTTGGACAG
Sct	GACCCCAAGACTCAGACG	TTTCTGTGTCCTGCTCGCT
Gcg	CTTCCCAGAAGAAGTCGCCA	GTGACTGGCACGAGATGTTG
Cck	GAAGAGCGGCGTATGTCTGT	CCAGAAGGAGCTTTGCGGA
Sst	GACCTGGGACTAGACTGACC	CCAGTTCCTGTTCCCGGTG
Gip	AACTGTTGGCTAGGGGACAC	TGATGAAAGTCCCCTCTGCG
Nts	TGCTGACCATCTCCAGCTC	GAATGTAGGGCCTTCTGGGT